ELECTRONIC AND MAGNETIC PROPERTIES OF ORDERED AND DISORDERED BINARY ALLOY Ni-Al

A THESIS SUBMITTED TO THE

CENTRAL DEPARTMENT OF PHYSICS

INSTITUTE OF SCIENCE AND TECHNOLOGY

TRIBHUVAN UNIVERSITY

NEPAL

FOR THE AWARD OF

DOCTOR OF PHILOSOPHY

IN PHYSICS

By

Saran Lamichhane

AUGUST 2019

ELECTRONIC AND MAGNETIC PROPERTIES OF ORDERED AND DISORDERED BINARY ALLOY Ni-Al

A THESIS SUBMITTED TO THE

CENTRAL DEPARTMENT OF PHYSICS

INSTITUTE OF SCIENCE AND TECHNOLOGY

TRIBHUVAN UNIVERSITY

NEPAL

FOR THE AWARD OF

DOCTOR OF PHILOSOPHY

IN PHYSICS

By

Saran Lamichhane

AUGUST 2019

DECLARATION

Thesis entitled **"Electronic and magnetic properties of ordered and disordered binary alloy Ni-Al "** which is being submitted to the Central Department of Physics, Institute of Science and Technology (IOST), Tribhuvan University, Nepal, for the award of the degree of Doctor of Philosophy (Ph.D.), is a research work carried out by me under the supervision of Prof. Dr. Narayan Prasad Adhikari, Central Department of Physics, Tribhuvan University, Kirtipur, Nepal.

This research is original and has not been submitted earlier in part or full in this or any other form to any university or institute, here or elsewhere, for the award of any degree.

.....

Saran Lamichhane

RECOMMENDATION

This is to recommend that **Saran Lamichhane** has carried out research entitled **"Electronic and magnetic properties of ordered and disordered binary alloy Ni-Al "** for the award of Doctor of Philosophy (Ph.D.) in **Physics** under my supervision. To my knowledge, this work has not been submitted for any other degree.

He has fulfilled all the requirements laid down by the Institute of Science and Technology (IoST), Tribhuvan University, Kirtipur for the submission of the thesis for the award of Ph.D. degree.

.....

Dr. Narayan Prasad Adhikari,
Supervisor
Professor
Central Department of Physics,
Tribhuvan University,
Kirtipur, Kathmandu,
Nepal

AUGUST 2019

LETTER OF APPROVAL

[Date:8/22/2019]

On the recommendation of **Prof. Dr. Narayan Prasad Adhikari** of Central Department of Physics, Tribhuvan, University, Kirtipur, Kathmandu, Nepal, this Ph.D. thesis submitted by **Saran Lamichhane**, entitled "**Electronic and magnetic properties of ordered and disordered binary alloy Ni-Al** " is forwarded by Central Department Research Committee (CDRC) to the Dean, Institute of Science and Technology (IoST), Tribuvuan University (TU).

.....

Dr. Binil Aryal
Professor,
Head,
Central Department of Physics,
Tribhuvan University
Kirtipur, Kathmandu,
Nepal

ACKNOWLEDGMENTS

First of all I would like to give sincere appreciation to my Ph.D. advisor Prof. Dr. Narayan Prasad Adhikari of Tribhuvan University, Kirtipur, Nepal for his single supervision.

I thank Prof. B. Aryal, HoD of Central Department of Physics who helped me from his side. I thank all those people whom I met during my three month stay in Michigan and Uppsala, who have helped me along this PhD journey and made my stay there a memorable experience, although their names not have been mentioned here. I also acknowledge Prof. R. Pandey, Prof. A. Mookerjee for the fruitful discussion. I would like to thank Novelist Dr. Tara Nath Sarma for his suggestion before starting Ph.D., and also expressing sentiments towards nationality.

Besides, I acknowledge seniors and labmates : Dr. G. C. Kaphle, Dr. N. P. Pantha, Mr. S. Pokharel, Mr. S. P. Khanal and Mr. R. P. Koirala for the help.

I thank The Abdul Salam International Centre For Theoretical Physics (ICTP) for the financial support.

The encouragement that I got from family, friends, Professors is the driving force that making me to move energetically in right direction in my life. Finally, thanking Ph.D. supervisor again...

Saran Lamichhane
AUGUST 2019

ABSTRACT

The order-disorder always exist in materials. The structural, electronic and magnetic properties of metals and metallic alloys have been the subject of intense research due to their applications in many technological purpose. Inter-metallic binary alloys of Ni and Al has attracted much attention in the field of science and technology because of their use in computer chips, variety of turbine components, medical implants and commercial applications etc. Magnetic properties and properties based on electronic structure of ordered alloys NiAl and Ni_3Al have been investigated using the first-principles study based on density functional theory and density functional perturbation theory. In order to understand the electronic properties, we have performed electronic band structure calculations. Our findings show that all the systems considered are metallic in nature. To know the contributions of the orbitals in the bands, the system is analyzed via fat bands which reveals most of the contributions on valence band of NiAl and Ni_3Al is due to d-orbital and the contributions on conduction band is due to s and p-orbitals. Furthermore, spin up and spin down calculations have been done to know the magnetic properties of the system. Our calculations also suggest the magnetic nature of Ni_3Al and non-magnetic nature of NiAl. It has been found that the magnetic moment of alloys containing Ni and Al increases with increasing Ni concentration. The study of Ni_3Al is of great interest from magnetic point of view as it has magnetic moment $0.52\mu_B$. The value of magnetic moment of NiAl and Ni_3Al obtained in the present work agrees with previous studies. From the study of liquid state of Ni-Al, it is found that the NiAl melt at 1873 K is ordering in nature which doesn't support de-mixing in the solid form.

In studying vibrational properties, phonon modes in Ni_3Al are observed via phonon dispersion relation, which is different than that from NiAl. Optical branches gets more uniformly shifted in frequency in Ni_3Al than in NiAl. Optical phonons have a non-zero frequency at the center of Brillouin zone and show no dispersion near that long wavelength limit. Modes are originated from electronic bands resulting to mode gap of 1.56 THz in NiAl and reduces the gap while increasing nickel content. Optical properties are analyzed through the calculations of dielectric function, reflectivity and refractive index. The maximum number of free electrons near the Fermi level in NiAl are responsible to change its reflectivity.

LIST OF ACRONYMS AND ABBREVIATIONS

BE	Binding Energy
BOA	Born-Oppenheimer Approximation
DFPT	Density Functional Perturbation Theory
DFT	Density Functional Theory
DOS	Density of States
ELF	Electron Localization Function
eV	Electron Volt
FCC	Face centred Cubic
FM	Ferromagnetic
GGA	Generalized Gradient Approximation
HEG	Homogeneous Electron Gas
HF	Hartree-Fock
H-K	Hohenberg-Kohn
ICTP	International Centre For Theoretical Physics
K. E.	Kinetic Energy
K-S	Kohn-Sham
LDA	Local Density Approximation
PBC	Periodic Boundary Condition
PBE	Perdew Burke and Ernzerhof
PDOS	Projected Density Of States
QE	Quantum ESPRESSO
Ry	Rydberg
SCF	Self Consistent Field
TB	Tight Binding
TDOS	Total Density Of States
TU	Tribhuvan University
TWAS	Third World Academy of Science
vdW	van der Waals
XC	Exchange Correlation

LIST OF TABLES

Page No.

LIST OF FIGURES

Page No.

TABLE OF CONTENTS

CHAPTER 1

1. INTRODUCTION

The study of materials and their properties has been ongoing for as long as the existence of human being. Men used stones as materials for tools to improve their lifestyles at the stone age. People learnt to melt copper and tin to make bronze ($\approx$ 2000 B.C.) and utilize it in proper way. Materials have played an integral role in forming the society that we have now. There is no usage of materials without interaction to the environment. Therefore, the knowledge of interaction from microscopic level to macroscopic level is essential in understanding the materials properties (Sands et al., 1990). The impact of any materials in environment is always interesting. Materials theory researches highlights on predicting, modelling, and designing materials what people encounter in their daily life. The main basis for understanding materials depends on understanding their electronic structure. Materials always interact in environment. Non living things interact to both living and non living environment. So, materials research area rely all branches of science and technology in today's world. This field has helped to make better connection between them. Interaction is different for different species/materials. Detail investigation on the matter is essential before using. Alloys are metallic substances composed of a mixture or metallic solid solution of two or more metals. They can even be composed of a metal and another element which may be non-metallic to produce an alloy. An alloy usually has different properties from the elements that it is composed of. Alloying has been found to be a pivotal role to address the shortcoming in the individual element. Desirable properties can be dragged on alloying two or more materials. Concentration variation in elements produces alloys with different properties. They can be classified into two types, substitutional or interstitial alloys which difference depends on the arrangement of the atoms that make up them. There are several combinations of alloys which can be received by combining different elements to have different properties and applicable for different purposes. The uses of alloys are wide, and they can be functionalized to help different works by mixing metals to get alloys with particular properties as we desired. It is used in industries, military operation and as medical instruments. Some examples of alloys are Al, Cu, stainless steel and bronze,

with each of them having distinct properties. It can be prepared to increase stability. Dealing the properties of alloys in liquid state provides unique information that can be used to improve the qualities of materials in the solid state. But the experimental study of the thermo-physical properties of alloys in molten state is a difficult task because of the problems created by high temperature, chemical reactivity etc. Alloys have been used for a very long time, even before modern technology. However, the progress in alloy technology since the last few decades. Copper was the first metal to be extracted from an ore and it was later combined with tin to create bronze. Today there are various combinations of alloys that fulfil the demand of today society. Nepal is rich in minerals. Occurrences of Ni are reported from different parts of the country however, they are limited so their proper utilization can be carried out only knowing its properties. Strength can be maintained after alloying. Alloys made out of the combination of copper and zinc is known as brass. These alloys are used to make musical instruments. All metals are not in pure form. Jewellery that made from silver and gold do not usually contain pure form of gold or silver but have a certain amount of Cu or other metals to provide the jewellery with longer lasting properties. Also, when iron is extracted from its ore, it produces alloys that have vary in amount of carbon.

1.1 Metallic alloys

Inter-metallics are a unique group of materials composed of two (or more) types of metal (or metal and non-metal) atoms, which exist as solid compounds and differ in a structure from that of the constituent components. In comparison to metals and alloys, used before, inter-metallic based alloys exhibit several distinct features. The study of the electronic properties of solids in terms of interaction of electrons in the solid, is one of the important interfaces between theories and experiments in the field of solid state science. There is no usage of materials without interaction to the environment. Some of the many interesting applications for inter-metallic compounds include hydrogen storage, superconductivity, energy storage (e.g. batteries) and magnetism. The basis for understanding any materials ultimately rests upon understanding their electronic structure (Probert, 2011; Martin, 2004; Lamichhane et al., 2015). The knowledge of interaction from microscopic level to macroscopic level is essential in understanding the materials properties. The impact of any materials in environment is always interesting. Materials theory researches focus on predicting, modelling, and designing materials what people encounter in their daily life. Materials consists of solids, alloys, ceramics, polymer etc.

Inter-metallic compounds have a wide area of properties ranging from metallic to non-metallic. Inter-metallics are interesting functional materials and also have attracted attention as structural materials for practical applications. An alloy is a metal composed

of more than one element and may have properties different from those of its original elements. An example of a man-made alloy is bronze made from Cu and Sn but is stronger than Cu and Sn and can be utilized to make various tools. Stability is changed after alloying and stable system is favoured by nature. Similarly, steel, a widely used alloy of Fe and C that is harder than pure Fe. The world of this century is of electromagnetism. Magnetic materials are characterized by their tendency towards magnetism. Magnetism of materials is the specific property, related to density of states. Magnetism is the property of a material which shows attraction or repulsion when an magnet is brought near to it. Since all matter somehow responds to a magnetic field, it is useful to introduce the concept magnetic materials. Magnetic materials can be classified by how their magnetic dipoles are oriented relative to each other; parallel, anti-parallel or not at all. There is always importance of spin while dealing magnetism of materials. Besides, distribution of magnetic moment in the system plays a vital role to determine the quality of materials.

1.2 Interactions in alloys

Nickel (Ni) belongs to transition element. Production of Ni is in large scale, increasing per year. The global production of nickel is used to stainless, non-ferrous alloys, in electroplating and in other uses. Nickel has gained its beauty with its fascinating properties. Nickel is used in many consumer products, including alnico magnets, coinage metals, rechargeable batteries, electric guitar strings, microphone capsules, plating on plumbing fixtures, and special alloys such as invar. It is used for plating and as a green tint in glass. Nickel is alloy metal, and its chief use is in nickel steels and nickel cast irons, in which it typically increases the tensile strength, toughness, and elastic limit. It is widely used in many other alloys, including nickel brasses and bronzes and alloys with Cu, Cr, Al, Au, Pb and Co. alloys are promising candidate for shape memory alloys. Ni is one of the widely used natural source of element. Besides its dominant presence in nature, it is superior over metals and ferromagnetic metal and super-alloys mainly due to good oxidation resistance, low density, which makes it useful in many applications such as aircraft turbine engines, medical implants, nuclear power plants and many chemical and petrochemical industries. (Darolia et al., 1999) So the development of today economy is highly dependent on the proper utilization of nickel based alloys.

The production of Ni is increasing day by day in the world. The production is creasing rapidly from 2012. So the importance of any materials depends on its proper utilization in daily life. The test on quality of materials is essential before using in practical purpose. Ni metal is reserved due to its importance in industry and commercial market.

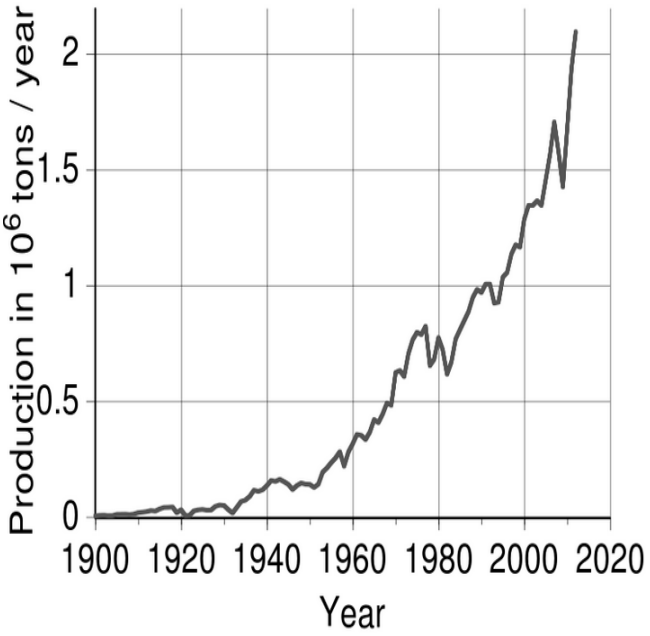

Figure 1: Production of Ni across the world, US Geological survey, 2014

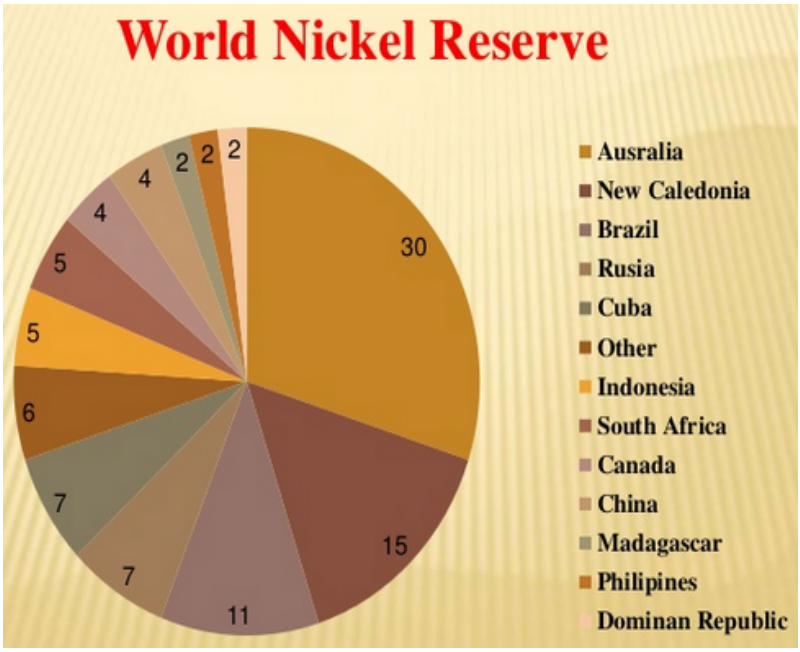

Figure 2: Reservation of Ni across the world, US Geological survey, 2014

Similarly, aluminium is a post-transition element which has a bit different characteristics from that of Ni. Properties such as light weight and great strength allow aluminium to be used in several different industries. Applications of aluminium include transportation, electrical applications, construction and medicine. The combination of these two element is expected to get desired properties for the modern science and technology. Ni, a ferromagnetic material, when alloyed with other Al, it is expected to observe synergistic effect as result we can tune the properties as we wish. When Ni alloyed with Al, it has given different properties as shown in table 1.

Table 1: Melting Point (MP), density and thermal conductivity(K) of Ni, Al and NiAl.

Properties	Ni	Al	NiAl
MP(K)	1728	933.4	1955
K (W/(m.K))	90.9	237	76
Density(gm/cm^3)	8.908	2.7	5.9

From table it is reported that Ni has lower thermal conductivity than that of Al. But alloying reduces its thermal conductivity. Besides, Ni forms $NiAl_3$, Ni_3Al, $NiAl_2$, after alloying with aluminium depending on the proportion of constituent. NiAl is found to be stable. Historical development on NiAl begun from 1960. During the early 1960, NiAl was supposed to have potential as a general high temperature structural material, and by the mid 1960 was known as a probable material to use in a super-alloy turbine vane(Singleton et al., 1966) Unfortunately, by the end of the 1960 no solution was found for the low-temperature brittleness and consequently industrial and governmental interest waned. Studies from about 1968 through 1980 focused to know the deformation mechanisms, after which research interest again reduced. In the mid-1980 the discovery could improve ductility in Ni,Al, along with the development of new processing techniques, deep interest in developing ductile intermetallic materials and NiAl research again decorated and has since grown slowly. NiAl has a much higher thermal conductivity than superalloys, the temperature distribution in a high-temperature component would be uniform, reducing the life-limiting hot spot temperature by 50 K (Darolia et al., 1999).

1.3 Rationale of the study

Metallic alloys are important because of their dominant occupancy in nature. Properties such as light weight and great strength allow Al to be used in several different industries. Ni has good oxidation resistance and it has own beauty. There are many debate regarding to the magnetization of Ni_3Al and Ni_3Ga. We will focus on it in our study. Hackenbracht and his co-workers (Darolia et al., 1999) used TB-LMTO-ASA for the study of electronic and magnetic properties. They found the magnetic moment of Ni_3Al as 0.09 μ_B per unit cell. Later on (El Fatmi & Ghazouani, 2011) investigated electronic and magnetic properties of Ni_3Al with magnetic moment 0.44 μ_B per unit cell. Hence due to various applications of NiAl and Ni_3Al and lack of detailed work or controversial results in experimental and theoretical works for values of magnetic moment, we focus to study the electronic and magnetic properties of these inter-metallic alloys

1.4 Objectives of the study

The main objectives of this thesis are summarized as follows.

(i) The changes in geometrical parameters and stability of NiAl and Ni_3Al as a function of lattice parameter is discussed by the first-principles technique.

(ii) Lattice parameters obtained from energetically stable structures is used to functionalize alloys, varying Ni concentrations and is studied their electronic properties along with its optical properties.

(iii) Spin fluctuation, magnetization, density of states and role of partial density of states in NiAl, Ni_3Al, NiGa and Ni_3Ga are studied to understand the magnetic properties.

(iv) Properties of solid NiAl and the same in molten state is studied to observe phase change stability.

1.5 Organization of the thesis

The structure of this thesis is organized as follows:

(i) In chapter 2, we shall discuss in detail the available literature related to the present work. The chapter is named as Literature Review, which aims to prepare the required background and justify the objectives of the study.

(ii) We present the theoretical background, formulas and algorithm that we have used during the entire work in Materials and Methods (Chapter 3). Basic introduction of density-functional theory with some special features including the systems under study are discussed in the chapter.

(iii) Chapter 4 presents and discusses the main findings of the present work.

(iv) The conclusions and possible extension of the present work are discussed in Chapter 5. The chapter is named as "Conclusions and Recommendations". "Summary" is written in chapter 6 before the list of references.

CHAPTER 2

2. LITERATURE REVIEW

The pursuit of modified alloys quality and efficiency is replacing ever increasing demands on today materials world. The discovery of alloys have attracted great interest because of its promising prospects in both basic and applied research point of views. Atomic-level computer simulations provides a powerful tool in bringing fundamental knowledge of materials processes and properties. Alloys are prepared to strengthen pure element and expected to get properties as we desired. The study of materials/alloys and their properties has been ongoing for as long as the existence of human being. Materials have played an integral role in forming the community that we have now. Alloying has been found to play a pivotal role in changing the limitation of element(pure element). No substances are found in use without interaction to the environment. The knowledge of interaction from microscopic level to macroscopic level is essential in understanding the materials properties. The properties of alloys are determined by its composition.

The study of inter-metallic alloys like NiAl and Ni_3Al have great interest because of their uses in high temperature materials, shape memory alloys and soft magnetic materials (Pun & Mishin, 2010). NiAl has been identified as a suitable material for making epitaxial contacts to III-V compound semiconductors. When Nickel is alloyed with Co, Al, Ti and other to form super alloys. Comparing to conventionally used alloys, intermetallic based alloys show many specific forms. Moreover, a development of composite materials with Ni_3Al based alloys as a matrix made solid by graphene, SiC and TiC is also observed (Jozwik et al., 2015; Deligoz et al., 2014). The low density of NiAl has helped to desirable decrement in the weight of turbine blades and aircraft parts. Due to low density and high thermal conductivity, Ni-Al alloys give reward as structural alloys in applications for gas turbine (Pun & Mishin, 2010; Lee et al., 2000). These noble characters of Ni-Al alloy have attracted the most current assent of the researches to investigate the structural, electronic, magnetic, thermodynamic and vibrational properties of Ni-Al solid and liquid alloys. The NiAl alloys which shows phase transformations in ranging 60 to 65 atomic percentage of nickel are widely used in technical field (Kazanc & Tatar, 2008). de Boer and co-workers used LMTO with in ASA to find optical con-

ductivity and band structure of NiAl and found a bit different band structure in terms of symmetric point R, comparing to previous calculations. NiAl decorates for suitable system to study on the simple phenomena in ordered alloys due to its crystal structure and, by natural elongations, reconstructions of its surface produced from bulk termination (Miracle et al., 1993). Additionally, NiAl is known as a suitable material for making contacts compound semiconductors (Sands et al., 1990). NiAl is appropriate material for many applications due to ratio of mass of Ni to Al greater than two as they yield gap (Mostoller et al., 1989; Ravindran et al., 1996), so it is important to know its phonon interaction. The STM data obtained due to correlation of simulation can be described as the nickel density of states dominating at the surface as Ni dominates in band structure and density of states of NiAl (Lamichhane et al., 2016) and is found to be strongly interacting system at 1873 K and ordering tendency is found to be in 40 and 60 % of Ni. The impact of any materials in environment is always interesting. Besides, materials with higher thermal conductivity can give uniform temperature distribution in a turbine air-foil (Darolia et al., 1999). Since NiAl has a much higher thermal conductivity than superalloys, the temperature distribution in a high-temperature component would be more uniform. NiAl also posses a greater oxidation resistance than any other high-temperature alloy or coating material. Thermal conductivity is one of the most important property in nickel based alloys and as it makes possible use for the design of turbine air-foil because of having lower density (5.9 g cm^{-3}) than other super-alloys. NiAl has four main advantages: its density (5.9 g cm^{-3}) is two-thirds the density of nickel-base superalloys; its thermal conductivity is 4-8 times that of nickel-base superalloys; it has excellent oxidation resistance; and its simple, ordered, BCC crystal structure makes plastic deformation easier compared to many other intermetallic compounds. These noble properties of Ni-Al and Ni-Ga alloy have attracted to researchers for the investigation of its electronic and magnetic properties. Many experimental and theoretical works (Hsu & Wang, 2004; Boucetta, 2014) on Ni-Ga have been performed to know the electronic, optical, magnetic, elastic properties of our interested compounds. However, electronic band structures along with electronic transitions are poorly described. In addition, the diverse nature in the value of magnetic moment of Ni_3Ga and Ni_3Al calculated in previous work (Aguayo et al., 2004) made us curious to know the reality behind it. From the previous study it is found that Ni-rich NiAl intermetallic alloys form stable $L1_2$ phase, with simple cubic structure Cu_3Au structure. Electronic and magnetic properties are studied using various techniques. However, Hackenbracht and his co-workers (Darolia et al., 1999) used TB-LMTO-ASA for the study of electronic and magnetic properties. They found the magnetic moment of Ni_3Al as 0.09 μ_B per unit cell. Later on (Zhu et al., 1998) investigated electronic and magnetic properties of Ni_3Al with magnetic moment 0.44 μ_B per unit cell. Hence due to various applications of NiAl and Ni_3Al and lack of detailed work or controversial experimental and theoreti-

cal values in magnetic moment, we intend to study the electronic and magnetic propertis of these intermetallic alloys. The spins fluctuation obtained stronger in Ni_3Ga than that found in Ni_3Al (Aguayo et al., 2004), and zero magnetic moment obtained in experimental work are still controversial. The limitations of local density approximation for physics of ferro-magnetism in Ni_3Al and Ni_3Ga qualitatively and unlike to ferromagnetic quantum critical point as suggested in previous work (Aguayo et al., 2004) is another problem in front of us. The concepts of spin polarization, nature of density of states will add other useful information to the present understanding of the alloy system. The calculated parameters related to magnetism are still in debate. Previously reported value (0.75 μ_B) of magnetic moment Ni_3Al (Hsu & Wang, 2004), which is greater than the experimental value 0.23 μ_B per unit cell (Aguayo et al., 2004). There is controversy in magnetic moment of Ni_3Al with the values ranging from 0 to 0.7 μ_B/cell (Moruzzi, 1990). Metallic properties of compounds have been studying by using standard models such as Landau Fermi liquid theory. However, the properties of metals near to magnetic phase transitions at low T are found to be different from these models. At ambient pressure both Ni_3Ga and Ni_3Al orders ferromagnetically below 41 K with a small average moment of 0.075μ_B/Ni in the low-temperature, low magnetic field limit (Smith, 2009). The ferromagnetism is decreased by the application of hydrostatic pressure and Ni_3Al is found to become paramagnetic above 82 kbar pressure. By contrast Ni_3Ga, which has the same crystal structure and a similar electronic structure (Smith, 2009), lies on the paramagnetic side of the quantum critical point. Therefore, these two materials form a good basis on which to test the SCR model in both the ferromagnetic and paramagnetic state. (Smith, 2009) suggested that Ni_3Al is found to be explained by the standard form of such a model, the data on Ni_3Ga require us to extend the model to take into account the fact that this system lies close to a tri-critical point.So difference of these compounds can have some hidden facts, which is to be solved. Interest on the importance of vibrational properties with vibrational entropy on thermodynamical stabilities order-disorder transition alloys phases. Although some key issues concerning the mechanical properties of NiAl are still unresolved, recent progress in increasing strength along with a better understanding of the deformation mechanisms, warrants optimism for the commercialization. The research interest on NiAl has been growing over the last 50 years and will continue to do so based on plans of research laboratory. Miedema and his group (Miedema et al., 1973) discussed the role of electronegativity in alloys formation. So the investigation on the electronic density of states, charge transfer phenomenon are also important to utilize the alloys in practise. It is reported that the degrees of charge transfer takes place from Al site to the transition metal sites as one goes from FeAl to CoAl to NiAl (Sundararajan et al., 1995) in which the magnetism of elements Ni, Co, Fe is mostly quenched in the stoichiometric phases, with only FeAl retaining a magnetic moment of about 0.7μ_B /atom. we have also made a target to check on NiAl

to know the reality behind them. Alloying behaviour of Ni_3Al important as its research progress carried on 1984 with other similar compounds Ni_3Ga and Ni_3Si. (Ochial et al., 1984). Diffusion of Ni is sensitive as suggested in previous work (Hancock & McDonnel, 1971) has made additional interest on Ni based superalloys with its electronic and magnetic properties. Graphene is 2D materials with its unique properties. It is also used on Ni to know different characteristics. (Zhao et al., 2011) Mechanical characters of NiAl alloy was studied and found that the strengthening produced by vacancies in Al-rich region of alloys was greater than that in Ni-rich alloys. Recently oxidation was carried out (Ma & Gunther, 2018) by STM simulation on Ni_3Al to know its surface properties. Theoretical and experimental studies on magnetization in Ni_3Al and Ni_3Ga are still in debate as magnetic moment range (0.1-0.7μ_B/cell) observed for Ni_3Al (0-0.8μ_B/cell) observed for Ni_3Ga. No connection has done in between electronic and vibrational properties of NiAl. Roles of DOS of Ni and hybridization effect in Ni based alloys are not well understood. Most of investigations are limited to solid phase of NiAl without connection to molten state. So, we motivated to investigate the properties of Ni-Al in different environment.

CHAPTER 3

3. MATERIALS AND METHODS

3.1 Theoretical Background

Most of properties of materials are determined by state of electrons and nuclei of atom in the crystal structure of materials. The atomic and molecular properties such as magnetic, optical, transport and crystal structures of materials depend on the respective electronic structure. Therefore, study of the electronic structure has always been in the target of condensed matter physics. No materials are found unaccompanied by interaction to environment. This is why the solutions of the electronic structure are not so easy due to the fact that the electronic interactions in matter are quantum mechanical in nature and the complexity of describing them in a quantum mechanical system increases significantly with the increasing number of the electrons. This leads to many-body physics, which gives the shape to know the collective behaviour of interacting electrons. Quantum mechanical problem cannot be solved exactly because of the number of variables (3N number of particles) and the complexity of the equations. We solve the Schrodinger equation given by,

$$\hat{H}\Psi = E\Psi \tag{3.1}$$

3.1.1 Born-Oppenheimer approximation

Born-Oppenheimer approximation is the most powerful adiabatic approximation because it is decoupled to 2 degree of freedom, only consider 1 degree of freedom taking ions as frozen. The physical system such as atoms, molecules and solids contain not only electron but also of nuclei, and each of these particles moves in the field generated by others. Electrons are much lighter than nuclei. The proton weighs $\approx$ 1800 times heavier than that of an electron. So, the motion of nucleus is negligible in comparison to motion of electron. General methods for many-body problems involve approximations. In the continuum, a two body problem can be solved analytically. There is no

solution for more than two bodies. There may be chance of breakdown the uncontrolled approximations. One needs a method to test out, approximate methods to find range of validity. This implies that the exactness of simulation is essential in this kind of research. Thus we consider nucleus as being fixed in Born- Oppenheimer approximation. It allows the construction of energy eigenfunction by separating the dependence of eigenfunctions on electronic and nuclear co-ordinates. The hamiltonian for a molecular system of N-electrons and M-nuclei can be expressed as

$$\begin{aligned}\hat{H} &= -\sum_{j=1}^{N}\frac{\hbar^2}{2m}\nabla_j^2 - \sum_{\alpha=1}^{M}\frac{\hbar^2}{2M_\alpha}\nabla_\alpha^2 - \sum_{j=1}^{N}\sum_{\alpha=1}^{M}\frac{Z_\alpha e^2}{|\vec{r}_j - \vec{R}_\alpha|} \\ &\quad + \sum_{k>j}^{N}\sum_{j=1}^{N}\frac{e^2}{|\vec{r}_j - \vec{r}_k|} + \sum_{\beta>\alpha}^{M}\sum_{\alpha=1}^{M}\frac{e^2 Z_\alpha Z_\beta}{|\vec{R}_\alpha - \vec{R}_\beta|} \\ &= \mathbf{T}_e + \mathbf{T}_n + \mathbf{V}_{ne} + \mathbf{V}_{ee} + \mathbf{V}_{nn}\end{aligned} \tag{3.2}$$

The first and second terms represent the kinetic energy of the electrons and nuclei respectively. The third term represents the coulomb attraction between electrons and nuclei, the forth term represents the Coulomb repulsion between the electrons and the last term represents the Coulomb repulsion between nuclei, whereas M_α is the mass of nucleus α, m is the mass of electron, Z_α and Z_β are the atomic number of atoms α and β respectively, $\vec{r}_j$ and $\vec{R}_\alpha$ are the positions of the electrons and nucleus respectively.

In this approximation, the KE of the nuclei can be ignored and repulsion between nuclei is assumed as constant. Any constant added to an operator only adds to the operator eigen values and has no significant effect on the operator eigen function. We think here only the relative measurement so the constant term can be removed to get electronic hamiltonian as,

$$\begin{aligned}\hat{H} &= \mathbf{T}_e + \mathbf{V}_{ne} + \mathbf{V}_{ee} \\ &= \sum_{j=1}^{N}\left[-\frac{\hbar^2}{2m}\nabla_j^2 - \sum_{\alpha=1}^{M}\frac{Ze^2}{|\vec{r}_j - \vec{R}_\alpha|}\right] + \sum_{j=1}^{N}\sum_{k>j}\frac{e^2}{|\vec{r}_j - \vec{r}_k|}\end{aligned} \tag{3.3}$$

3.1.2 Hatree's Self-Consistent Field Approximation

The motion of each electron in the periphery of the (N-1) electron systems is ruled by a one particle Schrödinger equation. The self-consistency of the electronic charge distribution with its own field follows Hartree equations then it can be modified as,

$$\hat{H} = \sum_{j=1}^{N}\left[-\frac{\hbar^2}{2m}\nabla_j^2 + \sum_{k>j}\frac{e^2}{|\vec{r}_{jk}|} - \frac{Ze^2}{|\vec{r}_j|}\right] \tag{3.4}$$

Then the Schrödinger wave equation for the system of N-electrons is given by

$$\hat{H}\Psi(r_1, r_2, \ldots, r_N) = E\Psi(r_1, r_2, \ldots r_N) \tag{3.5}$$

where E is the total energy of the atom; is that amount of energy would require to dissociate $(N + 1)$ particle system completely.

From above equation, it can be seen that the total wave function describing motion of electrons is the product of Ψ, and is independent to each other ie. each electron moves independently.

$$\Psi(r_1, r_2, \ldots r_N) = \Psi_1(r_1)\Psi_2(r_2) \cdots \Psi_N(r_N) \tag{3.6}$$

With this product wave function the Hartree equation are obtained by the optimization of any approximation accordance with the variational principle which leads to ground state property of wave function, followed by normalization in which the probability of finding N electrons anywhere in space is made unity. However, fermionic nature of electrons were not considered in Hatree approximation.

3.1.3 Hatree-Fock Approximation

The total wave function of N-electron system is written as simple product of one electron wave function $\psi_i(r_i)$ in Hartree-Self consistent field method. But, it doesn't obey the antisymmetry principle, which states that a wave function describing fermions should be antisymmetric w.r.t. interchange of any set of spin-space co-ordinate by spin-spin co-ordinates. It means that fermions have not only three degree of freedom, but also an intrinsic spin co-ordinate having two possible states, denoted by the spin functions α or β. Unless magnetic interactions are included in the Hamiltonian, space and spin variable for each electron are separable. A product of spin-orbitals of the form,

$$\psi(1, 2, 3, \ldots., N) = \phi_1(r_1)\phi_2(r_2)\phi_3(r_3)\phi_4(r_4) \cdots \phi_N(r_N) \tag{3.7}$$

which is known as Hartree product.

This wave function is not antisymmetric, hence it does not fulfill the requirement of Pauli exclusion principle. In order to meet this requirement, HF used slater determinant as

$$\phi(x_1, x_2, \ldots x_N) = \frac{1}{\sqrt{N!}} \begin{vmatrix} \phi_1(x_1) & \phi_2(x_1) & .. & .. & \phi_N(x_1) \\ \phi_1(x_1) & \phi_2(x_2) & .. & .. & \phi_N(x_2) \\ .. & .. & .. & .. & .. \\ \phi_1(N_1) & \phi_2(N_2) & .. & .. & \phi_N(x_N) \end{vmatrix} \tag{3.8}$$

Let us take electrons 1 and 2,

$$\phi(x_1, x_2) = \frac{1}{\sqrt{2!}} \begin{vmatrix} \phi_j(x_1) & \phi_k(x_2) \\ \phi_j(x_1) & \phi_k(x_2) \end{vmatrix} \tag{3.9}$$

If both electrons exist in the same orbital(j=k) then ψ is zero which follows the Pauli exclusion principle. Then,

$$\int dx \phi_k^*(x_j)\phi_k(x_j) = \delta_{jk} \tag{3.10}$$

and

$$E = \sum_{j=1}^{N} H_j + \frac{1}{2} \sum_{j \neq J}^{N} \sum_{j=1}^{N} [C_{jk} - E_{jk}] \tag{3.11}$$

H_j is the one electron integral and C_{jk} is the Coulomb integral. These are same as Hartree since spin parts contribute only factor of unity. The E_{jk} terms called exchange integrals differs from E_{jk} only by the interchange of last two indices j and k. Coulomb integral explains direct interaction. These term arises from the permutations inherent in the determinants form C_{jk} vanishes due to spin orthogonality. The exchange integral accounts for energy differences between the singlet(antisymmetric function with lower energy) and the triplet (symmetric function with higher energy) configurations.

Using exchange operator and the Lagrange undetermined multiplier, we rewrite above Hatree equations as,

$$\begin{aligned} \sum_{j=1}^{N} \epsilon_j &= \sum_{j=1}^{N} H_j + \sum_{j \neq k}^{N} \sum_{k=1}^{N} (C_{jk} - E_{jk}) \\ &= E + \frac{1}{2} \sum_{j \neq k}^{N} \sum_{k=1}^{N} (C_{jk} - E_{jk}) \end{aligned} \tag{3.12}$$

We can write again as,

$$\sum_{j=1}^{N} \epsilon_j = \sum_{j=1}^{N} H_j + \frac{1}{2} \sum_{j=1} (\epsilon_j - H_j)$$

$$\text{or} \quad E = \frac{1}{2} \sum_{j=1}^{N} (\epsilon_j + H_j)$$

The H-F method does not yield an exact solution of the N-electron Schrödinger equation only the best solution of determination form, the approximation inherent in self-consistent field approach is equivalent to replacing particle like $(\frac{1}{|\vec{r}_{jk}|})$ Coulomb interactions by continuous electrostatic interactions among charge clouds. Correlation energy

is the measure of how much the movement of electrons is influenced by presence of other electrons. According to HF, for two electrons with different spins, the probability of finding electron is not zero and thus electrons are uncorrelated but for two electrons with same spins, the probability of finding electron $P(r_1, r_2) = 0$. No two electrons with the same spin can exist at the same place, the case is Fermi hole. Therefore, same spin electrons are correlated in HF. HF method takes into account the so called spin correlation. Electron correlation is mainly caused by the instantane- ous repulsion of the electrons, which is not covered by the effective HF potential. The electrons get often too close to each other in the Hartree-Fock scheme, because the electrostatic interaction is treated in only an average manner. As a result, the electron-electron repulsion term becomes large resulting in energy in HF being above E_0. Both Hartree and Hartree-Fock methods are wave function based so they are computationally expensive for large system sizes. Wave function is a complicated quantity which cannot be measured experimentally. It depends on 4N variables, three spatial and one spin variable for each N electrons. Electron density, a real quantity, has reduced degrees of freedom and thus it can reduce the computational expanses significantly, if used as variables. The use of electron density as variable to solve many body SchrÃűdinger equation gives foundation of the most popular and versatile method in modern day condensed matter physics and materials science called the Density Functional Theory.

3.1.4 Densiy Functional Theory(DFT)

The first effort in 1927 to treat all molecules in many-electron systems on the basis of electron density instead of tedious wave functions by Thomas and Fermi (Thomas & Fermi, 1928) was failed as it couldn't give the stability of molecular system w.r.t. their fragments. However, This method is having roots for the foundation of density functional theory. DFT with LDA/GGA and plane waves as basis functions give reliable outcomes in low costs in condensed matter physics calculations comparing to experimental results. It is materials specific theory. DFT has become a useful theory to handle correlated many-body systems widely used in electronic structure calculations. So, it has been a leading method for electronic calculations after including correlation and exchange interaction on conventional Hatree and HF methods. The basic idea of this theory is that any property of the ground state of a system can be described as a functional of the ground state electron density. Therefore, we would transform our 3N variable problem (wave function of N electrons) as is the case of N interacting electrons, to a 3 variable problem with the electronic density (function of position). In the next sections, we will present the theorems that prove this statement. However, the exact expression for this functional is not known and some approximations must be made. The theory itself does not provide any guidance for constructing the functionals. However,

as we will see, there are many approximations available for these functionals that work well. Also, much work is still done in the scientific community in order to find new functionals and to improve those already established.

Hohenberg-Kohn theorems

As correlation was neglected in HF theory, one of the most useful and fundamental approach to take into account of electron correlation is the density functional theory. In the DFT, the electronic orbitals are the solutions to a many-electrons schrödinger equation, which depends upon electron density rather than the one-electron spin orbitals as in the Hartree-Fock approach. The basic approach of the DFT is to approximate the electron correlation by means of general functional of electron density ρ_0. The heart of DFT is HK theorems. For this, we first describe the first and second Hohenberg-Kohn theorems proposed in 1964 followed by the Kohn-Sham approach (Kohn & Sham, 1965) for the calculation of exchange-correlation potential.

Consider the electronic Hamiltonian of many-electron system obtained within the Born-Oppenheimer approximation expressed as

$$\mathbf{H} = \mathbf{T} + \mathbf{V}_{ne} + \mathbf{V}_{ee} \tag{3.13}$$

where the first term represents the kinetic energy of electrons, the second term represents the Coulomb attraction between electrons and nuclei and the third term is for the Coulomb repulsion among electrons. The second term in equation for N electrons and M nuclei system can be written as

$$\mathbf{V}_{ne} = \sum_{j=1}^{N}\sum_{n=1}^{M}\frac{Z_n}{|\mathbf{r}_j - \mathbf{R}_n|} = \sum_{j=1}^{N} V_{ext}(\mathbf{r}_j) \tag{3.14}$$

where

$$V_{ext}(\mathbf{r}_j) = \sum_{n=1}^{M}\frac{Z_n}{|\mathbf{r}_j - \mathbf{R}_n|}$$

is called the external potential on the j^{th} electron due to M nuclei present in the system. With this Hamiltonian, the ground state energy can be written as

$$E_0 = \langle\psi_0|\mathbf{T}|\psi_0\rangle + \langle\psi_0|\mathbf{V}_{ne}|\psi_0\rangle + \langle\psi_0|\mathbf{V}_{ee}|\psi_0\rangle = T + V_{ne} + V_{ee} \tag{3.15}$$

where $|\psi_0\rangle$ is the ground state wave function for N-electron system.

First H-K Theorem

Hohenberg and Kohn presented two theorems that helps to shift the many-body problem in terms of the many body wave function to one in terms of the electronic density. The first Hohenberg-Kohn theorem (Hohenberg & Kohn, 1964) states that the external potential $V_{ext}(\mathbf{r})$ is a unique functional of electron density $\rho(\mathbf{r})$. The ground-state energy from Schrodinger equation is a unique functional of the electron density. ie, electron density is the basic variable which uniquely determines the Hamiltonian operator characterizing the ground state system. So, this field is known as density functional theory.

To show that the external potential $V_{ext}(\mathbf{r})$ is the unique functional of $\rho(\mathbf{r})$, let us suppose that a different $V_{ext}(\mathbf{r})$ also gives the same ground state charge density distribution $\rho(\mathbf{r})$ and the Hamiltonian whose potentials are given by $V_{ext}(\mathbf{r})$ and $V'_{ext}(\mathbf{r})$ be $\hat{H}$ and $\hat{H}'$ with their eigenvalues and eigenfunctions as E_0, E'_0, ψ and ψ' respectively. Then, the variational principle for the ground state energy E_0 yields,

$$\begin{aligned} E_0 &= \langle\psi|\hat{H}'|\psi\rangle < \langle\psi'|\hat{H}|\psi'\rangle \\ &= \langle\psi'|\hat{H}'|\psi'\rangle + \langle\psi'|\hat{H} - \hat{H}'|\psi'\rangle \\ &= E'_0 + \int \rho(\mathbf{r})[V_{ext}(\mathbf{r}) - V'_{ext}(\mathbf{r})]d\mathbf{r} \end{aligned} \tag{3.16}$$

Analogously,

$$\begin{aligned} E'_0 &= \langle\psi'|\hat{H}|\psi'\rangle < \langle\psi|\hat{H}'|\psi\rangle \\ &= \langle\psi|\hat{H}|\psi\rangle + \langle\psi'|\hat{H}' - \hat{H}|\psi'\rangle \\ &= E_0 + \int \rho(\mathbf{r})[V'_{ext}(\mathbf{r}) - V_{ext}(\mathbf{r})]d\mathbf{r} \end{aligned} \tag{3.17}$$

Adding equations (3.16) and (3.17), we get absurd result as

$$E_0 + E'_0 < E_0 + E'_0 \tag{3.18}$$

Thus there can't be two different external potentials which implies $V_{ext}(\mathbf{r})$ is a unique functional of $\rho(\mathbf{r})$; since, $V_{ext}(\mathbf{r})$ fixes $\hat{H}$. This is the first Hohenberg-Kohn theorem.

Second H-K Theorem

The second Hohenberg-Kohn theorem states that the fuctional $F[\rho_0]$, that gives the ground state energy of the system, provides the lowest energy if and only if the initial density is the true ground state density ρ_0 i.e. for every trial density function $\rho(\mathbf{r})$ that satisfies $\int \rho(\mathbf{r})d\mathbf{r} = N$ and $\rho(\mathbf{r}) \geq 0$ and which is connected to external potential $V_{ext}(\mathbf{r})$.

For a given potential $V_{ext}(\mathbf{r})$, we define energy functional as

$$E_v[\rho(\mathbf{r})] = \int \rho(\mathbf{r}) V_{ext}(\mathbf{r}) d\mathbf{r} + F_{HK}[\rho(\mathbf{r})] \tag{3.19}$$

where

$$F_{HK}[\rho(\mathbf{r})] = \langle\psi|(\mathbf{T} + \mathbf{V}_{ee})|\psi\rangle = T[\rho(\mathbf{r})] + V_{ee}[\rho(\mathbf{r})] \tag{3.20}$$

is a universal functional, valid for any number of the particles and any external potential, $[T\rho(\mathbf{r})] = \langle\psi|\mathbf{T}|\psi\rangle$ and $V_{ee}[\rho(\mathbf{r})] = \langle\psi|V_{ee}|\psi\rangle$ are the sum of the kinetic energy functional and electron-electron interaction functional respectively. In the both cases, $|\psi\rangle$ is the complete many-particle ground-state functional.

The explicit form of the functional F_{HK} is not known as the explicit form of $V_{ee}[\rho(\mathbf{r})]$ is not known. However, the electron-electron interaction $V_{ee}[\rho(\mathbf{r})]$ can split into two parts as the sum of classical and non-classical terms.

$$E_{ee}[\rho(\mathbf{r})] = \frac{1}{2}\int\int \frac{\rho(\mathbf{r})\rho(\mathbf{r}')}{|\vec{\mathbf{r}} - \vec{\mathbf{r}'}|} d\mathbf{r} + E_{ncl}[\rho(\mathbf{r})] \tag{3.21}$$

where

$$J[\rho(\mathbf{r})] = \frac{1}{2}\int\int \frac{\rho(\mathbf{r})\rho(\mathbf{r}')}{|\vec{\mathbf{r}} - \vec{\mathbf{r}'}|} d\mathbf{r}$$

The first term represents the classical Coulomb part and the second part, $E_{ncl}[\rho(\mathbf{r})]$, is the non-classical contribution to the electron-electron interaction containing all the effects of self-interaction, exchange and coulomb correlations. If the explicit form of the functional F_{HK} were known exactly, the ground state energy in a given external potential can be determined as it requires merely the minimization of a functional of the three-dimensional density function.

However, the explicit forms of the functional are not known, and Hohenberg-Kohn theorems do not provide a process to find these functional. The theme of this theorem is that electron density contains all information required to study the ground state properties of system. A main step towards approaching these unknown functional has been formulated by Kohn and Sham.

Kohn-Sham Approach

H-K theorems can be verified for any type of particle-particle interaction. It also holds good for non-interacting system. Due to this, there exists a unique non-interacting system that replicates a ground state density, known as KS system. Kohn and Sham approach descibes self-consistent equations for homogeneous mathematical model includ-

ing exchange and correlation effects in HK theorems. It requires the idea of chemical potential, of a homogeneous electron gas as a function of density. Kohn and Sham in 1965, introduced the concept of a non-interacting reference system made from the set of orbitals, for which the expression for the Hamiltonian is given by

$$\hat{H}_s = -\frac{1}{2}\sum_{j=1}^{N}\nabla_j^2 + \sum_{j=1}^{N} V_s(\mathbf{r}) \tag{3.22}$$

where N is the number of non-interacting electrons in the reference system and $V_s(\mathbf{r})$ is a 'local effective potential'. Since the exact wave functions of non-interacting electrons for the non-degenerate states are Slater determinants, the ground state wave function of the Hamiltonian operator can be written as

$$\phi_s = \frac{1}{\sqrt{N!}}\begin{vmatrix} \phi_1(\mathbf{x}_1) & \phi_2(\mathbf{x}_1) & .. & .. & \phi_N(\mathbf{x}_1) \\ \phi_1(\mathbf{x}_2) & \phi_2(\mathbf{x}_2) & .. & .. & \phi_N(\mathbf{x}_2) \\ .. & .. & .. & .. & .. \\ \phi_1(\mathbf{x}_N) & \phi_2(\mathbf{x}_N) & .. & .. & \phi_N(\mathbf{x}_N) \end{vmatrix} \tag{3.23}$$

The spin orbitals ϕ_j's are termed as Kohn-Sham orbitals and are given by

$$\mathbf{F}_{ks}\phi_j = \epsilon_j\phi_j \tag{3.24}$$

where

$$\mathbf{F}_{ks} = -\frac{1}{2}\nabla^2 + V_s(\mathbf{r})$$

is the one-electron Kohn-Sham operator and ϵ_j's are Kohn-Sham orbital energies unlike the molecular orbital energies.

The artificial non-interacting reference system can be related to the real interacting system with the selection of effective local potential $V_s(\mathbf{r})$, making exact ground state electron density ρ_0 of the reference system equals to the ground state electron density $\rho_s(\mathbf{r})$ of the real system i.e.

$$\rho_s(\mathbf{r}) = \sum_{j=1}^{N} |\phi_j(\mathbf{r})|^2 = \rho_0(\mathbf{r}) \tag{3.25}$$

The kinetic energy of the non-interacting reference system with the same density as the real interacting one can be obtained by the expression

$$T_s = -\frac{1}{2}\sum_{j=1}^{N}\langle\phi_j|\nabla^2|\phi_j\rangle \tag{3.26}$$

The kinetic energy (T_s) of non-interacting system is not equal to the true kinetic energy

(T) of the real interacting system and the difference can be accounted by thinking the following separation of functional $F[\rho(\mathbf{r})]$ as

$$F_{HK}[\rho(\mathbf{r})] = T_s[\rho(\mathbf{r})] + J[\rho(\mathbf{r})] + E_{xc}[\rho(\mathbf{r})] \tag{3.27}$$

where $E_{xc}[\rho(\mathbf{r})]$ is the exchange-correlation energy functional which again can be written in this way

$$\begin{aligned} E_{xc}[\rho(\mathbf{r})] &= (T[\rho(\mathbf{r})] - T_s[\rho(\mathbf{r})]) + (V_{ee}[\rho(\mathbf{r})] - J[\rho(\mathbf{r})]) \\ &= T_c[\rho(\mathbf{r})] + E_{ncl}[\rho(\mathbf{r})] \end{aligned} \tag{3.28}$$

where $T_c[\rho(\mathbf{r})]$ is the residual part of the true kinetic energy which is not covered by T_s and $E_{ncl}[\rho(\mathbf{r})]$ is the non-classical contribution to the electron-electron interaction. The exchange-correlation energy functional $E_{xc}[\rho(\mathbf{r})]$ includes all the unknown terms; non-classical effect of self interaction correction, exchange and correlation to the potential energy of the system and a portion of kinetic energy. The energy expression of non-interacting system contains only two terms: the kinetic energy (T_s) and the energy due to the interaction with the external potential $V_{ext}(\mathbf{r})$. According to HK theorems, the total energy must be a functional of electron density $\rho(\mathbf{r})$. Hence, T_s is also a functional of electron density $\rho(\mathbf{r})$. Thus, the total energy of the reference system can be expressed as

$$E[\rho] = T_s[\rho] + \int \rho(\mathbf{r}) V_{ext}(\mathbf{r}) d\mathbf{r} \tag{3.29}$$

In terms of Kohn-Sham orbitals ϕ_j, we have

$$E[\phi_j^*, \phi_j] = -\frac{1}{2}\sum_{j=1}^{N} \langle \phi_j | \nabla^2 | \phi_j \rangle + \sum_{j=1}^{N} \int |\phi_j(\mathbf{r})|^2 V_{ext}(\mathbf{r}) d\mathbf{r} \tag{3.30}$$

As the minimization of $E[\phi_j^*, \phi_j]$ in above equation is conditional, we make the conditional minimization to unconditional with the help of Langrange's undetermined multipliers method. Let's define a functional $G[\phi_j^*, \phi_j]$ as

$$G[\phi_j^*, \phi_j] = E[\phi_j^*, \phi_j] - \sum_j \epsilon_j \int \phi_j(\mathbf{r})^* \phi_j(\mathbf{r}) d\mathbf{r} \tag{3.31}$$

where ϕ_j^* and ϕ_j are treated as independent functional variables and ϵ_j denote the Lan-

grange's multipliers. From above equations, we have

$$\begin{aligned} G[\phi j^*, \phi_j] &= -\frac{1}{2}\sum_{j=1}^{N}\int \phi_j^*(\mathbf{r})\nabla^2\phi_j(\mathbf{r}) + \sum_{i=1}^{N}\int \phi_i^*(\mathbf{r})V_{ext}(\mathbf{r})\phi_i(\mathbf{r})d\mathbf{r} \\ &\quad -\sum_j \epsilon_j \int \phi_j^*(\mathbf{r})\phi_j(\mathbf{r})d\mathbf{r} \\ &= \sum_j \int \phi_j^*(\mathbf{r})\Big[-\frac{1}{2}\nabla^2 + V_{ext}(\mathbf{r}) - \epsilon_j\Big]\phi_j(\mathbf{r}) \end{aligned} \tag{3.32}$$

Taking the variation of G with respect of ϕ_j^* and ϕ_i, we get

$$\begin{aligned} \delta G[\phi_j^*, \phi_j] &= \sum_j \int \delta\phi_j^*(\mathbf{r})\Big[-\frac{1}{2}\nabla^2 + V_{ext}(\mathbf{r}) - \epsilon_j\Big]\phi_j(\mathbf{r})d\mathbf{r} \\ &\quad + \sum_j \int \phi_j^*(\mathbf{r})\Big[-\frac{1}{2}\nabla^2 + V_{ext}(\mathbf{r}) - \epsilon_j\Big]\delta\phi_j(\mathbf{r})d\mathbf{r} \end{aligned} \tag{3.33}$$

For the minimum value of G, we have $\delta G =$,

$$\Big[-\frac{1}{2}\nabla^2 + V_{ext}(\mathbf{r})\Big]\phi_i(\mathbf{r}) = \epsilon_j\phi_j(\mathbf{r}), \quad j = 1,2,...,N \tag{3.34}$$

and its complex conjugate equation (60) represents the single-particle Schröndinger equation for the non-interacting reference system.

Now, the energy expression for real interacting system can be written as

$$E[\rho(\mathbf{r})] = T_s[\rho(\mathbf{r})] + J[\rho(\mathbf{r})] + E_{xc}[\rho(\mathbf{r})] + V_{ext}[\rho(\mathbf{r})] \tag{3.35}$$

$$\text{or} \quad \left[-\frac{1}{2}\nabla^2 + V_{ext} + \frac{\delta E_{xc}[\rho(\mathbf{r})]}{\delta\rho(\mathbf{r})} + \int \frac{\rho(\mathbf{r}')}{|\mathbf{r}-\mathbf{r}'|}d\mathbf{r}'\right]\phi_j = \epsilon_j\phi_j$$

$$\text{or} \quad \Big[-\frac{1}{2}\nabla^2 + V_{eff}(\mathbf{r})\Big]\phi_j = \epsilon_j\phi_j, \quad j = 1,2,\ldots,N \tag{3.36}$$

where

$$V_{eff}(\mathbf{r}) = V_{ext}(\mathbf{r}) + \frac{\delta E_{xc}[\rho(\mathbf{r})]}{\delta\rho(\mathbf{r})} + \int \frac{\rho(\mathbf{r}')}{|\mathbf{r}-\mathbf{r}'|}d\mathbf{r}'$$

is the effective potential which depends on the density (i.e. one-electron orbitals) through Coulomb term. The set of N-coupled equations given by above equation and their complex conjugates are known as Kohn-Sham one-electron equations.

Then, we find that the effective potential $V_{eff}(\mathbf{r})$ is identical to the local potential $V_s(\mathbf{r})$ i.e.

$$V_s(\mathbf{r}) = V_{eff}(\mathbf{r}) = V_{ext}(\mathbf{r}) + V_{xc}(\mathbf{r}) + \int \frac{\rho(\mathbf{r}')}{|\mathbf{r}-\mathbf{r}'|}d\mathbf{r}' \tag{3.37}$$

where $V_{xc}(\mathbf{r})$ is the potential due to the exchange-correlation energy and is given by

$$V_{xc}(\mathbf{r}) = \frac{\delta E_{xc}}{\delta \rho} \tag{3.38}$$

The exchange-correlation potential $V_{xc}(\mathbf{r})$ is also known as the Kohn-Sham potential, which in general, is a local potential. But for a real system, the exchange-correlation potential has non local dependence on the density.

The local density approximation(LDA)/The generalized gradient approximation(GGA)

The case where the exchange-correlation energy functional $E_{xc}[\rho(\mathbf{r})]$ depends only on the local value of the density $\rho(\mathbf{r})$ for the slowly differing field but not on its gradients, we use local density approximation. This approximation uses only the local density to define the approximate exchange-correlation functional, so it is called the local density approxi- mation (LDA). The LDA gives us a path to define the Kohn- Sham equations, but the results from these equations do not exactly solve the true Schrodinger equation because we are not using the true exchange-correlation functional.

We can write

$$E_{xc}^{LDA}[\rho(\mathbf{r})] = \int \rho(\mathbf{r}) \mathrm{E}_{xc}[\rho(\mathbf{r})] d\mathbf{r} \tag{3.39}$$

where $\mathrm{E}_{xc}[\rho(\mathbf{r})]$ is the exchange and correlation energy per electron of hypothetical uniform electron gas of density $\rho(\mathbf{r})$. $\mathrm{E}_{xc}[\rho(\mathbf{r})]$ can be separated as

$$\mathrm{E}_{xc}[\rho(\mathbf{r})] = \mathrm{E}_{x}[\rho(\mathbf{r})] + \mathrm{E}_{c}[\rho(\mathbf{r})] \tag{3.40}$$

The exchange functional $\mathrm{E}_{x}[\rho(\mathbf{r})]$ which represents the exchange energy of an electron in a uniform electron gas, also defined as

$$\mathrm{E}_{x}[\rho(\mathbf{r})] = -\frac{3}{4}\left[\frac{3}{\pi}\right]^{\frac{1}{3}} [\rho(\mathbf{r})]^{\frac{1}{3}} \tag{3.41}$$

The best known class of functional after the LDA uses infor- mation about the local electron density and the local gradient in the electron density; this approach defines a generalized gradient approximation (GGA). We use GGA also for some cases when the exchange-correlation energy functional $E_{xc}[\rho(\mathbf{r})]$ depends on density gradient. The improvement on LSDA calculation has to be incorporated. One of the approach is to take the gradients of the density into account in the exchange-correlation energy and is known as the gradient corrected exchange-correlation functional. There are many gradient corrected exchange-correlation functional.

The E_{XC} in GGA can be written as;

$$E_{XC}^{GGA}[n(\mathbf{r})] = \int f[n(\mathbf{r}), \nabla n(\mathbf{r})] d\mathbf{r} \tag{3.42}$$

The symbol 'f' is some functional of '$n(\mathbf{r})$' and it's gradient '$\nabla n(\mathbf{r})$'.

Similar to LDA, the exchange-correlation energy E_{XC}^{GGA} of GGA approach contains exchange part (E_X^{GGA}) and correlation part (E_C^{GGA}). It can be expressed as;

$$E_{XC}^{GGA} = E_X^{GGA} + E_C^{GGA} \tag{3.43}$$

Different methods of construction for obtaining $f[n(\mathbf{r}), \nabla n(\mathbf{r})]$ (exchange correlation functionals) are developed by a number of groups of authors. Some of the popular functionals among them are proposed by Perdew and Wang (PW91), and by Perdew, Burke and Ernzerhof (PBE) (Perdew & Zunger, 1981). Further, Becke's formula for the exchange part is combined with Perdew's formula of correlation and also with the correlation functional of Lee, Yang and Parr to give BP88 and BLYP type of GGA functionals.

3.2 Density Functional Perturbation Theory (DFPT)

For the perturbed system, variation of energy and density around a fixed potential occurs so we use density functional perturbation theory. Since many physical properties are derivatives of the total energy, we calculate energy here with an aid of atomic displacement. We will use DFPT for phonons calculations of some metallic compounds. We use quantum espresso (Scandolo et al., 2005) software for DFT and DFPT based calculations.

CHAPTER 4

4. RESULTS AND DISCUSSION

In this chapter we present, discuss, and analyse the main findings of our work. Our work describes first-principles study of interactions of Ni with another transitional element Al in different environmental conditions. It consists of density functional theory level of calculations to fulfil the objectives of the study. The findings of the present work will cover the following topics.

1. Properties and applications of materials/alloys are strictly affected by stability and geometrical structure of compounds. Here, we describe total energy of alloy as a function of lattice parameter termed as energy minimization. Energy minimization is the key for the determination of further calculations.

2. No materials are found in nature without interaction, so Ni interact with Al in different way. It is relevant to determine whether it follows segregation or ordering nature in molten state.

3. As electronic properties of materials control other related properties, we emphasize in calculating structural and electronic properties in details.

4. Application for magnetic memory devices and related other applications limit the magnetism of material. Magnetization along with important physical parameter: magnetic moment is essential to test the quality of material in commercial market. Spin polarized calculation will be done to get effective magnetization. Beside this, To have a better understanding of the contributions of different orbitals, we will focus on PDOS. We add more in detail about propensity of Ni towards magnetism by increasing its concentration in NiAl and NiGa both.

5. The practical application of materials are also determined by their thermal properties: heat conduction, lattice vibration(phonons). In solids, there are atoms. Atoms in solid materials vibrates constantly at high frequency and low amplitudes. Atomic bonding also takes place in vibrations. For the mechanism of heat conduction in solid, heat is transported by free electrons and phonons.

6. Optical properties is also connected to electronic properties of compounds. So, it is natural to study optical and related other properties to know in detail the probable applications. To know the stability and other properties, it is required to deal of further experimental as well as theoretical research on these compounds as proof. Thus the present study will provide beneficial results regarding electronic, optical, magnetic, vibrational properties of intermetallic compounds.

4.1 Structural and electronic properties of Nickel

Since the mechanical properties of NiAl are sensitive to stoichiometry, concentration and lattice defects, it is obvious to to know the properties of individual element. Ni belongs to transition metal. The unit cell of nickel is a FCC with the lattice parameter of 0.352 nm (Hsu & Wang, 2004). The nickel atom has two electron configurations, [Ar] $3d^8$ $4s^2$ and [Ar] $3d^9$ $4s^1$, which are very close in energy. There is debate on which configuration has the lowest energy (Scerri et al., 2007). Some study says that the electronic configuration of Ni is [Ar] $4s^2$ $3d^8$, which can also be written [Ar]$3d^8$ $4s^2$ (Meissler et al., 1999). This configuration agrees with the Madelung energy ordering rule, which predicts that 4s is filled before 3d. It is supported by the experimental fact that state with the lowest energy of the nickel atom is a $3d^8$ $4s^2$ energy level, specifically the $3d^8$ $4s^2$. The energy with [Ar] $3d^9$ $4s^1$ is less than the average energy with configuration [Ar] $3d^8$ $4s^2$. Therefore, it has been confirmed that the ground state configuration is [Ar] $3d^9$ for Ni.

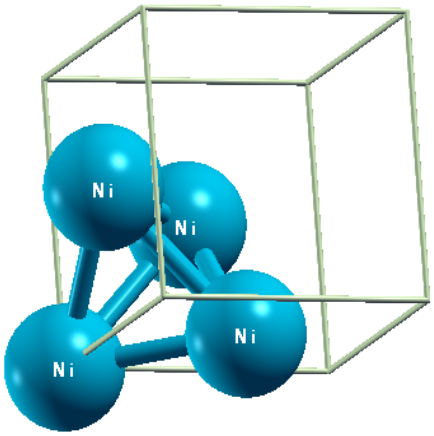

Figure 3: Unit cell of Ni

The total energy of Ni crystal is found to be -85.928 Ry with Fermi energy 14.25 eV. The Fermi energy of metal is few eV. Nickel, as a metallic and magnetic material, electrons fill up to higher level in comparison to Al metal. The bond length between Ni atoms is about 2.65 Å, indicates the strong bonds to bind within crystal.

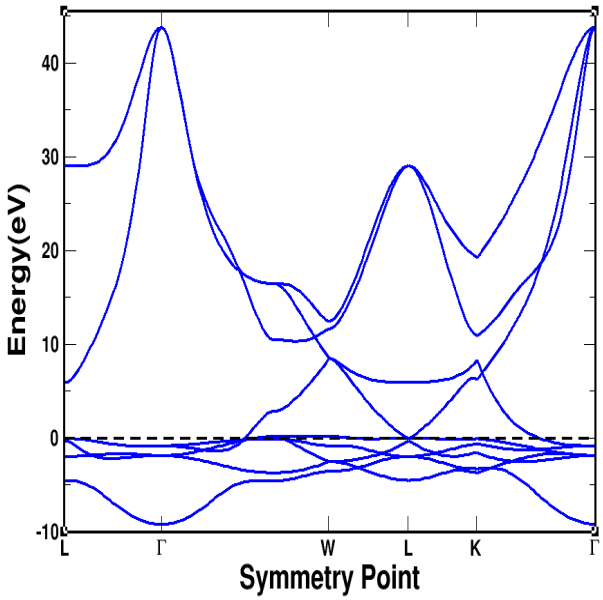

Figure 4: Band structure of Ni

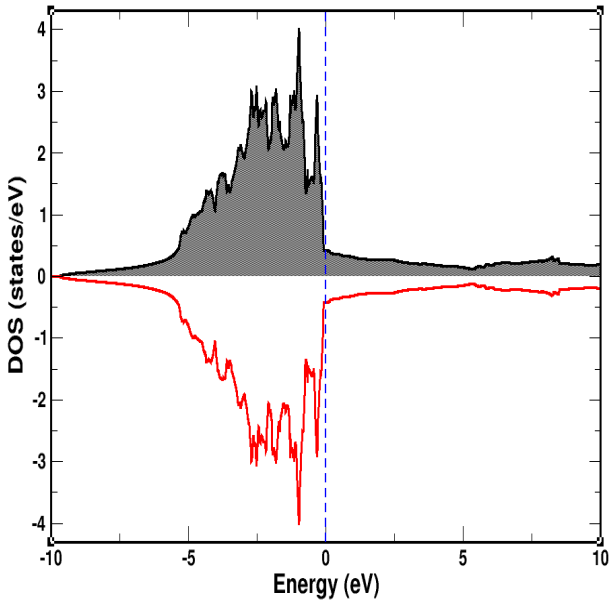

Figure 5: Density of states of Ni

To know the orbital contributions on TDOS, we have also investigated projected density of states in nickel.

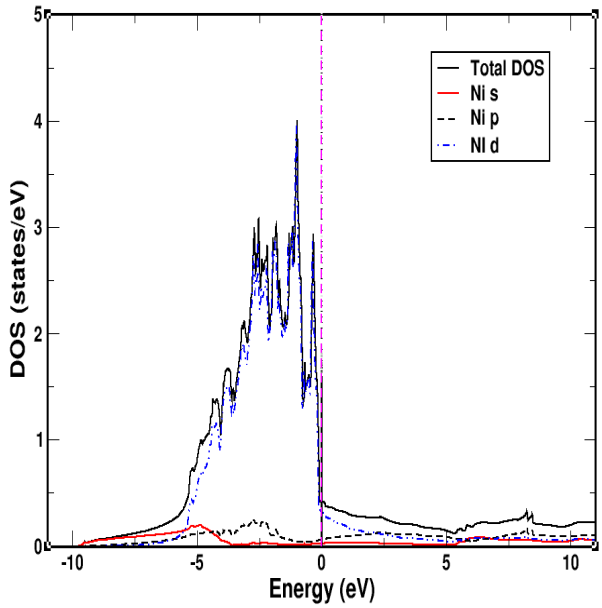

Figure 6: Projected density of states of Ni

From calculations, Ni is found as a magnetic metal with magnetic moment of $0.89\mu_B$. The origin of magnetic moment in nickel is due to its electronic configuration ($1s^2$, $2s^2$ $2p^6$,$3s^2$ $3p^6$ $3d^8$,$4s^2$). Only those magnetic substances which have unpaired electron(s) in their atomic orbital gives magnetic moment. The d-orbital which has more fraction of charge (86% in total), has created largest contributions to produce magnetic moment. These nature of density of states just below Fermi level shows the higher chances of magnetic fluctuations by changing the number of electrons (mainly d electron), however the charges in other orbital have been changed due to up and down spin competitions. The main contribution for the magnetic moment of this compound comes from Ni 3d electrons while sp electrons have no significant role to display such magnetic moment. Ni, a ferromagnetic material, when alloyed with Al, it is expected to observe synergistic effect as a result we can tune the properties as we wish.

4.2 Structural and electronic properties of NiAl

Ni and Al atoms are covalently/metallic bonded to form Ni-Al structure as in 7. In a body-centred cubic arrangement of atoms, the unit cell consists of eight atoms at the corners of a cube and one atom at the body center of the cube. NiAl is a metallic alloy which is available as bar, foil, sheet, shoot etc. (Neumann et al., 1976) and crystallises in the primitive cubic CsCl structure with lattice constant 0.288 nm and SG Pm-3m. This structure is also called inter-metallic ordered BCC B2 structure (Pearson et al., 1992), explaining in terms of two cubic cells where Al atoms cover the cube corners one sub-lattice and the Ni atoms stay the cube corners of another sub-lattice as in Figure 7.

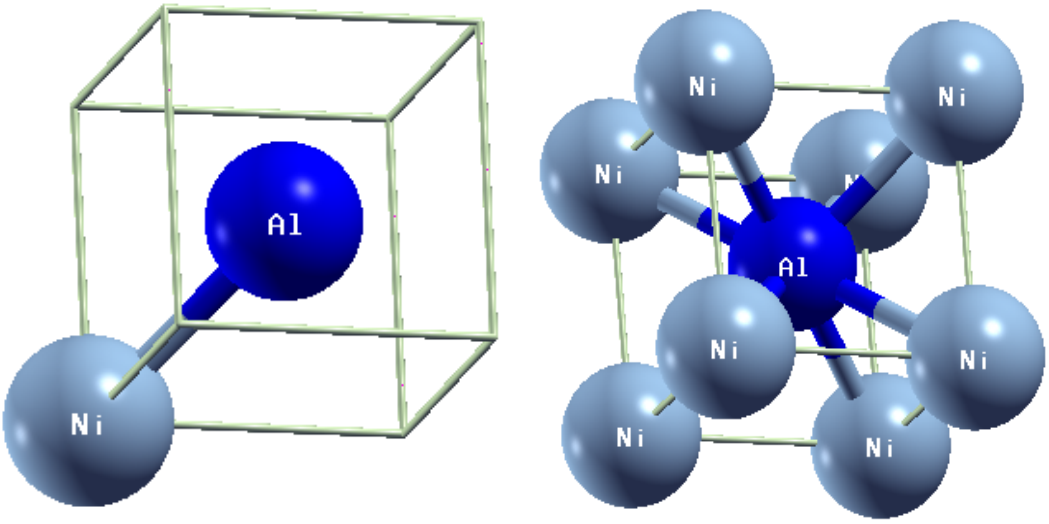

Figure 7: Unit cell and crystal structure of NiAl

For the band structure of NiAl, we used space group (SG) as 221(pm-3m) and optimized lattice parameter is calculated using energy minimization process as in Figure (24) and found the optimized lattice parameter as 2.87 Åwhich resembles with previously calculated theoretical results. The experimental value of lattice parameter is 2.887 Å. Our optimized lattice parameter is 0.34% less than experimental value and 0.59% less than theoretical value. All the further calculations are done by using the base of this value.

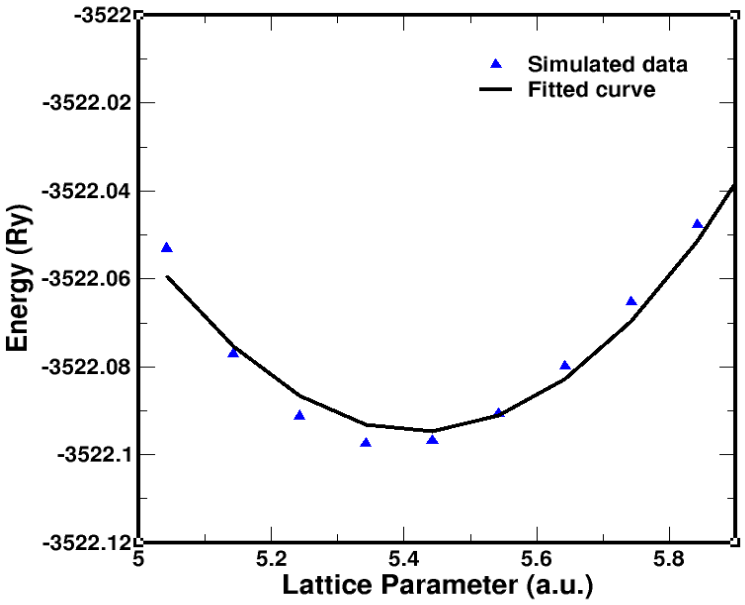

Figure 8: Energy Minimization in NiAl

NiAl is found to be bound system with binding energy of 0.36 eV. Electrons occupancy in bound system is systematically studied through band structure calculations. The band structure of NiAl is displayed in Figure 10. Conduction and valence bands are significantly overlapped at the Fermi level showing the metallic behaviour of NiAl. One

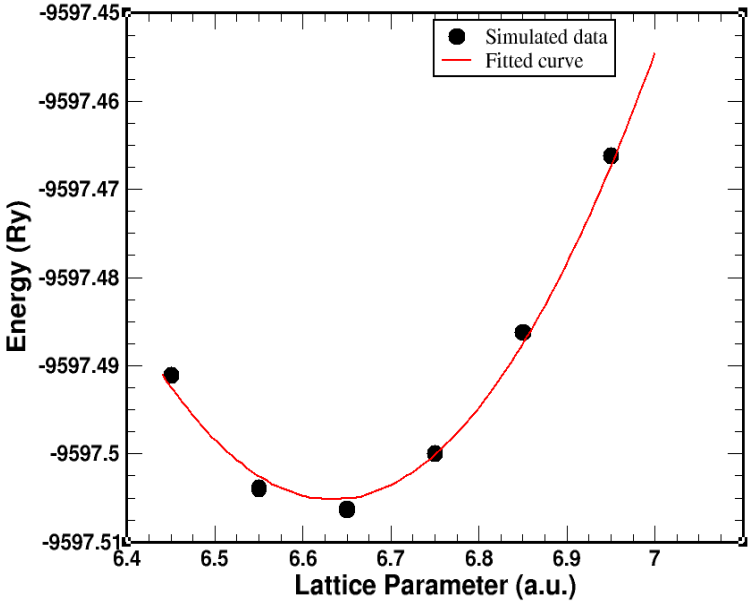

Figure 9: Energy Minimization in Ni_3Al

band from valence band region crosses the Fermi level and bands are originated from Γ-point. No gap at the Fermi level, represented by horizontal dotted line is seen. Since the valance and conduction bands overlap significantly at the Fermi level, as a result, both materials exhibit the metallic nature. Bands coincide for all K-values mentioned in structures within the BZ mostly in Γ point after 48 symmetry operation. The Ni 3d and Al 2p electrons are distributed over entire range of valence band. Light bands crossing the Fermi level in the region of Γ-X direction in Ni_3Al is steeper than that of NiAl which confirms the more metallic character of Ni_3Al.

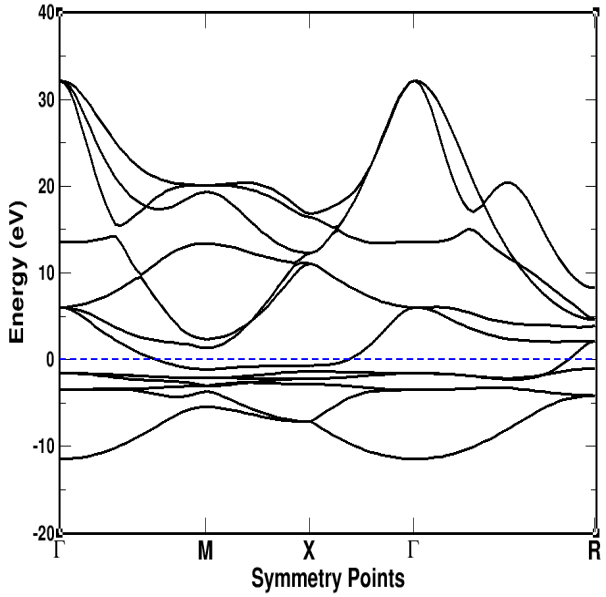

Figure 10: Band structure of NiAl

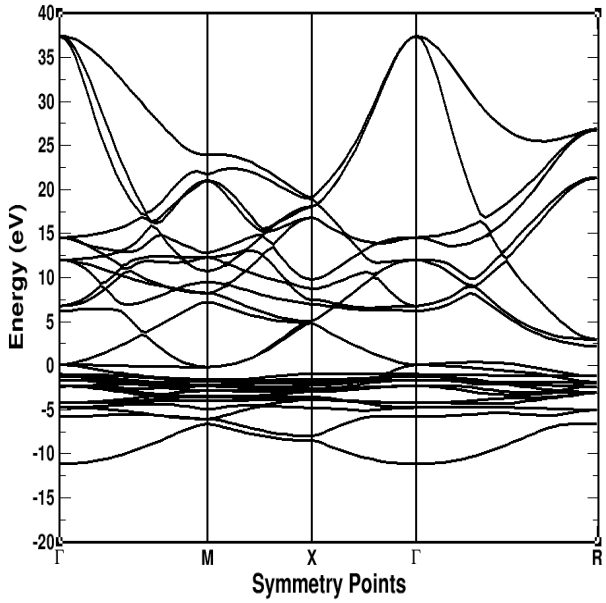

Figure 11: Band structure of Ni_3Al

The energy scale is relative to E_F in units of eV. There are altogether 13 bands observed in the bulk band structure of NiAl. The electron's occupancy at different orbitals of the atoms in NiAl alloy can be understood by studying the fatbands. It is seen that the 13 valence electron per unit cell which covers six-initial-state bands, with the seventh band is partially occupied. The contributions of d orbitals (t_{2g} and e_g sub-orbitals) is shown in Figure (13).

The electrons occupancy at different orbitals of the atoms in NiAl alloy can be understood by studying the fatbands. It is seen that the 13 valence electron per unit cell which fill six-initial-state bands, with the seventh band being partially occupied. The contribution of s and p orbitals in the energy bands of NiAl is shown in Figure (2) and contribution of d orbitals (t_{2g} and e_g suborbitals) is shown in Figure (13). Our findings shows that free-electron like character of bands are mostly from Al sand Al p states. These states are observed both at the bottom of the band and above the Fermi level. The Ni d bands are pd mixing range lies between -1.55 eV to -4.32 eV. It is also observed that Fermi level lying in the region of high t_{2g} density of states.

From Figure (12), it is observed that, s and p orbitals have made less contributions in the total energy band of NiAl than t_{2g} sub-orbital of d orbital of NiAl.

From the Figures (13), we see that the most of the contributions in the total energy band of NiAl comes from t_{2g} sub-orbital of d orbital of NiAl alloy near the Fermi level which indicates that filling of d bands supports in the present calculations. Our findings shows that free-electron like character of bands are mostly from Al s and Al p states. These states are observed at the bottom of the band and above the Fermi level. The Ni d

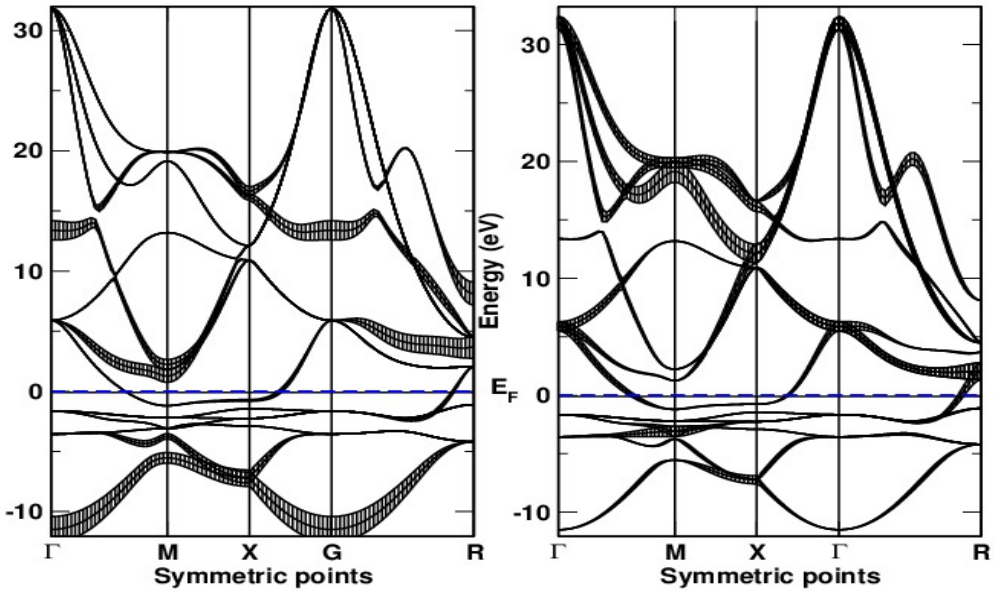

Figure 12: Fatbands of s and p orbitals of NiAl alloy

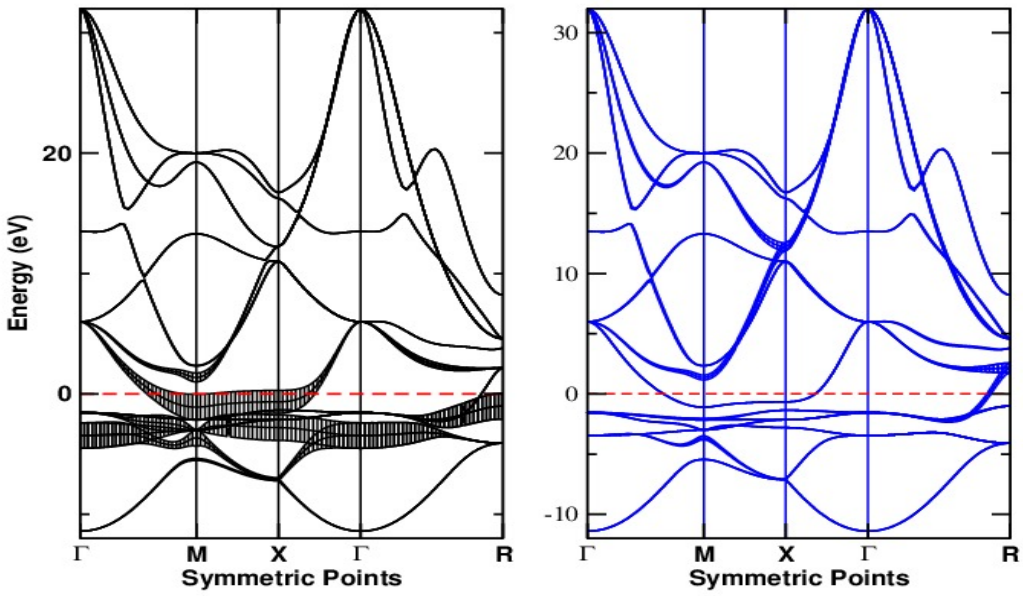

Figure 13: Fatbands of t_{2g} and e_g orbitals of NiAl alloy

bands are pd mixing range in between -1.55 eV to -4.32 eV. From the Figure, it is also observed that Fermi level lying in the region of high t_{2g} density of states.

4.3 Orbitals contributions in Ni_3Al

Occupancy of electrons on s,p,d orbitals of the atoms in Ni_3Al alloy can be investigated by studying the fatbands. The contributions of s and p orbitals in the energy bands of Ni_3Al is shown in Figure (14) and contribution of d orbitals (e_g and t_{2g} sub-orbitals) are shown in Figure (15). From the figure, it is seen that s ans p orbitals of Al mostly found at the lower part of the band and also above the Fermi energy. Nickel has made the largest contributions to display magnetism in Ni-Al system, that shows the tendency of Ni-based alloys toward the well performance in small magnetic memory devices. The Ni d bands are mostly observed in pd mixing range (-0.43 eV to -3.01 eV). It is also seen that e_g d band mostly dominate to other bands near the Fermi level. From the Figures 14 & 15, we see that most of the contribution in the total energy band of Ni_3Al comes from e_g suborbital of d orbital of Ni_3Al alloy. The occupancies s, p or d of electrons for the contribution of magnetic moments can be understood by DOS and PDOS plot which are described more detail in the next section.

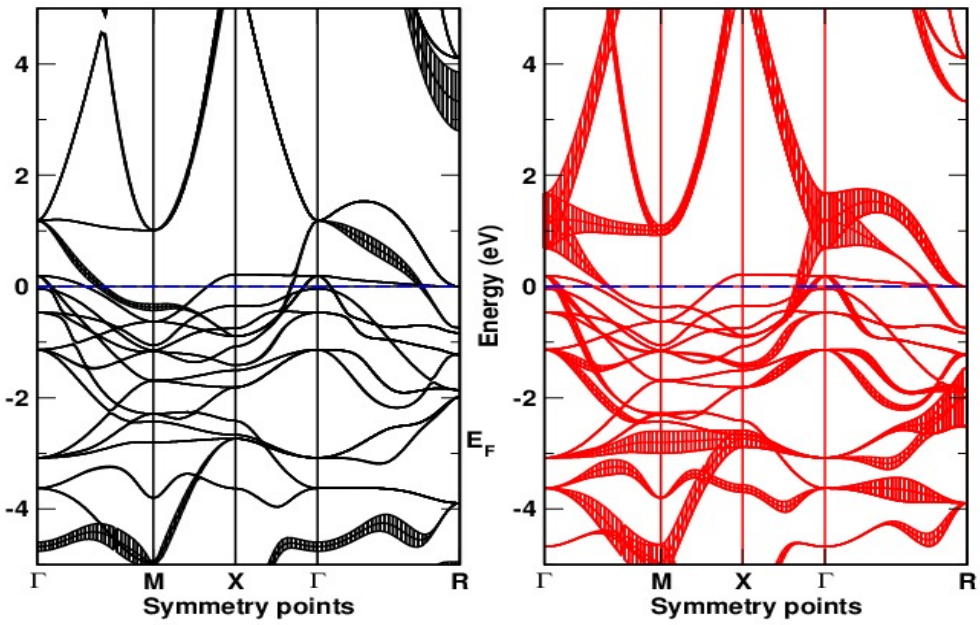

Figure 14: Fatbands of s and p orbitals of Ni_3Al alloy

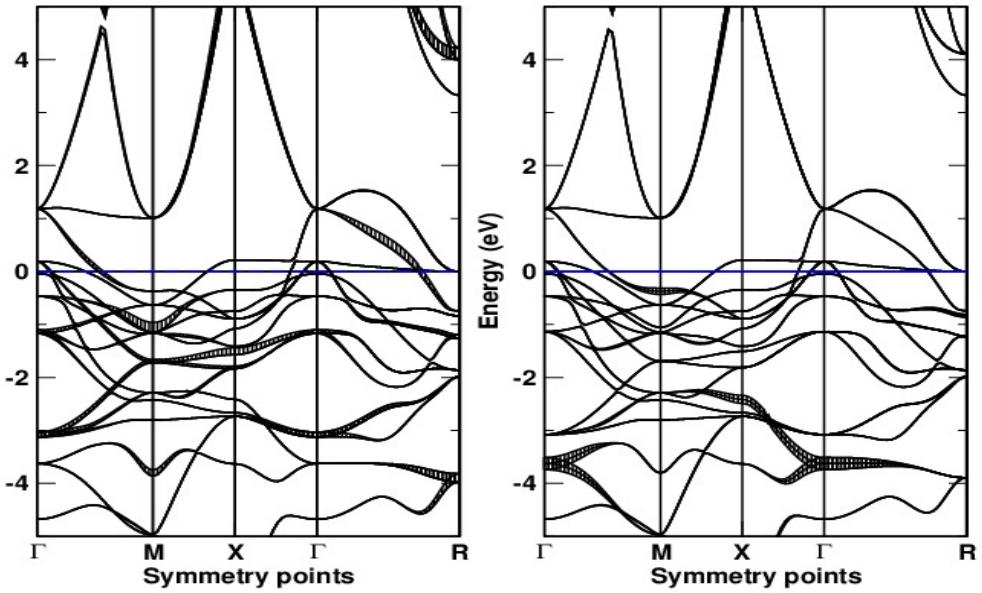

Figure 15: Fatbands of t_{2g} and e_g orbitals of Ni_3Al alloy

4.4 Density of States of NiAl

The calculated total density of states(TDOS) and Projected density of states(PDOS) of NiAl are shown in Figures (16) and (17) respectively. It shows that the number of peaks of Ni are less than Al. The bandwidth of Ni also found to be narrower than Al. This is the indication of hybridization of Al-2p and Ni-3d. Though states of Ni is higher than Al in up and down spins, there is strong competition between these spins resulting effective magnetic moment zero and the system as a whole becomes non-magnetic in nature. Our findings show that Ni has more fraction of charge in d-orbital. The major contributions on the density of states for up and down states is due to d-orbitals of Ni. The contributions of Al is due to s and p orbitals. Peaks in the density of states signifies the large number of states with corresponding energy. From Figure 17, it is found that the large peak is identified with Ni d band. The contribution of Al in the total DOS isn't significant. The difference in integrated up and down spins is found to be zero, which resembles with DOS plot showing non-magnetic nature of NiAl.

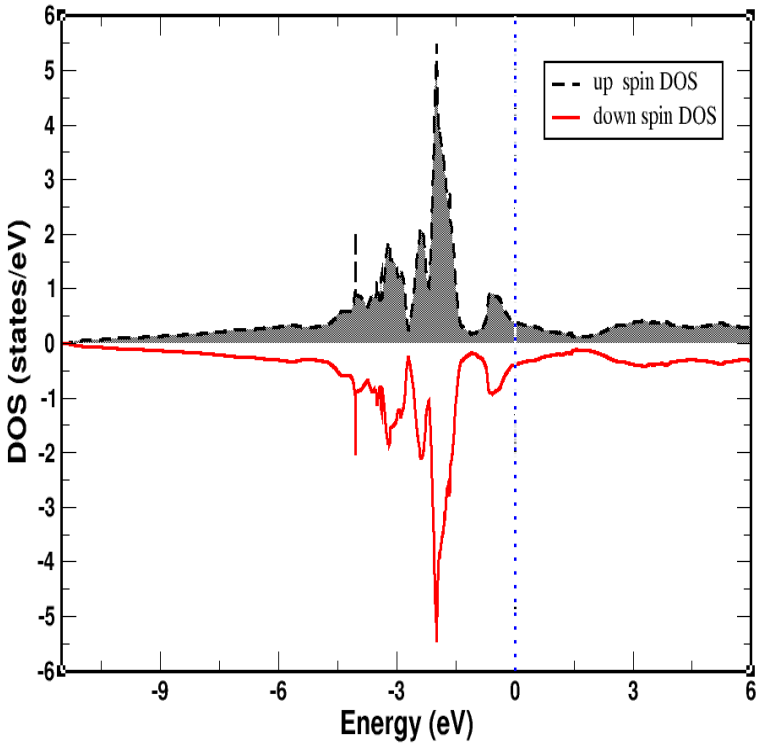

Figure 16: DOS of NiAl

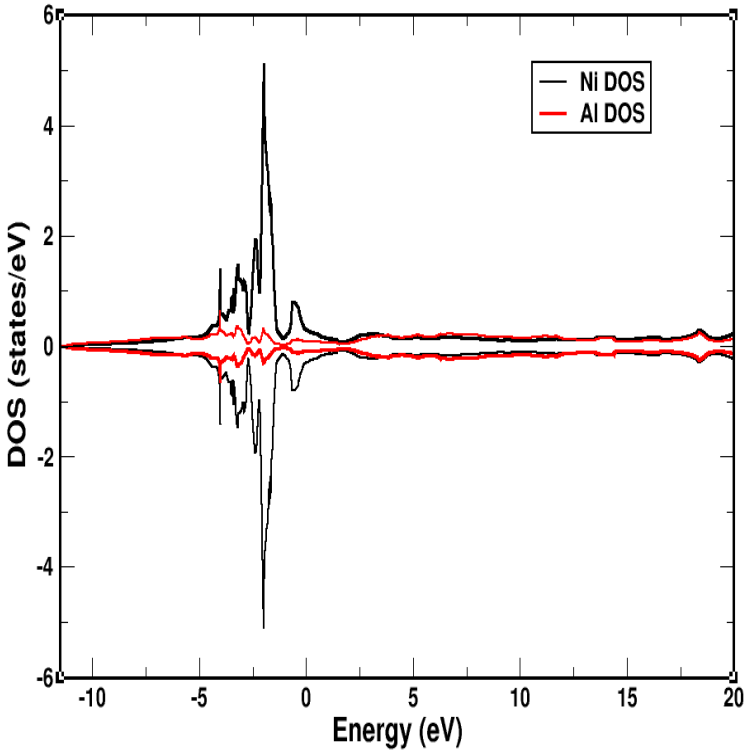

Figure 17: Individual DOS contributions of Ni and Al in NiAl alloy

4.5 Density of States of Ni_3Al

The calculated TDOS and PDOS of Ni_3Al in the present work is shown in Figures (18) and (19) respectively. From these figures, we observed that width of Ni band is higher than the width of Al. The peak of Ni also higher than Al. This is the indication of strong Ni d and Al p hybridization. The difference in integrated up and down spins up to the Fermi level gives the effective magnetic moments $0.52\mu_B$ indicating that it is ferromagnetic in nature. Density of states inform the large number of states at

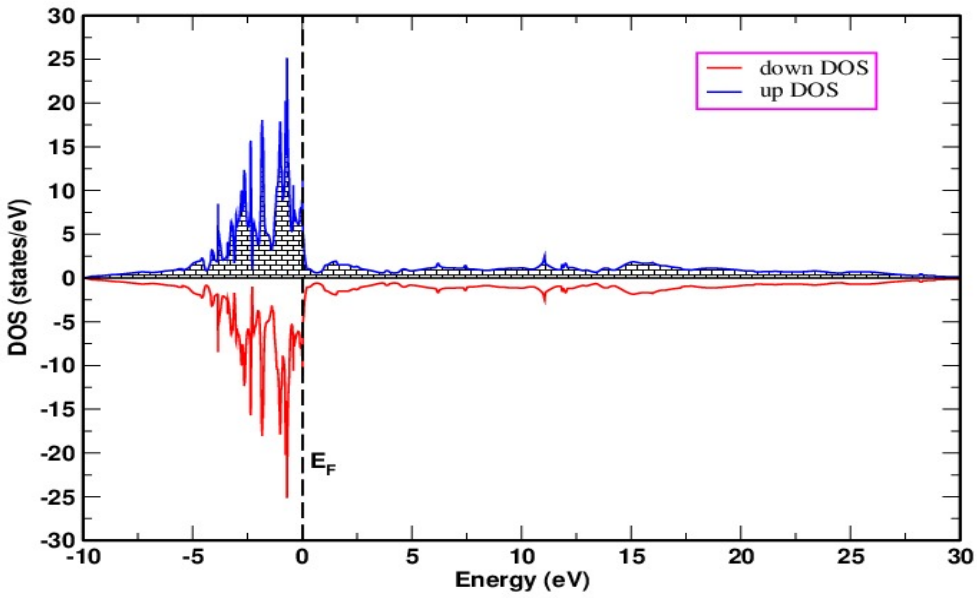

Figure 18: Density of states of Ni_3Al.

the corresponding energy and difference between integrated up and down spins gives the magnetization of the system. Most of the contributions for magnetism is due to d electrons of Ni in Ni_3Al. The TDOS and PDOS of the present work as shown in Figure (20) matches with the work of (El Fatmi & Ghazouani, 2011) using pseudo-potential plane-wave (pp-pw) method. The DOS at the Fermi level from the present work is found to be 12.4 states/eV-cell, which is $\approx$ 3% deviated to experimental value 11 states/eV-cell (Hsu & Wang, 2004). Further, the magnetic moment of the Ni_3Al from the present study is about 2% higher(0.44 μ_B) than the value reported in (Zhu et al., 1998).

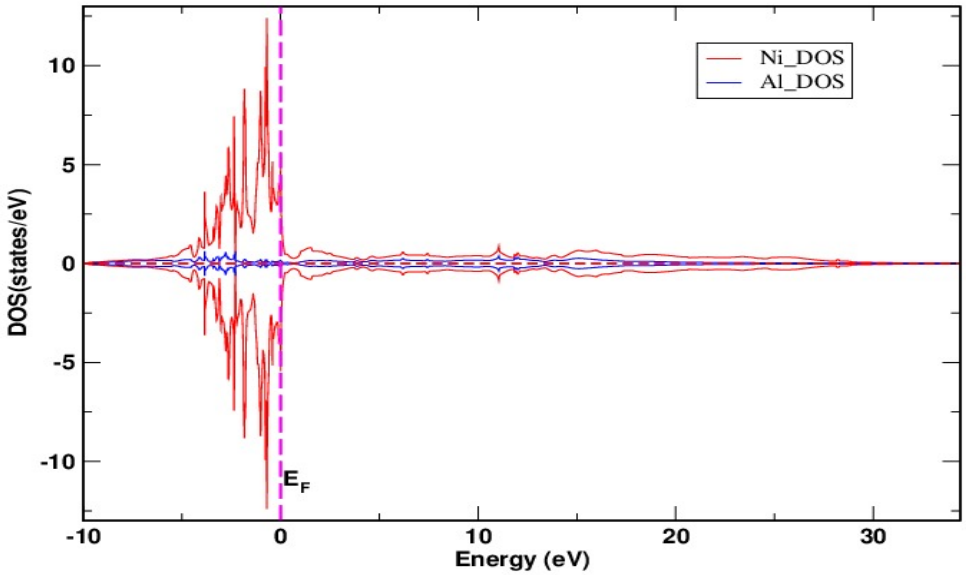

Figure 19: Individual DOS contributions of Ni and Al in Ni_3Al alloy

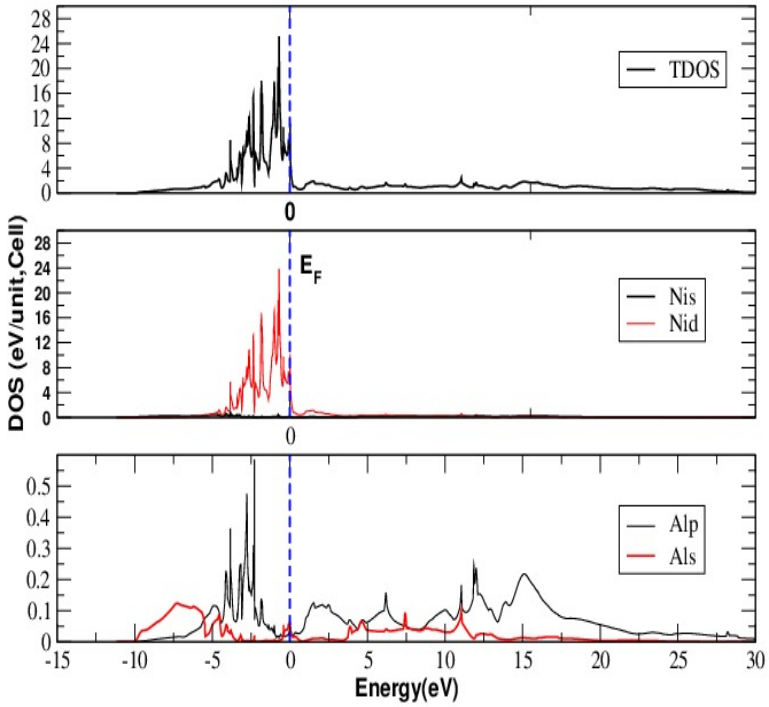

Figure 20: The calculated TDOS and PDOS for Ni_3Al, Fermi level is marked by vertical dotted line and set at zero energy.

4.6 Vibrational properties of NiAl

The study of lattice vibration is important for understanding how energy is absorbed in solids. Electronic term and lattice term both contribute to give effective specific heat in metallic alloys,

$$C = \alpha T + \beta T^3$$

The study of phonon or lattice vibration helps to explain different phenomena like specific heat of solid, superconductivity, transmission of sound etc. Higher-frequency phonons are responsible for rising the thermal capacity/specific heat capacity of solids. The vibrational properties of NiAl is calculated using the first-principles density functional perturbation theory. Phonon anomalies, originated from phonon dispersion curve is shown in Figures 21 and 22.

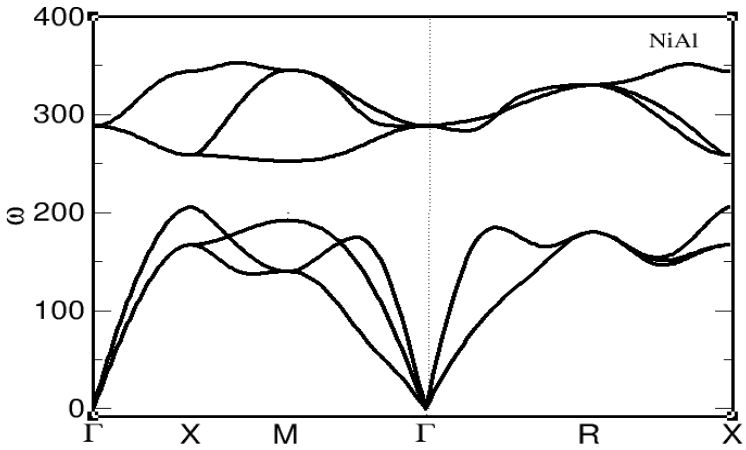

Figure 21: Phonon dispersion relation in NiAl at zero pressure

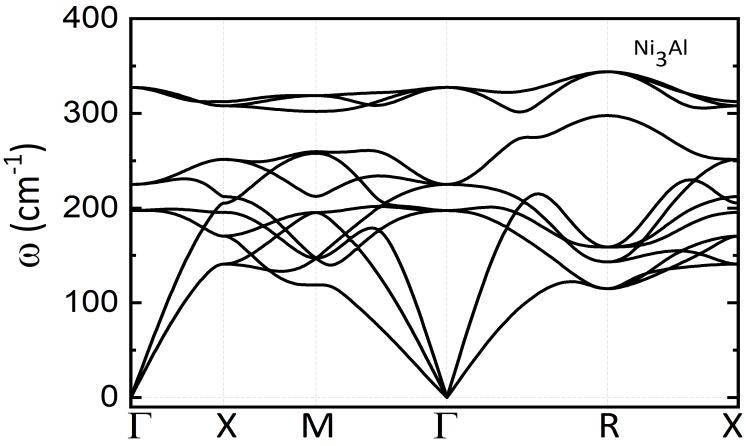

Figure 22: Phonon dispersion relation in Ni_3Al at zero pressure

From Figures 21 and 22, three optical and three acoustic modes are observed in NiAl

in which optical branches gets uniformly changed in frequency. Modes are originated from electronic band as in Figure 2 as phonon bands arising from Γ -points in each part. The energy gap between acoustic and optical branches of NiAl is found to be 52.4 cm^{-1}(1.56 THz), which is close to previously reported values (Huang et al., 2004; Mostoller et al., 1989). The gap is actually the gap between phonon branches of Ni and Al atoms. Acoustic modes are due to vibration of heavier(in atomic wt.) nickel atoms, observed at 254.4 cm^{-1} and optic modes are provided by vibration of aluminium atoms, at 202.0 cm^{-1}. Damping of phonon in both cases dominates at high wave vector (q) in acoustic mode. Similarly, phonon modes in Ni_3Al are observed, which in different than that from NiAl. Optical branches gets more uniformly shifted in frequency in Ni_3Al than in NiAl. Optical phonons have a non-zero frequency at the center of Brillouin zone and show no dispersion near that long wavelength limit. Four atoms/cell of Ni_3Al has created 12 phonon dispersion curves. The position of low frequency branch close to 4.5 Thz is intriguing. No dip is found below zero level which suggests that NiAl is thermodynamically stable at low pressure and temperature. The lower dip in longitudional branch justifies the stability of pair potential as our other theoretical work (Yadav et al., 2016) on NiAl melt at 1873 K. Oscillation are observed to be prominent in longitudional mode(LM) than transverse mode (TM). There is notable peak at R point of frequency $\approx$ 292 cm^{-1} in Ni_3Al, which is not seen in NiAl. Unlike Ni_3Al, NiAl contains many specific features. TA mode deviates in NiAl linearly beginning from one-third of Γ-R region.

4.7 Structural Properties of NiGa

We have also studied the properties of closely related compound NiGa to know the role of nickel in the composite system. The atomic structure of NiGa and Ni_3 Ga compounds resemble to the CsCl and Cu_3Au structures type with equilibrium lattice parameters 2.89 Åand 3.58 Årespectively. The initial unit cell structures of these compounds are made with reference to the experimental data as in Figure 24.

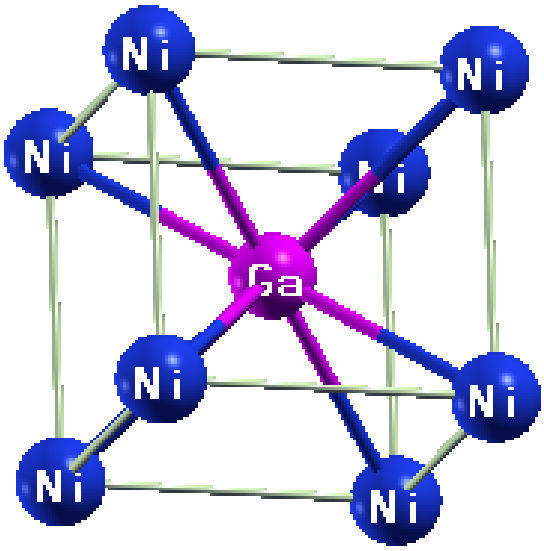

Figure 23: Crystal structures of NiGa

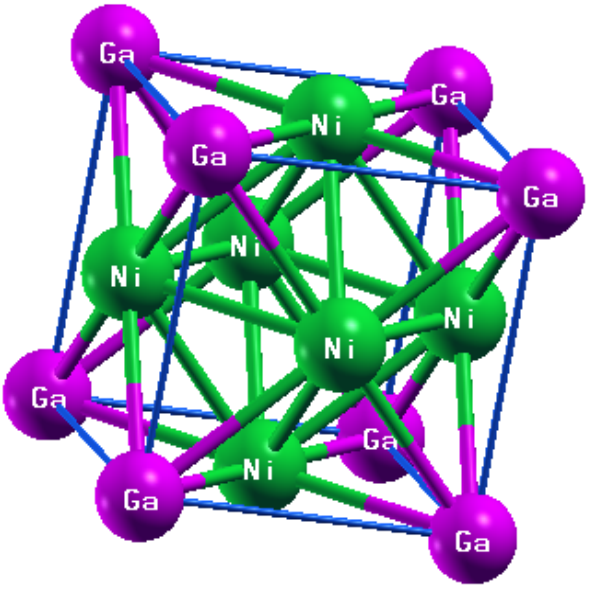

Figure 24: Crystal structures of Ni_3Ga

In nature, system tends to have minimum potential for stability. Energy minimization for NiGa is carried out by varying lattice parameter as in Figure 25. The lattice parameter corresponds to minimum energy is taken to achieve energetically stable structure.

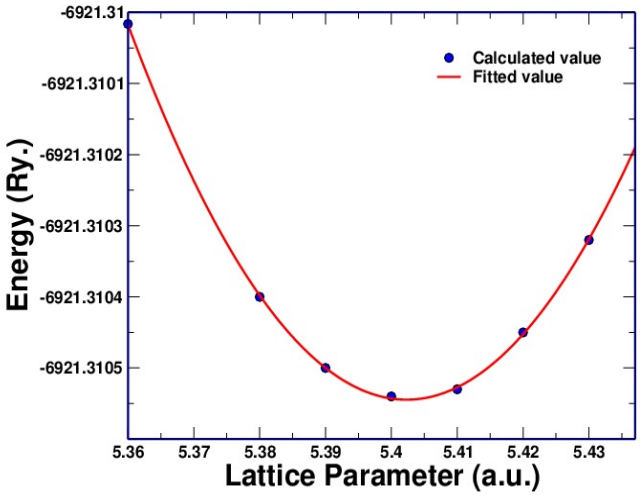

Figure 25: Energy versus lattice parameter(a) of NiGa alloy

The calculated lattice parameters for NiGa and Ni_3Ga are about 1% smaller than experimental value. To know the electron occupancy in energy level, electronic band structure is calculated using the same lattice parameter obtained by energy minimization.

For the visualisation of the wave vector-dependence of energy states, we need to go through a way of electronic band structure calculations along with possible electronic transitions. As LMTO-ASA works at 0 K, we are concentrated to study the electronic bands and electronic density of states of the system at the same environment. The coulomb interaction between Ni and Ga core and electrons while bringing together splits the energy levels and forms band as displayed in Figure 26. Looking into band structures, valance and conduction bands overlap significantly at the Fermi level, as a result, both materials exhibit the metallic nature. Bands coincide for all K-values mentioned in structures within the Brillouin zone, mostly in Γ point after 48 symmetry operations. Light bands crossing the Fermi level in the region of Γ-X direction in Ni_3Ga is steeper than that of NiGa which confirms the more metallic character of Ni_3Ga as suggested in previous work. Greater the overlapping of bands mean the stronger the interactions of electrons and hence the bands structure becomes wider in Ni_3Ga than that in NiGa.

4.8 Fat-band Structure

Fat bands calculations have been performed to know the contributions of different orbitals in these transition metal alloys.

From Figures 27, 28, 29 and 30, it is seen that e_g band dominates to remaining oth-

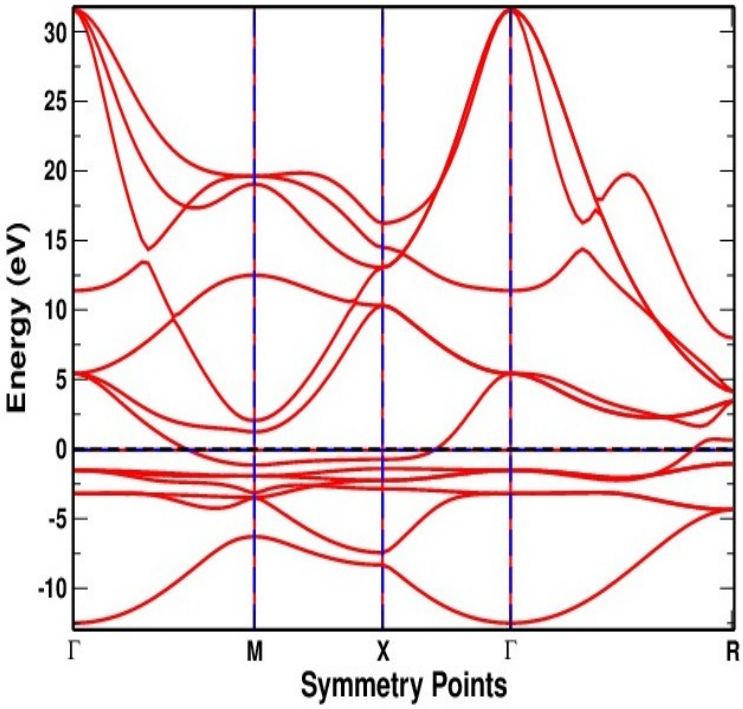

Figure 26: E(k) dispersion relation of NiGa along the major symmetry lines in the Brillouin zone

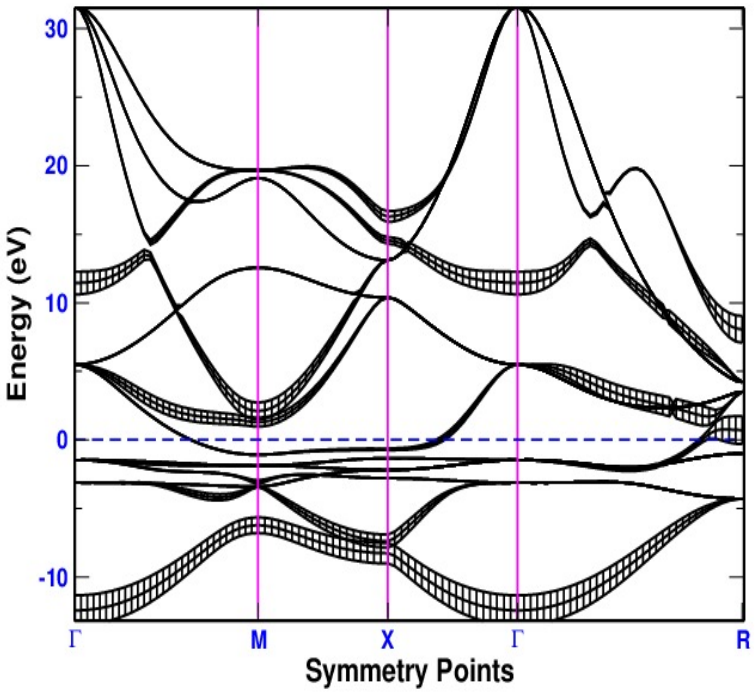

Figure 27: Fat-band structure showing s orbital contribution in NiGa along the high symmetry directions in the Brillouin zone

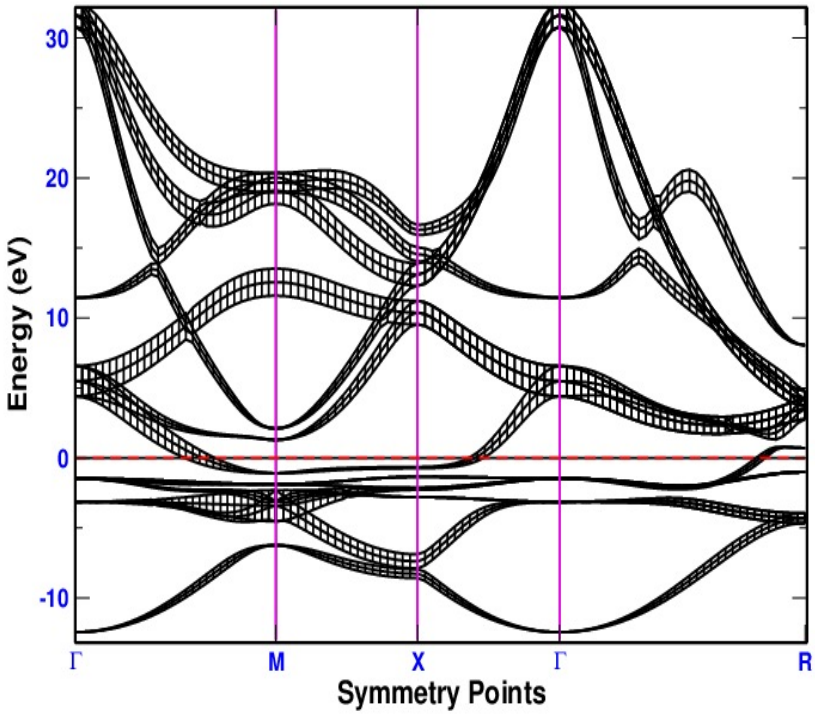

Figure 28: Fat-band structures showing p orbital contribution in NiGa along the high symmetry directions in the Brillouin zone

ers near Fermi level and s and p electrons tend to have much wider bands with potential implication for the mobility of electrons, which again helps to study the thermal conductivity of metallic alloys. This e_g band is highly responsible to make it metallic because of having highest contributions in the total energy band structure. In addition, s and p orbitals of gallium are mostly found at the bottom of band and above the Fermi level.

Similar trends of orbitals contributions are observed in Ni_3Ga as displayed in Figures 31,32, 33 and 34.

Similarly d-orbitals contribution on band structure is displayed below figures.

e_g band dominates near Fermi level and s and p electrons tend to have much wider bands with potential implication for the mobility of electrons. This e_g band is highly responsible to make it metallic because of having largest contributions in the total energy band structure. Besides, s and p orbitals of gallium are mostly found at the bottom of band and above the Fermi level.

From bands plot of NiGa and Ni_3Ga, it is observed that the light bands crossing the Fermi level in the region of Γ-X direction in Ni_3Ga is steeper than that of NiGa showing

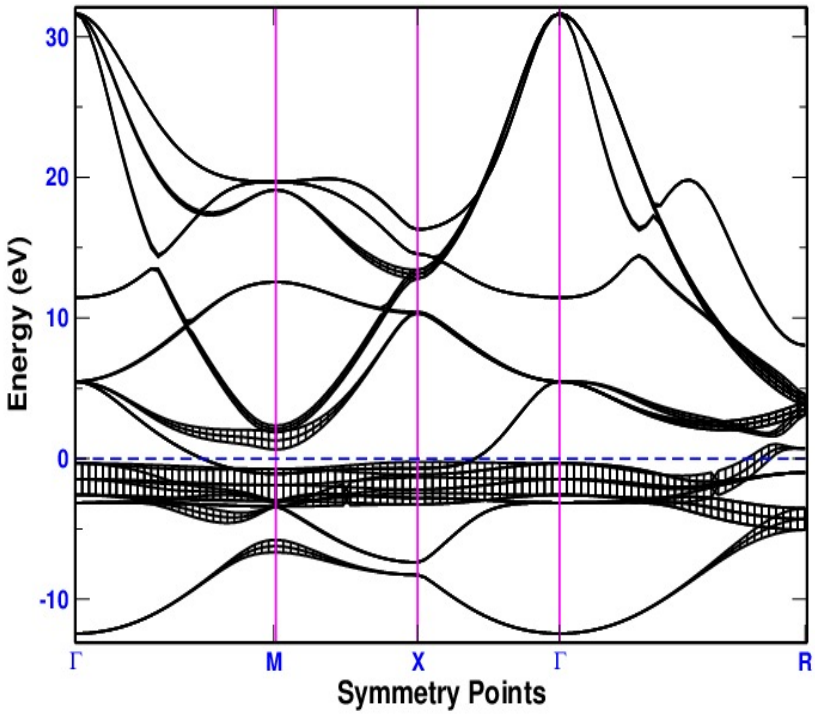

Figure 29: Fat-band structure showing t_{2g} orbital contribution in NiGa along the high symmetry directions in the Brillouin zone

the more metallic character of Ni_3Ga as suggested in previous work. Greater the overlapping of bands mean the stronger the interactions of electrons and hence the bands structure becomes wider in Ni_3Ga than that in NiGa.

4.9 Magnetization in Ni-Ga

Magnetism of materials is the specific property. It is related to density of states. Magnetism is the property of magnetic substances which shows attraction or repulsion nature when an external magnet is brought near to it. Since all matter somehow responds to magnetic field, it is useful to introduce a definition of the concept magnetic materials. Magnetic materials can be classified by how their magnetic dipoles are oriented relative to each other; parallel, anti-parallel or not at all. Since the electronic band structure tells the information about the bands along high symmetry directions(wave vector) and transition probability depends on how many states available in initial and final energies, we need density of states calculations across the entire BZ, not only the particular directions. The electron density of states is a key parameter for the determination of

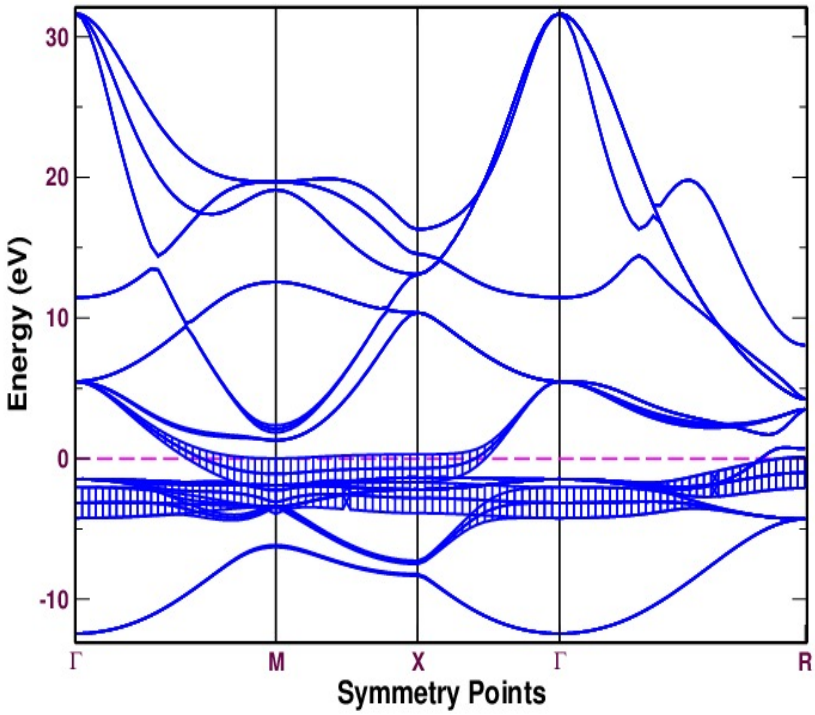

Figure 30: Fat-band structure showing e_g orbital contribution in NiGa along the high symmetry directions in the Brillouin zone

the physical phenomena of solids. The beauty of nickel is measured by making higher concentration in NiGa.

Table 2: value of charges in s, p, d orbital in NiGa .

Species	s	p	d	Total
Ga	0.530e	0.700e	0.169e	1.399e
Ni	0.298e	0.377e	4.480e	5.155e

Our findings show that nickel has higher amount of charges in d-orbital. The major contributions on the density of states for up and down states is due to d-orbitals of Ni. The contributions of Ga is due to s and p orbitals. Peaks in the density of states represent the large number of states at the corresponding energy. In Ni_3Ga, three main peaks 11.6 states/eV with energy 0.89 eV, 11.2 states/eV with energy -0.68 eV and 10.4 states/eV with energy -0.60 eV are observed. Two principal peaks 3.9 states/eV with energy -1.69 eV and 3.85 states/eV with energy 1.91 eV are clearly seen in NiGa. Sharp peak near Fermi level is the significance of localized d orbital and the case is positive spin polarised. These nature of DOS just below Fermi level shows the higher chances of magnetic fluctuations by changing the number of electrons. The electronic transi-

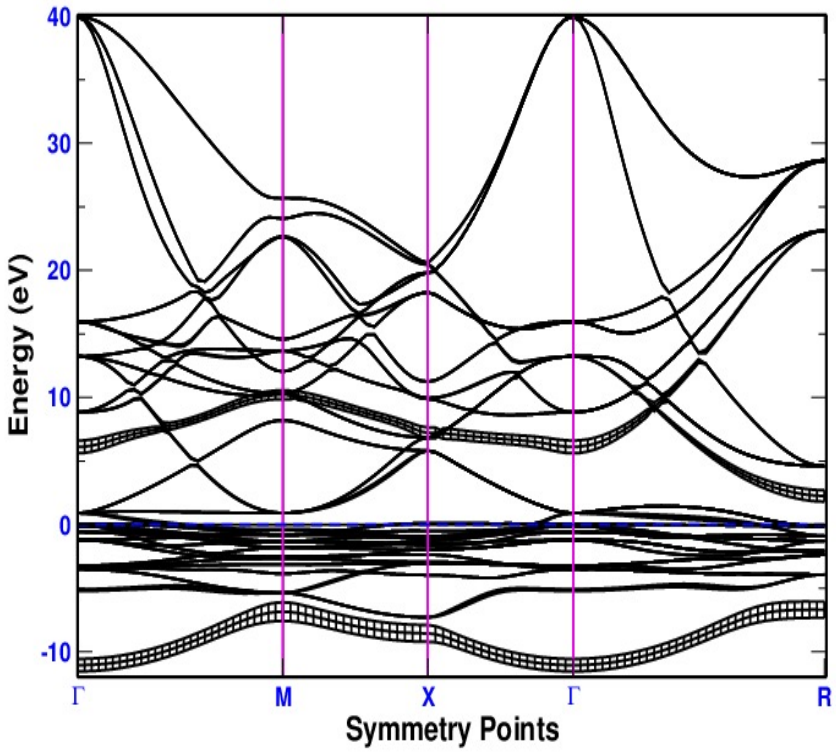

Figure 31: Fat-band structure showing s orbital contribution in Ni_3Ga along the high symmetry directions in the Brillouin zone

tions between Ni d bands hybridized with Ga sp characteristics are responsible for these peaks. The mechanical strength of materials are due to their strength of atomic bonding. The propensity towards magnetism can be described here in reference to density of states plot. Low density of states near the Fermi level signifies the strong bonding between Ni and Ga in NiGa and strong overlap of s, p and d orbitals and the DOS closer to E_F in the valence band contains contribution from e_g up spin state. Since the electronic DOS at the Fermi level for Ni_3Ga are higher than that for NiGa, contribution to the thermal expansion coefficient for Ni_3Ga are larger than NiGa. However, at low T (0 K), it can be less significant. The results of DOS for Ni_3Ga (ie. higher concentration of Ni) indicates that both phases are different in nature. The magnetic moment of Ni_3Ga corresponding to minimum energy is found to be $0.58\mu_B$/cell, which is 21% less than the value estimated in previous theoretical work (Aguago et al., 2004). The magnetization is dominated by nickel which is the beauty of Ni. The main contribution for the magnetic moment of this compound comes from Ni-3d electrons while sp electrons have no role to display the magnetic moment. Strong competition between up DOS channel and down DOS channel in NiGa results zero magnetic moment and the system as a whole

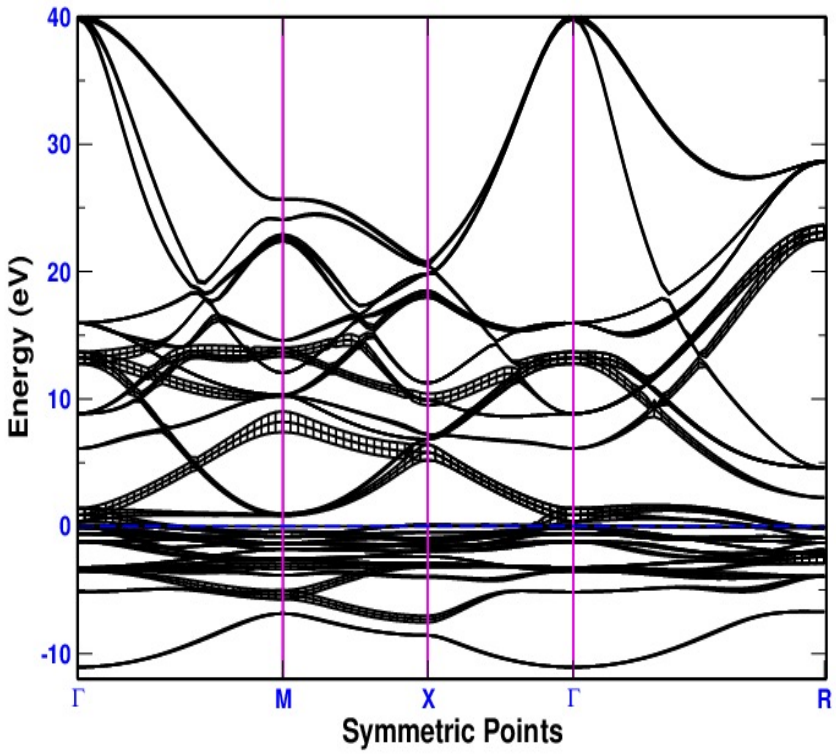

Figure 32: Fat-band structure showing p orbital contribution in Ni_3Ga along the high symmetry directions in the Brillouin zone

becomes non-magnetic in nature.

To have a better understanding of the contributions of different orbitals and different constituent of compounds, PDOS are calculated. The density of states can be resolved into its partial components according to different orbital of different atoms. The shape of DOS versus energy is determined by an overlap of orbitals as in Figures 38 and 39.

From the analysis of total and projected density of states, it has been found that a sharp bonding(anti-bonding) peaks is located in the region near -3.1 eV (1.4 eV) inNi_3 Ga. The contribution of Ga appear again very less, as observed in NiGa. Low density of states at E F suggest the bonding capability of Ni_3 Ga. The projected DOS of Ga is broader than that of Ni and also the number of Ga peaks is more than that of Ni suggest the hybridization of Ni-3d and Ga-2p with pd mixing range (-3.1 eV to 0.03 eV). This kind of pd-hybridization also tells the mechanical stability of inter-metallic compound Ni_3 Ga. The shoulder closer to Fermi level is related to d electron interaction of Ni and Ga. The largest contributions to DOS is given by d electrons because of higher concentration(high number ie. 9 per atoms). The ions a bit changes in total energy so

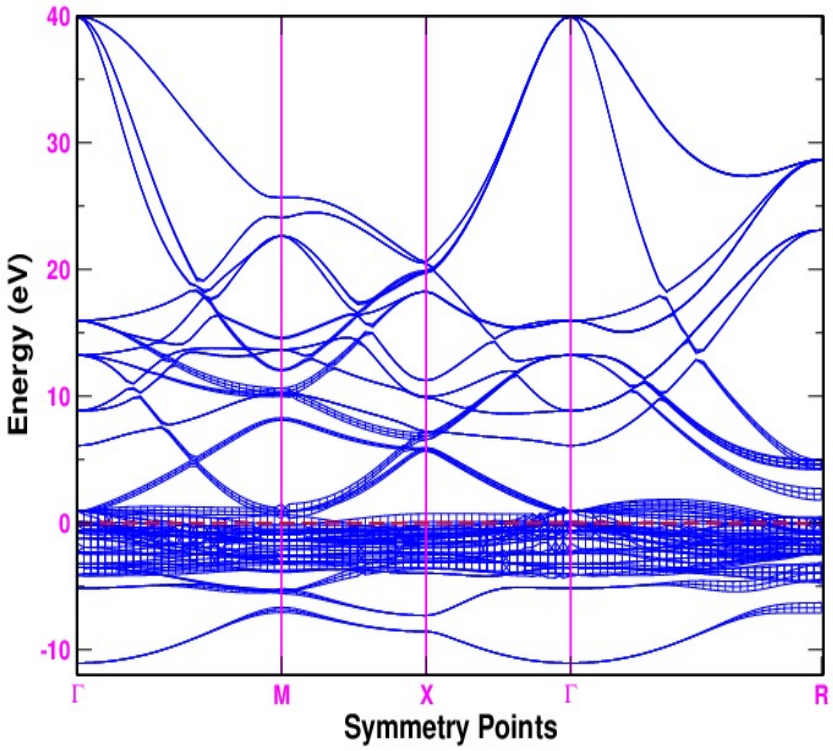

Figure 33: Fat-band structure showing t_{2g} orbital contribution in Ni_3Ga along the high symmetry directions in the Brillouin zone

magnetic fluctuation takes a main role to deviate magnetic moment. The addition of Ni concentration has contributed to make the system magnetised. The charge density increases with increasing Ni content.

The Ni d electrons are localized and basically take part in magnetism. Ni ions are in high spin level in NiGa so contributions to minority spin channel from 3d electrons are less significant. The pivotal role for the number of electron comes from the down spin electrons of Ni-3d. In NiGa, The d bands lie approximately 1.5 eV below the Fermi level, density of states at the Fermi level is low, illustrating the d-band filling of the alloy. In contrast, band structure of Ni_3Ga has the Fermi level lying in the region of d density of states. The magnetic moment of NiGa varies with energy as in Figure 40.

4.10 Spin fluctuation in Ni_3Al and Ni_3Ga

The study of fluctuations in spin affect the magnetization of system as a result it magnetic moment varies. The magnetization of the systems Ni_3Al and Ni_3Ga are checked

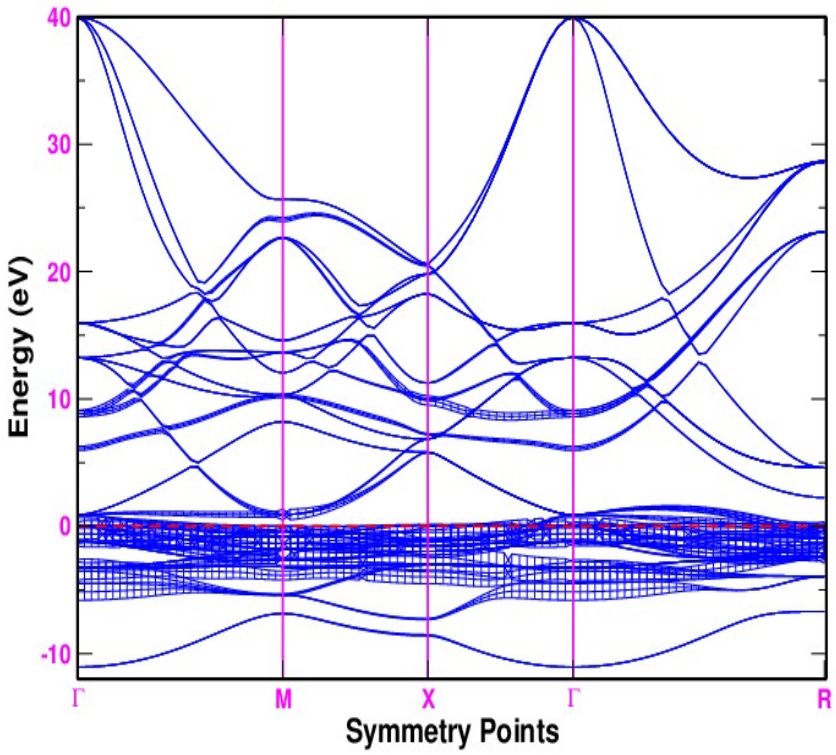

Figure 34: Fat-band structure showing e_g orbital contribution in Ni_3Ga along the high symmetry directions in the Brillouin zone

with energy. The value of magnetic moment is observed corresponding to minimum energy. There is no fluctuation in in up down spin observed in Ni_3Al. There is very small change in energy to cover the magnetic moment values ranging from 0.51 μ_B to 0.55μ_B Spin fluctuation in Ni_3Al is weaker than in Ni_3Ga. Spin fluctuates in Ni_3Ga frequently even in very small energy range.

We have summarized the value of estimated lattice parameter (a), calculated magnetic moment (μ_B), experimental magnetic moment value and density of states n(E_F) of different materials studied.

Table 3: Value of estimated lattice parameter (a), calculated magnetic moment (μ_B), experimental magnetic moment value and density of states n(E_F) of different materials

Material	Structure	a (nm)	Experimental μ_B	calculated μ_B	n(E_F)
NiAl	B2	0.287	0.00	0.00	3.7
Ni_3Al	L12	0.357	0.22	0.54	11.5
NiGa	B2	0.230	0.00	0.00	3.8
Ni_3Ga	L12	0.381	0.00	0.58	12.8

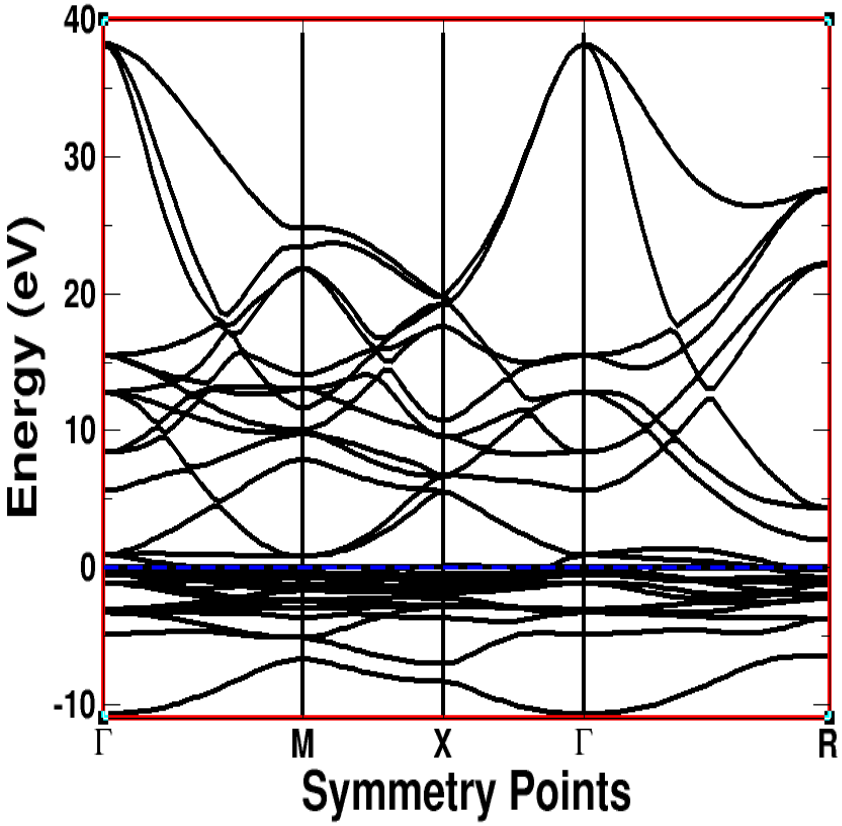

Figure 35: Band structures of Ni_3 Ga

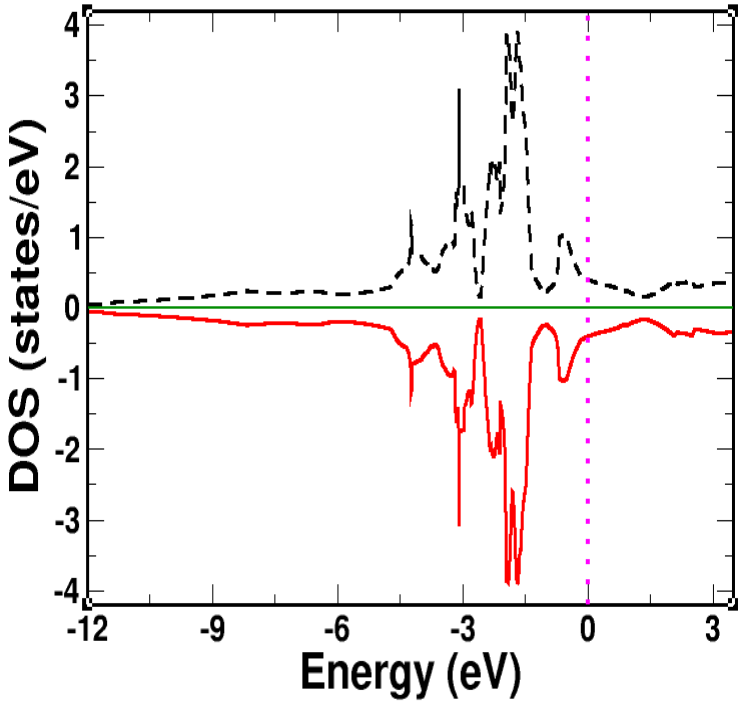

Figure 36: DOS of NiGa

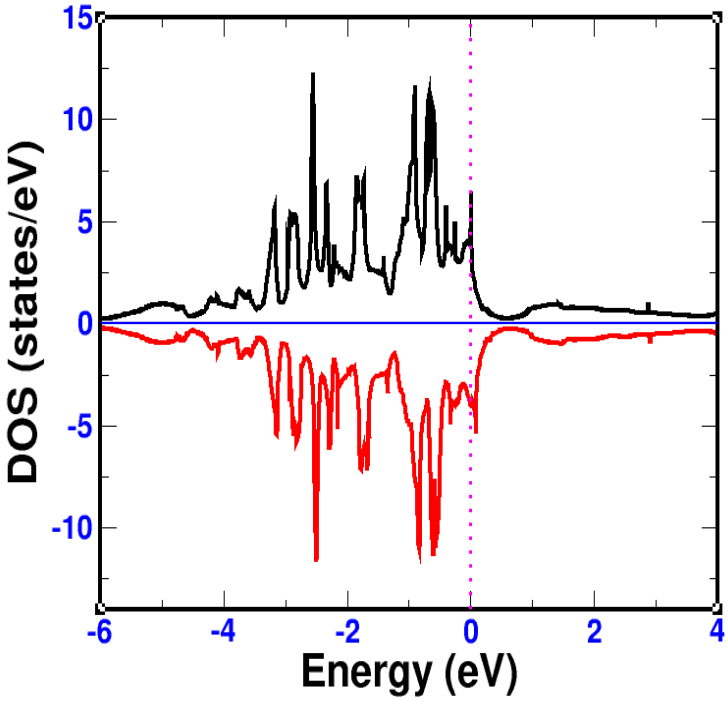

Figure 37: DOS of Ni_3Ga

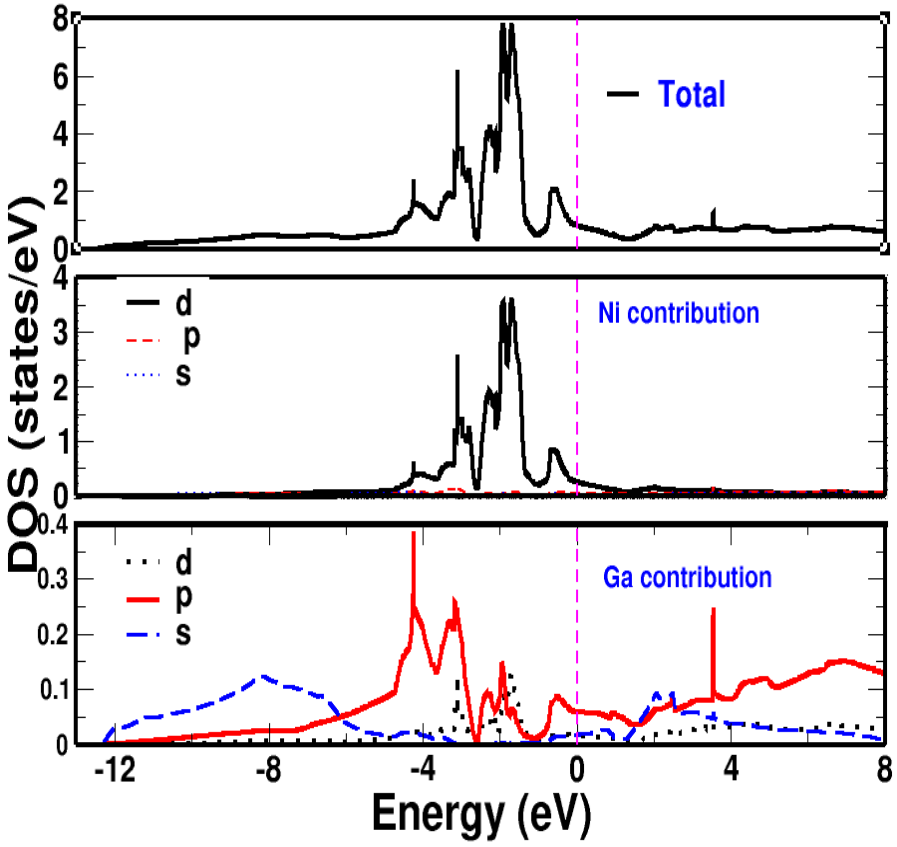

Figure 38: PDOS of NiGa

4.11 Charge Density

The charge density distribution gives more information about the interaction between same and different species. Interaction energy is also dependent on their bond length

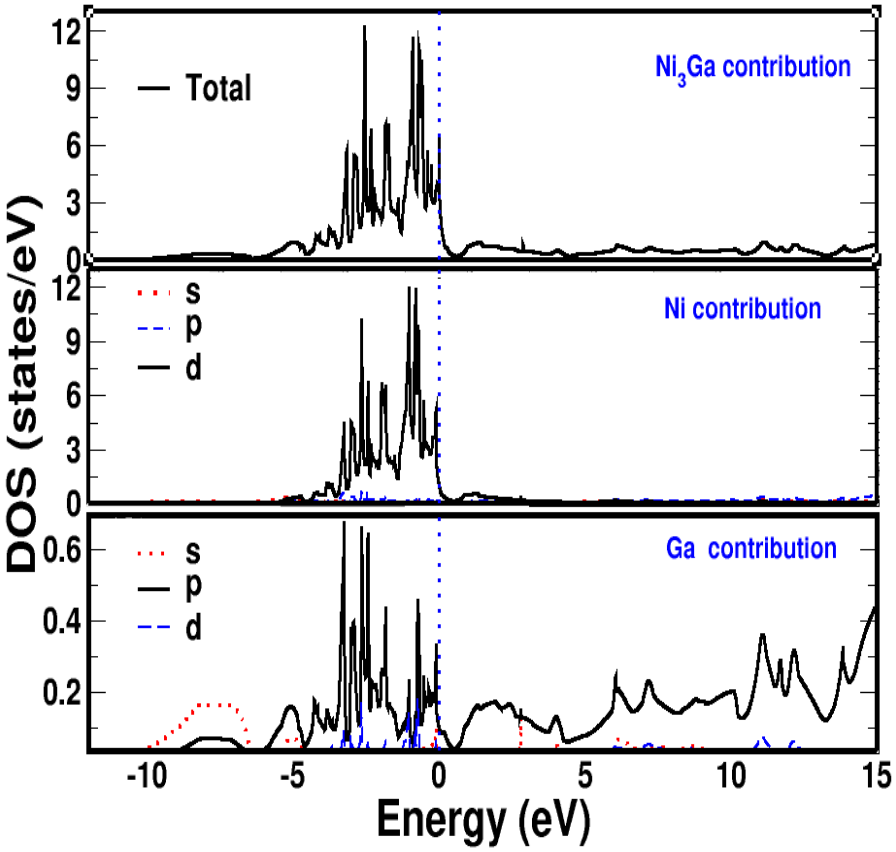

Figure 39: PDOS of Ni_3 Ga

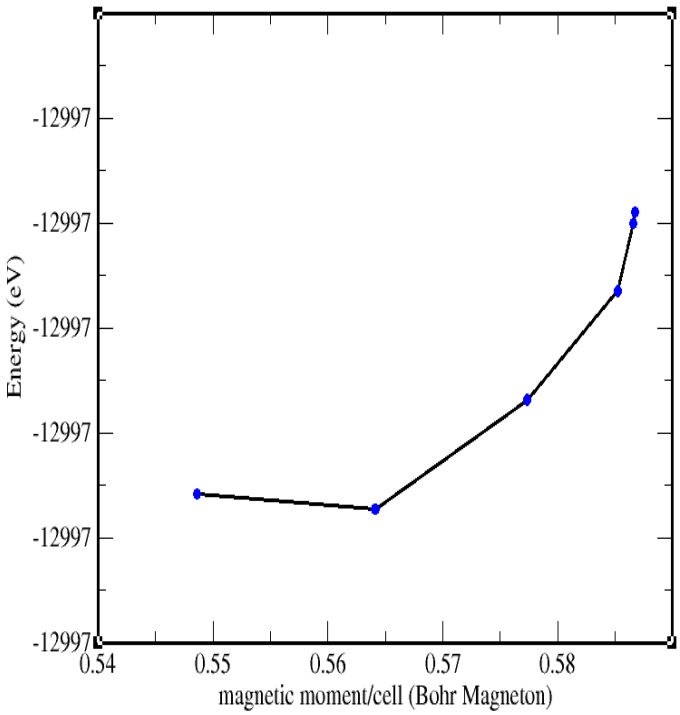

Figure 40: Energy versus magnetic moment of NiGa

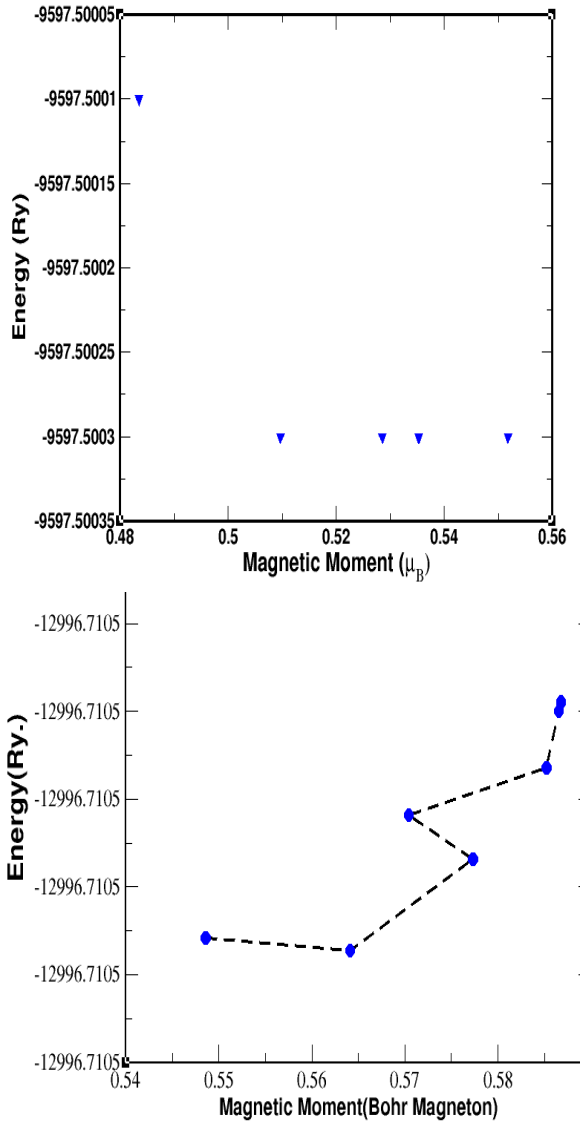

Figure 41: Spin fluctuation in Ni_3Al and Ni_3Ga

and charge.

The charge density distribution gives more information about the interaction between same and different species. Interaction energy is also dependent on their bond length and charge. The calculated Ni-Ni and Ni-Ga bond length for Ni_3Ga is the same 2.53 Å. More fraction of charges are accumulated near Nickel atom as in fig. 42. The charge population in species Ni and Ga are 0.314e, 0.376e, 4.452e and 0.539e, 0.662e, 0.168e, correspond to s, p and d orbitals charges in Ni_3Ga crystal respectively. Since the pauling electronegativity of nickel is 1.91 and that of gallium is 1.81, filled Ni d band may reflect that electrons transfer from Ga to Ni. There is no charge in the interestrial region nearest Al. Most of charge is shifted towards Ni atom means charge is increased at the centre of crystal. There is increase in charges in d orbital upon going from Ni to NiGa to Ni_3Ga, which is ensured by d band filling as well as charge density plot as in Figure 43. Charge

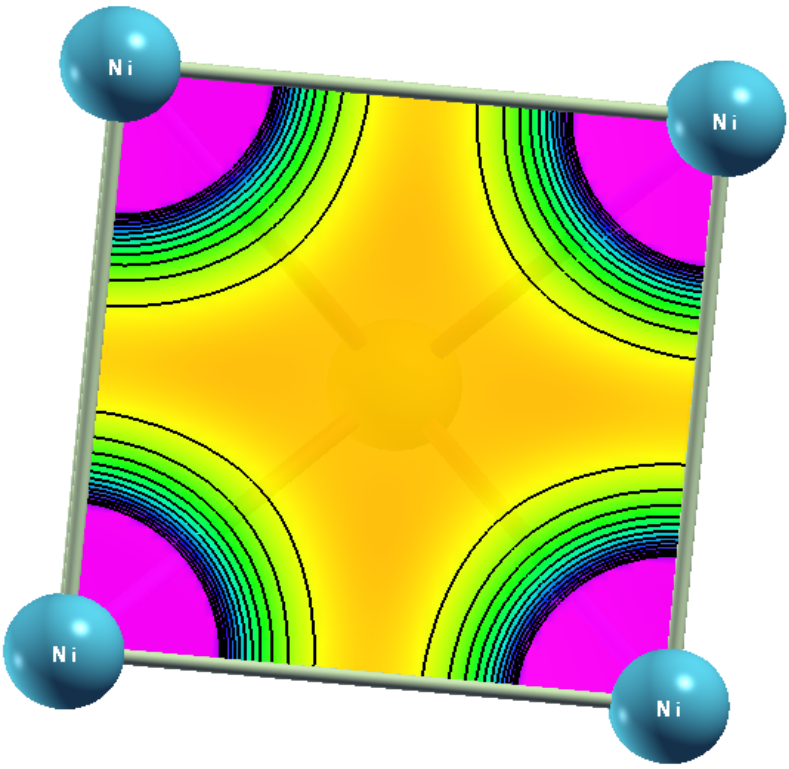

Figure 42: Contours of electron density of NiGa on [100] plane

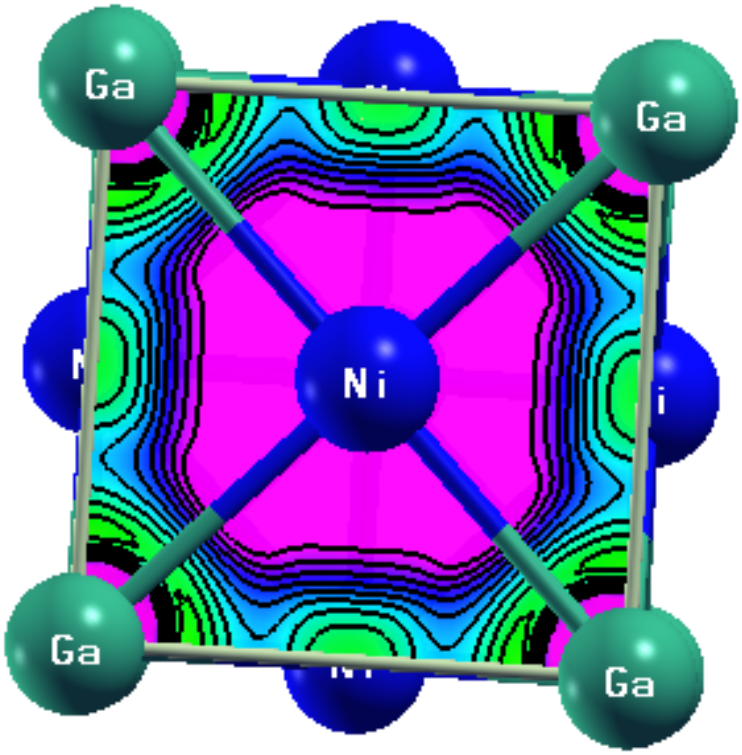

Figure 43: Contours of electron density of Ni_3Ga on [100] plane

is increased at the centre of crystal. The contours of increased electronic charge density can be seen at the centre indicated by maroon color and decreased charge density in

interestrial region represented by yellow color.

4.12 Mixing Behaviour of Ni-Al

Studying the properties of alloys in liquid state provides some unique information that can be used to improve the processing and qualities of materials in the solid state. Noble properties of Ni-Al alloy have attracted the most modern consent of the researches to predict the thermodynamic, structural and transport properties of Ni-Al liquid alloys. Concentration fluctuation limit is studied at different concentration. It is found that the Ni-Al liquid alloy at 1873 K is ordering in nature. Thus there is no de-mixing in the solid state. All the interaction energy parameters of regular associated solution model are found to be negative. The negative value of interaction parameter indicates that the atoms of Ni and Al are attracted towards each other in the liquid state whereas the negative value indicates that the atoms of Ni and Al are attracted towards the complex Ni_3Al in the liquid state. Free energy of mixing versus contration of nickel is shown in Figure 44.

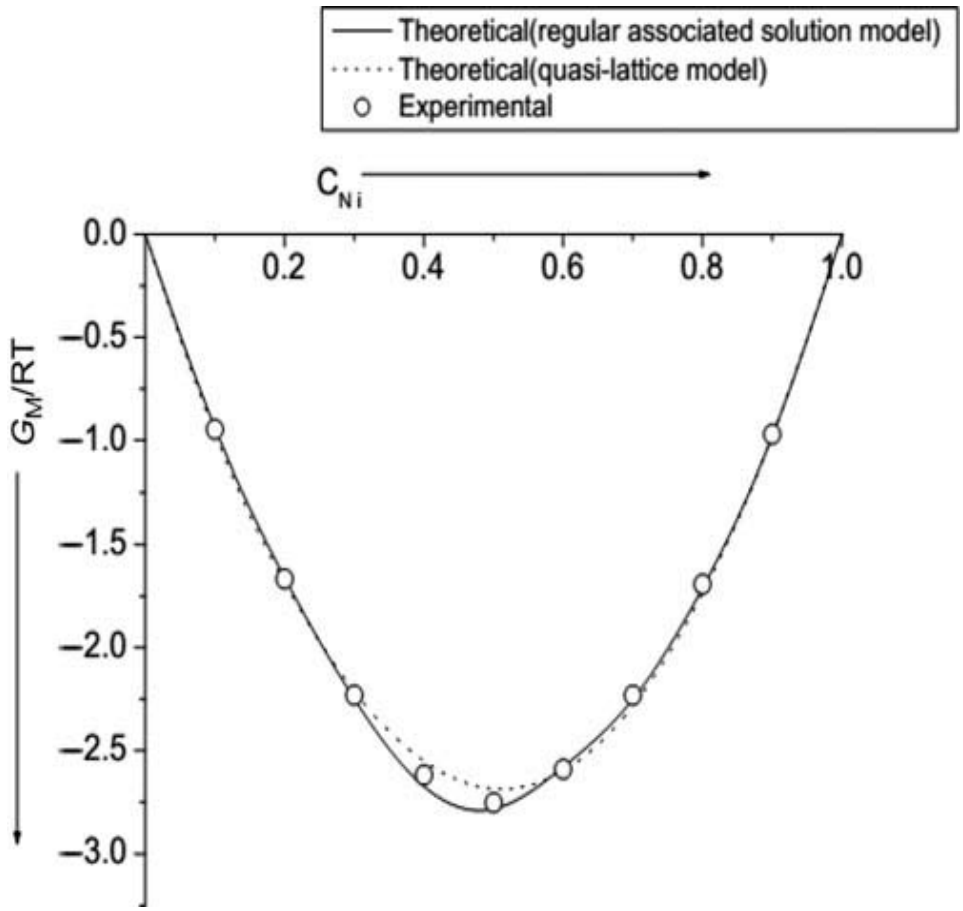

Figure 44: Free energy of mixing versus concentration of nickel at 1873 K

Although the alloys have largely uses in solid state, they are in general formed from the

liquid state. The liquid state is eventually a disordered state having only short range interactions in the nearest neighbourhood. The negative values of the ordering energy parameters $\omega = k_B T$ and $\omega AB = k_B T$ indicate that the NiAl melt is ordered in the liquid state. But the positive values of ωAA =k$_B$T represents that there is weak interaction among the Ni atoms in the liquid state. These model parameters are then used to find the theoretical values of the free energy of mixing from regular associated solution model and from quasi-lattice model.Thus, regular associated solution model better explains the free energy of mixing of the Ni-Al liquid alloy than that by quasi-lattice model. The minimum values of G$_M$ =RT are high negative (theoretical and experimental both) in the liquid state near the melting temperature. The Ni- Al liquid alloy at 1873 K is thus found to be highly interacting system. As this minimum value lies at equal concentration, this system is symmetric in the liquid state.

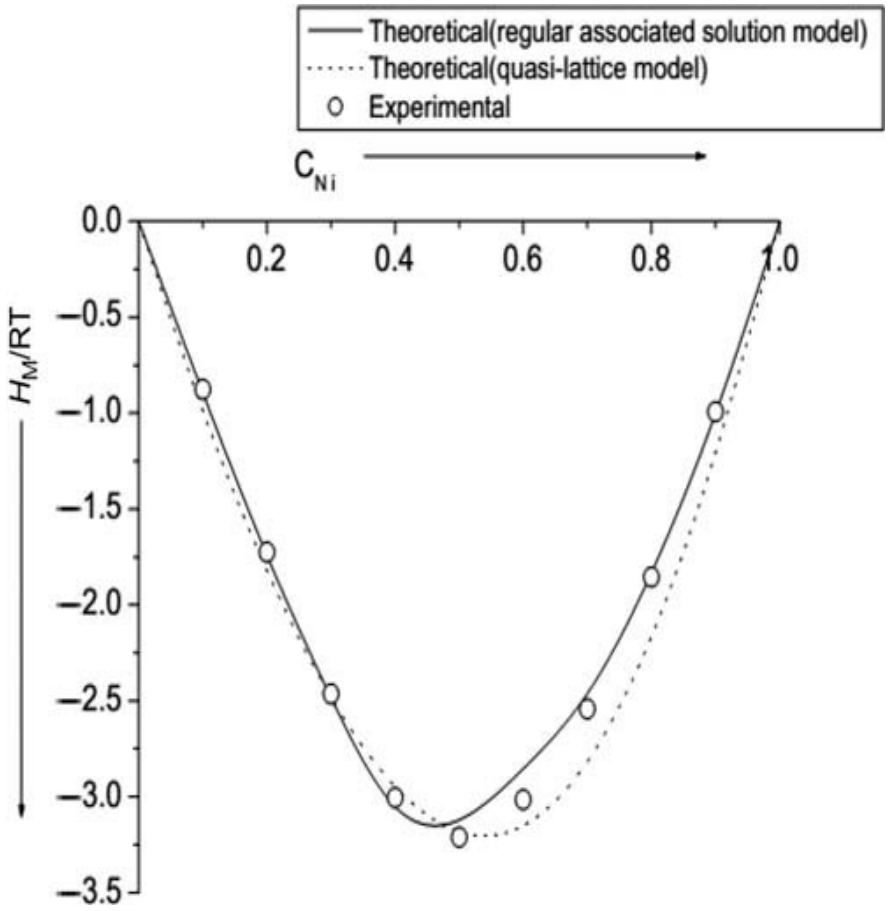

Figure 45: Heat energy of mixing versus concentration of nickel

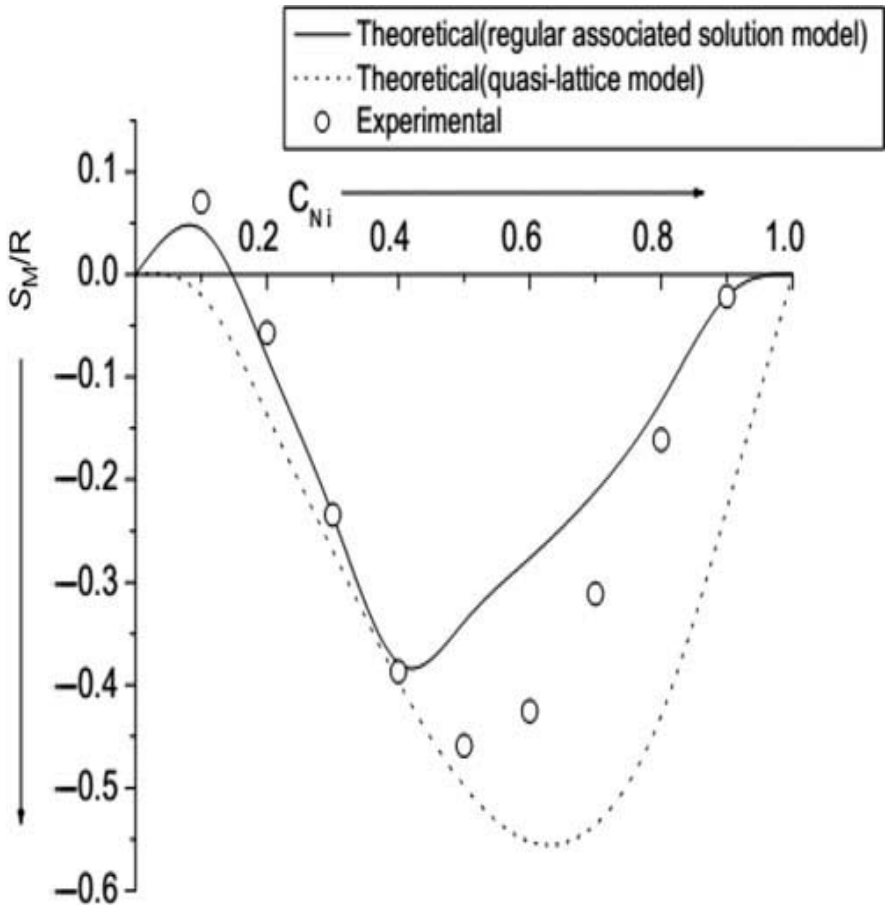

Figure 46: Entropy of mixing versus concentration of nickel

Temperature-dependent parameters of both models are found to have positive values. The enthalpy of mixing has high negative values, which tells that the bonding among the complex and the atoms is stronger. Values of entropy of mixing are found to be positive at C_Ni=0.1, which means alloy is less ordered at this composition whereas the computed value of entropy of mixing from quasi-lattice model is found to be slight negative at C_Ni=0.1, which suggests that the alloy is more ordered at this composition. These values obtained from both of the models are found to be negative at all other compositions, suggesting that the alloy is ordered at these compositions, which is in accordance with the experimental values. The theoretical values predicted by regular associated solution model are more close to the experimental values than that obtained by quasi-lattice model. The theoretical investigations thus shows that regular associated solution model is more appropriate in explaining the thermodynamics of the Ni-Al alloy at 1873 K than that of quasi-lattice model.

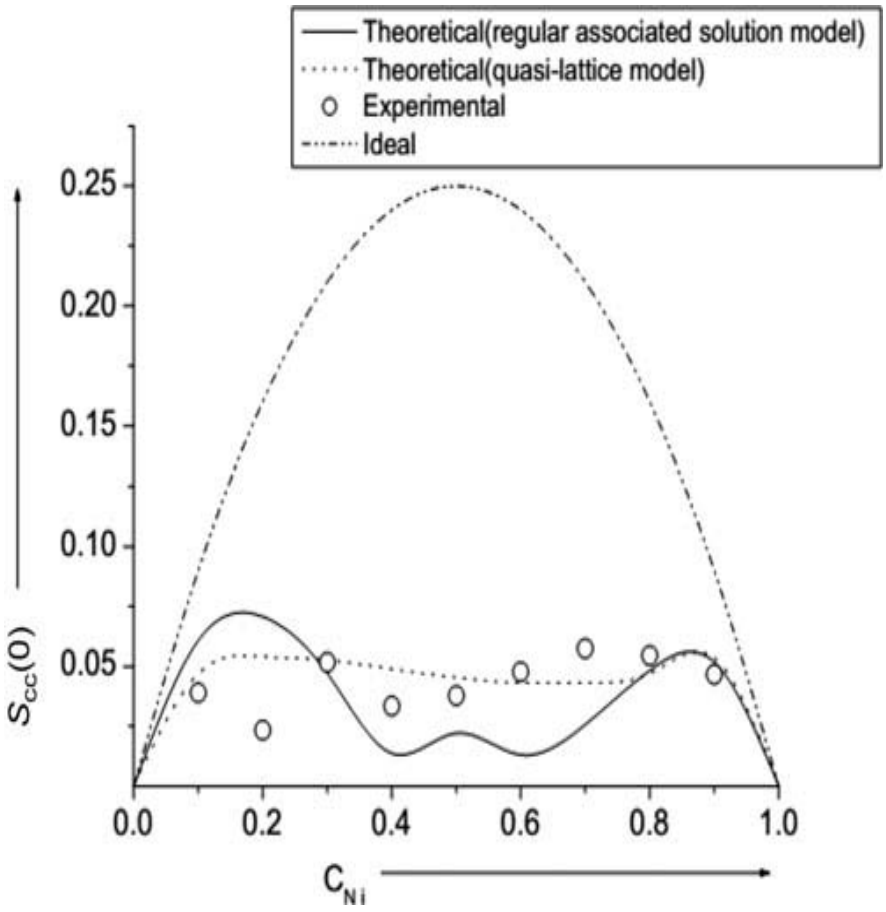

Figure 47: Concentration fluctuation in long wavelength limit versus concentration of nickel in 1873 K

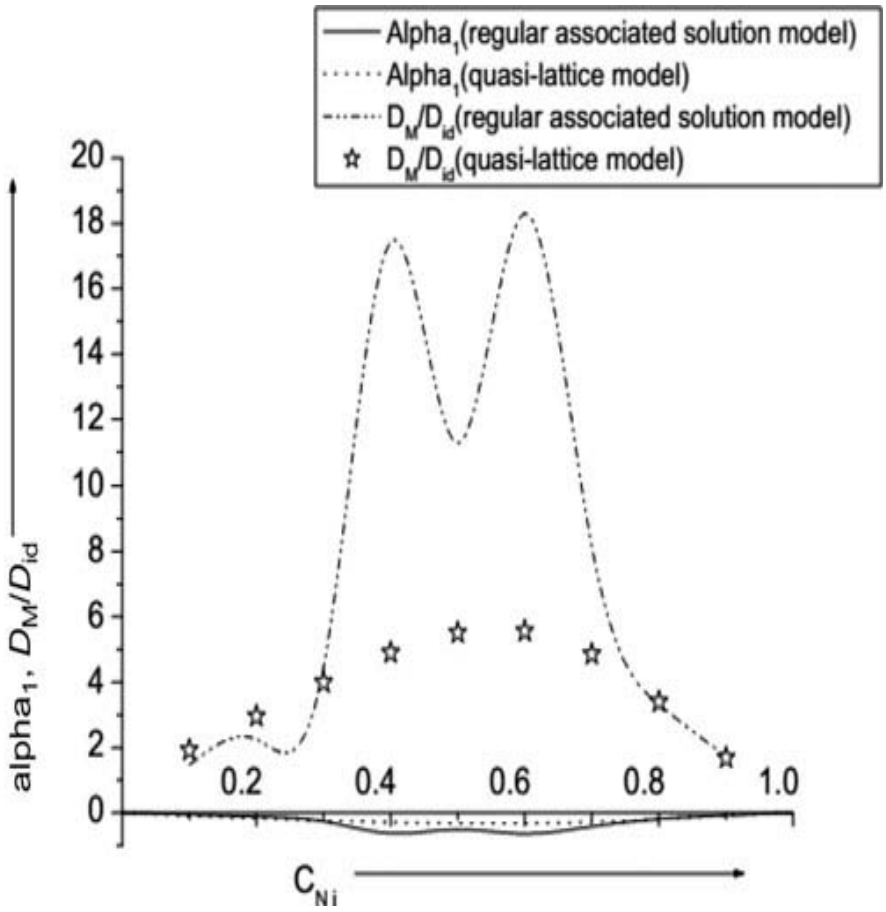

Figure 48: Short-range order parameter versus concentration of nickel at 1873 K

Ni-Al liquid alloy at 1873 K is ordered. Thus there is no de-mixing in the solid state. Since the liquid state is a disordered state having only short-range interactions in the nearest neighbourhood, the microscopic structural properties thus can be done by estimating Warren-Cowely short-range order parameter α whose values lie between -1 and +1 at equiatomic composition. Its minimum value is -1 , which indicates that there is complete ordering nature of the liquid alloy. The maximum possible value is 1, which indicates the complete segregating nature of the liquid alloy. Zero value of short-range order parameter indicates the random distribution of Ni and Al in this system.

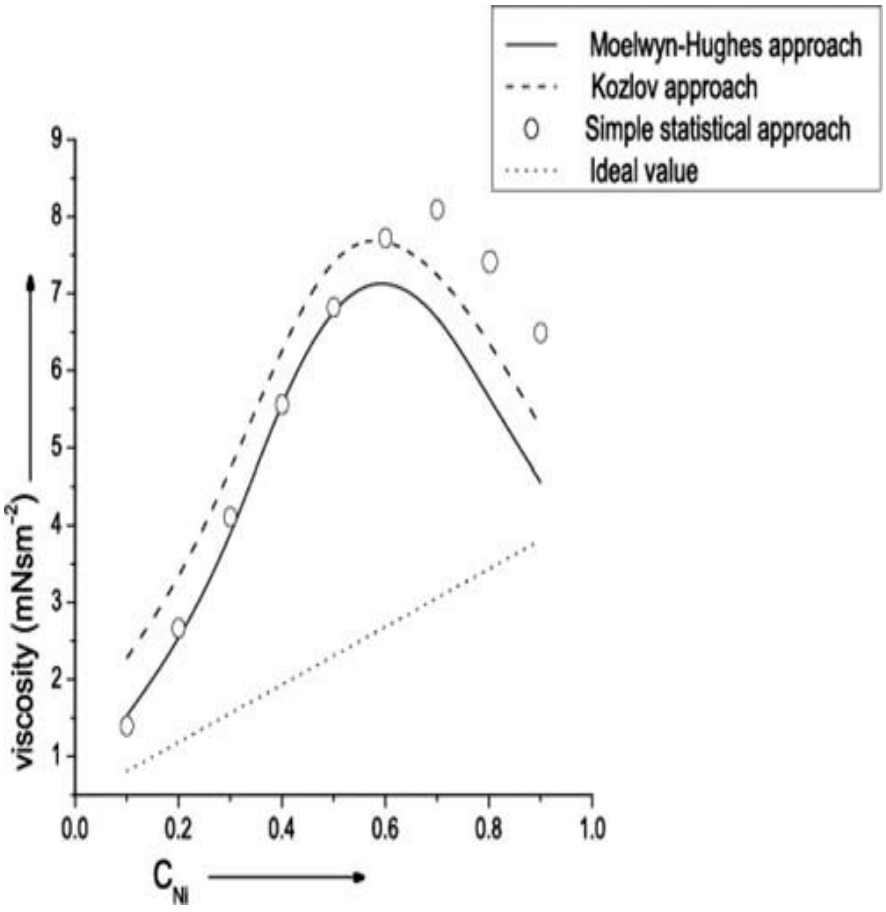

Figure 49: Viscosity of NiAl with different concentrations of nickel

Viscosity changes with concentration of Ni. Viscous property of NiAl confirms that Ni-Al is non-ideal system.

4.13 Optical properties of NiAl

Optical properties of materials is essential to know not only the unfilled and filled band also the character of band. Optical properties like atomic polarisation and dielectric constant depend on refractive index of materials which can be calculated from the knowledge of band structure. Transition from unfilled to filled bands in band structure at high symmetry points in the BZ is considered to observe optical spectra (King-Smith et al., 1992).

Dielectric function of a material is described in terms of complex

$$\epsilon(\omega) = \epsilon_1(\omega) + i\epsilon_2(\omega)$$

On the basis of electronic structure, the dielectric function of NiGa is calculated as displayed in Figure 50.

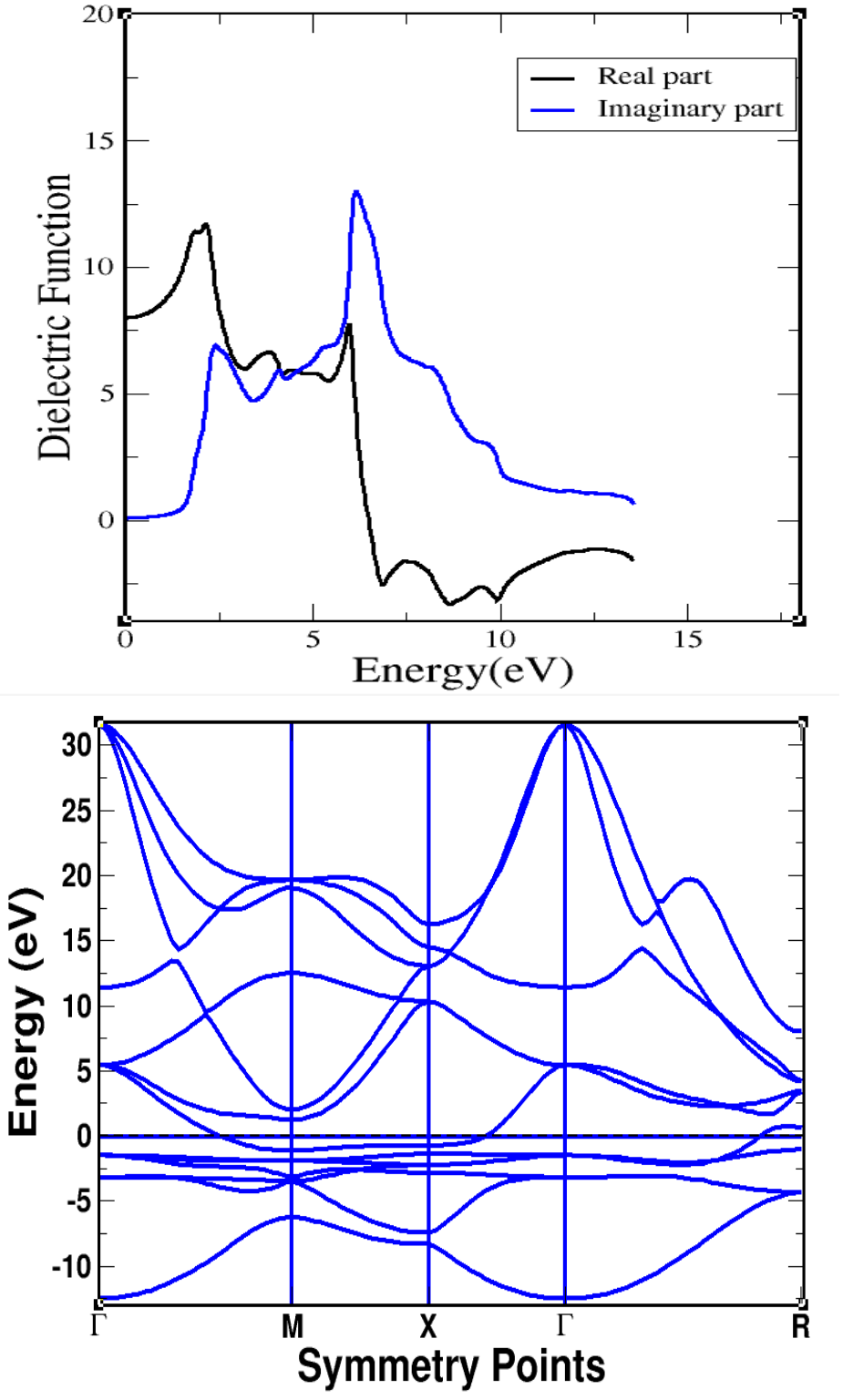

Figure 50: The calculated real and imaginary part of dielectric function as a function of photon energy for NiAl and its electronic band structure

The linear response of alloy to electro-magnetic(EM) radiation can be explained by dielectric function. The optical properties can be studied with the help of dielectric function $\epsilon(\omega) = \epsilon_1(\omega) + i\epsilon_2(\omega)$. The are two contributions of $\epsilon(\omega)$, basically, intra

and interband transitions. The contribution to $\epsilon(\omega)$ fron intraband is important only for metals. The interband transition is again divided in to direct and indirect transition. The contribution of direct inter-band transition to imaginary part of dielectric function comes from possible transition between occupied and unoccupied states for k-points over BZ and real part is described by Kramers-Kroing relation (Fox, 2001). Imaginary part of the dielectric function is seen to be a measure of energy absorption in a system as in Figure 50. This imaginary part of the dielectric function tells the plasmon density excitations in NiGa as well as loss of energy of propagation of light in the matter so it is positive as in Figure 50. But, real part has negative value indicating the role towards the stability of NiAl. A calculation of the real and imaginary part of the dielectric constant is performed in the energy range 0-13.5 eV. These types of calculations are useful for the quantitative determination of the electronic band structure of solids. Principal peaks originated in dielectric functions is from interband transitions. It is also related to electronic band structure in the sense that intra-band transition occurs in the energy range (-5 eV to 5 eV) at R point and again dielectric function contributed from both real and imaginary part occurs upto 10.5 eV). Real and imaginary parts combine to set amplitudes which does not depend on frequency. Broad peaks at $\approx$ 2.5 eV and 6 eV are caused number of band-band transitions.These transitions are due to free electrons of metallic alloy. It then falls slowly with increasing energy and reaches up to second peak $\approx$ 6 eV and again decreases gradually.

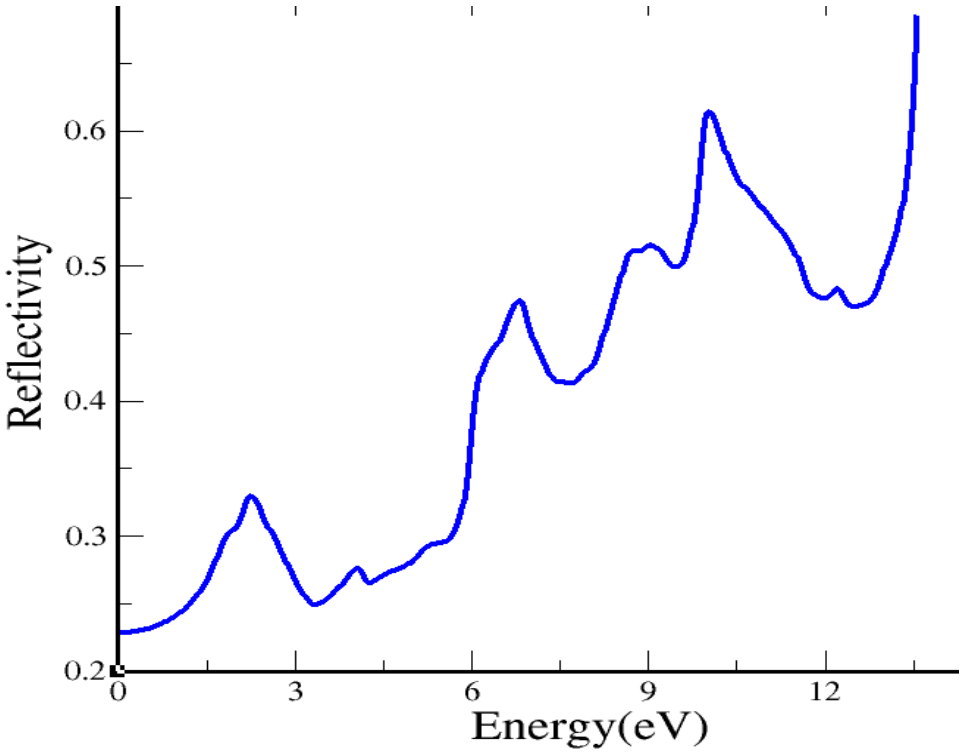

Figure 51: Reflectivity of NiAl

Reflectivity of material changes with photon energy and higher reflection with reflection coefficient 0.6 occurs around 10 eV as in Figure 51. As optical properties of metals, alloys are related to high reflectivity and low transmission, the maximum number of free electrons near the Fermi level in NiGa as in Figure 51 are the basic cause to increase its reflectivity.

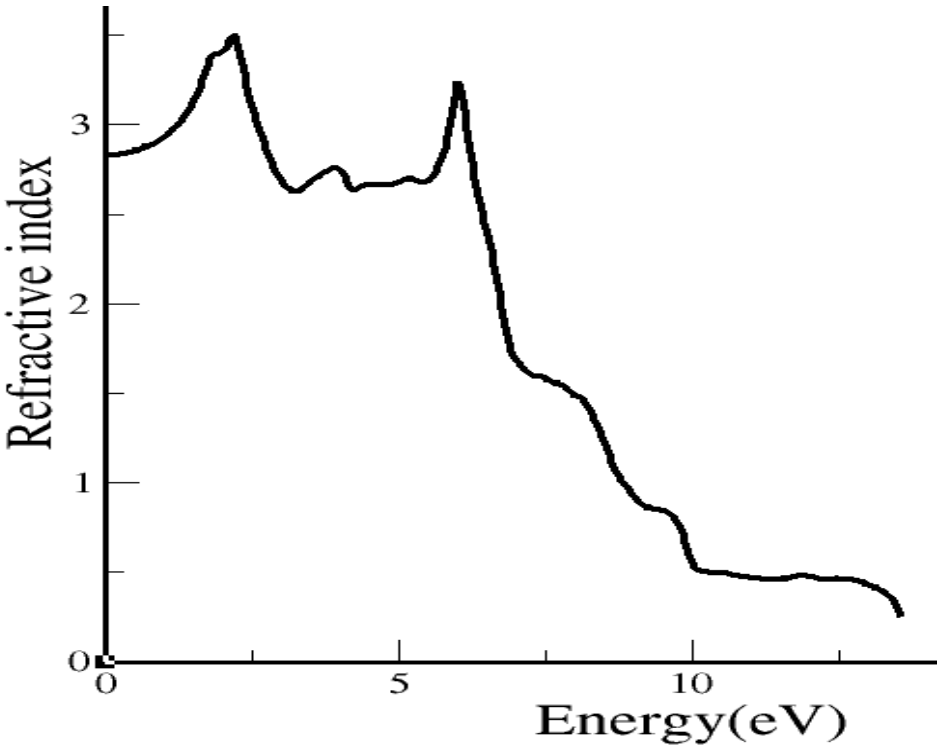

Figure 52: Refractive index of NiAl

The static refractive index is found to be 4.0 at 2.4 eV. That kind of change in refractive index is the cause of change in dielectric function. The nature of refractive index versus energy plot is found to be reverse nature of reflection as the total amount of light is the divided into transmitted, reflected and refracted parts. This type of curve helps to know the application of NiAl in specific purpose.

4.14 Stability of alkaline-earth metal fluorides

Two know the importance of other metals, we have also studied stability of alkaline-earth fluorides, generally known for their intrinsic optical properties and are well characterized with importance of CaF_2 as an ideal material for the detection of β-particle, MgF_2 in multilayer optical coating, SrF as a candidate for ultracold molecular structure for buffer gas cooling and BaF_2 for infra-red spectroscopy. Recently numerous computational work on bending effect of fluorides have been done however, study was

constrained to some symmetries and did not address the unsolved issue of bending potential. Systematic study of molecules gives the fundamental understanding on structural variation going from atoms to clusters. This is what we intended to do meaningful comparisons in four alkaline earth fluoride molecules namely MgF_2, CaF_2, SrF_2 and BaF_2 in regards to their structural and electronic properties along with nature of bonding of constituent atoms in a molecule. The DFT based B3LYP approach was chosen as a computational method due to reliability to calculate the geometries and vibrational properties of molecules containing heavy metals. Structural properties of Alkaline Earth Fluoride molecules MgF_2, CaF_2, SrF_2 and BaF_2 were carried out systematically on the basis of density functional theory with B3LYP approach using Gaussian 03 code. The basis set LanL2DZ were used for alkaline earth metal and 6-31G* and 6-311+6** were used for fluorine atoms with convergence criterion for the force of 0.02 eV/Å. We are interested to look configuration; linear Vs. bent configuration for these fluoride molecules and also to calculate the total energy, binding energy, bond length, bond angle, frequency and dipole moment. In order to know the ground state configurations of MF_2 with M=Mg, Ca, Sr and Ba, systematic study was performed which consisted several possible configurations to get energetically favourable one.

4.15 Structural Properties

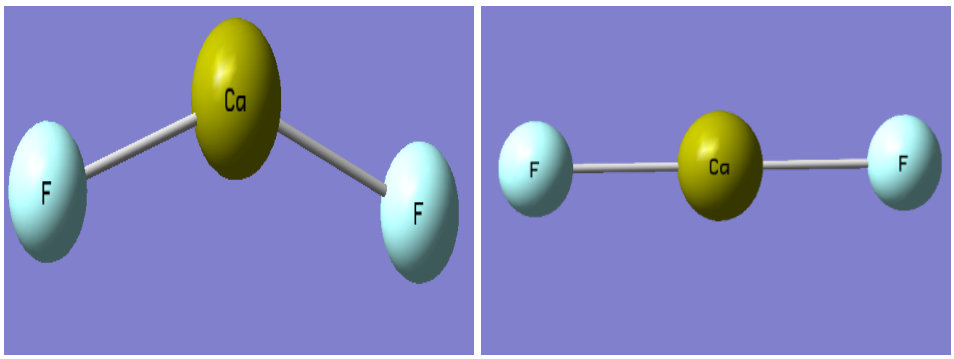

Figure 53: Diagram of geometry of CaF_2 considered to find minimum energy configuration(left) and its relaxed structure(right)

The ground state properties of all studied monomers in F-M-F linear and F-M-F bent configurations are summarized in Table 4.

Similarly, the ground state properties of MF_2 (M=Mg, Ca, Sr, Ba) in both M-F-F linear and bent configurations are presented in Table 5.

No dipole moment is observed in both linear and bent F-M-F configurations as M(M=Ca, Mg) share electrons equally to fluorine. But, bent F-M-F configurations of SrF_2 and BaF_2 molecules display small dipole interaction resulting to produce dipole moment of 1.34 D and 0.98 D respectively. Mg-F distance gets increased by 0.02 Åin the relaxed

Table 4: The ground state properties of MF_2 (M=Mg, Ca, Sr, Ba): total energy, optimum bond length(r_{M-F}) and angle in both F-M-F linear and bent configurations

Monomer	F-M-F	Basis Set	E(eV)	r(Å)	∡
MgF_2	Linear	6-31G*	-5458.9345	1.72	180
	Linear	6-311+G*	-5461.6219	1.76	180
	Bent	6-31G*	-5458.9345	1.72	180
	Bent	6-311+G*	-5461.6219	1.76	180
CaF_2	Linear	6-31G*	-6429.4999	2.06	180
	Linear	6-311+G*	-6433.3618	2.13	180
	Bent	6-31G*	-6429.4999	2.06	180
	Bent	6-311+G*	-6433.3618	2.13	180
SrF_2	Linear	6-31G*	-6262.3796	2.20	180
	Linear	6-311+G*	-6266.7515	2.28	180
	Bent	6-31G*	-6262.3801	2.20	172
	Bent	6-311+G*	-6433.3618	2.28	172.2
BaF_2	Linear	6-31G*	-6120.1723	2.33	180
	Linear	6-311+G*	-6124.0029	2.44	180
	Bent	6-31G*	-6120.1723	2.33	172
	Bent	6-311+G*	-6125.003	2.44	174.7

Table 5: The ground state properties of MF_2 (M=Mg, Ca, Sr, Ba): total energy, optimum bond length($r_{M-F,F-F}$) and angle in both M-F-F linear and bent configurations

MF	MFF	Basis	E(eV)	r(Å);MF,FF	∡
MgF_2	Linear	6-31G*	-5452.4338	1.74,2.00	180
	Linear	6-311+G*	-5455.2101	1.78,2.08	180
	Bent	6-31G*	-5458.9345	1.74,2.00	169.8
	Bent	6-311+G*	-5461.6219	1.78,2.08	168.7
CaF_2	Linear	6-31G*	-6424.4142	2.08,1.977	180
	Linear	6-311+G*	-6427.7661	2.117,2.135	180
	Bent	6-31G*	-6424.4250	2.08, 1.977	166.5
	Bent	6-311+G*	-6427.7791	2.117,2.135	164.4
SrF_2	Linear	6-31G*	-6257.8592	2.224,1.94	180
	Linear	6-311+G*	-6261.3842	2.244,2.181	180
	Bent	6-31G*	-6257.8702	2.224,1.95	165.3
	Bent	6-311+G*	-6261.4071	2.240,2.218	162.3
BaF_2	Linear	6-31G*	-6115.9334	2.357,1.992	180
	Linear	6-311+G*	-6119.8731	2.349,6.10	180
	Bent	6-31G*	-6115.9466	2.357,1.992	163.5
	Bent	6-311+G*	-6120.1860	2.36,9.012	168.7

structure of linear F-F-M than that of F-M-F. As the separation of charge increases, dipole moments of 7.96 D, 8.84 D, 8.90 D and 9.62 D are produced in MgF_2, CaF_2, SrF_2 and BaF_2 respectively.

Stability of monomeric MF_2 (M=Mg, Ca, Sr, Ba) are examined by calculating their binding energies with optimum bond length, as presented in Table 6.

Table 6: Binding energy of monomeric MF_2 (M=Mg, Ca, Sr, Ba) calculated using 6-31G* basis set

Monomer	Configuration	BE(eV)	r(Å)	∠
MgF_2	Linear F-M-F	-7.85	1.72	180
	Bent F-M-F	-7.85	1.72	180
	Linear F-F-M	-1.36	-	180
	Bent F-F-M	-1.36	-	169.8
CaF_2	Linear F-M-F	-5.99	2.06	180
	Bent F-M-F	-5.99	2.06	180
	Linear F-F-M	-0.91	-	180
	Bent F-F-M	-0.93	-	166.5
SrF_2	Linear F-M-F	-5.49	2.06	180
	Bent F-M-F	-5.49	2.20	172
	Linear F-F-M	-0.97	-	180
	Bent F-F-M	-1.0	-	165.3
BaF_2	Linear F-M-F	-5.30	2.33	180
	Bent F-M-F	-5.30	2.33	180
	Linear F-F-M	-1.03	-	180
	Bent F-F-M	-0.83	-	163.5

For the MF_2 monomer, the ground state configuration is linear F-M-F configuration with optimum M-F bond length of 1.72 Å, 2.06 Å, 2.2 Åand 2.33 Åfor MgF_2, CaF_2, SrF_2 and BaF_2 and respectively. Our predicted bond lenth of linearized CaF_2 after optimization is 2.06 Åwhich is equally close to previous both experimental result 2.10 Åtheoretically predicted value 2.011 Å. The results after testing possible bent geometries, the monomers of SrF_2 and BaF_2 are found to be bent, while CaF_2 shows linearity. Our work predicts MgF_2 to be linear. From table 1, It is clear that the total energy are in the order of $CaF_2 < SrF_2 < BaF_2 < MgF_2$, showing higher energy of CaF_2 than rest other. But, in contrast, bond length are in the order of $MgF_2 < CaF_2 < SrF_2 < BaF_2$. Energy, bond length and Mulliken charges are same in case of linear fluorene F-M-F and bent fluorine F-M-Fconfiguration for the same basis set. Energy, bond length, mulliken charges and bond angle are not exactly same in between relaxed configuration of linear M-F-F and bent M-F-F. M-F-F linear and bent both configurations are significantly higher (5 eV-6 eV) in energy than that of F-M-F configuration. The increase in M-F bond length going from MgF_2 to CaF_2 to SrF_2 to BaF_2 can be attributed to increase the size of cation. As in increase in basicity of cation, Mullikens charge is increased going from MgF_2 to BaF_2, suggesting that there is presence of shorter and stronger bond in MgF_2 than rest other depending on the size of alkaline earth metal.

Magnesium is higly bound to fluorine molecule with binding energy -7.85 eV in both linear and bent-FMF configurations that confirm more stability of MgF_2 than rest oth-

ers. Binding energy decreases in going from MgF_2 to CaF_2 to SrF_2 to BaF_2. Less binding energy found in FFM configuration is due to interaction of two fluoride atoms with higher optimum F-F bond length of 2.0 Å(eg. MgF_2) and Mg-F distance (1.74 Å) greater than 1.72 Å(bond length of MgF_2 in F-M-F). Rest other monomers follow the similar behaviour (Lamichhane & Adhikari, 2017).

4.16 Single Point Energy Calculations in Metal Fluorides

We went through the single point calculations to know the energy profile varying bent angle. Energy is calculated at their fixed bent geometries as displayed in fig 54.

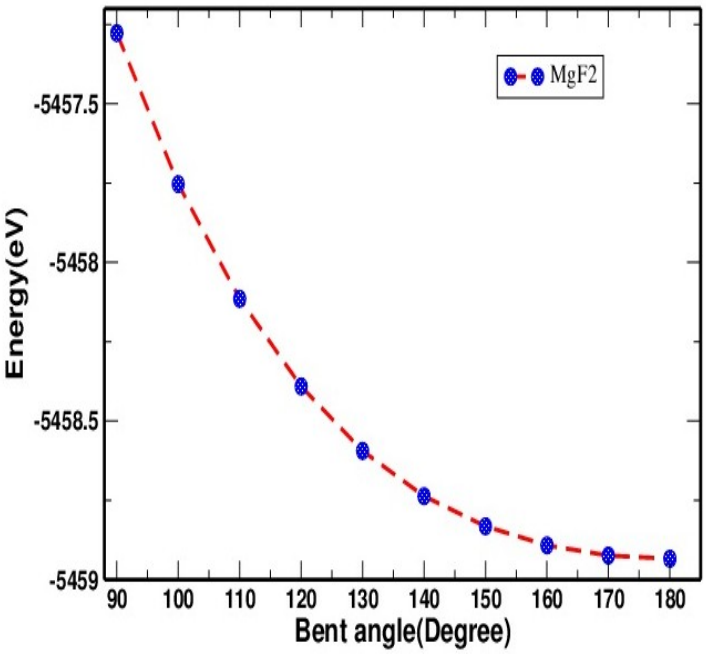

Figure 54: Energy versus bent angle in MgF_2

From the analysis of Figure 54, 55, 56 and 57, no expected variation is seen. However, higher energy difference ≈1 eV in MgF_2 and CaF_2, ≈0.5 eV in SrF_2 and BaF_2 are obtained by varying bent angle from 90^o to 180^o. The energy, therefore, differ by (0.1 eV-0.44 eV) as the molecules bent by 10^o. Our results strongly suggest the more genuinely bending capability of SrF_2 and BaF_2 than MgF_2 and CaF_2.

Metals Pt and Pd is used for the hydrogen gas storage in the presence of two dimensional material graphene. The inner cores for carbon, palladium and platinum are replaced by the corresponding pseudopotentials. The plane wave basis set with the kinetic energy cut-off of 35 Ry is used for the expansion of the ground state electronic wave function. The plane waves are chosen to have a periodicity compatible with the periodic boundary conditions of the simulating cell. The supercell dimensions are kept fixed during the relaxation. We have used our calculated value of the lattice constant obtained from the

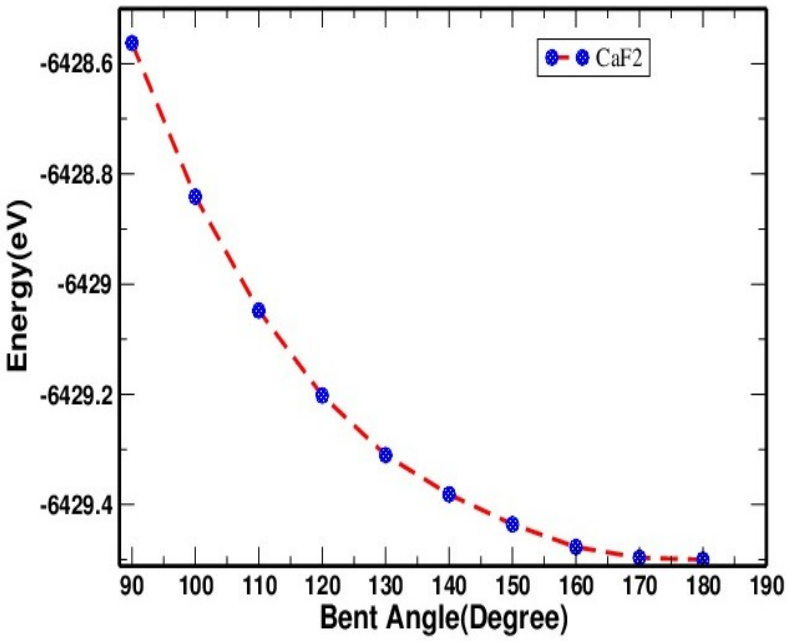

Figure 55: Energy versus bent angle in CaF_2

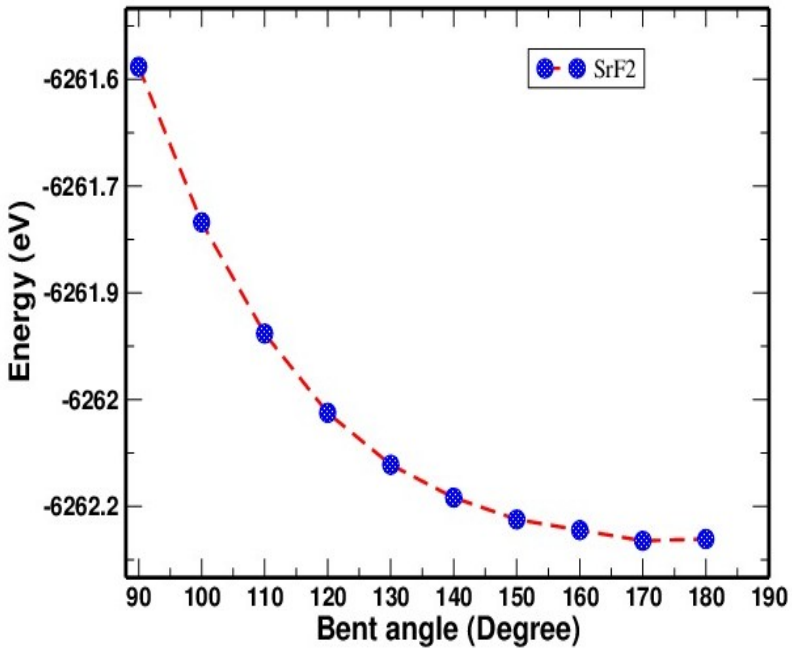

Figure 56: Energy versus bent angle in SrF_2

convergence test.

The adatom graphene system is modeled using single adatom in the 2×2, 3×3, and 4×4 supercells of graphene containing 8, 18 and 32 number of carbon atoms. In this work, the adsorption of Pt/Pd on graphene is performed on three different sites of high symmetry : the top (T) site directly above the carbon atom, the hollow (H) site at the center of hexagon, and the bridge (B) at the midpoint of C-C bond (fig.58). For each adsorption site for the adatom-graphene system, the adatom is relaxed along the z-direction and the

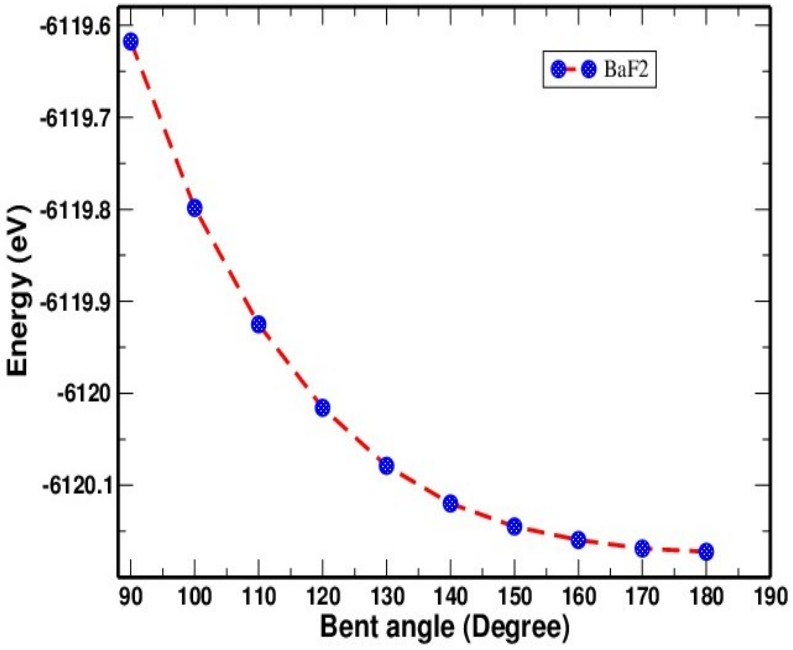

Figure 57: Energy versus bent angle in BaF_2

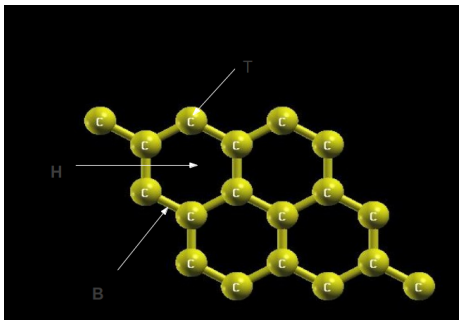

Figure 58: Schematic representation of the three most symmetric adsorption sites: Hollow(H), Bridge(B) and Top(T) on graphene

C atoms on graphene in all x, y, and z directions. To estimate the adsorption energy of Pd/Pt adatoms, the calculations for the isolated adatom, graphene and adatom-graphene system are performed with the same-sized supercell of graphene. In order to obtain the optimized geometry the system was fully relaxed until the total energy change is less than 10^{-4} Ry between two consecutive scf steps and force acting is less than 10^{-3} Ry/Bohr. For the self-consistent total energy calculations the brillioun zone of graphene is sampled in k-space using the Monkhorst-Pack scheme with a appropriate number of mesh of k-points. The calculation using different size of supercell approximates the interaction of isolated adatom with graphene. In order to avoid the interaction between the adatoms on adjacent supercells, vaccum length of supercell was made large enough i.e. 20 Åalong z- axis. The density of states of pure graphene and Pd/Pt-adsorbed graphene are calculated for 3×3 supercell of graphene using $5\times5\times1$ mesh.

The first-principles calculations are performed to study the adsorption of hydrogen

molecule on single platinum/palladium decorated 3×3 supercell of graphene. At first, we optimized H_2 molecule which gives the bond length of 0.75 Åbetween two hydrogen atom which is nearly equal to its experimental value, 0.74 Å. The hydrogen molecule is placed within the graphene supercell(height 20 Å) which is very large in comparison to the bond length of H_2 molecule which ensures that there is no interaction between two hydrogen molecules of two adjacent supercells within that separation. Platinum/Palladium binds hydrogen moecule with B.E. 0.116eV and 0.437eV, greater than binding energy for hydrogen molecule on intrinsic graphene (0.068eV-0.075eV). This range of binding energy is comparable with the previous study (0.053-0.072)eV, performed by Young (Young et al., 1984), we interested to adsorb upto eight numbers of hydrogen molecule/s on Pt/Pd decorated graphene to get desirable binding energy, surface area and density to enhance the catalytic performance and hydrogen storage capacity.

In the present work, we study the adsorption of individual Pt and Pd atoms on different symmetry sites of 2×2, 3×3, and 4×4 supercells of pure graphene. Further, we extend our work to study the adsorption of hydrogen molecules on pure graphene and Pd/Pt-adsorbed graphene.

4.17 Binding of adatoms on graphene

4.17.1 A. Binding energy and geometry

The Binding energy of adatom on graphene, (ΔE) is defined as,

$$\Delta E = E_{adatom} + E_G - E_{G+adatom} \tag{4.1}$$

where, $E_{G+adatom}$ is the total energy of the adatom and graphene system, E_G is the energy of pure graphene sheet and E_{adatom} is the energy of an isolated adatom. These energies are calculated using the same size of hexagonal supercell of graphene. Out of the three adsorption sites (H, B, T) considered, the site with the highest adsorption energy is reffered to as the favoured site for adsorption.

The adsorption geometry is obtained from the positions of the atoms after relaxation. The adatom height (h) is defined as the difference in z coordinates of adatom and the average of the z coordinates of the carbon atoms in the graphene layer. We have also caculated the distance (d_{Ac}) between the adatom and its nearest carbon atom. The adsorption of adatom on graphene produced significant distortion which is quantified by computing the maximum deviation in the z direction of the C atoms in the graphene layer from the average of their positions. The distortion of the graphene layer upon the

adsorption is also calculated in terms of change in dihedral angles. Here, we report the adsorption of single adatom on monolayer graphene containing 8,18 and 32 numbers of carbon atoms. The energetic properties including binding energy and structural properties including adatom height, nearest carbon distance from adatom and distortion in the graphene plane for the hollow (H), bridge (B), and Top (T) sites of adatom adsorbed on 2×2, 3×3, and 4×4 supercell of graphene are summarized in table (7).

Table 7: Structural and energetic properties of Pd adsorption on high symmetric sites of 2×2, 3×3, and 4×4 supercell of graphene containing 8, 18, and 32 number of carbon atoms. The properties listed in the table are binding energy (ΔE), adatom height from graphene plane (h (Å)), adatom-carbon distance (d_{AC} (Å)), and distortion in the graphene plane (d_{GC} (Å)).

Adatom	size of graphene supercell	Site of adsorption	binding Energy (eV)	Height of Pd atom from graphene plane (Å)	Distance of nearest carbon atom (Å)	distortion (Å)
Pd	2×2	H	0.828	2.01	2.46	0.023
		B	1.114	2.15	2.10	0.063
		T	1.112	2.15	2.10	0.047
	3×3	H	1.173	1.99	2.44	0.018
		B	1.426	2.15	2.18	0.093
		T	1.414	2.15	2.09	0.068
	4×4	H	1.162	2.00	2.44	0.031
		B	1.433	2.19	2.10	1.030
		T	1.421	2.19	2.09	0.086

Table 8: Structural and energetic properties of Pt adsorption on high symmetric sites of 2×2, 3×3, and 4×4 supercell of graphene containing 8, 18, and 32 number of carbon atoms. The properties listed in the table are binding energy (ΔE), adatom height from graphene plane (h (Å)), adatom-carbon distance (d_{AC} (Å)), and distortion in the graphene plane (d_{GC} (Å)).

Adatom	size of graphene supercell	Site of adsorption	binding Energy (eV)	Height of Pt atom from graphene plane (Å)	Distance of nearest carbon atom (Å)	distortion (Å)
Pt	2×2	H	1.087	2.12	2.48	0.09
		B	1.175	2.09	2.12	0.11
		T	1.083	2.13	2.55	0.09
	3×3	H	1.305	1.95	2.41	0.02
		B	2.022	2.15	2.10	0.17
		T	1.905	2.16	2.03	0.01
	4×4	H	1.317	1.95	2.40	0.03
		B	2.048	2.20	2.10	0.22
		T	1.917	2.20	2.03	0.16

The table (7 and 8) clearly show that the adsorption of palladium and Platinum atoms on different sites of pure graphene sheet is feasible. The adsorption energy of both atoms is found to increase with increasing the size of the graphene sheet. The adsorption energy of atoms are maximum for bridge site for all supercell of graphene in comparison to the other symmetric sites. So, it can be concluded that bridge site is the most favourable site for adsorption. There is small increment in the binding energy of adatoms for 4×4 supercell of graphene in comparison to 3×3 supercell suggesting that the adsorption of Pd/Pt adatoms on graphene sheet with 18 or more number of carbon atoms is almost equally stable. Our calculated highest B.E.(B-site) of Pd with 4×4 supercell graphene is found to be 1.43eV. Palladium and platinum on graphite are used for catalytic hydrogenation and dehydrogenation reactions on organic chemistry and in petroleum cracking. When

the metal is distributed over the finely divided carbon, the surface area is larger and the catalyst becomes more reactive. Due to two dimensional structure, graphene is suitable to give more surface area to metallic nature. So, the feasibility of the adsorption of Pd and Pt on graphene shows the great promise for the enhanced catalytic behavior. The distortion in the raphene plane due to the adsorption of adatom is also calculated and the maximum distortion is observed at the bridge site for both Pt and Pd. The adsorption of palladium atom on bridge site of graphene involves the hybridization of adatom d-orbitals with the orbitals of graphene. This hybridization between the adatom and the graphene changes some of the graphene sp^2-like orbital character to a more covalently reactive sp^3-like character. Due to this reason, significant distortion of 0.13 Åin the graphene plane (4×4 supercell) is observed. But such significant distortion is not seen in case of Pt-adsorped graphene table (8). The pure graphene sheet has bond length of 1.42 Åbetween two carbon atoms, bond angle of 120^o made by carbon atoms and dihedral angle of 0^o. Deformation takes place after the adsorption of Pd atom on graphene. The maximum change in bond length of 0.02 Å, bond angle of about 0.8^o and dihedral angle of 6.50^o are observed for the adsorption of Pd atom on bridge site of 4×4 supercell of graphene. In case of Pt, The maximum change in bond length of 0.02 Å, bond angle of about 0.9^o and dihedral angle of 12.07^o are observed on bridge site of 3×3 supercell of graphene.

4.17.2 B. Electronic structures

We have also computed the electronic density of states (DOS) and band structures of pure graphene and adatom graphene system. The Kohn-Sham DOS is computed for adatoms adsorbed on the favourable bridge site of the 3×3 supercell of graphene using 15×15×1 Γ-centered Brillouin zone-sampling. The spin up and spin down calculations of pure graphene are plotted taking Fermi energy as reference as in Figure (59). At the Dirac point, where DOS is nearly equal to zero, is clearly visible. The Dirac point is at the Fermi level, indicating that the valence and conduction band meet at the Fermi level with zero band gap. The density of states for spin up and spin down are same which shows the non magnetic nature of pure graphene.

Fig (60) is the plot of DOS for Pd and Pt adatom graphene. The DOS is plotted with Fermi level as reference. From Figure (60), it is seen that Fermi level of graphene again appears to remain at Dirac points, where DOS is nearly equal to zero. Near the Fermi level the DOS of adatom graphene system has been modified after the adsorption. In case of Pd adsorbed graphene system, the 4d orbitals of Pd atom strongly hybridize with the graphene states. These states lie below the Fermi level. Due to the strong hybridization of 4d orbital on graphene large peak in DOS appeared 1.5 eV below the Fermi

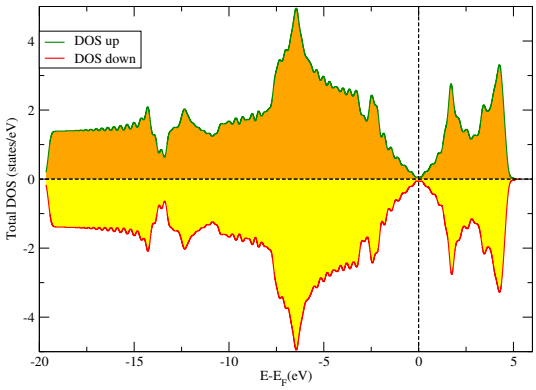

Figure 59: Plot of density of states for pure graphene. Solid line with dark shadow on line represents the DOS of up spin and dotted line with light shadow on line represents DOS of down spin.

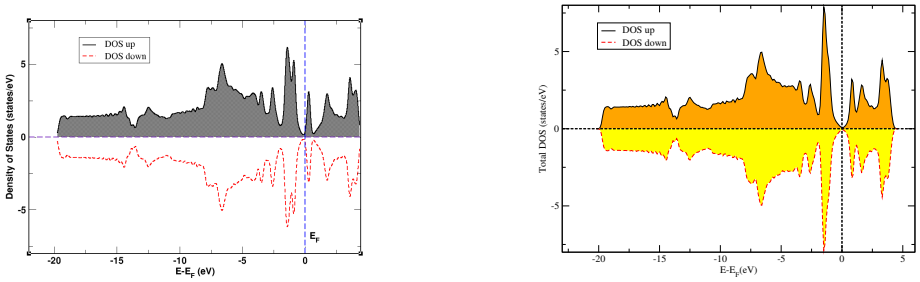

Figure 60: Plot of density of states for Pt(left) and Pd(right) absorbed graphene. Solid line represents the DOS of up spin and dotted line represents DOS of down spin.

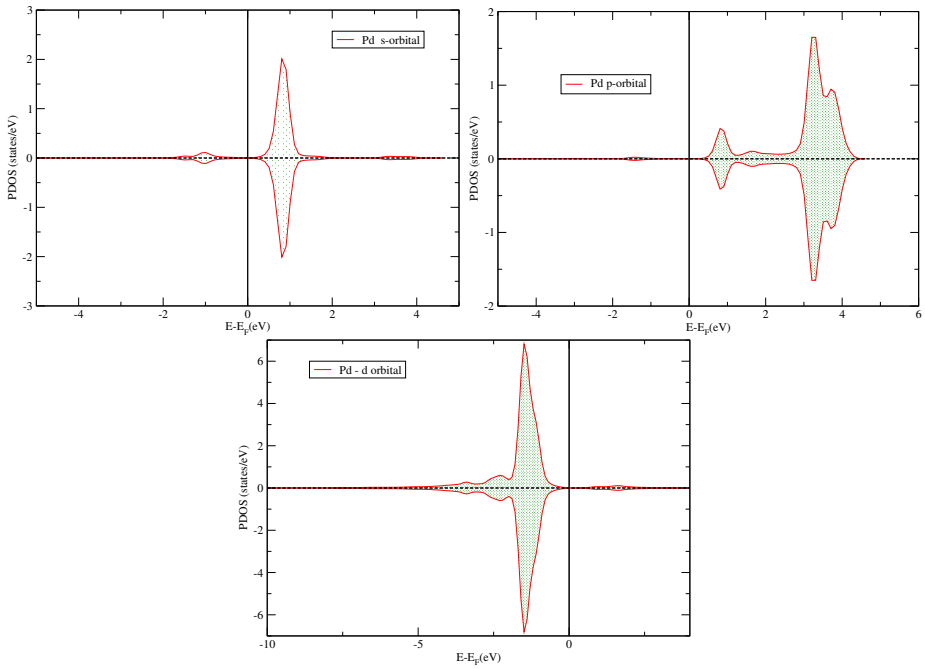

Figure 61: Plot of partial density of states(PDOS) for spin up and spin down of s, p, and d-orbital of Palladium adsorbed graphene.

level. Similarly, Pd 5s peak lies about 0.9 eV above the Fermi level and is unoccupied. The contribution of different orbital of Pd atom in the DOS plot of Pd adatom system is shown in fig (61) and the contribution of different orbital of Pt atom in the DOS of Pt

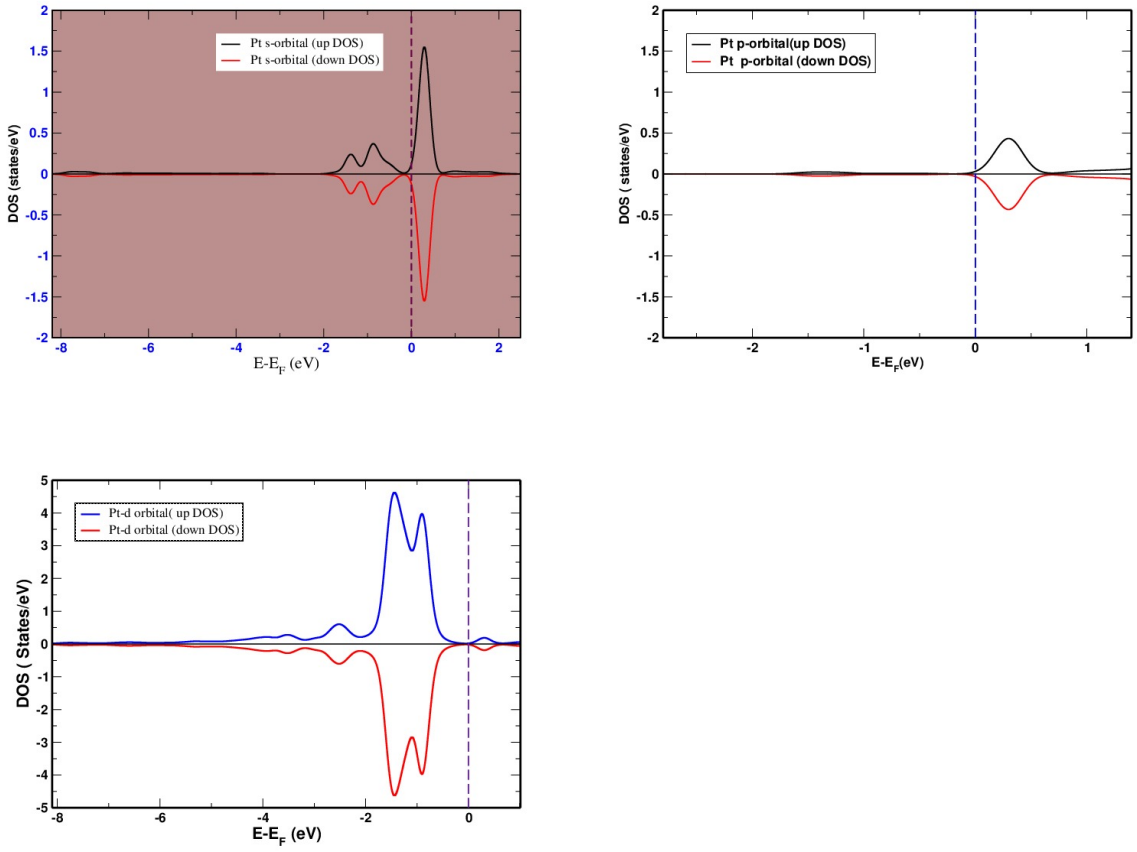

Figure 62: Plot of partial density of states(PDOS) for spin up and spin down of s, p, and d-orbital of platinum adsorbed on graphene.

adatom system is shown in fig (62). Since Pt has unfilled 5d shell, 5d orbital hybridize with graphene states when Pt is adsorped on B-site of graphene. The Pt 6s peak lies about 0.3eV above E_F. The Fermi level of graphene appear to remain at Diract point. Two main 5d peaks lie approximately at 0.8eV and 1.4eV below the Fermi level whereas 2P states are found mostly above E_F. DOS at -6.5eV is unaltered by adatom adsorption but near the Fermi level density of states are strongly modified. The DOS plot for spin up and down is exactly same which indicates that the adatom-graphene system is non magnetic in nature. Further. we have plotted the band structure of graphene along the path $K-\Gamma-M-K$ in a irreducible brillouin zone. The band structure of pure graphene is shown in Figure (63) which exhibits unique feature like a point-like Fermi surface and overlapping of bands but meet at a point known as Dirac point.

After the adsorption of Pd on graphene, gap of 0.045eV between conduction ($\pi*$) and valence (π) band are observed. The interaction of the adatom with π and $\pi*$ states of the carbon atoms breaks the symmetry of graphene and band gap occurs at the Fermi level. The Fermi level of pure graphene is at -2.351eV whereas Fermi level shifts to -1.585eV after the adsorption of palladium atom. It shows that Fermi level gets shifted

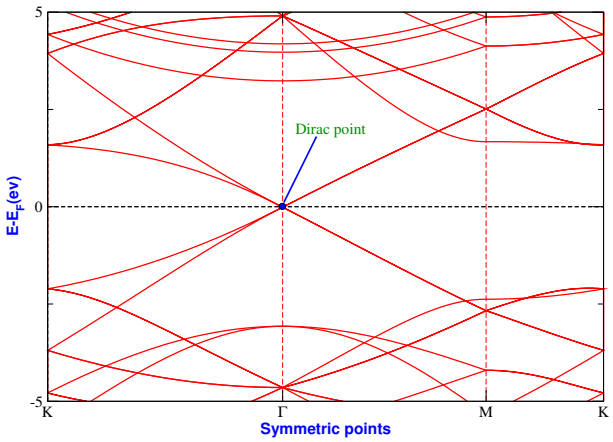

Figure 63: Band structure of the 3 ÃŮ 3 supercell of pure graphene along $K - \Gamma - M - K$ path of the irreducible brillouin zone.

up by 0.766 eV. New bands starting from Pt and bands of graphene has modified the band structure of Pt-graphene system as a result metallicity of graphene is decreased with the band gap of 0.61eV at the Fermi energy.

4.17.3 C. Charge transfer

Charge transfer is an important feature of adatom-graphene interaction in which electron transfers between the adatom and graphene. In this section we discuss about the charge transfer during adsorption of adatoms on bridge site of 3×3 supercell of graphene. The study of charge transfer is important to know the bonding of adatom and the graphene. Charge transfer is the most sensible in case of ionic bonding. But in covalent bonding, there is sharing of charge in the bond between adsorbate and substrate. In such case charge transfer becomes less relevant. Although it is an ambiguous quantity and difficult to determine accurately, we have calculated the charge transfer by integrating the electron density in the adatom and graphene system. At first, an adatom graphene system is relaxed for optimization. With the help of optimized coordinates of the atoms, the charge density for pure graphene layer, isolated adatom, and adatom graphene system is calculated. Then we define the charge-density difference as

$$\Delta\rho(r) = \rho_{AG}(r) - \rho_A(r) - \rho_G(r) \tag{4.2}$$

Where $\rho_{AG}(r)$ is the charge density of the adatom-graphene system. The charge density of an isolated adatom, $(\rho_A(r))$ and graphene, $(\rho_G(r))$ are calculated with the adatom and graphene separately in the same positions of the supercell as done in adatom-graphene calculations. The charge-density difference quantifies the redistribution of electronic charge due to the adatom-graphene interaction. By knowing the charge density difference as a function of z coordinate along the height of supercell and the area of the

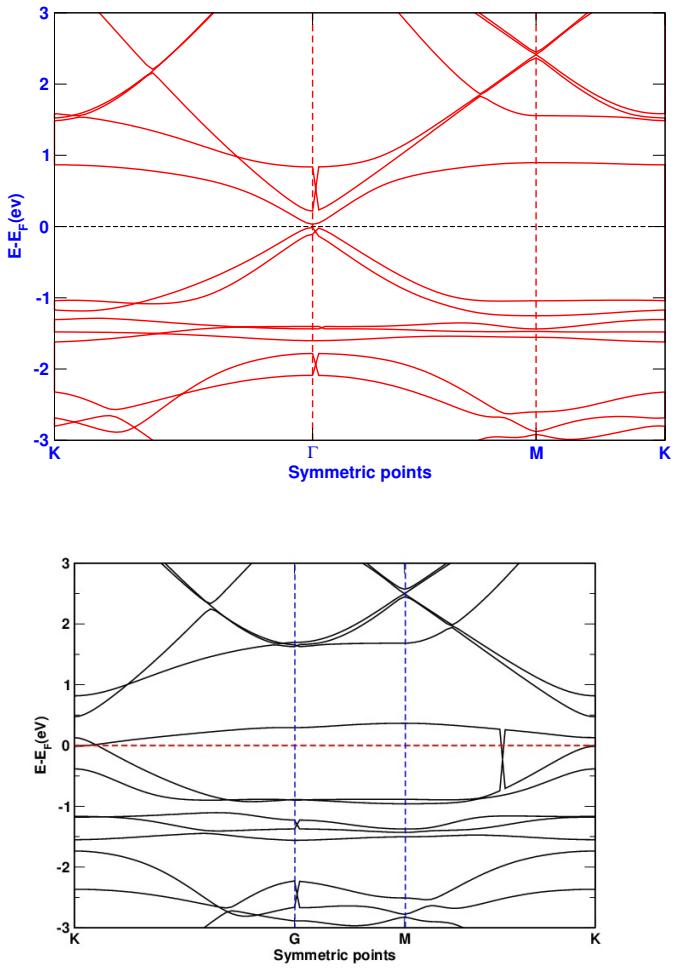

Figure 64: Band structures of the Pd and Pt adsorbed graphene along $K-\Gamma-M-K$ path of the irreducible brillouin zone.

supercell, charge transfer can be calculated. This gives linear charge density difference as a function of position.

Figure (65) shows the planar averaged linear charge density difference as a function of z, position along the height of supercell, for Pd on B-site of graphene. The position of planar graphene sheet is at $z = 0$ Bohr. Increase in electron density near the position of graphene sheet and decrease of electron density near adatom illustrates the transfer of electron from adatom to graphene. To calculate the charge transfer using the linear charge density, the region of the space belonging to graphene or adatom must be specified. For this purpose we adopt the definition used in the previous work. An adsorbate-substrate cutoff distance Rcut is defined as the distance from the graphene plane to the point between the plane and the adatom at which charge accumulation changes to charge depletion for electron transfer from the adatom to the graphene. In the Figure (65) the region with $z < R_{cut}$ is assigned to the substrate, and the region with $z > R_{cut}$ is assigned to the adatom. The charge transfer is obtained by the integral of linear charge density difference in the substrate region. The value of charge transfer

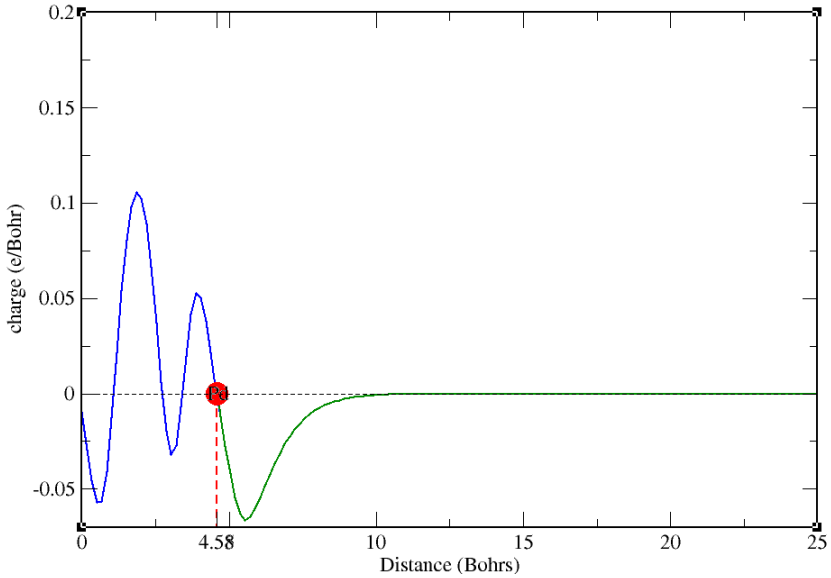

Figure 65: Planar averaged electron charge difference for Pd on graphene at B site as a function of position in the z direction.

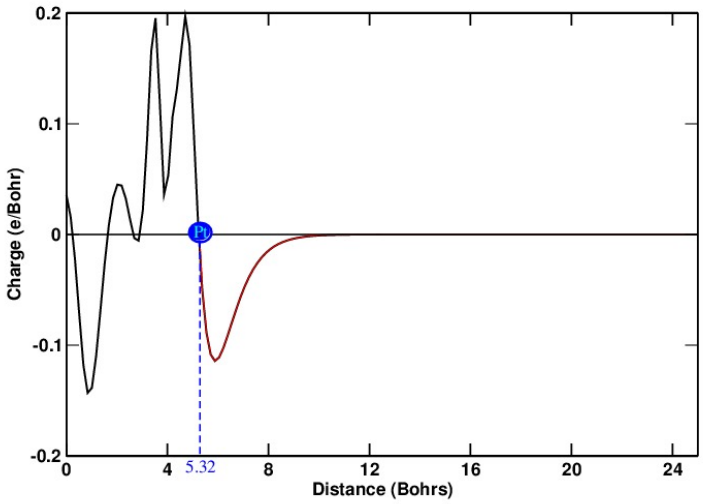

Figure 66: Planar averaged electron charge difference for Pt on graphene at B site as a function of position in the z direction. The vertical line at $z = 0$ represents the position of graphene sheet and line at $z = 5.32$ Bohrs indicate R_{cut}. The integration between the region $z = 0$ and $z = 5.32$ Bohrs gives total charge transfer.

from Pd to graphene is found to be $0.093e$, where e is electronic charge, comparing to previously reported value, 0.17e. And the value of charge transfer from Pt to graphene is found to be 0.18e. Higher value of charge transfer of Pt is expected to affect the electronic structure and therefore the performance of catalytic activities of the system.

4.18 Adsorption of hydrogen molecule/s on adatom adsorbed graphene

We have also performed the first-principles calculations to study the adsorption of hydrogen molecule in the Pd and Pt decorated graphene system. The system is modeled by the adsorption of hydrogen molecules on a single Pd and Pt decorated 3×3 supercell of graphene. The adsorption is carried out for maximum eight number of H_2 molecules. The binding energy of H_2 molecule (Δ E) is calculated using the formula,

$$B.E.(\Delta E) = E_{G+adatom} + E(H_2) - E_{G+adatom+H_2} \tag{4.3}$$

Where $E_{G+adatom+H_2}$ is the energy of the system containing graphene, adatom and H_2 molecules, $E_{G+adatom}$ is the energy of the Pd or Pt-graphene system and $E(H_2)$ is the energy of the H_2 molecule. Furthermore, binding energy/H_2 molecule is calculated as,

B.E/H_2 molecule = $\frac{\Delta E}{N}$, where N denotes the number of the hydrogen molecules.

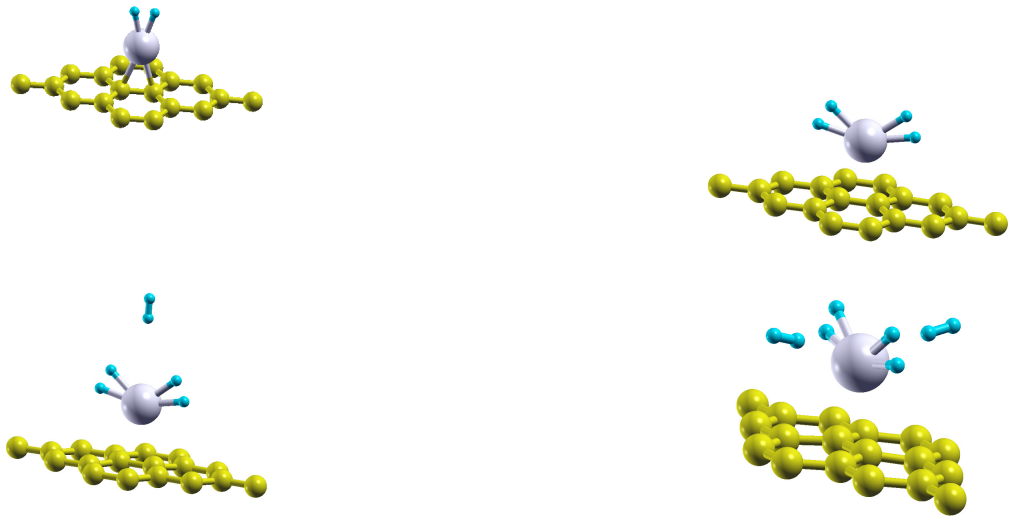

Figures (67) and (68)represent the optimized structures for the adsorption of hydrogen molecules on pd and Pt decorated graphene system. These figures show that two hydrogen molecules dissociate into atomic hydrogen and a complex, due to interaction with adatom. Most of the H_2 molecules in larger systems seem to be attracted by long-range dispersion forces. The total energy, binding energy of hydrogen molecules and binding energy per H_2 molecule, for the adsorption of H_2 molecules in Pd and Pt decorated graphene are presented in the separate tables (9) and (10).

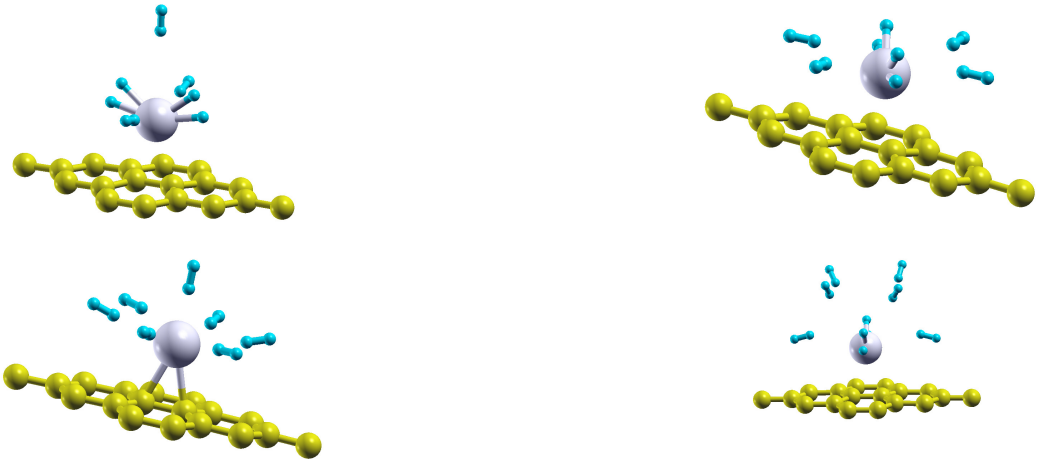

Figure 67: Optimized geometry for the adsorption of the H_2 molecules in the Pd-decorated graphene system.

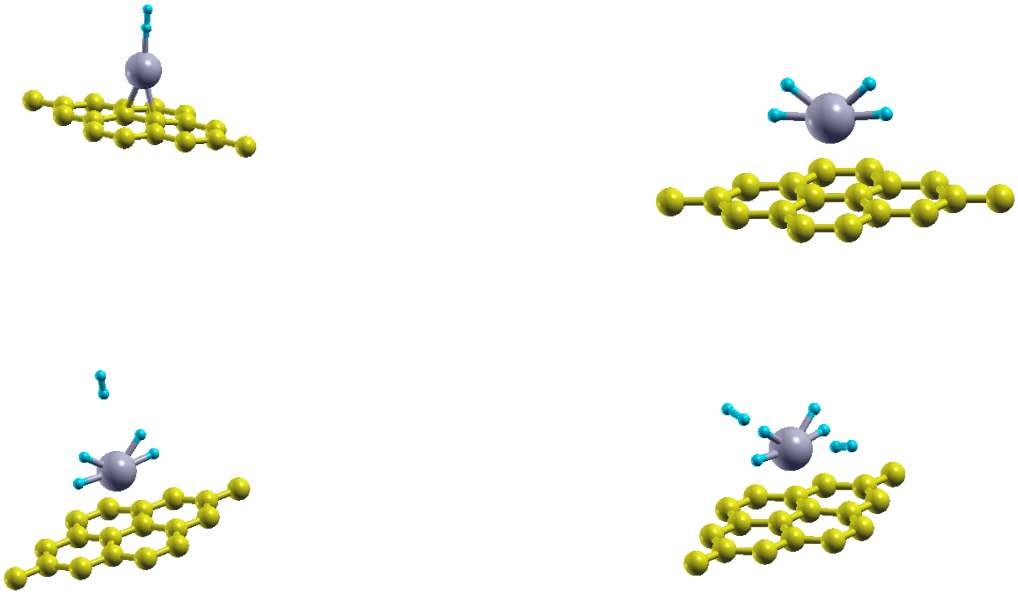

The variation of the binding energy per H_2 molecule with the total number of H_2 molecules adsorbed on Platinum and Palladium decorated graphene is shown in Figure 69. Table (9) represents the observed value of energy of total system, binding energy of H_2 molecules and binding energy per H_2 molecule. From the table (9), it is clearly seen that the observed values of binding energy per H_2 molecule is in decreasing order with increasing the number of hydrogen molecules adsorbed in system. The maximum binding energy for H_2 molecule is 0.946 eV when single hydrogen molecule is adsorbed in Pd-graphene system. The binding energy per hydrogen molecule for the adsorption of one to eight number of H_2 molecules is in the range (0.94-0.15)eV. When single hy-

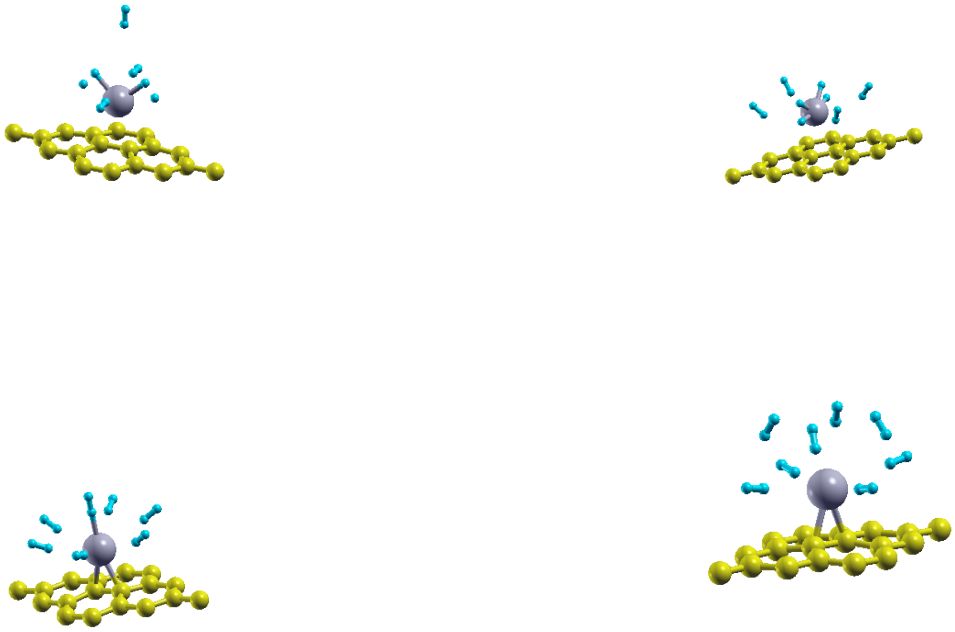

Figure 68: Optimized geometry for the adsorption of the H_2 molecules in the Pt-decorated graphene system.

drogen molecule is adsorbed in Pt-graphene system, the maximum binding energy for H_2 molecule is found to be 1.84eV. The binding energy per hydrogen molecule for the adsorption of one to eight number of H_2 molecules is in the range (1.84 -0.13). Our calculated binding energy per hydrogen molecule meet the U.S. DoE proposed goal as (0.2eV-0.7eV). The binding energy per hydrogen molecule curve for the Pt-adsorption with H_2 molecules is steeper than that of Pd adsorped graphene. It means Pt binds with H_2 molecules less uniformly than Pd on graphene. The main purpose of the adsorption of hydrogen molecule on graphene is for the gas storage. The binding energy of H_2 molecule in pure graphene is low (0.06-0.07)eV, whereas its value is increased significantly in case of Pt/Pd- decorated graphene. It clearly shows that the hydrogen molecule is more stable in Pd/Pt-decorated graphene than pure graphene. The hydrogen storage capacity of single Pd/Pt decorated graphene for the adsorption of 8 H_2 molecules are 4.72 wt % and 3.74% per substrate respectively, comparing to US DoE target (more than 6 wt %), for the practical applications. The estimated results display the potential application of Pt and Pd-decorated graphene as hydrogen gas storage material. In summary, we studied the structural and electronic properties of pure graphene and palladium/platinum adsorped graphene. From the analysis of estimated values of binding energies of Pd and Pt atoms, the bridge site is energetically favourable for their adsorption on graphene. The adsorption of adatoms on the bridge site of the graphene changes some of the graphene sp^2 like orbital character to a more covalently reactive sp^3 like

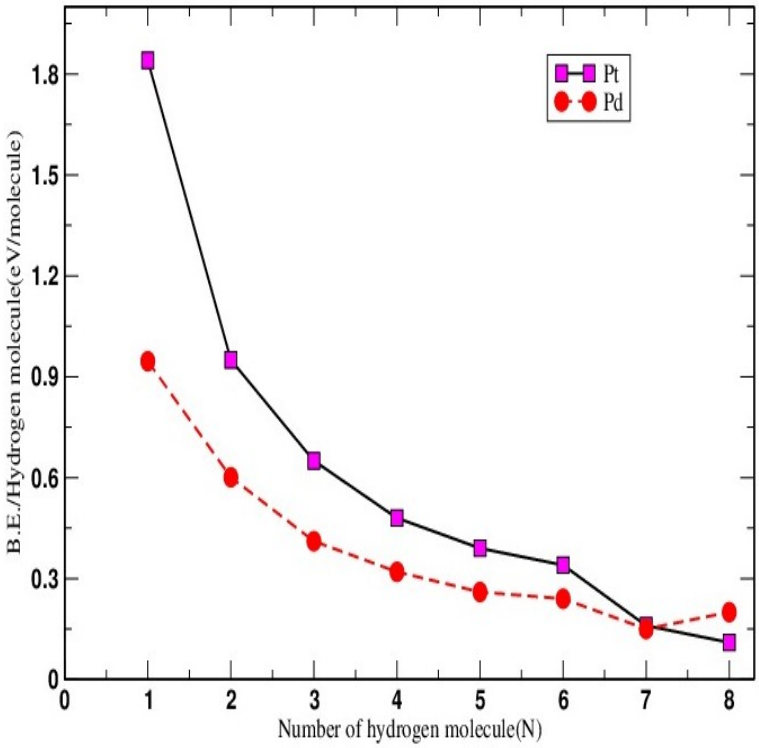

Figure 69: Variation of binding energy per H_2 molecule with the number of hydrogen molecule adsorbed in platinum and palladium adsorbed graphene.

character which is accounted by calculating the deformation on graphene sheet. From the analysis of the adsorption energy, we can say that Pd and Pt-adsorbed graphene can be used as a catalyst. Due to the adsorption of adatoms on graphene small gaps of 0.045eV for Pd and 0.61eV for Pt are observed in between two bands which can be accounted for the breaking of symmetry of the graphene We have also studied the adsorption of the hydrogen molecules on Pt and Pd decorated graphene in order to investigate the hydrogen storage capacity of the Pt and Pd-decorated graphene. The adsorption energy per H_2 molecule for the adsorption of one to eight number of carbon atoms on Pd decorated graphene is within (0.946 - 0.152)eV and that of Pt decorated graphene is within (1.847-0.134)eV. The hydrogen storage capacity of single Pd and Pt decorated graphene for the adsorption of 8 H_2 molecules are 4.72 wt % and 3.72 %. These results are progessive towards one of the US DoE criteria (more than 6 wt %) for the practical applications (Lamichhane et al., 2014). It shows that Pd and Pt decorated graphene has the potential applications as a hydrogen storage material. However the long term stability of materials and devices with affordable cost are still need to overcome the current limitations in practice.

Table 9: The ground state energy of the Pd-H_2-graphene system, binding energy of H_2 on the Pd-H_2-graphene system, and binding energy per H_2 molecules respectively.

Number of H_2 molecules	Binding energy (eV)	Binding energy per H_2 molecule (eV)
1	0.946	0.946
2	1.202	0.601
3	1.234	0.411
4	1.304	0.326
5	1.345	0.269
6	1.480	0.247
7	1.068	0.152
8	1.654	0.206

Table 10: The ground state energy of the Pt-H_2-graphene system, binding energy of H_2 on the Pt-H_2-graphene system, and binding energy per H_2 molecules respectively.

Number of H_2 molecules	Binding energy (eV)	Binding energy per H_2 molecule (eV)
1	0.415	1.847
2	1.914	0.957
3	1.957	0.652
4	1.937	0.484
5	1.985	0.397
6	2.076	0.346
7	1.137	0.162
8	0.904	0.134

CHAPTER 5

5. CONCLUSIONS AND RECOMMENDATIONS

The electronic and magnetic properties, and also its related vibrational and optical properties of NiAl, Ni_3Al, and closely related compound Ni-Ga have been studied by the first-principles calculations. Alloys of transition element Ni and post-transition element Al have been considered to see their stability, nature of interactions, alloys formation, electronic structures, and more importantly for the expansion of knowledge and to explore its technical applications. We have observed the electronic structures, structural properties, magnetic properties, vibrational characters, optical properties, charge density distribution of constituents in NiAl binary alloy. The band structures show that the valence and conduction bands are overlapped with each other indicating that both NiGa and Ni_3Ga are metallic in nature. The formation of 13 numbers of bands in NiAl/NiGa and 31 numbers of bands in Ni_3Al/Ni_3Ga confirm the more metallic nature of the compound Ni_3Al/Ni_3Ga than NiAl/NiGa. Hybridization with pd mixing range (-3.1 eV to 0.03 eV) shape the mechanical strength of inter-metallic compound Ni_3Ga. The understanding of mechanical and magnetic properties of materials strongly depend on their structural and electronic properties. Furthermore, most of the bands are occupied with d-orbitals below the Fermi level as expected. Above Fermi level, bands are occupied mostly with s and p orbitals. We also studied the density of states of all the systems. Furthermore, we have calculated the fat band structure of NiAl and Ni_3Al. We observed that below Fermi level, most of the bands are occupied with d-orbitals as expected. Above Fermi level, we see that the bands are occupied mostly with s and p orbitals. We also studied the density of states of all the systems. The magnetic moment of NiAl is found to be zero i.e non-magnetic and magnetic moment of Ni_3Al is found to be $0.52\mu_B$ i.e. ferromagnetic in nature.

The magnetization of the systems Ni_3Al and Ni_3Ga are checked with its self consistent energy at different consecutive steps. The value of magnetic moment is observed corresponding to minimum energy. There is no fluctuation in up down spin observed in Ni_3Al. There is very small change in energy to cover the magnetic moment values ranging from 0.51 μ_B to $0.55\mu_B$. Spin fluctuation in Ni_3Al is weaker than in Ni_3Ga.

Spin fluctuates in Ni_3Ga frequently even in very small energy range that has made it different from NiAl.

The magnetic moment of NiGa is found to be zero i.e non-magnetic and magnetic moment of Ni_3Ga is $0.58\mu_B$ i.e. ferromagnetic in nature. The nickel is magnetic while NiGa is non-magnetic, Ni_3Ga is, however, observed to be weak ferromagnet which suggest that nickel has made the largest contributions to display magnetism that shows the tendency of Ni-based alloys toward the well performance in small magnetic memory devices. Optical properties are analysed through the calculated dielectric function and refractive index. The maximum number of free electrons near Fermi level are responsible to change reflectivity in NiAl. From the calculation of phonon dispersion relations, three optic and three acoustic branches are observed in NiAl where which optic branches gets slightly and uniformly shifted in frequency and acoustic have linear dispersion at low q. Modes are originated from electronic bands resulting to mode gap of 1.56 THz in NiAl and reduces the gap while increasing nickel content. NiAl is observed to be stable at low pressure, agrees with experiment. We recommend that this kind of research is essential for the country full of natural resources like Nepal. In addition, this work can be extended to study MD simulation as well as adsorption of Ni on 2D materials to know the defect of effect of Nickel.

CHAPTER 6

6. SUMMARY

Electronic and magnetic properties of Ni-Al have studied using first-principles technique. Besides, additional properties like vibrational and optical are studied to understand the electronic properties in detail. The nickel is magnetic while NiAl is non-magnetic, Ni_3Al is, however, observed to be weak ferromagnet which suggest that nickel has made the largest contributions to display magnetism in Ni-Al system, that shows the tendency of Ni-based alloys toward the well performance in small magnetic memory devices. The value of magnetic moment of NiAl and Ni_3Al obtained in the present work agrees with previous studies. NiAl melt at 1873 K is found to be ordering in nature which can't support the de-mixing in the solid state. The understanding of mechanical and magnetic properties of materials strongly depend on their structural and electronic properties. Optical properties are investigated through the calculated dielectric function and refractive index. The understanding of mechanical, optical and magnetic properties of materials strongly depend on their structural stability and electronic properties. Alloy made of transition element Ni and post-transition element Al have been found to be stable at equal concentration after the investigation on its nature of interactions, electronic structures. Thus, studied materials and alloys are found to be useful for the expansion of knowledge and to explore technological applications of such metallic alloys. NiAl and Ni_3Al can overcome the limitation seen in pure metal in terms of strength. More extensive investigation on Ni-based alloys is essential to make it more as a functional materials. Alloying has been observed to be pivotal role to overcome the limitation seen in single material.

REFERENCES

Aguayo, A., Mazin, I., & Singh, D. (2004). Why Ni_3Al is an itinerant ferromagnet but Ni_3Ga is not. *Physical Review Letters*, *92*(14), 147201.

Boucetta, S. (2014). Theoretical study of elastic, mechanical and thermodynamic properties of MgRh intermetallic compound. *Journal of Magnesium and Alloys*, *2*(1), 59.

Darolia, R., Walston, W., Noebe, R., Garg, A., & Oliver, B. (1999). Mechanical properties of high purity single crystal NiAl. *Intermetallics*, *7*(10), 1195.

Deligoz, E., Ozisik, H., Colakoglu, K., & Ciftci, Y. (2014). First principles prediction of structural stability, elastic, lattice dynamical and thermal properties of osmium carbides. *Materials Science and Technology*, *30*(7), 842.

El Fatmi, R., & Ghazouani, N. (2011). Higher order composite beam theory built on saint-venants solution. part-i: Theoretical developments. *Composite Structures*, *93*(2), 557.

Hancock, G. F., & McDonnel, B. R. (1971). Diffusion in the intermetallic compound NiAl. *Physica Status Solidi (a)*, *4*(1), 143.

Hohenberg, P., & Kohn, W. (1964). Inhomogeneous electron gas. *Physical Review*, *136*(3B), B864.

Hsu, L.-S., & Wang, Y.-K. (2004). Optical properties of Ni_3Al, Ni_3Ga, and Ni_3In. *Journal of Alloys and Compounds*, *377*(1-2), 29.

Jozwik, P., Polkowski, W., & Bojar, Z. (2015). Applications of Ni_3Al based intermetallic alloys current stage and potential perceptivities. *Materials*, *8*(5), 2537.

Kazanc, S., & Tatar, C. (2008). Investigation of the effect of pressure on some physical parameters and thermoelastic phase transformation of NiAl alloy. *International Journal of Solids and Structures*, *45*(11-12), 3282.

Kohn, W., & Sham, L. J. (1965). Self-consistent equations including exchange and correlation effects. *Physical Review*, *140*(4A), A1133–A1138.

Lamichhane, S., & Adhikari, N. P. (2017). Basis set effect on alkaline-earth fluoride structures. *Journal of Computational and Theoretical Nanoscience*, *14*, 2315.

Lamichhane, S., Aryal, B., Kaphle, G., & Adhikari, N. (2015). Structural and electronic properties of perovskite hydrides acah3 (a= cs and rb). *BIBECHANA*, *13*, 94.

Lamichhane, S., Kaphle, G., & Adhikari, N. (2016). Electronic structures and magnetic properties of NiAl and Ni_3Al. *Quantum Matter*, *5*(3), 356.

Lamichhane, S., Pantha, N., & Adhikari, N. (2014). Hydrogen storage on platinum decorated graphene: a first-principles study. *Bibechana*, *11*(1), 107.

Lee, J. I., Hong, S., Mannstadt, W., & Freeman, A. (2000). Rippled surface structure and electronic and magnetic properties of ni3al (001). *Physical Review B*, *62*(11), 6982.

Ma, X., & Gunther, S. (2018). Imaging the confined surface oxidation of NiAl (111) by in situ high temperature scanning tunneling microscopy. *Phys. Chem. Chem. Phys.*, *20*, 21844.

Martin, R. M. (2004). *Electronic structure: basic theory and practical methods*. Cambridge university press.

Miedema, A. R., de Boer, F. R., & de Chatel, P. F. (1973). Empirical description of the role of electronegativity in alloy formation. *Journal of Physics F: Metal Physics*, *3*(8), 1558.

Moruzzi, V. (1990). Magnetic instabilities in invar. *Physica B: Condensed Matter*, *161*(1-3), 99.

Mostoller, M., Nicklow, R., Zehner, D., Lui, S. C., Mundenar, J., & Plummer, E. (1989). Bulk and surface vibrational modes in NiAl. *Physical Review B*, *40*(5), 2856.

Ochial, S., Oya, Y., & Suzuki, T. (1984). Alloying behaviour of Ni_3Al, Ni_3Ga, Ni_3Si and Ni_3Ge. *Acta Metallurgica*, *32*(2), 289.

Perdew, J. P., & Zunger, A. (1981). Self-inter action correction to density-functional approximations for many-electron systems. *Physical Review B*, *23*(10), 5048.

Probert, M. (2011). *Electronic structure: Basic theory and practical methods, by richard m. martin: Scope: graduate level textbook. level: theoretical materials scientists/condensed matter physicists/computational chemists.* Taylor & Francis.

Pun, G. P., & Mishin, Y. (2010). Molecular dynamics simulation of the martensitic phase transformation in NiAl alloys. *Journal of Physics: Condensed Matter*, *22*(39), 395403.

Ravindran, P., Subramoniam, G., & Asokamani, R. (1996). Ground-state properties and relative stability between the l 1 2 and do a phases of ni 3 al by nb substitution. *Physical Review B*, *53*(3), 1129.

Sands, T., Palmstrom, C., Harbison, J., Keramidas, V., Tabatabaie, N., Cheeks, T., ... Silberberg, Y. (1990). Stable and epitaxial metal/iii-v semiconductor heterostructures. *Materials Science Reports*, *5*(3), 99.

Scandolo, S., Giannozzi, P., Cavazzoni, C., de Gironcoli, S., Pasquarello, A., & Baroni, S. (2005). First-principles codes for computational crystallography in the quantum-espresso package. *Zeitschrift für Kristallographie-Crystalline Materials*, *220*(5/6), 574.

Smith, R. (2009). Magnetic properties of Ni_3Al and Ni_3Ga: emergent states and the possible importance of a tri-critical point. *Journal of Physics: Condensed Matter*, *21*(9), 095601.

Sundararajan, V., Sahu, B. R., Kanhere, D. G., Panat, P. V., & Das, G. P. (1995). Cohesive, electronic and magnetic properties of the transition metal aluminides FeAl, CoAl and NiAl. *Journal of Physics: Condensed Matter*, *7*(30), 6019.

Yadav, S. K., Lamichhane, S., Jha, L. N., Adhikari, N. P., & Adhikari, D. (2016). Mixing behaviour of NiAl melt at 1873 k. *Physics and Chemistry of Liquids*, *54*(3), 370.

Zhao, W., Kozlov, S. M., Hofert, O., Gotterbarm, K., Lorenz, M. P. A., Vines, F., ... Steinruck, H. P. (2011). Graphene on Ni(111): Coexistence of different surface structures. *The Journal of Physical Chemistry Letters*, *2*(7), 759.

Zhu, S., Tjong, S., & Lai, J. (1998). Creep behavior of a NiAl precipitation strengthened FeCrNiAl alloy. *Acta Materialia*, *46*(9), 2969.

Appendix A: Publications

(A) **International Peer-reviewed Journals**

(1) Lamichhane, S., Adhikari, N. P. (2017). Basis set effect on Alkaline Earth Metal Fluorides structures. *Journal of Computational and Theoretical Nanoscience*, *14*, 2315.

(2) Lamichhane, S., Kaphle, G. C., Adhikari, N. P. (2016). Electronic Structures and Magnetic Properties of NiAl and Ni_3Al. *Quantum Matter*, *5*, 256.

(3) Lamichhane, S., Lage, P., Khatri, G., Pantha, N., Adhikari, N. P., Sanyal, B. (2016). First Principles study of adsorption of halogens molecules on graphene-MoS_2 hetero-system. *J. Phy. Conf. Ser. IOP Publishing*, *765*, 012011.

(4) S. K. Yadav, Lamichhane, S., Jha L. N., Adhikari, N. P. Adhikari, D. (2016). Mixing behavior of Ni-Al melt at 1873 K. *Journal of Physics and Chemistry of Liquids, 54*(3) 370.

(5) Adhikari, N. P., Khaniya, A., Lamichhane, S., N. Pantha. (2015). Adsorption of molecular hydrogen on Pd(Pt) decorated graphene *Bulletin of the American Physical Society, 60*(1).

(6) Adhikari, N. P., Lamichhane, S., Sanyal. (2018). Adsorption of CO and NO molecules on MoS_2-graphene heterostructure. *Bulletin of the American Physical Society*.

(B) **National Peer-reviewed Journals**

(1) Lamichhane, S., Aryal, B., Kaphle, G. C., Adhikari, N. P. (2016). Electronic and magnetic properties of perovskite hydrides; $ACaH_3$ (A=Cs and Rb). *Bibechana, 13*, 94.

(2) Lamichhane, S. , Pantha, N., Adhikari, N. P. (2014). Hydrogen storage on Platinum decorated Graphene, A first-pinciples study. *Bibechana, 11*(1), 107.

Appendix B: Participation in Conferences, Summer Schools and Seminars

(a) **International E-Workshop on Computational Condensed Matter Physics and Materials Science (IWCCMP-2013). ABV-Indian Institute of Information Technology and Management, Gwalior, 27-29 November 2013. (Participated with Poster Presentation on Electronic Properties and Magnetic Properties of NiAl and Ni_3Al)**

(b) **Presented a work 'Hydrogen storage on Pt/Pd decorated graphene' at Department of Physics, Michigan Technological University, USA on May 15, 2014.**

(c) **Presented a poste entitled a Electronic structures and concentration dependent magnetism on NiGa and Ni_3Ga at the meeting of TWAS Regional Conference of Young Scientists during Feb 18-20, 2015, JNCASR, Bangalore, India.**

(d) **International Conference on a Functional Materials-Today and Tomorrow in The Hotel Hindustan, Kolkata, India on Feb, 2006. (Participated with poster presentation)**

(e) **Actively participated on DFT based lectures provided by Dr. B. Sanyal during May-June, 2017 at Department of Physics and Astronomy, Uppsala University, Sweden**

(f) **Participation on Kathmandu Summer School on ab initio Simulation of Solids (KaSSAISS-2013): School and workshop. 14-19 April, 2013, CDP, TU, Kirtipur, Nepal**

(g) **Second Microsymposium On Applied Sciences-2013 Material Science held in August 3, 2013, Kathmandu, Nepal**

(h) **Presented a paper entitled a Hydrogen storage on Pt-decorated graphene in International Conference on Emerging Trends in Science and Technology, March 22-23, 2014, Biratnagar, Nepal. (Oral Presentation)**

(i) **Participated in scientific interaction of IEEE/EDS Mini-Colloquium on physics of electronic and spintronic materials held at CDP, TU in 2015.**

(j) **Presented a Talk on a Computational Physics and its role to understand physics in program Awishkaar Science Festival, St. Xavier's College, Kathmandu on Jan 30, 2016**

(k) **Presented a research work entitled Electronic structures and concentration dependent magnetism on NiGa and Ni_3Ga in 33rd Annual Convention of NPS on July 2, 2016 at PN Campus, Pokhara (Oral Presentation)**

(l) **Participation on Training on Computational Physics capacity development program held at CDP, TU during May 14-15, 2016.**

(m) **Presented a poster entitled Electronic structures and concentration dependent magnetism on NiGa and Ni_3Ga in 13 International conference on Quasicrystal (ICQ13), 18-23 September, 2016, Kathmandu.**

(n) **Actively participation on lectures based on Statistical Physics by Prof. S. Shenoy during 2 May-6 May 2017 at CDP**

(o) **Participation with Oral Presentation on Electric field effect of water on Graphene/MoS_2 heterostructures at St. Xavier's College in International Conference on Physics of Space and Materials (2-3 Sept 2017)**

(p) **Actively participated on DFT based lectures by Dr. B. Sanyal of Uppsala University during Jan 31-Feb 1, 2017 at CDP, TU**

(q) **Participated with oral presentation on Adsorption of CO and NO molecules on Graphene/MoS_2 heterostructures at PK College, TU in NPS Annual Meeting, 23 Dec 2017.**

(r) **Presented a poster on Electronic and magnetic properties of NiAl and Ni_3Al in High Energy Physics Winter School, 6 Jan 2018 at CDP, TU**

Journal of
Computational and Theoretical Nanoscience
www.aspbs.com/ctn

VOLUME 14, NUMBER 5
MAY 2017

2077–2583 (2017)
ISSN: 1546-1955, EISSN: 1546-1963

Manuscript Submission

Submit your manuscript electronically as a PDF or MS Word file to the Editor-in-Chief, Prof. Dr. Wolfram Schommers or one of the Associate Editors listed above.

Journal of
Computational and Theoretical Nanoscience
www.aspbs.com/ctn

VOLUME 14, NUMBER 5
MAY 2017

2077–2583 (2017)
ISSN: 1546-1955, EISSN: 1546-1963

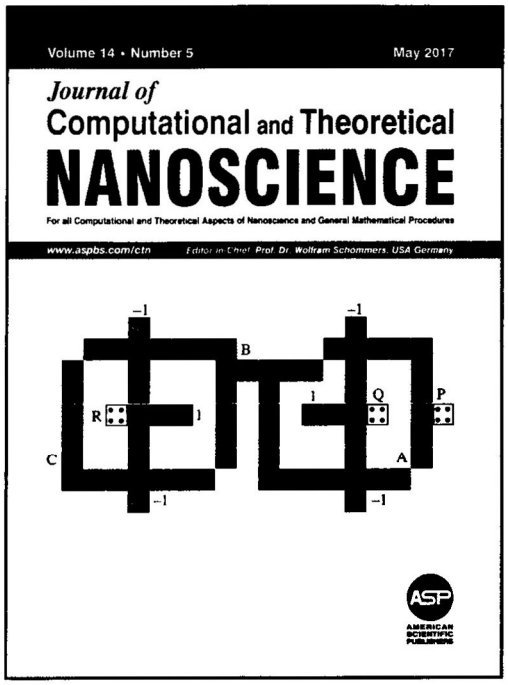

ON THE COVER: Proposed Quantum-dot Cellular Automata (QCA) based binary to grey and grey to binary code converter circuit. As an example, consider A, B, C are the three inputs of a grey code and P, Q, R are the three consistent bits of the binary code. The logical demonstration of 3-bit grey to binary code converter can be stated as $A = P$, $A \oplus B = Q$ and $A \oplus B \oplus C = R$. The logical representation express that output P is similar as input bit A. The output value Q is XOR-ed of inputs A, B; while the output R is XOR-ed value of inputs A, B, and C. More details are given in the article by *Md. Abdullah-Al-Shafi and Ali Newaz Bahar*, pp. 2416–2421 of this issue.

REVIEWS

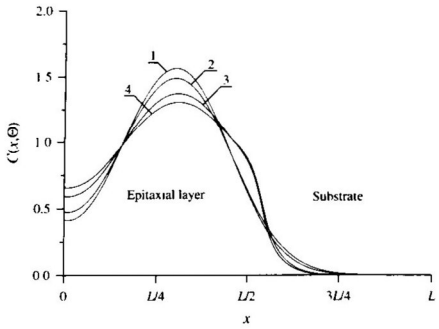

Journal of
Computational and Theoretical Nanoscience
Vol. 14, 2315–2318, 2017

Basis Set Effect on Alkaline-Earth Fluoride Structures

S. Lamichhane and N. P. Adhikari*

Central Department of Physics, Tribhuvan University, Kirtipur, Kathmandu, 44613, Nepal

Structural properties of alkaline earth fluoride molecules MF_2 (M = Mg, Ca, Sr and Ba) were carried out systematically on the basis of density functional theory with B3LYP approach. Careful attention has been given to detail of the basis sets used and then have been extended until the convergence were obtained. The ground state configurations of MgF_2 and CaF_2 are found to be linear while that of SrF_2 and BaF_2 are found to be non-linear. Our results suggest that there is presence of shorter and stronger bond in MgF_2 depending on the size of alkaline earth metal and highly bound nature of Mg to fluorine. The energy, differ by (0.1 eV–0.44 eV) as the alkaline earth fluoride molecules bent by 10°. Our results also add the more genuinely bending capacity of SrF_2 and BaF_2 than MgF_2 and CaF_2. The orbital hybridization and core polarization are responsible for the deviation from linearity of molecules.

Keywords: Alkaline-Earth Fluoride, DFT, Mulliken Charge, Structural Properties.

1. INTRODUCTION

Alkaline-Earth Fluorides are generally known for their intrinsic optical properties and are well characterized with importance of CaF_2 as an ideal material for the detection of β-particle, MgF_2 in multilayer optical coating, SrF as a candidate for ultracold molecular structure for buffer gas cooling and BaF_2 for infra-red spectroscopy.[1–3] Recently numerous computational work on bending effect of fluorides have been done,[4,5] however, study was constrained to some symmetries and did not address the unsolved issue of bending potential. Dekock et al.[6] reported that the ground state of CaF_2, CaH_2, CeO_2 and $YbCl_2$ are bent and MgF_2 is predicted to be strongly linear. Very disparate results reported previously[2,7–11] about the shape of monomeric CaF_2, quasilinear behaviour of calcium difluoride[12] motivated us to compare with closely related monomers MgF_2, SrF_2 and BaF_2. The non-linearity of CaF_2, confirmed first by electric deflection experiment,[8] contary to our general understanding based on Walsh's rule[13] and VSEPR theory,[14] have become questionable and great matter of interest for many theoreticians. Core polarization as a responsible factor for the non-linearity of monomeric CaF_2 suggested previously[11] couldn't clarify either ionic or covalent bonding present in CaF_2 molecule. Systematic study of molecules gives the fundamental understanding on structural variation going from atoms to clusters. This is what we intended to do meaningful comparisons in four alkaline earth fluoride molecules namely MgF_2, CaF_2, SrF_2 and BaF_2 in regards to their structural and electronic properties along with nature of bonding of constituent atoms in a molecule.

The rest of the manuscript are arranged as follows. In Section 2, we have described the computational details used in our calculations. Results and discussion of our study will be given in Section 3. Finally, conclusion are presented in Section 4 before the list of references.

2. COMPUTATIONAL DETAILS

The DFT based B3LYP approach was chosen as a computational method due to reliability to calculate the geometries and vibrational properties of molecules containing heavy metals. Structural properties of Alkaline Earth Fluoride molecules MgF_2, CaF_2, SrF_2 and BaF_2 were carried out systematically on the basis of density functional theory with B3LYP approach using Gaussian 03 code. The basis set LanL2DZ were used for alkaline earth metal and 6-31G* and 6-311+6** were used for fluorine atoms with convergence criterion for the force of 0.02 eV/Å. We are interested to look configuration; linear versus bent configuration for these fluoride molecules and also to calculate the total energy, binding energy, bond length, bond angle, frequency and dipole moment.

3. RESULTS AND DISCUSSION

In order to know the ground state configurations of MF_2 with M = Mg, Ca, Sr, Ba, systematic study was performed

*Author to whom correspondence should be addressed.

 1546-1955/2017/14/2315/004 doi:10.1166/jctn.2017.6826

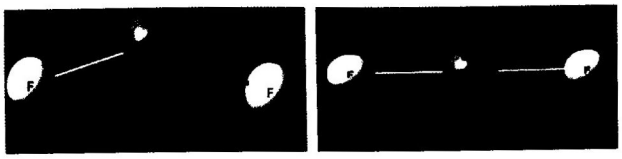

Fig. 1. Diagram of geometry of CaF_2 considered to find minimum energy configuration (left) and its relaxed structure (right).

which consisted several possible configurations to get energetically favourable one.

3.1. Structural Properties

The ground state properties of all studied monomers in F–M–F linear and F–M–F bent configurations are summarized in Table I.

Similarly, the ground state properties of MF_2 (M = Mg, Ca, Sr, Ba) in both M–F–F linear and bent configurations are presented in Table II.

No dipole moment is observed in both linear and bent F–M–F configurations as M (M = Ca, Mg) share electrons equally to fluorine. But, bent F–M–F configurations of SrF_2 and BaF_2 molecules display small dipole interaction resulting to produce dipole moment of 1.34 D and 0.98 D respectively. Mg–F distance gets increased by 0.02 Å in the relaxed structure of linear F–F–M than that of F–M–F. As the separation of charge increases, dipole moments of 7.96 D, 8.84 D, 8.90 D and 9.62 D are produced in MgF_2, CaF_2, SrF_2 and BaF_2 respectively.

Stability of monomeric MF_2 (M = Mg, Ca, Sr, Ba) are examined by calculating their binding energies with optimum bond length, as presented in Table III.

For the MF_2 monomer, the ground state configuration is linear F–M–F configuration with optimum M–F bond length of 1.72 Å, 2.06 Å, 2.2 Å and 2.33 Å for MgF_2, CaF_2, SrF_2 and BaF_2 and respectively. Our predicted bond length of linearized CaF_2 after optimization is 2.06 Å which is equally close to previous both experimental result 2.10 Å[7] and theoretically predicted value 2.011 Å.[11] The results after testing possible bent geometries, the monomers of SrF_2 and BaF_2 are found to be bent, while CaF_2 shows linearity, contary to previous result about CaF_2 as quasilinear.[5] Our work predicts MgF_2 to be linear as in previous work.[15] From Table I, It is clear that the total energy are in the order of $CaF_2 < SrF_2 < BaF_2 < MgF_2$, showing higher energy of CaF_2 than rest other. But, in contrast, bond length are in the order of $MgF_2 < CaF_2 < SrF_2 < BaF_2$. Energy, bond length and Mulliken charges are same in case of linear fluorene F–M–F and bent fluorine F–M-F configuration for the same basis set. Energy, bond length, Mulliken charges and bond angle are not exactly same in between relaxed configuration of linear M–F–F and bent M–F–F. M–F–F linear and bent both configurations are significantly higher (5 eV–6 eV)

Table I. The ground state properties of MF_2 (M = Mg, Ca, Sr, Ba): Total energy, optimum bond length (r_{M-F}) and angle in both F–M–F linear and bent configurations.

Monomer	F–M–F	Basis set	E (eV)	r (Å)	∠
MgF_2	Linear	6-31G*	−5458.9345	1.72	180
	Linear	6-311+G*	−5461.6219	1.76	180
	Bent	6-31G*	−5458.9345	1.72	180
	Bent	6-311+G*	−5461.6219	1.76	180
CaF_2	Linear	6-31G*	−6429.4999	2.06	180
	Linear	6-311+G*	−6433.3618	2.13	180
	Bent	6-31G*	−6429.4999	2.06	180
	Bent	6-311+G*	−6433.3618	2.13	180
SrF_2	Linear	6-31G*	−6262.3796	2.20	180
	Linear	6-311+G*	−6266.7515	2.28	180
	Bent	6-31G*	−6262.3801	2.20	172
	Bent	6-311+G*	−6433.3618	2.28	172.2
BaF_2	Linear	6-31G*	−6120.1723	2.33	180
	Linear	6-311+G*	−6124.0029	2.44	180
	Bent	6-31G*	−6120.1723	2.33	172
	Bent	6-311+G*	−6125.003	2.44	174.7

Table II. The ground state properties of MF_2 (M = Mg, Ca, Sr, Ba): Total energy, optimum bond length ($r_{M-F, F-F}$) and angle in both M–F–F linear and bent configurations.

MF	MFF	Basis	E (eV)	r (Å); MF, FF	∠
MgF_2	Linear	6-31G*	−5452.4338	1.74, 2.00	180
	Linear	6-311+G*	−5455.2101	1.78, 2.08	180
	Bent	6-31G*	−5458.9345	1.74, 2.00	169.8
	Bent	6-311+G*	−5461.6219	1.78, 2.08	168.7
CaF_2	Linear	6-31G*	−6424.4142	2.08, 1.977	180
	Linear	6-311+G*	−6427.7661	2.117, 2.135	180
	Bent	6-31G*	−6424.4250	2.08, 1.977	166.5
	Bent	6-311+G*	−6427.7791	2.117, 2.135	164.4
SrF_2	Linear	6-31G*	−6257.8592	2.224, 1.94	180
	Linear	6-311+G*	−6261.3842	2.244, 2.181	180
	Bent	6-31G*	−6257.8702	2.224, 1.95	165.3
	Bent	6-311+G*	−6261.4071	2.240, 2.218	162.3
BaF_2	Linear	6-31G*	−6115.9334	2.357, 1.992	180
	Linear	6-311+G*	−6119.8731	2.349, 6.10	180
	Bent	6-31G*	−6115.9466	2.357, 1.992	163.5
	Bent	6-311+G*	−6120.1860	2.36, 9.012	168.7

Table III. Binding energy of monomeric MF_2 (M = Mg, Ca, Sr, Ba) calculated using 6-31G* basis set.

Monomer	Configuration	BE (eV)	r (Å)	∠
MgF_2	Linear F–M–F	−7.85	1.72	180
	Bent F–M–F	−7.85	1.72	180
	Linear F–F–M	−1.36	–	180
	Bent F–F–M	−1.36	–	169.8
CaF_2	Linear F–M–F	−5.99	2.06	180
	Bent F–M–F	−5.99	2.06	180
	Linear F–F–M	−0.91	–	180
	Bent F–F–M	−0.93	–	166.5
SrF_2	Linear F–M–F	−5.49	2.06	180
	Bent F–M–F	−5.49	2.20	172
	Linear F–F–M	−0.97	–	180
	Bent F–F–M	−1.0	-	165.3
BaF_2	Linear F–M–F	−5.30	2.33	180
	Bent F–M–F	−5.30	2.33	180
	Linear F–F–M	−1.03	–	180
	Bent F–F–M	−0.83	–	163.5

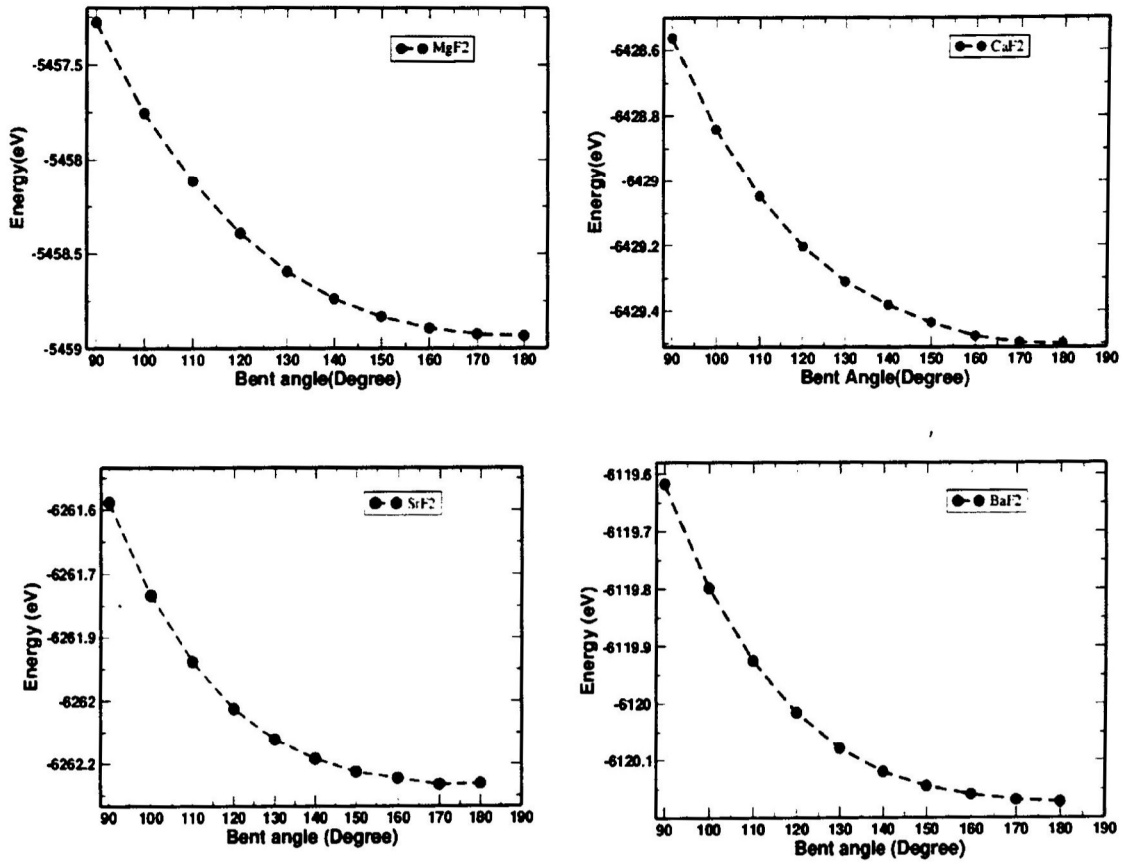

Fig. 2. Energy versus bent angle in MgF_2, CaF_2, SrF_2 and BaF_2.

in energy than that of F–M–F configuration. The increase in M–F bond length going from MgF_2 to CaF_2 to SrF_2 to BaF_2 can be attributed to increase the size of cation. As in increase in basicity of cation, Mullikens charge is increased going from MgF_2 to BaF_2, suggesting that there is presence of shorter and stronger bond in MgF_2 than rest other depending on the size of alkaline earth metal.

Magnesium is highly bound to fluorine molecule with binding energy −7.85 eV in both linear and bent-FMF configurations that confirm more stability of MgF_2 than rest others. Binding energy decreases in going from MgF_2 to CaF_2 to SrF_2 to BaF_2. Less binding energy found in FFM configuration is due to interaction of two fluoride atoms with higher optimum F–F bond length of 2.0 Å (e.g., MgF_2) and Mg–F distance (1.74 Å) greater than 1.72 Å (bond length of MgF_2 in F–M–F). Rest other monomers follow the similar behaviour.

3.2. Single Point Energy Calculations

We went through the single point calculations to examine the energy profile varying bent angle. Energy is calculated at their fixed bent geometries as displayed in Figure 2.

From the analysis of Figure 2, no expected variation is seen. However, higher energy difference ≈1 eV in MgF_2 and CaF_2, ≈0.5 eV in SrF_2 and BaF_2 are obtained by varying bent angle from 90° to 180°. The energy, therefore, differ by (0.1 eV–0.44 eV) as the molecules bent by 10°. Our results strongly suggest the more genuinely bending capability of SrF_2 and BaF_2 than MgF_2 and CaF_2.

4. CONCLUSIONS

In the present work, our attempt has been made to investigate structural properties of alkaline earth fluoride molecules; MgF_2, CaF_2, SrF_2 and BaF_2 systematically. All species considered are ionic and structurally stable system either in linear or bent F–M–F configuration. Increase in Mullikens charge going from MgF_2 to BaF_2, suggesting that there is presence of shorter and stronger bond in MgF_2 depending on the size of alkaline earth metal. The intermolecular interaction basically in fluorine are likely to be responsible for F–F–M bent monomers. More genuinely bending capability of SrF_2 and BaF_2 is the fascinating factor for too many applications. The detail arguements is still in need to believe the deviation from linearity of monomeric alkaline-earth fluorides.

Acknowledgments: S. Lamichhane acknowledges the support of Michigan Technological University (MTU) for funding under the exchange visitor program.

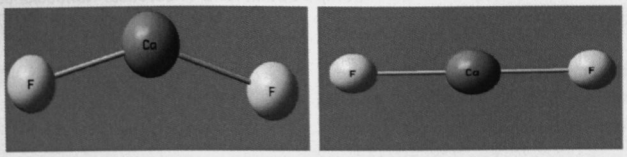

Fig. 1. Diagram of geometry of CaF_2 considered to find minimum energy configuration (left) and its relaxed structure (right).

which consisted several possible configurations to get energetically favourable one.

3.1. Structural Properties

The ground state properties of all studied monomers in F–M–F linear and F–M–F bent configurations are summarized in Table I.

Similarly, the ground state properties of MF_2 (M = Mg, Ca, Sr, Ba) in both M–F–F linear and bent configurations are presented in Table II.

No dipole moment is observed in both linear and bent F–M–F configurations as M (M = Ca, Mg) share electrons equally to fluorine. But, bent F–M–F configurations of SrF_2 and BaF_2 molecules display small dipole interaction resulting to produce dipole moment of 1.34 D and 0.98 D respectively. Mg–F distance gets increased by 0.02 Å in the relaxed structure of linear F–F–M than that of F–M–F. As the separation of charge increases, dipole moments of 7.96 D, 8.84 D, 8.90 D and 9.62 D are produced in MgF_2, CaF_2, SrF_2 and BaF_2 respectively.

Stability of monomeric MF_2 (M = Mg, Ca, Sr, Ba) are examined by calculating their binding energies with optimum bond length, as presented in Table III.

For the MF_2 monomer, the ground state configuration is linear F–M–F configuration with optimum M–F bond length of 1.72 Å, 2.06 Å, 2.2 Å and 2.33 Å for MgF_2, CaF_2, SrF_2 and BaF_2 and respectively. Our predicted bond length of linearized CaF_2 after optimization is 2.06 Å which is equally close to previous both experimental result 2.10 Å[7] and theoretically predicted value 2.011 Å.[11] The results after testing possible bent geometries, the monomers of SrF_2 and BaF_2 are found to be bent, while CaF_2 shows linearity, contary to previous result about CaF_2 as quasilinear.[5] Our work predicts MgF_2 to be linear as in previous work.[15] From Table I, It is clear that the total energy are in the order of $CaF_2 < SrF_2 < BaF_2 < MgF_2$, showing higher energy of CaF_2 than rest other. But, in contrast, bond length are in the order of $MgF_2 < CaF_2 < SrF_2 < BaF_2$. Energy, bond length and Mulliken charges are same in case of linear fluorene F–M–F and bent fluorine F–M-F configuration for the same basis set. Energy, bond length, Mulliken charges and bond angle are not exactly same in between relaxed configuration of linear M–F–F and bent M–F–F. M–F–F linear and bent both configurations are significantly higher (5 eV–6 eV)

Table I. The ground state properties of MF_2 (M = Mg, Ca, Sr, Ba): Total energy, optimum bond length (r_{M-F}) and angle in both F–M–F linear and bent configurations.

Monomer	F–M–F	Basis set	E (eV)	r (Å)	∠
MgF_2	Linear	6-31G*	−5458.9345	1.72	180
	Linear	6-311+G*	−5461.6219	1.76	180
	Bent	6-31G*	−5458.9345	1.72	180
	Bent	6-311+G*	−5461.6219	1.76	180
CaF_2	Linear	6-31G*	−6429.4999	2.06	180
	Linear	6-311+G*	−6433.3618	2.13	180
	Bent	6-31G*	−6429.4999	2.06	180
	Bent	6-311+G*	−6433.3618	2.13	180
SrF_2	Linear	6-31G*	−6262.3796	2.20	180
	Linear	6-311+G*	−6266.7515	2.28	180
	Bent	6-31G*	−6262.3801	2.20	172
	Bent	6-311+G*	−6433.3618	2.28	172.2
BaF_2	Linear	6-31G*	−6120.1723	2.33	180
	Linear	6-311+G*	−6124.0029	2.44	180
	Bent	6-31G*	−6120.1723	2.33	172
	Bent	6-311+G*	−6125.003	2.44	174.7

Table II. The ground state properties of MF_2 (M = Mg, Ca, Sr, Ba): Total energy, optimum bond length ($r_{M-F,F-F}$) and angle in both M–F–F linear and bent configurations.

MF	MFF	Basis	E (eV)	r (Å); MF, FF	∠
MgF_2	Linear	6-31G*	−5452.4338	1.74, 2.00	180
	Linear	6-311+G*	−5455.2101	1.78, 2.08	180
	Bent	6-31G*	−5458.9345	1.74, 2.00	169.8
	Bent	6-311+G*	−5461.6219	1.78, 2.08	168.7
CaF_2	Linear	6-31G*	−6424.4142	2.08, 1.977	180
	Linear	6-311+G*	−6427.7661	2.117, 2.135	180
	Bent	6-31G*	−6424.4250	2.08, 1.977	166.5
	Bent	6-311+G*	−6427.7791	2.117, 2.135	164.4
SrF_2	Linear	6-31G*	−6257.8592	2.224, 1.94	180
	Linear	6-311+G*	−6261.3842	2.244, 2.181	180
	Bent	6-31G*	−6257.8702	2.224, 1.95	165.3
	Bent	6-311+G*	−6261.4071	2.240, 2.218	162.3
BaF_2	Linear	6-31G*	−6115.9334	2.357, 1.992	180
	Linear	6-311+G*	−6119.8731	2.349, 6.10	180
	Bent	6-31G*	−6115.9466	2.357, 1.992	163.5
	Bent	6-311+G*	−6120.1860	2.36, 9.012	168.7

Table III. Binding energy of monomeric MF_2 (M = Mg, Ca, Sr, Ba) calculated using 6-31G* basis set.

Monomer	Configuration	BE (eV)	r (Å)	∠
MgF_2	Linear F–M–F	−7.85	1.72	180
	Bent F–M–F	−7.85	1.72	180
	Linear F–F–M	−1.36	–	180
	Bent F–F–M	−1.36	–	169.8
CaF_2	Linear F–M–F	−5.99	2.06	180
	Bent F–M–F	−5.99	2.06	180
	Linear F–F–M	−0.91	–	180
	Bent F–F–M	−0.93	–	166.5
SrF_2	Linear F–M–F	−5.49	2.06	180
	Bent F–M–F	−5.49	2.20	172
	Linear F–F–M	−0.97	–	180
	Bent F–F–M	−1.0	–	165.3
BaF_2	Linear F–M–F	−5.30	2.33	180
	Bent F–M–F	−5.30	2.33	180
	Linear F–F–M	−1.03	–	180
	Bent F–F–M	−0.83	–	163.5

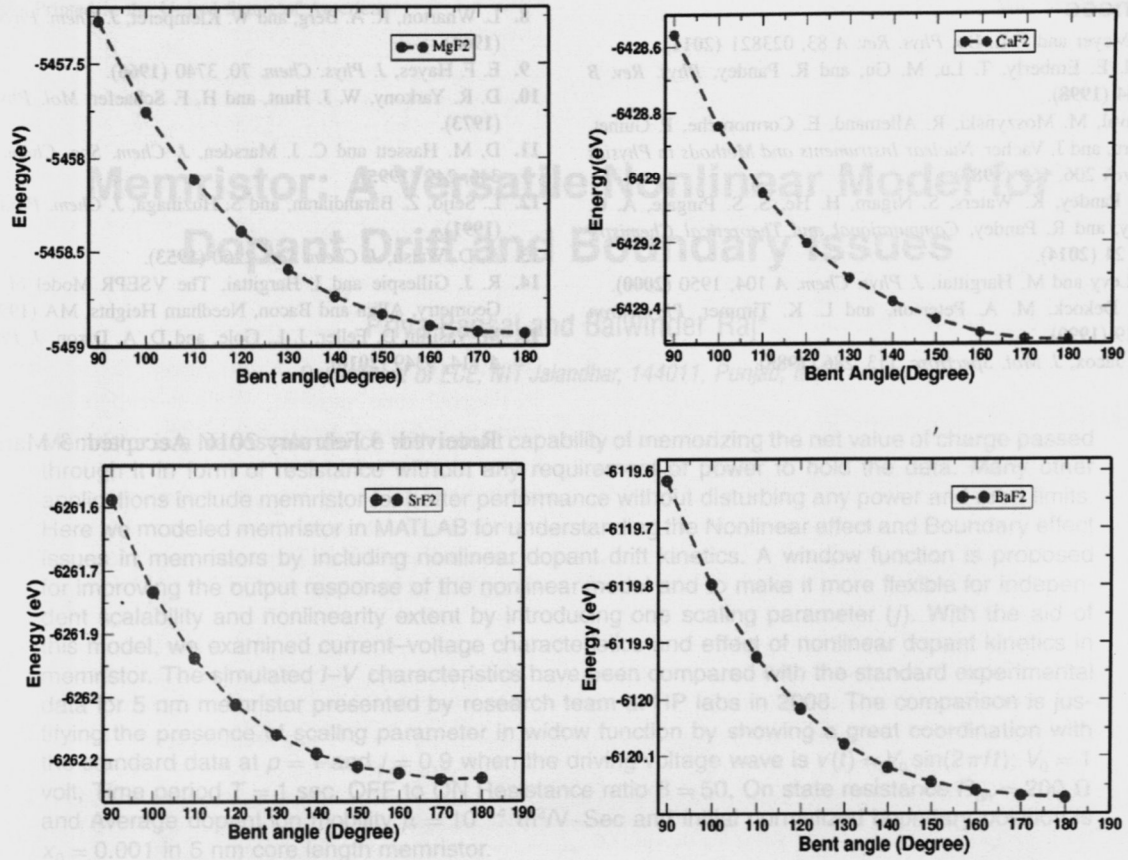

Fig. 2. Energy versus bent angle in MgF_2, CaF_2, SrF_2 and BaF_2.

in energy than that of F–M–F configuration. The increase in M–F bond length going from MgF_2 to CaF_2 to SrF_2 to BaF_2 can be attributed to increase the size of cation. As in increase in basicity of cation, Mullikens charge is increased going from MgF_2 to BaF_2, suggesting that there is presence of shorter and stronger bond in MgF_2 than rest other depending on the size of alkaline earth metal.

Magnesium is highly bound to fluorine molecule with binding energy −7.85 eV in both linear and bent-FMF configurations that confirm more stability of MgF_2 than rest others. Binding energy decreases in going from MgF_2 to CaF_2 to SrF_2 to BaF_2. Less binding energy found in FFM configuration is due to interaction of two fluoride atoms with higher optimum F–F bond length of 2.0 Å (e.g., MgF_2) and Mg–F distance (1.74 Å) greater than 1.72 Å (bond length of MgF_2 in F–M–F). Rest other monomers follow the similar behaviour.

3.2. Single Point Energy Calculations

We went through the single point calculations to examine the energy profile varying bent angle. Energy is calculated at their fixed bent geometries as displayed in Figure 2.

From the analysis of Figure 2, no expected variation is seen. However, higher energy difference ≈1 eV in MgF_2 and CaF_2, ≈0.5 eV in SrF_2 and BaF_2 are obtained by varying bent angle from 90° to 180°. The energy, therefore, differ by (0.1 eV–0.44 eV) as the molecules bent by 10°. Our results strongly suggest the more genuinely bending capability of SrF_2 and BaF_2 than MgF_2 and CaF_2.

4. CONCLUSIONS

In the present work, our attempt has been made to investigate structural properties of alkaline earth fluoride molecules; MgF_2, CaF_2, SrF_2 and BaF_2 systematically. All species considered are ionic and structurally stable system either in linear or bent F–M–F configuration. Increase in Mullikens charge going from MgF_2 to BaF_2, suggesting that there is presence of shorter and stronger bond in MgF_2 depending on the size of alkaline earth metal. The intermolecular interaction basically in fluorine are likely to be responsible for F–F–M bent monomers. More genuinely bending capability of SrF_2 and BaF_2 is the fascinating factor for too many applications. The detail arguements is still in need to believe the deviation from linearity of monomeric alkaline-earth fluorides.

Acknowledgments: S. Lamichhane acknowledges the support of Michigan Technological University (MTU) for funding under the exchange visitor program.

References

1. E. R. Meyer and J. L. Bo, *Phys. Rev. A* 83, 023821 **(2011)**.
2. J. Vail, E. Emberly, T. Lu, M. Gu, and R. Pandey, *Phys. Rev. B* 57, 764 **(1998)**.
3. M. Laval, M. Moszyński, R. Allemand, E. Cormoreche, P. Guinet, R. Odru, and J. Vacher, *Nuclear Instruments and Methods in Physics Research* 206, 169 **(1983)**.
4. R. K. Pandey, K. Waters, S. Nigam, H. He, S. S. Pingale, A. C. Pandey, and R. Pandey, *Computational and Theoretical Chemistry* 1043, 24 **(2014)**.
5. J. B. Levy and M. Hargittai, *J. Phys. Chem. A* 104, 1950 **(2000)**.
6. R. L. Dekock, M. A. Peterson, and L. K. Timmer, *Ployhedron* 9, 1919 **(1990)**.
7. M. E. Jacox, *J. Mol. Spectrosc.* 113, 286 **(1985)**.
8. L. Wharton, R. A. Berg, and W. Klemperer, *J. Chem. Phys.* 39, 2023 **(1963)**.
9. E. F. Hayes, *J. Phys. Chem.* 70, 3740 **(1966)**.
10. D. R. Yarkony, W. J. Hunt, and H. F. Schaefer, *Mol. Phys.* 26, 941 **(1973)**.
11. D. M. Hassett and C. J. Marsden, *J. Chem. Soc. Chem. Commun.* 346, 249 **(1995)**.
12. L. Seijo, Z. Barandiaran, and S. Huzinaga, *J. Chem. Phys.* 94, 3762 **(1991)**.
13. A. D. Walsh, *J. Chem. Soc.* 2260 **(1953)**.
14. R. J. Gillespie and I. Hargittai, The VSEPR Model of Molecular Geometry, Allyn and Bacon, Needham Heights, MA **(1991)**.
15. M. Vasiliu, D. Feller, J. L. Gole, and D. A. Dixon, *J. Phys. Chem. A* 114, 9349 **(2010)**.

Received: 3 February 2016. Accepted: 3 March 2016.

RESEARCH ARTICLE

AMERICAN SCIENTIFIC PUBLISHERS

Quantum Matter
Vol. 5, 1–5, 2016

Electronic Structures and Magnetic Properties of NiAl and Ni_3Al

S. Lamichhane, G. C. Kaphle*, and N. P. Adhikari

Central Department of Physics, Tribhuvan University, Kirtipur, Kathmandu, Nepal

Intermetallic binary alloys of Ni and Al has attracted much attention in the field of science and technology because of their use in computer chips, variety of turbine components, medical implants and commercial applications etc. Magnetic properties and properties based on electronic structure of ordered alloys NiAl and Ni_3Al have been studied using tight binding linear muffin-tin orbitals atomic sphere approximation (TB-LMTO-ASA). In order to understand the electronic properties, we have performed band structure calculations. Our findings show that all the systems considered are metallic in nature. To know the contributions of the orbitals in the bands, the system is analyzed via fat bands which reveals most of the contributions on valence band of NiAl and Ni_3Al is due to *d*-orbital and the contributions on conduction band is due to *s* and *p*-orbital. Our calculations agree with the previously reported data. Furthermore, spin up and spin down calculations have been done to understand the magnetic properties of the system. Our calculations also suggest the magnetic nature of Ni_3Al and non magnetic nature of NiAl. It is obtained that the magnetic moment of alloys containing Ni and Al increases with increasing Ni concentration. The study of Ni_3Al is of great interest from magnetic point of view as it displays magnetic moment 0.52 μ_B.

Keywords: Atomic Sphere Approximation, Density Functional Theory, Fat Band, Magnetic Properties, Binary Alloys.

1. INTRODUCTION

The main basis for understanding materials ultimately rests upon understanding their electronic structure.[1] Due to this, various researchers have shown their interest on electronic structure and properties of materials.[2,3] The cohesive, electronic, optical, magnetic and super-conducting properties of solids are dominated by the behavior of valence electrons moving in the field of the ion-core of constituent atoms. To know the behavior of valance electrons and study the electronic and magnetic properties of alloys, various techniques have been developed.[4–6] Out of them tight-binding linear muffin-tin orbital method with atomic sphere approximation (TB-LMTO-ASA) is the widely used technique. The electronic and magnetic properties of ordered and disordered binary alloys have been done previously[7–9] using modified form of it indicating that it is one of the most powerful technique for electronic structure calculation. The study of intermetallic compounds NiAl and Ni_3Al has great interest because of their use in high temperature materials, shape memory alloys and soft magnetic materials.[10] NiAl is binary compound which crystallizes in to CsCl structure.[11] Electronic properties of it is measured by photoemission previously[12] and observed that NiAl is good metal. Same thing can be described by band theory. The main aim of present study is to find out the band structure and contribution of *s*, *p* and *d* orbitals on it. X-ray and UV-photoemission results[13] and early band-structure calculations show that the Ni *d* band in NiAl is filled and density of states (DOS) at the Fermi level is low. One of the main goal of this study is to analyze it theoretically and to compare our results with available experimental data. From the previous study it is found that Ni-rich NiAl intermetallic alloys form stable $L1_2$ phase, with simple cubic structure Cu_3Au structure. Electronic and magnetic properties are studied using various techniques.[14] However, Kubler et al.[15] used TB-LMTO-ASA for the study of electronic and magnetic properties. He found the magnetic moment of Ni_3Al as 0.09 μ_B per unit cell. Later on Min et al.[16] investigated electronic and magnetic properties of Ni_3Al with magnetic moment 0.44 μ_B per unit cell. Hence due to various applications of NiAl and Ni_3Al and lack of detailed work or controversial experimental and theoretical values in magnetic moment, we intend to study the electronic and magnetic properties of these intermetallic alloys.

The rest of the paper is arranged as follows. In Section 2, we have described the calculation procedure used in our calculations. Results and discussion of the present study is given in Section 3 which contains the description of electronic and magnetic properties through band structure and DOS analysis. Finally conclusions are presented in Section 4 before the list of references.

*Author to whom correspondence should be addressed.

2. COMPUTATIONAL DETAILS

All the systems considered are studied using Tight Binding Linear Muffin-Tin Orbitals Atomic Sphere Approximation (TB-LMTO-ASA). All the calculations are carried out from self-consistent calculations (SCF) based on density functional theory within the framework of the local-density approximation (LDA).[17] SCF solve the Kohn-Sham equation using the exchange-correlation potential of Von Barth and Hedin[18] with the help of minimal basis sets and partial wave method implemented in TB-LMTO-ASA code. The crystal potential is constructed of overlapping Wigner-Seitz spheres for each atom in the unit cell. According to the spirit of the TB-LMTO-ASA procedure, only the energetically higher-lying valence states have been included in the self-consistent calculations of the effective crystal potential.[19,20] The deeper lying core states are treated as atomic like in the so called frozen core approximation. For the calculation of Ni (BCC) and Al (FCC) structure same basis set were used at which $(8 \times 8 \times 8)$ k-points were sampled in the irreducible wedge of Brillouin Zone (BZ). These parameters are sufficient in leading to well converged total energy and other related parameters. The magnetic moment was calculated by differentiating up and down DOS. After the convergence of SCF we analyzed all the data required for band structure, total energy, DOS etc. All the calculations were iterated to self-consistency with accuracy of 10^{-6} Rydberg.

3. RESULTS AND DISCUSSION

This section contains the results of present calculations related to band structure and density of states of NiAl and Ni_3Al.

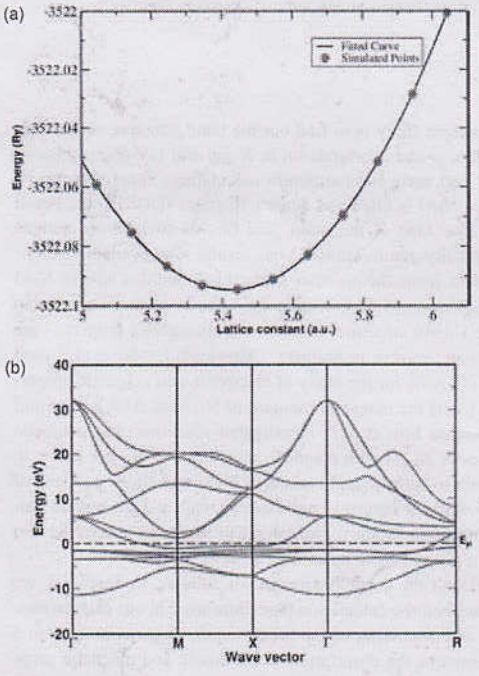

Fig. 1. (a) Energy minimization curve and (b) Energy band-structure of NiAl.

The comparable study of occupation of s, p and d orbital and the formation of magnetic moments are also described.

3.1. Band Structure of NiAl

Electronic band structure of materials determine the several characteristics in particular the electrical and optical properties like Fowler-Nordheim Field emission from quantum confined opto-electronic materials in the presence of light wave[21] and influence of light wave with its intensity, numerical magnitude on effective electron mass in quantum well.[22]

For the band structure of NiAl, we used space group (SG) as 221(pm-3m) and optimized lattice parameter is calculated using energy minimization process as in Figure 1(a) and found the optimized lattice parameter as 2.87 Å which resembles with previously calculated theoretical results.[23] The experimental value of lattice parameter is 2.887 Å.[24] Our optimized lattice parameter is 0.34% less than experimental value and 0.59% less than theoretical value. All the further calculations are done by using the base of this value.

The calculated band structure of NiAl along the higher symmetry directions G, M, X and R in the Brillouin zone are given in Figure 1(b). The energy scale is relative to E_F in units of eV. There are altogether 13 bands observed in the bulk band structure of NiAl. It is also observed that valence and conduction bands are overlapped showing that NiAl compound bears a metallic character. The electron's occupancy at different orbitals of the atoms in

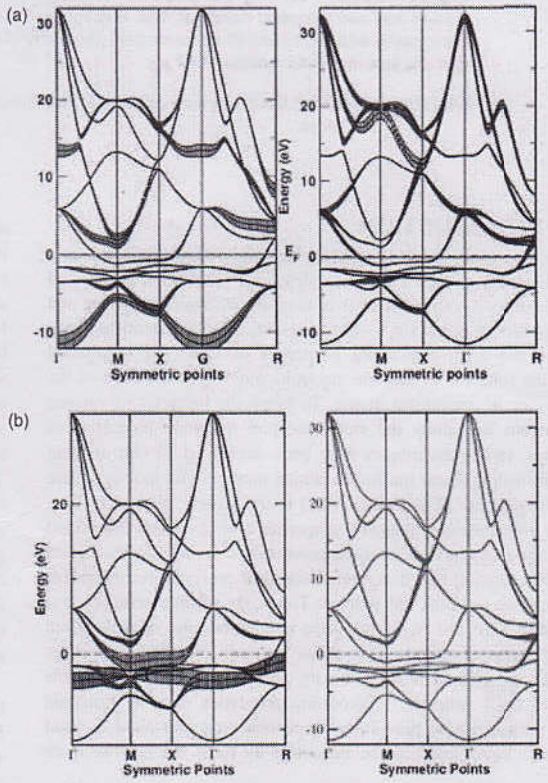

Fig. 2. Fat bands of (a) s and p orbitals and (b) t_{2g} and e_g orbitals of NiAl.

NiAl alloy can be understood by studying the fat bands. It is seen that the 13 valence electron per unit cell which fill six-initial-state bands, with the seventh band being partially occupied.

The contribution of s and p orbitals in the energy bands of NiAl is shown in Figure 2(a) and contribution of d orbitals (t_{2g} and e_g sub-orbital's) is shown in Figure 2(b). Our findings show that free-electron like character of bands is mostly from Al s and Al p states. These states are observed both at the bottom of the band and above the Fermi level. The Ni d bands are p and d mixing range lies between −1.55 eV to −4.32 eV. From the figure, it is also observed that Fermi level lying in the region of high t_{2g} density of states.

From the Figures 2(a and b), we see that most of the contribution in the total energy band of NiAl comes from t_{2g} sub-orbital of d orbital of NiAl alloy near the Fermi level. This indicates that the filling of d bands is supported in the present calculations.

3.2. Band Structure of Ni_3Al

The crystal structure of the Ni_3Al is FCC[25] with Ni atoms on the face and Al atom on the corner. The optimized lattice parameter is calculated using energy minimization process as in Figure 3(a) and found the optimized lattice parameter as 3.49 Å which resembles with previously calculated theoretical results.[26] The optimized lattice parameter of present study is 0.08% less than theoretical value.

The calculated band structure of Ni_3Al is shown in Figure 3(b). Our findings show that there is no band gap at the Fermi level indicating that valence and conduction bands overlap significantly at the Fermi level. This means Ni_3Al alloy also exhibit the metallic character as NiAl.

The electron's occupancy at different orbitals of the atoms in Ni_3Al alloy can be understood by studying the fat bands. The contributions of s and p orbitals in the energy bands of Ni_3Al are shown in Figure 4(a) and contribution of d orbitals (e_g and t_{2g} sub-orbitals) are shown in Figure 4(b). From the figure, it is seen that s and p orbitals of Al mostly found at the bottom of the band and above the Fermi energy. The Ni d bands are mostly found in pd mixing range (−0.43 eV to −3.01 eV). It is also seen that e_g d band mostly dominate to other bands near the Fermi level. From the Figures 4(a and b), we see that most of the contribution in the total energy band of Ni_3Al comes from e_g sub-orbital of d orbital of Ni_3Al alloy. The occupancies s, p or d of electrons for the contribution of magnetic moments can be understood by DOS and PDOS plot which are described more detail in the following section.

3.3. Density of States of NiAl

The calculated total density of states (TDOS) and Projected density of states (PDOS) of NiAl are shown in Figures 5(a and b) respectively. It shows that the number of peaks of Ni is less than Al. The bandwidth of Ni is also found to be narrower than Al. This is the indication of hybridization of Al 2p and

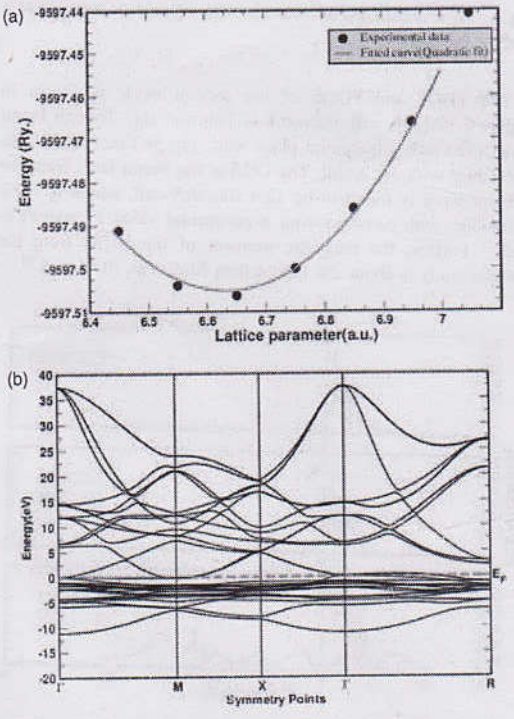

Fig. 3. (a) Plot of total Energy versus Lattice parameter and (b) Band-structure of Ni_3Al along with the high symmetry directions.

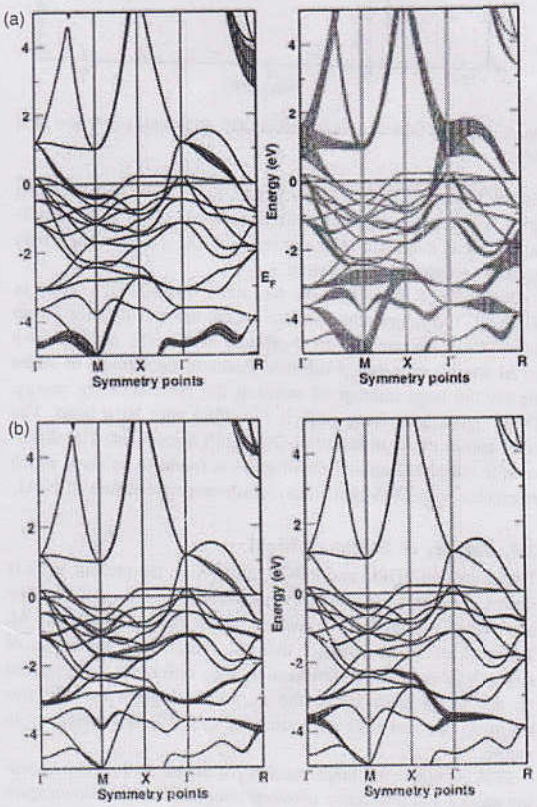

Fig. 4. (a) Fat bands of s and p orbitals and (b) t_{2g} and e_g orbital of Ni_3Al.

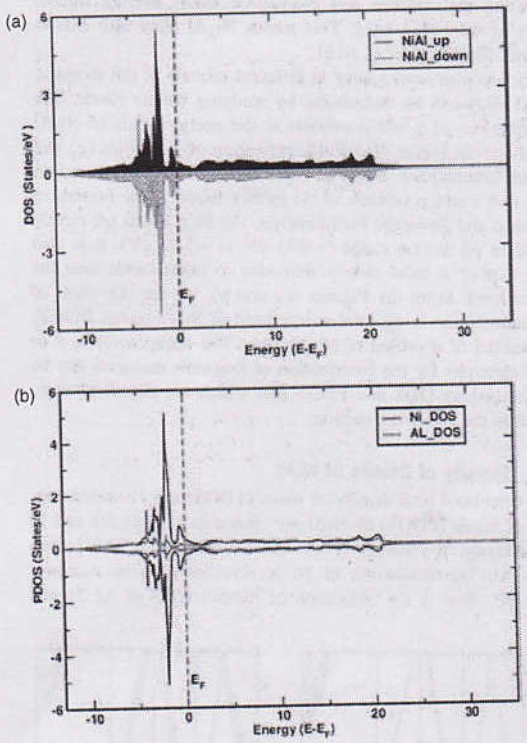

Fig. 5. (a) Total DOS and (b) Individual DOS contributions of Ni and Al in NiAl.

Ni 3d. Though states of Ni is higher than Al in up and down spins, there is strong competition between these spins resulting effective magnetic moment zero and the system as a whole becomes nonmagnetic in nature.

Our findings show that Ni has more fraction of charge in d-orbital. The major contributions on the density of states for up and down states are due to d-orbitals of Ni. The contributions of Al are due to s and p orbitals. Peaks in the density of states signify the large number of states at the corresponding energy. From Figure 5(b), large peak is identified with Ni d band. The contribution of Al in the total DOS isn't significant. The difference in integrated up and down spins is found to be zero, which resembles with DOS plot showing nonmagnetic nature of NiAl.

3.4. Density of States of Ni_3Al

The calculated TDOS and PDOS of Ni_3Al in the present work is shown in Figures 6(a and b) respectively. From these figures we observed that width of Ni band is higher than the width of Al. The peak of Ni also higher than Al. This is the indication of strong Ni d and Al p hybridization. The difference in integrated up and down spins up to the Fermi level gives the effective magnetic moment 0.52 μ_B indicating that it is ferromagnetic in nature.

DOS signifies the large number of states at the corresponding energy and difference between integrated up and down spins gives the magnetic moments. Most of the contributions for magnetism is due to d electrons of Ni in Ni_3Al.

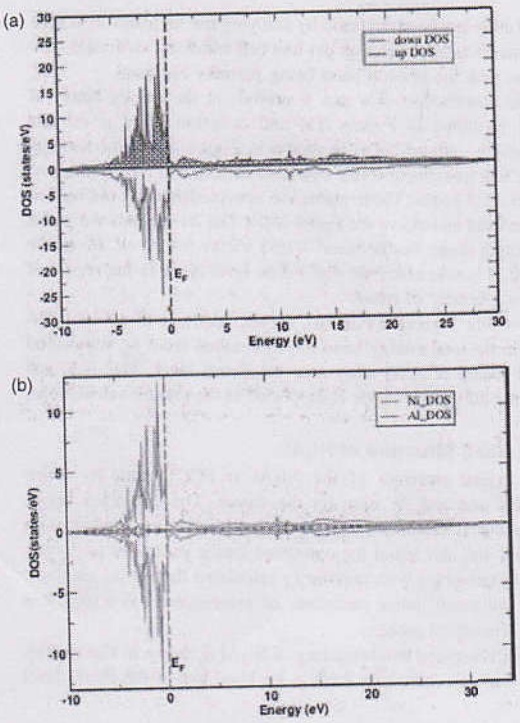

Fig. 6. (a) Total DOS and (b) Individual DOS contributions of Ni and Al in Ni_3Al.

The TDOS and PDOS of the present work as shown in Figure 7 matches with the work of Fatmi et al.[25] Though Fatmi et al. used pseudo-potential plane-wave (pp-pw) method it quite resembles with our result. The DOS at the Fermi level from the present work is found to be 12.4 states/eV-cell, which is ~3% resembles with corresponding experimental value 11 states/eV-cell.[27] Further, the magnetic moment of the Ni_3Al from the present study is about 2% higher than Min et al. (0.44 μ_B).[16]

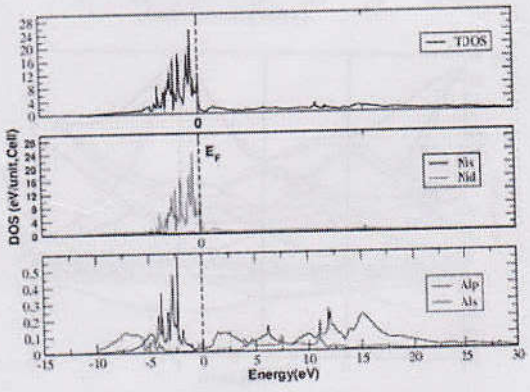

Fig. 7. Total Density of States (TDOS) and Projected Density of States (PDOS) for Ni_3Al. Fermi level is taken as a zero energy.

4. CONCLUSIONS

In the present work, we have studied the band structure and density of states of ordered binary alloys NiAl and Ni_3Al by using TB-LMTO-ASA technique. We have observed the electronic and magnetic properties of NiAl and Ni_3Al. We have found 13 bands in NiAl and 31 bands in Ni_3Al. The band structures show that the valence and conduction bands are overlapped with each other indicating that both NiAl and Ni_3Al are metallic in nature.

Furthermore, we have calculated the fat band structure of NiAl and Ni_3Al. We observed that below Fermi level, most of the bands are occupied with d-orbitals as expected. Above Fermi level, we see that the bands are occupied mostly with s and p orbitals. We also studied the density of states of all the systems. The magnetic moment of NiAl is found to be zero (nonmagnetic) and magnetic moment of Ni_3Al is found to be 0.52 μ_B i.e., ferromagnetic in nature. Finally, we can conclude that TB-LMTO-ASA is good technique to calculate the electronic structure of ordered alloys.

Acknowledgments: One of us G. C. Kaphle is grateful to Professor A. Mookerjee for fruitful discussion. We also acknowledge the partial supports by The Abdus Salam International Centre for Theoretical Physics (ICTP), Italy through office of external activities (OEA) NET-56 project.

References and Notes

1. R. M. Martin, Electronic Structure: Basic Theory and Practical Methods, Cambridge University Press, United Kingdom **(2004)**.
2. M. Mellaoui, S. Belaidi, D. Bouzidi, and N. Gherraf, *Quantum Matter* 3, 435 **(2014)**.
3. A. Srivastava, S. Jain, and A. K. Nagawat, *Quantum Matter* 2, 469 **(2013)**.
4. H. L. Skriver, The LMTO Method Muffin-Tin Orbitals and Electronic Structure, Springer-Verlag **(1984)**, Vol. 41.
5. O. K. Anderson, *Phys. Rev. B* 12, 3060 **(1975)**.
6. O. K. Andersen and O. Jepsen, *Phys. Rev. Lett.* 53, 2571 **(1984)**.
7. G. C. Kaphle, S. Ganguly, R. Banerjee, R. Khanal, C. M. Adhikari, N. P. Adhikari, and A. Mookerjee, *Journal of Physics: Condensed Matter* 24, 295501 **(2012)**.
8. S. Ganguly, M. Costa, A. B. Kalautau, A. Bergman, B. Sanyal, A. Mookarjee, and O. Eriksson, *Phys. Rev. B* 83, 094407 **(2011)**.
9. S. Pandey, G. C. Kaphle, and N. P. Adhikari, *BIBECHANA* 11, 60 **(2014)**.
10. G. P. P. Pun and Y. Mishin, *J. Phys: Condens. Matter* 22, 395403 **(2010)**.
11. S. C. Lui, J. W. Davenport, E. W. Plummer, D. M. Zehner, and G. W. Fernando, *Phy. Rev. B* 42, 1582 **(1990)**.
12. H. J. Levinson, F. Greutter, and E. W. Plummer, *Phy. Rev. B* 27 727 **(1983)**.
13. J. C. Fuggle, F. U. Hillebrecht, R. Zeller, Z. Zoxneirek, and P. A. Bennette, *Phy. Rev. B* 22, 2145 **(1983)**.
14. B. I. Min, A. J. Freeman, and H. J. F. Jansen, *Phy. Rev. B* 137, 6757 **(1998)**.
15. D. Hackenbracht and J. Kubler, *J. Phys. F: Metal Phys.* 10, 427 **(1980)**.
16. B. I. Min, T. Oguchi, H. J. F. Jawsen, and A. J. Freeman, *Phy. Rev. B* 12, 1091 **(2003)**.
17. P. Hohenberg and W. Kohn, *Phys. Rev. B* 136, 864 **(1964)**.
18. U. V. Barth and L. Hedin, *J. Phys. C* 5, 1629 **(1972)**.
19. N. W. Ashcroft and N. D. Mermin, Solid State Physics, 2nd edn., Thomson Books, USA **(1976)**.
20. U. Mizutani, The Electron Theory of Metals, 1st edn., Cambridge University Press, New York **(2001)**.
21. K. P. Ghatak, S. Bhattacharya, A. Mondal, S. Debbarma, P. Ghorai, and A. Bhattacharjee, *Quantum Matter* 2, 25 **(2013)**.
22. P. K. Bose, N. Paitya, S. Bhattacharya, D. De, S. Saha, K. M. Chatterjee, S. Pahari, and K. P. Ghatak, *Quantum Matter* 1, 89 **(2012)**.
23. A. Taylor and N. J. Doyle, *J. Appl. Crystallogr.* 5, 201 **(1972)**.
24. X. Ren, K. Otsuka, and M. Kogachi, *Scr. Matter* 41, 907 **(1999)**.
25. M. Fatmi, M. A. Ghebouli, B. Ghebouli, T. Chihi, S. Boucetta, and Z. K. Heiba, *Rom. Journ. Phys.* 56, 937 **(2011)**.
26. G. K. Dey, *Sadhana* 28, 247 **(2003)**.
27. L.-S. Hsu, Y. K. Wang, and G. Y. Guo, *J. Appl. Phys.* 92, 1419 **(2002)**.

Received: 12 December 2013. Accepted: 28 May 2014.

First-Principles Study of Adsorption of Halogen Molecules on Graphene-MoS_2 Bilayer Hetero-system

2016 J. Phys.: Conf. Ser. 765 012011

(http://iopscience.iop.org/1742-6596/765/1/012011)

First-Principles Study of Adsorption of Halogen Molecules on Graphene-MoS_2 Bilayer Hetero-system

S. Lamichhane[1], P. Lage[1], G. B. Khatri[1], N. Pantha[1], N. P. Adhikari[1*] and B. Sanyal[2]

[1]*Central Department of Physics, Tribhuvan University, Kathmandu, Nepal.*
[2]*Division of Materials Theory, Department of Physics and Astronomy, Uppsala University, Sweden.*

*email: npadhikari@tucdp.edu.np

Abstract

We have performed density functional theory based first-principles calculations to study the stability, geometrical structures and electronic properties of pure 3×3 supercell of MoS_2, 4×4 supercell of graphene, graphene-MoS_2 bilayer hetero-system, F_2, Cl_2, Br_2 and I_2 molecules on hetero-system within the DFT- D_2 level of approximations. The preferable site and adsorption energy of halogen molecules are studied. The most stable geometries are considered to study their electronic band structure, Density of states and magnetic properties with reference to individual 2D components, graphene and MoS_2 .

1. Introduction

The strongest, thinnest and most stretchable material arranged in honeycomb lattice of thick sheet of sp^2-bonded carbon atoms termed as graphene is at focus of many research works worldwide due to its peculiar properties like observable quantum Hall effect at room temperature and existence of two-dimensional gas of massless Dirac fermions [1-5]. These nobel properties of graphene with its applications in the areas of spintronics, hydrogen storage, sensing [6-9] have attracted the most modern consent of researchers to predict other desirable properties.

On complementary to graphene, MoS_2 belonging to 2D transition metaldichalcogenide, well known as band gap semiconductor is becoming most studied material in the last 5 years [10-12]. MoS_2 is a layered transition metal dichalcogenide semiconductor with an indirect band gap in which Mo and S atoms are stacked together to give S-Mo-S sandwiches coordinated in a triangular prismatic arrangement [13]. In recent time, MoS_2 is attracting the attention of many researchers as it is excessively available in the form of a natural mineral, molybednite [14]. MoS_2 monolayer is widely used to produce transistors [15], integrated logic circuits, signal amplifiers [16], photodetectors and flexible optoelectronic devices. It is a promising material with highly potential applications in solar cells [17], photocatalysts, signal amplifiers and lubrication [18]. However, its properties are limited by band gap. The graphene-MoS_2 bilayer hetero-structure as shown in figure [1] offers the excellent mechanical flexibility, electronic properties, optical transparency, photoconductivity and favorable transport properties [19].

The association of two materials with their distinct electronic properties is believed to drag the desired properties in practical applications. Moreover, the adsorption of foreign atoms on hetrostructure is one of the promising approach to modify and exploit unwanted properties of any constituent. Combination of two materials standing for a brand new family with halogen, commonly known as reactive non metal and highly electronegative elements of periodic table is highly expected to start new direction towards mate-rials science research.Heterostructure may bee important to study the properties beyond the capacities of constituents as well as to eliminate the negative properties and drag desirable one.

Although the graphene-MoS_2 hetero-structure is used to study the adsorption of different metals on nano-scale channels [20], it has not been tested for the ability of heterostructure with reactive non-metals. Previous work for the adsorption of halogens on graphene layers opens very small gap (3-75 meV, highest in fluorine). Since MoS_2 is band gap material, we are interested to test halogens on graphene-MoS_2 bilayer to obtain high band gaps and particularly the role of fluorine to change the electronic structure. From both scientific and technological point of view, investigation of halogen adsorption on semiconducting surface is very important as halogen and its compounds are widely used in the etching technologies. To make comparison for the interaction of halogens and semiconductor surface is of prime importance. In this work, we consider adsorption of diatomic halogen molecules on graphene-MoS_2 bilayer hetero-system.

The remaining part of the paper is organized in the following way. In Sec. II, we discuss the computational details and the systems under our study. Sec. III gives a brief description of results of adsorption of F_2, Cl_2 , Br_2 and I_2 molecules on graphene-MoS_2 bilayer hetero-system. Here, we present the analysis of adsorption sites, binding energies, band structures and density of states. The last conclusion section summarizes the major findings and possible extensions of the ongoing research.

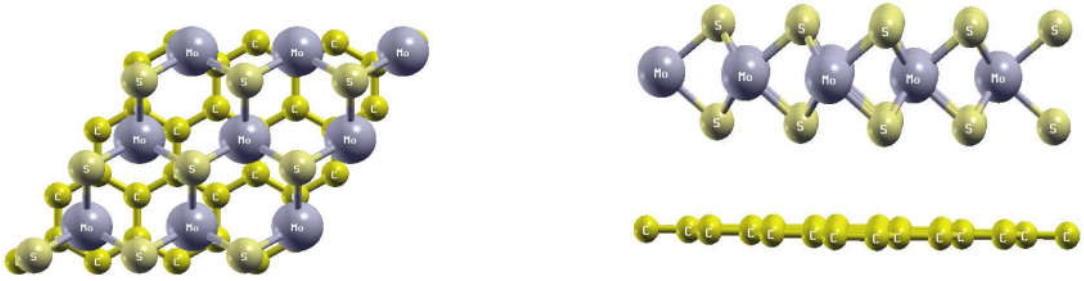

Figure 1: 3×3 supercell of MoS_2 Monolayer and 4×4 super cell of graphene to form a MoS_2 -graphene bilayer hetero-system, (a) Top-view and (b) Side-view respectively

.

2. Computational Details

In the present work, we have incorporated Density Functional Theory (DFT) [21, 22] implemented in the Quantum Espresso (QE) [23] code to study the geometrical and structural properties of 3×3 supercell of MoS_2 , 4×4 supercell of graphene, graphene-MoS_2 bilayer hetero-structure and halogen molecules adsorbed graphene- MoS_2 bilayer hetero-structure. The Perdew-Burke-Ernzerhof (PBE) form of generalized gradient approximation (GGA) [24] with van Der Waals interaction via Grimme's model [25, 26] is used to treat inter electron interaction. The bfgs algorithm with Rappe-Rabe-Kaxiras-Joannopoulos (RRKJ) model of ultrasoft pseudopotential is used to account the interaction between the ion cores and valence electrons. The unit cell is optimized with respect to lattice parameter 'a', kinetic energy cut-off (E_{cut}) for plane wave and the number of k-points along x- and y-axes respectively. Based on these convergence tests, we obtained the lattice constant 'a' for the unit cell of MoS_2 as 3.176 ˚A which agrees with the previous results [13, 14].
For the 3×3 supercell of MoS_2 the lattice constant is three times that of the unit cell. Further, the plot of the total energy verses the number of k-points reveals that the energy of the unit cell of monolayer MoS_2 is almost constant after n_{kx} equal to 10. Hence a mesh of 10×10×1 k-points, in case of unit cell,

could be used for the Brillouin-zone integration. The mesh was reduced to 4×4×1 for 3×3 as per relations of direct and reciprocal lattice geometries, which helps to minimize the computational cost. A plane wave basis set with energy cut-off values of 476 eV (35 Ry) for the wave-function and 4760 eV (350 Ry) for the charge density is used for the expansion of the ground state electronic wave functions.

3. Results and Discussion

3.1 Adsorption of halogen molecules on Graphene-MoS_2 bilayer hetero-structure:

The MoS_2/graphene heterostructures is made using 3 × 3 supercell of MoS_2 and 4 × 4 supercell of graphene by considering the lattice mismatch. There are two possibilities for the construction of the heterostructures accounting the difference in lattice parameters between 18.006 Bohrs of MoS 2 and 18.600 Bohrs of graphene. If lattice constant of MoS_2 is used (i.e MoS_2 is taken reference and graphene is modelled on it), there will be compressive strain of 3.3 % on graphene sheet. If lattice constant of graphene is used i.e graphene as reference and MoS_2 is modelled on it, there will be 3.2 % tensile strain to MoS_2 . In this study, Both cases are taken with the different stacking and configurations to find the minimum energy state for the calculations of the electronic structurs of the heterostructures. Vaccum length is made greater than 20 ˚A along z- axis to avoid the interactions between the adjacent supercells. We have considered six different occupation sites of high symmetry : the hollow site, at the center of hexagonal plane of MoS_2 , top of molybdenum atom (Mo-Top), top of sulphur atom (S-Top) from MoS_2 side and hollow site at the center of hexagon of graphene (C-Hollow), bridge between two carbon atoms (C-Bridge) and top of carbon atom (C-Top) from graphene side as shown in figure [2]. The adsorbates (halogens) were kept in two different orientations before optimization, viz. Parallel and Perpendicular to the graphene and MoS 2 sheets. Reverse to the order of bond dissociation energy in halogen molecules (Cl_2 >Br_2 >F_2 >I_2), the B.E. of halogens on MoS_2 sheet is found in the order Cl_2 <Br_2 <F_2 <I_2 . The reason is obvious, the halogen molecule with the stronger intra-atomic bonding gain its inert state and becomes less reactive towards MoS_2 monolayer.

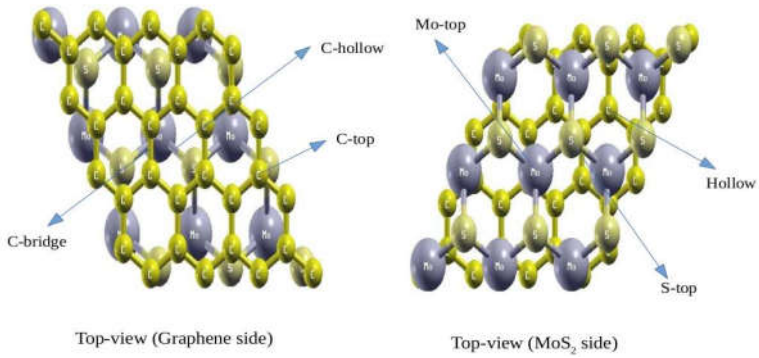

Figure 2: Different possible adsorption sites for the adsorption of halogen molecules on graphene-MoS_2 bilayer hetero-structure.

The binding energy (adsorption energy) of a halogen molecule on graphene-MoS_2 bilayer hetero-system is calculated by using the relation

$$\Delta E = E_{hal} + E_{graphene-MoS2} - E_{hal-graphene-MoS2} \quad (1)$$

where E_{hal} is ground state energy of a fully relaxed halogen molecule, $E_{graphene-MoS2}$ is the ground state energy of graphene-MoS_2 bilayer hetero-structure and $E_{hal-graphene-MoS2}$ is the ground state energy of halogen adsorbed graphene-MoS_2 bilayer hetero-structure. The positive binding energy reflects the stability of the system. The total energy of a halogen molecule adsorbed graphene- MoS_2 bilayer hetero-structure is calculated in 3×3 supercell of MoS_2 and 4×4 supercell of graphene. Out of the six adsorption sites, the site with the largest binding energy is indicated as the most favourable site for adsorption of the halogen molecule. The different parameters obtained from our calcula-tions are shown in tables below.

Table 1: Table for Binding Energy (E), perpendicular distance of centre of adsorbed molecule from sulphur plane of MoS_2 (h_1), reference (h_1)*[27], distortion on MoS_2 sheet (d_{MoS2}) and observed bond length of adsorbed halogen molecule (d) along graphene side of graphene- MoS_2 bilayer heterostructure

Halogen	Orientation	C-hollow					C-bridge					C-top				
		ΔE (eV)	h_1 (Å)	h_1^* (Å)	d_{MoS2} (Å)	d (Å)	ΔE (eV)	h_1 (Å)	h_1^* (Å)	d_{MoS2} (Å)	d (Å)	ΔE (eV)	h_1 (Å)	h_1^* (Å)	d_{MoS2} (Å)	d (Å)
F_2	Parallel	1.882	3.560	3.230	0.119	2.823	0.417	3.700	3.170	0.011	3.010	1.012	3.720	3.230	0.014	1.650
	perpendicular	0.284	3.900	3.700	0.001	2.610	0.234	3.380	3.470	0.008	3.088	0.437	3.390	3.460	0.003	1.640
Cl_2	Parallel	0.163	3.580	3.580	0.035	1.900	0.189	3.590	3.630	0.040	2.000	0.182	3.540	3.640	0.041	2.000
	perpendicular	0.153	4.170	4.340	0.007	2.000	0.188	4.110	4.210	0.005	2.010	0.194	4.180	4.210	0.006	2.020
Br_2	Parallel	0.239	3.610	3.770	0.020	2.310	0.267	3.690	3.740	0.013	2.310	0.258	3.660	3.770	0.030	2.310
	perpendicular	0.225	4.510	4.670	0.002	2.320	0.273	4.320	4.510	0.005	2.330	0.281	4.200	4.450	0.005	2.340
I_2	Parallel	0.365	3.590	3.850	0.019	2.699	0.389	3.520	3.800	0.002	2.695	0.383	3.650	3.830	0.001	2.694
	perpendicular	0.315	4.600	4.730	0.019	2.699	0.352	4.698	4.740	0.017	2.709	0.359	4.750	4.850	0.020	2.709

Table 2: Table for Binding Energy (E), perpendicular distance of centre of adsorbed molecule from sulphur plane of MoS_2 (h_1), distortion on MoS_2 sheet (d_{MoS2}) and observed bond length of adsorbed halogen molecule (d) along MoS_2 side of graphene-MoS_2 bilayer heterostructure

Halogen	Orientation	hollow				Mo-top				S-top			
		ΔE (eV)	h_1 (Å)	d_{MoS2} (Å)	d (Å)	ΔE (eV)	h_1 (Å)	d_{MoS2} (Å)	d (Å)	ΔE (eV)	h_1 (Å)	d_{MoS2} (Å)	d (Å)
F_2	Parallel	0.291	3.002	0.001	1.527	0.229	3.990	0.001	1.526	0.199	3.800	0.001	1.527
	perpendicular	0.261	3.600	0.021	1.538	0.284	3.475	0.000	1.532	0.732	3.200	0.079	1.798
Cl_2	Parallel	0.158	3.400	0.060	1.990	0.162	3.370	0.065	1.995	0.156	3.430	0.070	2.000
	perpendicular	0.159	4.040	0.004	2.010	0.150	4.060	0.054	2.010	0.247	3.980	0.008	2.060
Br_2	Parallel	0.238	3.390	0.040	2.310	0.239	3.400	0.040	2.310	0.239	3.250	0.070	2.310
	perpendicular	0.244	4.200	0.003	2.330	0.226	4.220	0.050	2.320	0.404	4.020	0.001	2.330
I_2	Parallel	0.387	3.398	0.003	2.695	0.385	3.394	0.004	2.695	0.379	3.459	0.003	2.694
	perpendicular	0.344	4.445	0.014	2.712	0.325	4.550	0.011	2.706	0.489	4.150	0.024	2.764

Tables 1 & 2 show the binding energy values of different structures at different occupation sites. The perpendicular distance of centre of adsorbed molecule from sulphur plane of MoS_2 (h_1) is found to agree well with the reference values of (h_1) [27]. The bond length of adsorbed molecule on graphene-MoS_2 bilayer hetero-structure is not obtained to be significantly changed during adsorption process because the obtained molecule-surface interaction is much weaker than the intra molecular bonding in halogens. Here, we consider the system with the highest B.E. or the least total energy is most stable one. The fluorine adsorbed graphene- MoS_2 bilayer hetero-structure is most stable at the hollow site (C-Hollow) at the center of hexagon of the graphene sheet in the parallel configuration. But all the remaining halogen molecules adsorbed hetero-structures are obtained to be most stable while they are perpendicular to the sheet and above the sulphur atom of MoS_2 sheet (S-Top). The highest value of B.E. are 1.882 eV, 0.247 eV, 0.404 eV and 0.489 eV respectively for fluorine atom, Cl_2, Br_2 , and I_2 molecules adsorbed hetero-structures. The geometrical structures with the highest B.E. are considered to draw the various properties of the respective systems. In addition, the distance between two F-atoms increases when it is bound more strongly to MoS_2 sheet of graphene- MoS_2 bilayer hetero-structure. This result indicates that the bonding of F or F_2 with the substrate happens on the cost of weakening of F-F interaction. The adsorption geometries of molecular halogens (i.e. perpendicular and parallel orientations) above the graphene side of hetero-structure is shown in figure [3], while the optimized structures of different halogens on hetero-structure at the most stable occupation site are shown in figure [4].

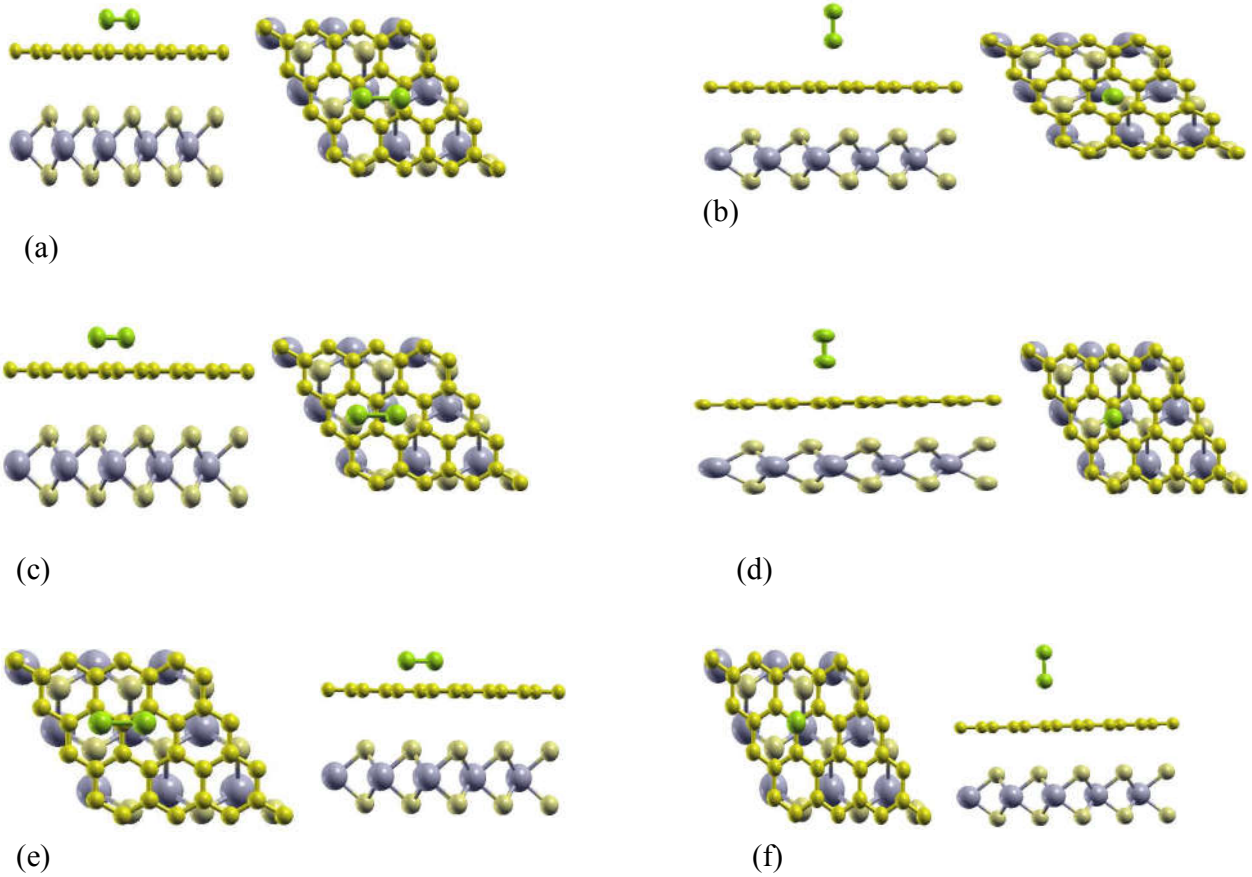

Figure 3: Top and Side view respectively for the adsorption of halogen molecules with different orientations of adsorbates in the direction parallel ((a), (c), (e)) and perpendicular (fig. (b), (d), (f)) to the graphene sheet. Figures (a) and (b) show the adsorption in C-Hollow (H) region, (c) and (d) at C-Bridge and (e) and (f) at C-Top, respectively.
Similarly, the adsorption of halogen molecules with different orientations of adsorbates in the parallel and perpendicular direction to the Mo $_2$ sheet are tested to know the most occupation site.

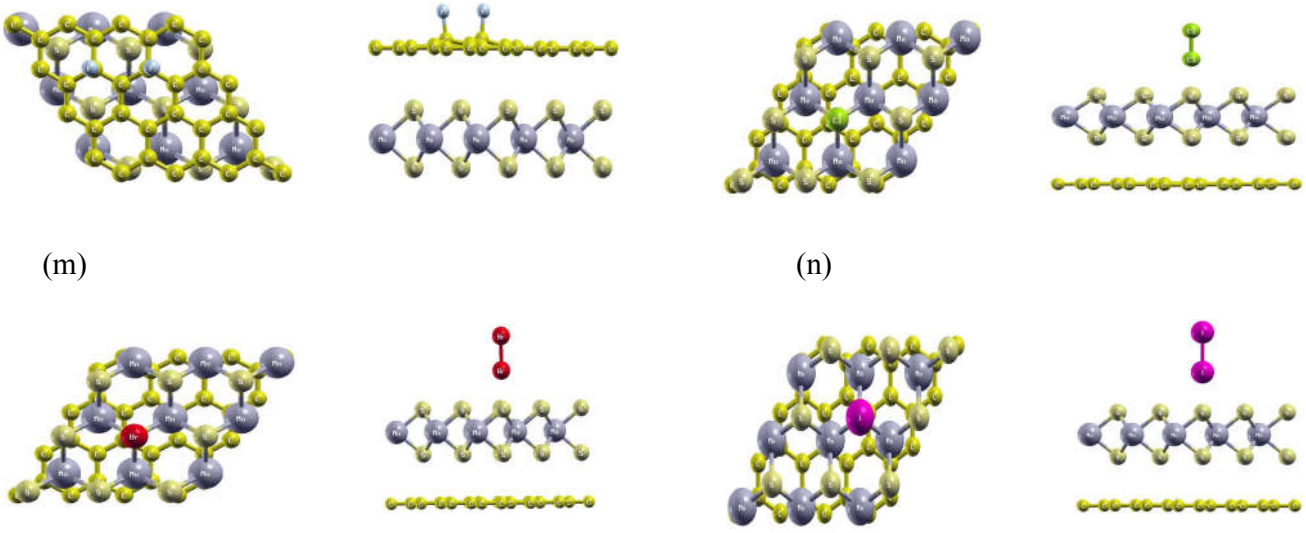

(m) (n)

(o) (p)

Figure 4: Optimized geometries of a halogen molecule adsorbed graphene-MoS_2 bilayer hetero-structure with top and side-view respectively. The figures, (m) fluorine atoms parallel to graphene plane at Hollow-site (C- hollow), (n) Cl_2 molecule perpendicular to MoS_2 plane at S-Top site (o) Br_2 molecule perpendicular to MoS_2 plane at S-Top site, (p) I_2 molecule perpendicular to MoS_2 plane at S-Top site.

3.2. Electronic structure calculations:

In order to understand the impact of adsorption of halogen molecules, we first need to understand the electronic properties of 3×3 sheet of MoS_2 monolayer as shown in figure [5(a)], 4×4 sheet of graphene as in figure [5(b)] and graphene-MoS_2 bilayer hetero-structure as in figure [5(c)]. Figure [5(a)] shows the band structure of 3×3 sheet of MoS_2 monolayer. Since, the conduction band minimum and valence band maximum lie at the same symmetric point, it is a direct band gap semiconductor with band gap of 1.65 eV. In case of 4×4 sheet of graphene, there is no band gap as conduction band and valence band coincides at Fermi level indicating that the graphene is a zero band gap semiconductor. Figure [5(c)] shows the band structure of graphene-MoS_2 bilayer hetero-structure. Here, the Dirac point shifts about 0.40 eV above the Fermi level which shows that the graphene-MoS_2 bilayer hetero-structure is metallic in nature. Afterwards, we have studied the effect of adsorption of halogen molecules on the hetero-structure along graphene plane and MoS_2 plane. The band structures of different systems are shown in figures [5(d)], [5(e)], [5(f)], and [(5(g).

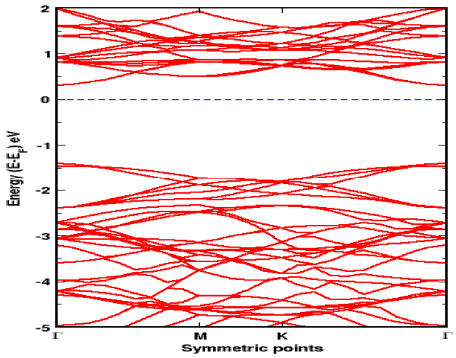
Energy (E-E$_F$) eV
Γ
M
K
Γ
Symmetric points

(a)

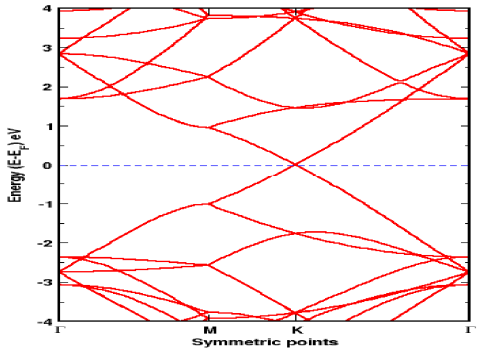
Energy (E-E$_F$) eV
Γ
M
K
Γ
Symmetric points

(b)

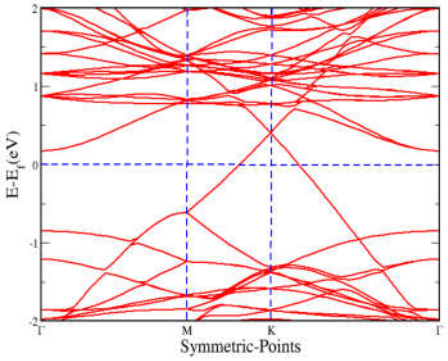
E-E$_F$ (eV)
Γ
M
K
Γ
Symmetric-Points

(c)

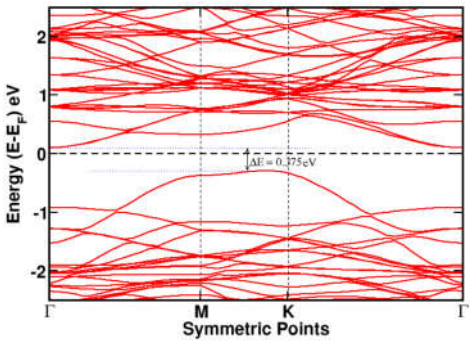
Energy (E-E$_F$) eV
ΔE = 0.375 eV
Γ
M
K
Γ
Symmetric Points

(d)

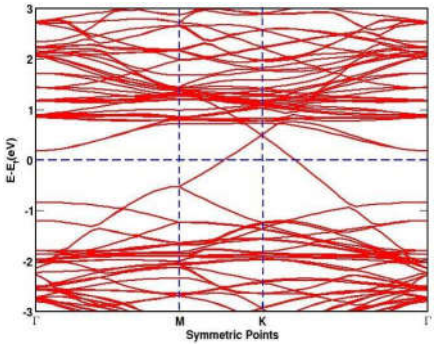
E-E$_F$(eV)
Γ
M
K
Γ
Symmetric Points

(e)

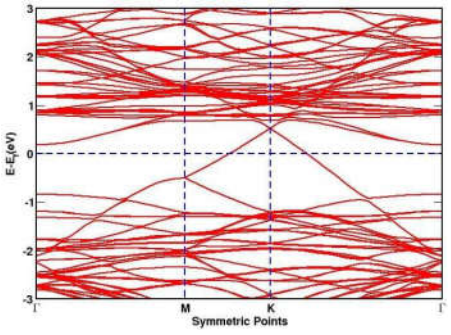
E-E$_F$(eV)
Γ
M
K
Γ
Symmetric Points

(f)

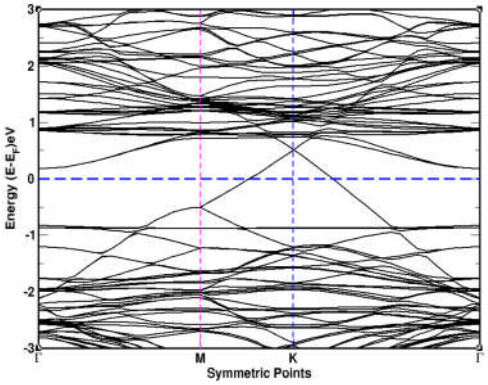

(g)

Figure 5: Band structures of (a) 3×3 sheet of MoS_2 monolayer (b) 4×4 sheet of graphene (c) graphene-MoS_2 bilayer (d) fluorine atoms (e) Cl_2 (f) Br_2 (g) I_2 molecule adsorbed graphene-MoS_2 bilayer hetero-structure.

The modifications in band structures is illustrated in table [3]:

Table 3: Electronic properties of halogen adsorbed Graphene/MoS2 system.

Optimized structure	Band Gap (eV)	Fermi Energy (eV)	Dirac Point(eV)	Dirac Shift (eV)
Graphene-MoS_2 bilayer	-	1.819	0.400	-
F_2-graphene MoS_2	0.375	1.174	-	-
Cl_2-graphene MoS_2	-	1.868	0.480	0.080
Br_2-graphene MoS_2	-	1.870	0.500	0.100
I_2-graphene MoS_2	-	1.996	0.520	0.120

From table [3], it is clearly seen that the band gap of 0.375 eV is found in the case of fluorine atoms adsorbed graphene-MoS_2 bilayer but in other halogen adsorbed bilayer, Dirac point shifted above the Fermi level. The formation of band gap in fluorine adsorbed system is due to the bonding and anti-bonding states of the electrons in the orbitals ans also due to band folding property of electrons in the orbitals. The band structures of other halogen adsorbed systems resembles the band structure of graphene-MoS_2 bilayer. The shift of Dirac point increases from Cl_2 to I_2 adsorbed graphene-MoS_2 bilayer. Also the Fermi energy is seen to be in the increasing order from Cl_2 to I_2 adsorbed graphene-MoS_2 bilayer. Since fluorine atom has the highest electronegative value among halogens, it could easily go for interaction in presence of other reacting species. This could be seen at the B.E. values in table [1]. Our results strongly show the favourable condition to absorb halogens particularly fluorine molecule in excited mode as done to store hydrogen molecule/s on metal decorated graphene [28]. Similarly, the magnetic properties of our system are studied with the help of information displayed by density of states (DOS) as shown in figure [6]

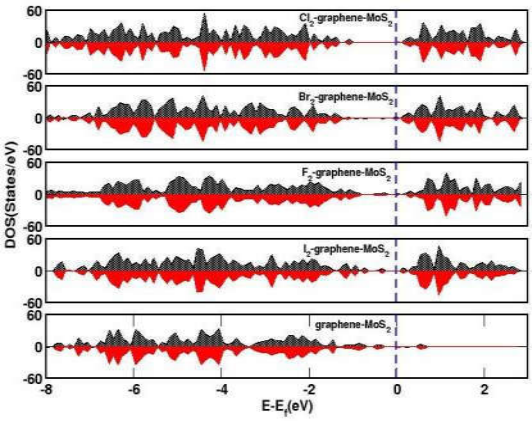

Figure 6: DOS of graphene- MoS_2 bilayer hetero-structure and halogen adsorbed graphene- MoS_2 bilayer hetero-structure. The curve above zero x-axis in each plot represents up-DOS, and that below the axis represents down-DOS.

The plot of DOS shows that both up-DOS and down-DOS are symmetrical about the axis in graphene-MoS_2 bilayer hetero-system as well as halogen molecules adsorbed bilayer hetero-structures. This means, the non magnetic nature of graphene-MoS_2 bilayer hetero-structure is still preserved with adsorption of halogens on it. From figure [6], it is clear that the DOS shift above the Fermi level due to adsorption of halogen molecules on hetero-structure.

4. Conclusions:

We have studied a first-principles study of geometrical and electronic properties of graphene-MoS_2 bilayer hetero-structure and halogen molecules adsorbed hetero-structures. The adsorption sites and orientations are tested to draw the most stable configurations. The fluorine atoms adsorbed system is stable at hollow site of hexagonal plane of graphene (C-Hollow) in parallel configuration with the binding energy 1.882 eV. The Cl_2 , B_2 and I_2 adsorbed hetero-structures all are most stable in the perpendicular configuration above the sulphur atoms of MoS_2 plane (S-Top) with binding energies 0.247 eV, 0.404 eV and 0.489 eV respectively. Band structure unalters in case of Cl_2 , B_2 and I_2 adsorbed graphene-MoS_2 bilayer hetero-structure but Dirac point shifts above the Fermi level. The band gap of 0.375 eV is found in fluorine atoms adsorbed hetero-structure. Our work suggests a way to tune the electronic properties of heterostructure with adsorption of halogens. We then analyzed DOS of respective systems and concluded that monolayer MoS_2 and halogen adsorbed system are non magnetic.

5. Acknowledgements:

The authors acknowledge to Swedish Research Links for partial support.

References

[1] Geim A K and Novoselov K S 2007 *Nature Materials* **6**, 183
[2] Novoselov K S, Geim A K, Morozov S V, Jiang D, Zhang Y, Dubonos S V Grigorieva I V and Firsov A A 2004 *Science* **306**, 666
[3] Zhang Y, Tan Y W, Stormer H L, Kim P, 2005 *Nature* **438**, 201
[4] Zhang Y, Jiang Z, Small J P, Purewal M S, Tan Y W, Fazlollahi M, Chudow J W, Jaszczak J A, Stormer H L and Kim P 2006 *Phys. Rev. Lett.* **96**, 136806
[5] Novoselov K S, Geim A K, Morozov S V, Jiang D, Katsnelson M I, Grigorieva I V, Dubonos S V and Firsov A A 2005 *Nature* **438**, 197
[6] Pak N, Hong S, Kim G and Jhi S H 2007 *J. AM. CHEM SOC.* **129**, 8999
[7] Lin Y, Jenkins M, Valdes-Garcia K A, Small A, Farmer J P, Avouris D P 2009 *Nano Lett*. **9**, 422
[8] Lamichhane S, Pantha N and Adhikari N P 2014 *BIBECHANA* **1**, 113
[9] Zanella, Fagan I, Mota S B and Fazzio R 2008 *A. J. Phys. Chem. C* **112,** 9163
[10] Butler S Z, Hollen S M, Cao L, et al., 2013 ACS *Nano* **7**, 2898
[11] Wilson J A and Yoffe A D 1969 *Adv. Phys.* **18**, 193
[12] Asl M G, Enyashin A N, Kuc A and Heine T 2013 *Phys. Rev. B* **88**, 245440
[13] Kadantsev E S, Hawrylak P 2012 *Sol. St. Comm*. **152,** 909
[14] Lembke D, Bertolazzi S and Kis A, 2015 *Acc. Chem. Res.* **1**, 48
[15] Zhang Y J, Ye J T, Matsuhashi Y and Iwasa Y 2012 *Nano Lett.* **12**, 1136
[16] Radisavljevic B, Whitwick M B and Kis A 2012 *Appl. Phys. Lett.* **101**, 043103
[17] Fornarini L, Stirpe F and Scrosati B 1981 Solar Energy Mater. **5**, 107
[18] Hu K H, Hu X G, Wang J, Xu Y F and Han C L 2012 Tribol. Lett. **47**, 79
[19] Debbichi L, Eriksson O and Lebegue S 2014 *Phys. Rev. B* **89**, 205311
[20] Gelb L D, Gubbins K E, Radhakrishnan R and Sliwinska-Bartkowiak M 1999 *Rep. Prog. Phys*. **62**, 1573
[21] Hohenberg P and Kohn W 1964 *Phys. Rev. B* **136**, 864
[22] Kohn W and Sham L J 1965 *Phys. Rev. B.* **140**, 1133
[23] Giannozzi P, Baroni S, Bonini N, Calandra M, Car R, Cavazzoni C, *et al*. 2009 *J. Phys., Condens. Matter* **21**, 395502
[24] Perdew J P, Burke K, Ernzerhof M 1996 *Phys. Rev. Lett.* **77**, 3865
[25] Grimme S 2004 *J. Comput. Chem.* **25**, 1463
[26] Grimme S 2006 *J. Comput. Chem.* **27**, 1787
[27] Rudenko A N, Keil F J, Katsnelson M I *et. al.* 2010 *Phys. Rev. B.* **82**, 035427
[28] Pantha N, Khaniya A, Adhikari N P 2015 *International Journal of Modern Physics B* **29**, 1550143

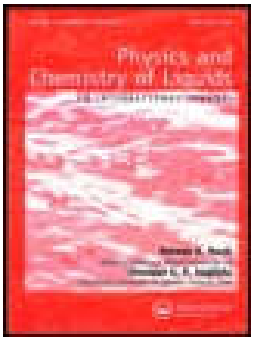

Taylor & Francis
Taylor & Francis Group

Physics and Chemistry of Liquids
An International Journal

ISSN: 0031-9104 (Print) 1029-0451 (Online) Journal homepage: http://www.tandfonline.com/loi/gpch20

Mixing behaviour of Ni–Al melt at 1873 K

S. K. Yadav, S. Lamichhane, L. N. Jha, N. P. Adhikari & D. Adhikari

To cite this article: S. K. Yadav, S. Lamichhane, L. N. Jha, N. P. Adhikari & D. Adhikari (2015): Mixing behaviour of Ni–Al melt at 1873 K, Physics and Chemistry of Liquids, DOI: 10.1080/00319104.2015.1095640

To link to this article: http://dx.doi.org/10.1080/00319104.2015.1095640

PHYSICS AND CHEMISTRY OF LIQUIDS, 2015
http://dx.doi.org/10.1080/00319104.2015.1095640

Taylor & Francis
Taylor & Francis Group

Mixing behaviour of Ni–Al melt at 1873 K

S. K. Yadav[a,b], S. Lamichhane[a], L. N. Jha[a], N. P. Adhikari[a] and D. Adhikari[b]

[a]Central Department of Physics, Tribhuvan University, Kirtipur, Nepal; [b]Department of Physics, Mahendra Morang Adarsh Multiple Campus, Tribhuvan University, Biratnagar, Nepal

ABSTRACT

Regular associated solution model and quasi-lattice model have been employed to study the thermodynamic and microscopic properties of Ni–Al liquid alloy at 1873 K. In thermodynamic properties, we have estimated free energy of mixing (G_M), enthalpy of mixing (H_M) and entropy of mixing (S_M), and in microscopic structural properties, we have studied concentration fluctuation in long wave length limit ($S_{CC}(0)$) and Warren–Cowely short-range-order parameters (α_1). Additionally, transport properties, such as ratio of mutual and intrinsic diffusion coefficients (D_M/D_{id}) and the viscosity of Ni–Al melt at 1873 K have been computed using different approaches.

ARTICLE HISTORY
Received 10 July 2015
Accepted 26 August 2015

KEYWORDS
Ni–Al liquid alloy; mole fractions; transport properties; super alloys.

1. Introduction

Nickel when alloyed with aluminium, chromium, cobalt, titanium, rhenium, ruthenium and other elements forms super alloys. Ni-based super alloys can tolerate adverse environments as they exhibit high temperature resistance, corrosion resistance and acid resistance.[1] As a result, they form ideal materials for the use in pumps, valves, piping systems, process equipment and assemblies in the marine, chemical processing, nuclear reactors, oil and gas, aerospace, turbines and military industries.[1] Their high operating temperatures and higher efficiency in gas turbines and jet engines can reduce carbon dioxide emission which will retard the rate of climate change. Among the Ni-based super alloys, Ni–Al alloy have desirable properties, such as high melting temperature, low density, good oxidation resistance, corrosion resistance, high thermal conductivity, attractive modulus elasticity, metal-like properties above a modest ductile-to-brittle transition temperature, accessible and affordable costs.[1] The low density of Ni–Al alloys attributed to significant reduction in the weight of turbine blades, discs and aircraft parts. Its high thermal conductivity enhances the cooling efficiency, reduction in air foil temperatures and thermal gradients.[2,3] These noble properties of Ni–Al alloy have attracted the most modern consent of the researches to study and predict the thermodynamic, structural and transport properties of Ni–Al liquid alloys.

Studying the properties of alloys in liquid state provides some unique information that can be used to improve the processing and qualities of materials in the solid state. But the experimental study of the thermo-physical properties of alloys in molten state is a difficult task because of the difficulties caused by high temperature, chemical reactivity, crystallisation triggered by the walls of the container, etc. [4]. Therefore, several theoretical models have been proposed to investigate the thermodynamic, structural [5–13] and transport [14–16] properties of alloys in liquid state. In this work, we have used regular associated solution model [17–19] and quasi-lattice model [20–22] to

CONTACT D. Adhikari adksbdev@yahoo.com

study the thermodynamic and microscopic properties, and different approaches [15,16] to study the transport properties of Ni–Al alloy in liquid state at 1873 K.

Formation of the chemical complexes in the liquid state of the binary solution is assumed in both of these models. According to the regular associated solution model, when atoms of the type A (= Ni) and B (= Al) are mixed in liquid state near their melting points, there is tendency of associations among A, B; A, A and B, B. The regular solution is thus treated as the ternary mixtures of the complex (A–B) and the unassociated atoms (A and B). These associations are named as, 'complexes', 'pseudomolecules', 'clusters' or 'associations'.[17,18] The expressions for different thermodynamic and microscopic functions are derived by assuming unequal interactions among the associated and unassociated atoms. However, in quasi-lattice model, the expressions of these properties are obtained by assuming the grand partition functions for the clusters of two lattice sites.[13,20] The phase diagram of Ni–Al alloys [23] shows the existence of different phases, such as ε, 'Al_3Ni' having an orthorhombic structure isotropic with CFe_3; δ, 'Al_3Ni_2' having an ordered trigonal prototype structure; β′, 'AlNi' having an ordered bcc structure isotropic with C_3Cl; α′, 'Al_3Ni_5' having an orthorhombic structure isotropic with Ga_3Pt_5; α″, '$AlNi_3$' having an ordered fcc (Li2) structure isotropic with $AuCu_3$. Among these phases, we have assumed the existence of Ni_3Al complex in the liquid state and estimated its thermodynamic and microscopic properties on the basis of regular associated solution model and quasi-lattice model at 1873 K. The viscosity of the respective alloy has been studied using three different approaches, such as Moelwyn–Hughes approach, Kozlov equation and simple statistical approach.

2. Formalism

2.1. *Regular associated solution model*

Consider a mole of binary liquid solution having n_1 atoms of monomer A (= Ni) and n_2 atoms of monomer B (= Al) of the form A–B. According to Lele and Ramchandrarao,[17] it is assumed that the chemical complexes $A_\mu B$ ($A_\mu B \Leftrightarrow \mu A + B$) exists in the initial melt, where μ = 3 is a small integer whose value is determined from the compound forming concentration (= μ/(μ +1)) in the solid state. The liquid mixture thus can be considered as the ternary mixtures of free atoms A and B and the complex $A_\mu B$. Let n_A, n_B and $n_{A_\mu B}$ moles are the respective concentrations of free atoms A, B and the complex $A_\mu B$ in the melt. Then according to the conservation of mass, the formation of the complex $A_\mu B$ in the partially associated solution requires $n_1 = n_A + \mu n_{A_\mu B}$ and $n_2 = n_B + n_{A_\mu B}$. But the thermodynamic and microscopic structural behaviours of the complexes in the melt are governed by their true mole fractions x_A, x_B and $x_{A_\mu B}$ rather than their gross mole fractions x_1 and x_2, where $x_1 = n_1/(n_1 + n_2)$, $x_2 = n_2/(n_1 + n_2)$, $x_A = n_A/(n_A + n_B + n_{A_\mu B})$, $x_B = n_B/(n_A + n_B + n_{A_\mu B})$ and $x_{A_\mu B} = n_{A_\mu B}/(n_A + n_B + n_{A_\mu B})$.

Using the above expressions, the relation between the true and gross mole fractions can be derived as

$$x_A = x_1 - \mu x_2 x_{A_\mu B} \text{ and } x_B = x_2 - (1 - \mu x_2) x_{A_\mu B} \tag{1}$$

According to the regular associated solution model, it is assumed that the gross chemical potentials of the components 1 and 2 are equal to the chemical potentials of the free monomers A and B.[24] According to Jordan,[18] the activity coefficients of monomers γ_A, γ_B and that of complex $\gamma_{A_\mu B}$ can be represented in terms of pairwise interaction energies as

$$RT \ln\gamma_A = x_B^2 \omega_{12} + x_{A_\mu B}^2 \omega_{13} + x_B x_{A_\mu B} (\omega_{12} - \omega_{23} + \omega_{13}) \tag{2a}$$

$$RT \ln\gamma_B = x_{A_\mu B}^2 \omega_{23} + x_A^2 \omega_{12} + x_A x_{A_\mu B} (\omega_{23} - \omega_{13} + \omega_{12}) \tag{2b}$$

$$RT\ \ln\gamma_{A_\mu B} = x_A^2\ \omega_{13} + x_B^2\ \omega_{23} + x_A x_B\ (\omega_{13} - \omega_{12} + \omega_{23}) \tag{2c}$$

where ω_{12}, ω_{13} and ω_{23} represent the pairwise interaction energies for the species A, B; A, $A_\mu B$ and B, $A_\mu B$, respectively. T and R represent temperature and universal real gas constant, respectively.

The equilibrium constant k for the reaction $A_\mu B \Leftrightarrow \mu A + B$ can be expressed in terms of mole fraction and activity coefficients as

$$k = \frac{x_A^\mu x_B \gamma_A^\mu \gamma_B}{x_{A_\mu B}\gamma_{A_\mu B}} \tag{3}$$

Solving Equations (2) and (3), the relation for the equilibrium constant can be obtained as

$$\begin{aligned} \ln k = \ln\left(\frac{x_A^\mu x_B}{x_{A_\mu B}}\right) + \frac{\omega_{12}}{RT} + \frac{\omega_{12}}{RT}\left[\mu x_B(1 - x_A) + x_A\right] + \frac{\omega_{13}}{RT}\left[\mu x_{A_\mu B}(1 - x_A) - x_A\right] \\ + \frac{\omega_{23}}{RT}\left[x_{A_\mu B}(1 - \mu x_B) - x_B\right] \end{aligned} \tag{4}$$

and the free energy of mixing (G_M) is given as [17]

$$\begin{aligned} G_M = \frac{1}{1 + \mu x_{A_\mu B}} RT\Big[\left(x_A x_B \frac{\omega_{12}}{RT} + x_A x_{A_\mu B}\frac{\omega_{13}}{RT} + x_B x_{A_\mu B}\frac{\omega_{23}}{RT}\right) \\ + (x_A \ln X_A + x_B \ln X_B + x_{A_\mu B}\ln X_{A_\mu B}) + x_{A_\mu B}\ln k\Big] \end{aligned} \tag{5}$$

The other thermodynamic functions, such as heat of mixing (H_M), entropy of mixing (S_M) and concentration fluctuation in the long wavelength limit (S_{CC} (0)), are related with free energy of mixing (G_M) by the following standard thermodynamic relations:

$$H_M = G_M - T\left(\frac{\partial G_M}{\partial T}\right)_P \tag{6a}$$

$$S_M = \frac{H_M - G_M}{T} \tag{6b}$$

$$S_{CC}(0) = RT\left(\frac{\partial^2 G_M}{\partial x_1^2}\right)_{T,P}^{-1} \tag{6c}$$

$$S_{CC}(0) = x_2\alpha_1\left(\frac{\partial \alpha_1}{\partial x_1}\right)_{T,P}^{-1} = x_1\alpha_2\left(\frac{\partial \alpha_2}{\partial x_2}\right)_{T,P}^{-1} \tag{6d}$$

Using Equation (5) in Equation (6a), the expression for the enthalpy of mixing can be obtained as

$$\begin{aligned} H_M = \frac{1}{1 + \mu x_{A_\mu B}}\Big[\left(x_A x_B \omega_{12} + x_A x_{A_\mu B}\omega_{13} + x_B x_{A_\mu B}\omega_{23}\right) \\ - T\left(x_A x_B \frac{\partial \omega_{12}}{\partial T} + x_A x_{A_\mu B}\frac{\partial \omega_{13}}{\partial T} + x_B x_{A_\mu B}\frac{\partial \omega_{23}}{\partial T}\right) - x_{A_\mu B} RT^2 \frac{d\ln k}{dT}\Big] \end{aligned} \tag{7}$$

The expression for the concentration fluctuation in the long-wavelength limit ($S_{CC}(0)$) can be obtained by using Equation (5) in Equations (6c) and (6d) as

$$S_{CC}(0) = 1/\left[\left(\frac{1}{1 + \mu x_{A_\mu B}}\right)\left\{\frac{2}{RT}\left(x_A' x_B' w_{12} + x_A' x_{A_\mu B}' w_{13} + x_B' x_{A_\mu B}' w_{23}\right) + \left(\frac{x_A'^2}{x_A} + \frac{x_B'^2}{x_B} + \frac{x_{A_\mu B}'^2}{x_{A_\mu B}}\right)\right\}\right] \tag{8}$$

Here, $\frac{\partial^2 G_M}{\partial x_1^2} > 0$ for $\frac{\partial G_M}{\partial x_1} = 0$. The prime denotes the differentiations with respect to concentrations, and $x_A^{'}$ and $x_B^{'}$ are obtained by using Equation (1). $x_{A_\mu B}^{'}$ is obtained using Equation (4) with the condition $\frac{d\ln k}{dx_1} = 0$.[9,19]

The concentration fluctuation in long wavelength limit (S_{CC} (0)) has been developed as an important tool to understand the nature of atomic ordering in the binary liquid alloys. At a given concentration, if $S_{CC}(0) < S_{CC}^{id}$ (0), then ordering (unlike atoms pairing) is expected and if S_{CC} (0) > S_{CC}^{id} (0), then segregation (like atoms pairing) is expected, where $S_{CC}^{id}(0) = x_1 x_2$. The experimental values of $S_{CC}(0)$ can be obtained from Equation (6d).[26,27]

The degree of local ordering in such liquid systems can be studied by estimating Warren–Cowley short-range-order parameter (α_1) with the knowledge of ($S_{CC}(0)$).[25–27] The expression for α_1 in terms of $S_{CC}(0)$ is given as

$$\alpha_1 = \frac{S-1}{S(Z-1)+1} \text{where}, S = \frac{S_{CC}(0)}{S_{CC}^{id}(0)} \text{ and } S_{CC}^{id}(0) = x_1 x_2 \tag{9}$$

where Z is the coordination number and Z = 10 is taken for our calculation. We note that varying the value of Z doesn't have any effect on the position of the minima of α_1; the effect is to vary the depth while the overall features remain unchanged.

The pairwise interaction energies and the mole fractions of the complexes can be estimated as follows:

On solving Equations (2a) and (2b), we obtain

$$\frac{\omega_{13}}{RT} = \frac{x_B \ln\left(\frac{\alpha_2}{x_B}\right) + (1-x_B)\ln\left(\frac{\alpha_1}{x_A}\right) - x_B(1-x_B)\frac{\omega_{12}}{RT}}{x_{A_\mu B}^2} \tag{10a}$$

$$\frac{\omega_{23}}{RT} = \frac{x_A \ln\left(\frac{\alpha_1}{x_A}\right) + (1-x_A)\ln\left(\frac{\alpha_2}{x_B}\right) - x_A(1-x_A)\frac{\omega_{12}}{RT}}{x_{A_\mu B}^2} \tag{10b}$$

where $\alpha_1 = x_1\gamma_1$ and $\alpha_2 = x_2\gamma_2$ are activities of components 1 and 2, respectively.

The pairwise interaction energies, the equilibrium constants and the activity coefficients at infinite dilution can be related as [17]

$$\ln \gamma_1^0 = \frac{\omega_{12}}{RT} \tag{11a}$$

$$k \exp\left(\frac{\omega_{13}}{RT}\right) = \left(\frac{\gamma_1^0 \gamma_2^0}{\gamma_1^0 - \gamma_2^0}\right) \tag{11b}$$

On solving Equations (4), (10) and (11), we obtain

$$\ln k + \frac{\omega_{13}}{RT} = \left(\frac{1+x_A}{x_{A_\mu B}}\right)\ln\left(\frac{\alpha_1}{x_A}\right) + \frac{x_B}{x_{A_\mu B}}\left[\ln\left(\frac{\alpha_1}{x_A}\right) - \frac{\omega_{12}}{RT}\right] + \ln\left(\frac{a_1^\mu a_2}{x_{A_\mu B}}\right) \tag{12}$$

2.2. *Quasi-lattice model*

Let one mole of binary liquid alloys A–B having preferable chemical complex of the form $x_{A_\mu B_\vartheta}$(where A = Ni, B = Al, μ = 3 and ϑ = 1) among the constituent species. The expression for excess free energy of mixing (G_M^{xs}) then can be given by [20,25,26]

$$G_M^{xs} = Nk_BT\left[x_1 x_2 \frac{\omega}{k_BT} + \phi_{AB}\frac{\Delta\omega_{AB}}{k_BT} + \phi_{AA}\frac{\Delta\omega_{AA}}{k_BT} + \phi_{BB}\frac{\Delta\omega_{BB}}{k_BT}\right] \tag{13}$$

where N is Avogadro's number, k_B is Boltzmann constant, T is temperature and ω's are the ordering energies. $x_1 (= C_{Ni})$ is the concentration of A, x_2 (=1−x_1 = C_{Al}) is the concentration of B and ϕ_{ij} (i, j = A, B) are the simple polynomials in x depending upon μ. The ordering energy coefficient $\Delta\omega_{AA} = 0$, if μ = 1 and the ordering energy coefficient $\Delta\omega_{BB} = 0$, if $\vartheta = 1$. For the Ni_3Al liquid binary alloy, the values of ϕ's are expressed as [20,25]

$$\phi_{AB} = \frac{1}{5}x_1 + \frac{2}{3}{x_1}^3 - {x_1}^4 - \frac{1}{5}{x_1}^5 + \frac{1}{3}{x_1}^6 \tag{14a}$$

$$\phi_{AA} = -\frac{3}{20}x_1 + \frac{2}{3}{x_1}^3 - \frac{3}{4}{x_1}^4 + \frac{2}{5}{x_1}^5 - \frac{1}{6}{x_1}^6 \tag{14b}$$

$$\phi_{BB} = 0 \tag{14c}$$

The free energy of mixing (G_M) can be expressed in terms of excess free energy of mixing (G_M^{xs}) by

$$G_M = G_M^{xs} + RT(x_1 \ln x_1 + x_2 \ln x_2) \tag{15}$$

The excess entropy of mixing (S_M^{xs}) is related to G_M^{xs} with the standard thermodynamic relation

$$S_M^{xs} = -\left(\frac{\partial G_M^{xs}}{\partial T}\right)_P \tag{16a}$$

Using Equation (13) in Equation (16a) yields

$$S_M^{xs} = -Nk_B\left(\frac{1}{k_B}\frac{\partial\omega}{\partial T}x_1x_2 + \frac{1}{k_B}\frac{\partial(\Delta\omega_{AB})}{\partial T}\phi_{AB} + \frac{1}{k_B}\frac{\partial(\Delta\omega_{AA})}{\partial T}\phi_{AA} + \frac{1}{k_B}\frac{\partial(\Delta\omega_{BB})}{\partial T}\phi_{BB}\right) \tag{16b}$$

The theoretical values of entropy of mixing then can be expressed as

$$S_M = S_M^{xs} - R(x_1 \ln x_1 + x_2 \ln x_2) \tag{16c}$$

The enthalpy of mixing can be expressed in terms of G_M^{xs} and S_M^{xs} by using Equations (13) and (16b) as follows

$$H_M = G_M^{xs} + TS_M^{xs} \tag{17}$$

Theoretical and the experimental values of $S_{CC}(0)$ can be, respectively, expressed in terms of G_M and the activity as

$$S_{CC}(0) = Nk_BT\left(\frac{\partial^2 G_M}{\partial x_1^2}\right)^{-1}_{T,P,N} \tag{18a}$$

$$S_{CC}(0) = x_2\left(\frac{\partial a_A}{\partial x_1}\right)^{-1}_{T,P,N} = x_1\left(\frac{\partial a_B}{\partial x_2}\right)^{-1}_{T,P,N} \tag{18b}$$

where a_A and a_B are the activities of monomers A and B, respectively.

The expression for the theoretical values of $S_{CC}(0)$ thus can be yielded by using Equation (15) in Equation (18a) as

$$S_{CC}(0) = \frac{x_1x_2}{1 + x_1x_2\left[\frac{-2\omega}{k_BT} + \frac{\Delta\omega_{AB}}{k_BT}\phi''_{AB} + \frac{\Delta\omega_{AA}}{k_BT}\phi''_{AA} + \frac{\Delta\omega_{BB}}{k_BT}\phi''_{BB}\right]} \tag{19}$$

where $\phi''_{ij} = \frac{\partial^2\phi_{ij}}{\partial x^2}$ (i, j = A, B).

The ideal values of $S_{CC}(0)$ and short-range-order parameter (α_1) can be obtained by following the similar procedures as regular associated solution model.

2.3. *Transport properties*

The greater insight in the properties of an alloy in liquid state can be done by evaluating transport properties, such as diffusion coefficients and viscosity of the alloy. The ratio of mutual and intrinsic diffusion coefficients is expressed in terms of $S_{CC}(0)$ by using Darken thermodynamic Equation [27,28] as

$$\frac{D_M}{D_{id}} = \frac{x_1 x_2}{S_{CC}(0)} \tag{20}$$

where D_M stands for the chemical or mutual diffusion coefficient and D_{id} stands for the intrinsic diffusion coefficient for an ideal mixture which are related as [20,27]

$$D_M = D_{id}\frac{\partial \ln a_A}{\partial x_1}, \text{ with } D_M = x_1 D_B + x_2 D_A \tag{21}$$

where D_A and D_B are the self-diffusion coefficient of pure components A and B, respectively.

The viscosity of an alloy in the liquid state can be studied by using different approaches. The Moelwyn–Hughes approach for the study of viscosity of liquid mixture is based on fact that the viscous flow becomes more difficult when the cohesion energy of the alloy is increased and at a temperature T, it is given as [16]

$$\eta = (x_1\eta_1 + x_2\eta_2)\left(1 - \frac{2x_1 x_2 H_M}{RT}\right) \tag{22}$$

where η is the viscosity of the alloy, η_k(k = 1,2) is the viscosity of the pure components Ni and Al, respectively. For most metals the variation of viscosity, η_k with temperature T may be expressed as [27,29]

$$\eta_k = \eta_{ok}\ \exp\left(E/RT\right) \tag{23}$$

where η_{ok} and E are constants for pure metal, in units of viscosity and energy per mole, respectively.

The another approach for the study of viscosity of binary mixture has been derived in a theoretical way with the correlation in semi-logarithmic coordinates, which is known as the Kozlov equation and is given as [14]

$$\ln\eta = x_1 \ln\eta_1 + x_2 \ln\eta_2 - H_M/3RT \tag{24}$$

where the symbols have the same meanings as those in Equation (22).

For the computation of viscosity, a simple statistical approach [27,29] can also be used as

$$\eta = \eta_{id}[(1 - x_1 x_2)(2\omega/k_B T)] \tag{25}$$

where ω is, as usual, the interchange energy or order energy given by quasi lattice theory.

3. Results and discussion

3.1. *Thermodynamic properties*

The model parameters of regular associated solution model ω_{12}/RT and $\ln k + \omega_{13}/RT$ for Ni–Al liquid alloy at 1873 K are first determined by using Equations (11a) and (11b), respectively, with the help of observed values of activity coefficients at infinite dilutions.[23] The mole fractions of the complex $x_{A_\mu B}$ (= x_{Ni_3Al}) are then estimated from Equation (12) and the observed values of activities [23] throughout the entire concentrations by iterative procedure. The true mole fractions

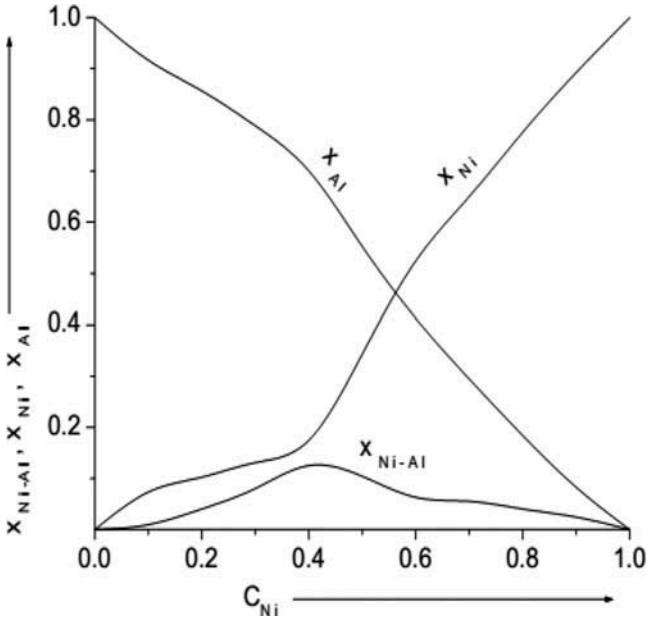

Figure 1. Mole fractions of the complex (x_{Ni-Al}) and unassociated atoms (x_{Ni} and x_{Al}) *vs.* concentrations of Ni (C_{Ni}) of Ni–Al liquid alloy at 1873 K.

of the free monomers x_A (= x_{Ni}) and x_B (= x_{Al}) are obtained from Equation (1) with the aid of determined values of $x_{A_\mu B}$. Figure 1 shows the compositional dependence of the mole fractions of the complex and free monomers. Theoretically, it is found that the maximum association of the complex occurs at $C_{Ni} = 0.424$, and at this composition, about 12.64 mole % of liquid alloy is associated. The knowledge of mole fractions of the free monomers and the complex can be obtained only by using regular associated solution model but not by quasi-lattice model.

The pairwise interaction energies ω_{12}/RT, ω_{13}/RT and ω_{23}/RT, and the equilibrium constants k for regular associated solution model are then computed from Equations (10), (11) and (5) by the successive approximation to explain the experimental values of free energy of mixing.[23] The best fit values so obtained are found to be

$$\frac{\omega_{12}}{RT} = -6.65,$$
$$\frac{\omega_{13}}{RT} = -4.01,$$
$$\frac{\omega_{23}}{RT} = -20.5$$

and

$$k = 0.267$$

All the interaction energy parameters of regular associated solution model are found to be negative. The negative value of ω_{12}/RT indicates that the atoms of Ni and Al are attracted towards each other in the liquid state whereas the negative values of ω_{13}/RT and ω_{23}/RT, respectively, indicate that both the atoms of Ni and Al are attracted towards the complex Ni_3Al in the liquid state.

The energy parameters of the alloy for quasi-lattice model have been obtained by using Equation (13) and the experimental values of integral excess free energy of mixing [23] by successive approximation. The best fit values are found to be

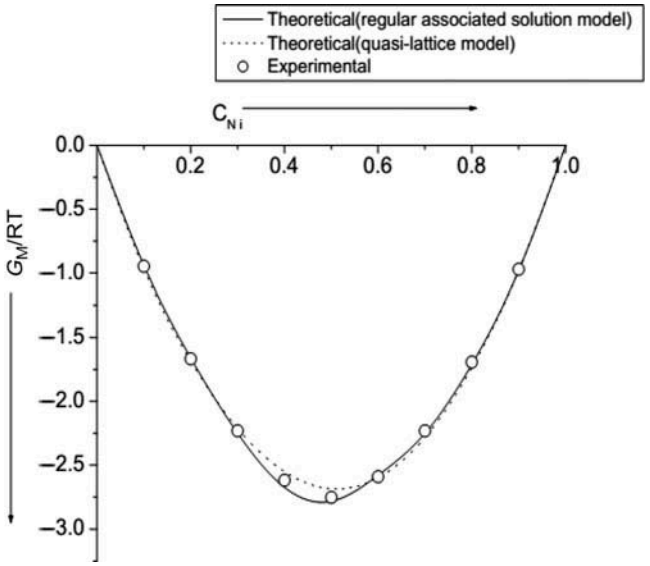

Figure 2. Free energy of mixing (G_M/RT) *vs.* concentrations of Ni (C_{Ni}) of Ni–Al liquid alloy at 1873 K.

$$\frac{\omega}{k_B T} = -3.91,\ \frac{\Delta\omega_{AB}}{k_B T} = -5.53,\ \frac{\Delta\omega_{AA}}{k_B T} = 12.25,\ \frac{\Delta\omega_{BB}}{k_B T} = 0$$

The negative values of the ordering energy parameters ω/k_BT and ω_{AB}/k_BT indicate that the Ni–Al melt is ordered in the liquid state. But the positive values of ω_{AA}/k_BT indicates that there is weak interaction among the Ni atoms in the liquid state.

These model parameters are then utilised to estimate the theoretical values of the free energy of mixing from Equation (5) for regular associated solution model and from Equations (13) and (15) for quasi-lattice model. The compositional dependence of the theoretical and the experimental values G_M/RT obtained from both of the models are shown in Figure 2. The theoretical as well as the experimental values of G_M/RT are found to be minimum at $C_{Ni} = 0.5$ (the theoretical value of $\frac{G_M}{RT} = -2.78259$ from regular associated solution model whereas $\frac{G_M}{RT} = -2.68540$ from quasi-lattice model and the experimental value of $\frac{G_M}{RT} = -2.75223 \pm 0.513739$ [23]). Both the theoretical (obtained from regular associated solution model) and the observed values of the free energy of mixing are in well agreement (Figure 2). The theoretical values of G_M/RT (obtained from quasi-lattice model) differ slightly from the observed values near equiatomic composition and are in good agreement (Figure 2) in rest of the compositions. Thus, regular associated solution model better explains the free energy of mixing of the Ni–Al liquid alloy than that by quasi-lattice model. The minimum values of G_M/RT are high negative (theoretical as well as experimental) in the liquid state near the melting temperature. The Ni–Al liquid alloy at 1873 K is thus found to be highly interacting system. As this minimum value lies at equiatomic composition, this system is symmetric in the liquid state.

The interaction energy parameters are assumed to be temperature dependent in case of regular associated solution model. If they are assumed to be independent of temperature, then $\frac{\partial\omega}{\partial T} = 0$ and the expression for the enthalpy of mixing would eventually become

$$H_M = \frac{1}{1 + \mu x_{A_\mu B}}\left[\left(x_A x_B \omega_{12} + x_A x_{A_\mu B}\omega_{13} + x_B x_{A_\mu B}\omega_{23}\right) - x_{A_\mu B} RT^2 \frac{d\ln k}{dT}\right]$$

The enthalpy of mixing then can be computed with the help of the interaction energy parameters and $RT^2 \frac{d\ln k}{dT}$. The values of H_M and S_M so obtained are found to have poor agreement with the

observed values. It thus clarifies the dependency of interaction energy parameters with the temperature.

The temperature-dependent model parameters of regular associated solution model are estimated by using Equation (7) and the observed values of H_M [23] by successive approximation. The best fit values of these parameters are found to be

$$\frac{\partial\omega_{12}}{\partial T} = +23.00\ \text{Jmol}^{-1}\text{K}^{-1},\ \frac{\partial\omega_{13}}{\partial T} = +54.01\ \text{Jmol}^{-1}\text{K}^{-1},$$
$$\frac{\partial\omega_{23}}{\partial T} = +51.00\ \text{Jmol}^{-1}\text{K}^{-1} \text{ and } RT^2\frac{d\ln k}{dT} = 69000 \pm 8900\ \text{Jmol}^{-1}$$

The temperature-dependent energy parameters of quasi-lattice model are obtained from Equation (16b) with the knowledge of the experimental values of integral excess entropy of mixing [23] by successive approximation. The best fit values so obtained are found to be

$$\frac{1}{k_B}\frac{\partial\omega}{\partial T} = +3.44, \frac{1}{k_B}\frac{\partial\Delta\omega_{AB}}{\partial T} = +3.31, \frac{1}{k_B}\frac{\partial\Delta\omega_{AA}}{\partial T} = +2.27, \frac{1}{k_B}\frac{\partial\Delta\omega_{BB}}{\partial T} = 0$$

The theoretical values of H_M/RT for regular associated solution model are obtained from Equation (7) and the theoretical values of entropy of mixing (S_M/R) for quasi-lattice model are calculated from Equations (16b) and (16c) with the aid of above-determined temperature-dependent energy parameters of the respective models. The theoretical values of H_M/RT for quasi-lattice model are then obtained from Equation (17) by using the above-determined integral excess value of the free energy of mixing and the entropy of mixing. The minimum values of the theoretical (for both of the models) as well as observed values of enthalpy of mixing lies at $C_{Ni} = 0.5$ (theoretical value of $\frac{H_M}{RT} = -3.12088$ from regular associated solution model, $\frac{H_M}{RT} = -3.18234$ from quasi-lattice model and observed value of $\frac{H_M}{RT} = -3.21106 \pm 0.0963260$ [23]). The theoretical values of H_M/RT obtained from regular associated solution model are in well agreement with the experimental values while the values obtained from quasi-lattice model deviate slightly from experimental values (Figure 3). This finding again clarifies

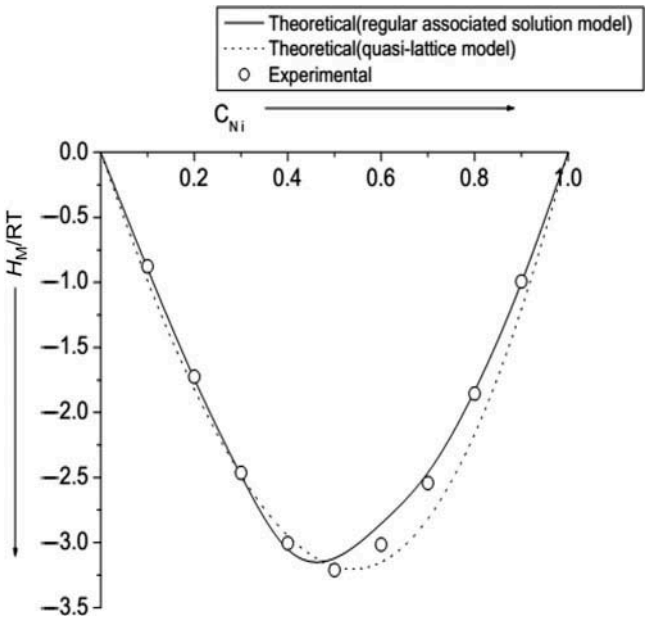

Figure 3. Heat of mixing (H_M/RT) *vs.* concentrations of Ni (C_{Ni}) of Ni–Al liquid alloy at 1873 K.

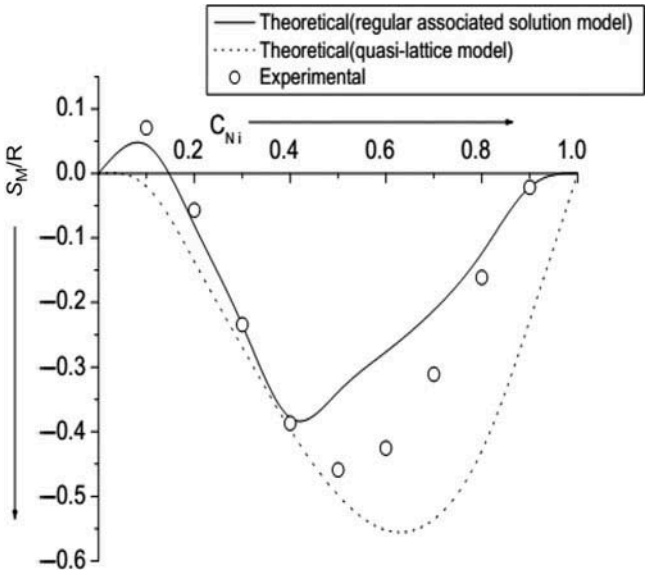

Figure 4. Entropy of mixing (S_M/R) *vs.* concentrations of Ni (C_{Ni}) of Ni–Al liquid alloy at 1873 K.

that regular associated solution model better explains the enthalpy of mixing of Ni–Al liquid alloy than that by quasi-lattice model.

All the temperature-dependent parameters of both of the models are found to have positive values. The enthalpy of mixing has high negative values, which reveals that the bonding among the complex and the atoms is stronger.

The theoretical values of S_M/R for the regular associated solution model are obtained from Equation (6b) with the help of the theoretically determined values of G_M and H_M, whereas the theoretical values of S_M/R for quasi-lattice model are obtained from Equation (16c). Both the theoretical and the observed values of S_M/R (for both of the models) are found to be in reasonable agreement (Figure 4). The computed (from regular associated solution model) and the observed [23] values of entropy of mixing are found to be positive at $C_{Ni} = 0.1$, which indicates that the Ni–Al liquid alloy is less ordered at this composition whereas the computed value of entropy of mixing from quasi-lattice model is found to be slight negative at $C_{Ni} = 0.1$, which suggests that the alloy is more ordered at this composition. These values obtained from both of the models are found to be negative at all other compositions from $C_{Ni} = 0.2$ to 0.9 indicating that the alloy is ordered at these compositions, which is in accordance with the experimental values. The theoretical values of S_M/R predicted by regular associated solution model are more close to the experimental values than that predicted by quasi-lattice model. The theoretical investigations thus reveal that regular associated solution model is more appropriate in explaining the thermodynamics of the Ni–Al liquid alloy at 1873 K than that of quasi-lattice model.

3.2. *Microscopic structural properties*

The estimation of the concentration fluctuation in long wave length ($S_{CC}(0)$) gives the greater insight of the microscopic structural properties of the liquid alloys. The theoretical and the experimental values of $S_{CC}(0)$ are computed from Equations (8) and (6d), respectively, for regular associated solution model, whereas from Equations (19) and (18b), respectively, for quasi-lattice model using the same values of the model parameters as used for the thermodynamic functions. The ideal values of $S_{CC}(0)$ are computed from Equation (9). The theoretical as well as the

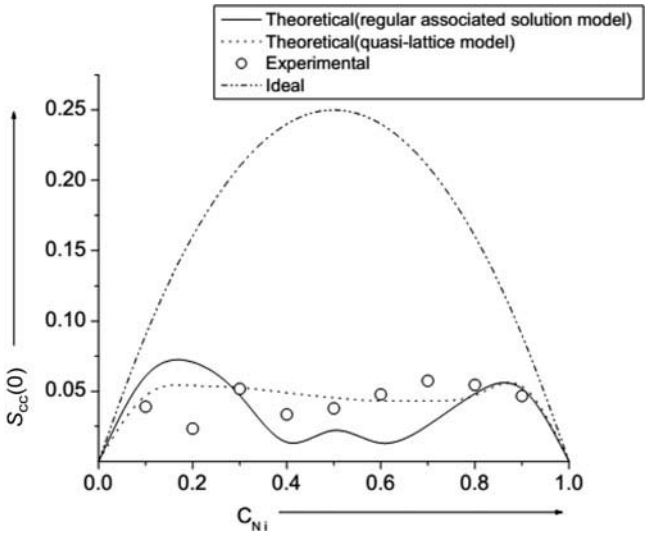

Figure 5. Concentration fluctuation in long-wavelength limit ($S_{CC}(0)$) *vs.* the concentration of Ni (C_{Ni}) of Ni–Al liquid alloy at 1873 K.

experimental values of $S_{CC}(0)$ are found to be less than the ideal values at all compositions (Figure 5). At a given concentration, if $S_{CC}(0) < S^{id}_{CC}(0)$, then ordering (unlike atoms pairing) is expected, and if $S_{CC}(0) > S^{id}_{CC}(0)$, then segregation (like atoms pairing) is expected, where $S^{id}_{CC}(0) = x_1x_2$. This indicates that the Ni–Al liquid alloy at 1873 K is hetero-coordinating (ordering) in nature. Thus there is no demixing in the solid state. The theoretical and the experimental values $S_{CC}(0)$ are found to be reasonable agreement (Figure 5). The theoretical values of $S_{CC}(0)$ are depressed at $C_{Ni} = 0.4$ and 0.6, which indicates that complexes corresponding to these compositions may be the stable complexes (Figure 5). The theoretical values of $S_{CC}(0)$ obtained from regular associated solution model are more in accordance with the experimental values than that obtained from quasi-lattice model.

Though the alloys have multidisciplinary uses in the solid state, they are generally grown from the liquid state. The liquid state is eventually a disordered state having only short-range interactions in the nearest neighbourhood. The greater peep into the microscopic structural properties thus can be done by estimating Warren–Cowely short-range order parameter (α_1). The values of α_1 lie between −1 and +1 at equiatomic composition. Its minimum possible value is $\alpha_1 = -1$, which indicates that there is complete ordering nature of the liquid alloy. The maximum possible value of α_1 is $\alpha_1 = +1$, which indicates the complete segregating nature of the liquid alloy. If $\alpha_1 = 0$, then it indicates the random distribution of atoms in the liquid state of the alloy. The values of α_1 for both of the models are obtained from Equation (9). The theoretical value of α_1 for Ni–Al alloy in liquid state is found to be negative throughout the entire compositions of Ni (Figure 6), which further verifies the hetero-coordinating behaviour of Ni–Al melt at 1873 K.

3.3. *Transport properties*

The compound forming and the demixing nature of the liquid alloy can also be examined by estimating D_M/D_{id}. If $D_M/D_{id} > 1$, it signifies the tendency of complex formation, and if $D_M/D_{id} < 1$, it signifies the demixing or phase separation. But D_M/D_{id} approaches 1 for the ideal mixing. The values of D_M/D_{id} obtained from both of the models are found to be greater than one in the entire compositions which indicates the presence of chemical order in the alloy. When the ratio

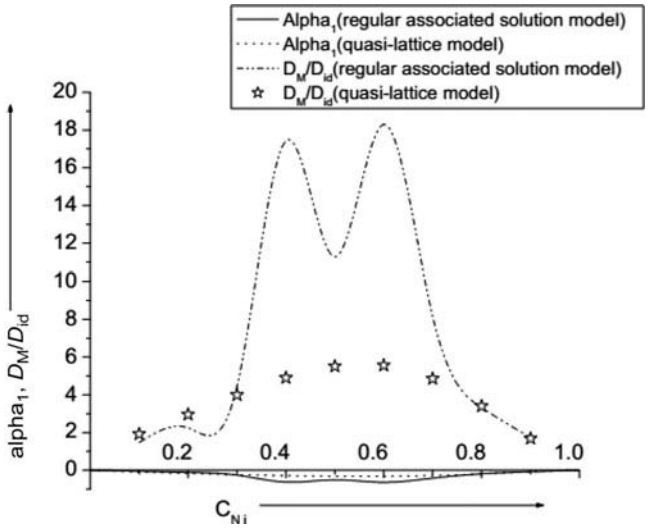

Figure 6. Short-range-order parameter (α_1) and the ratio of mutual and intrinsic coefficients (D_M/D_{id}) *vs*. the concentration of Ni (C_{Ni}) of Ni–Al liquid alloy at 1873 K.

Table 1. Input parameters for viscosity.

Metal	E (kJ/mol)	η_{ok} (mNs/m^2)
Al	16.5	0.1492
Ni	50.2	0.1663

of mutual and intrinsic diffusion coefficients is computed from regular associated solution model, there are sharp increases in the peaks of D_M/D_{id} at $C_{Ni} = 0.4$ and 0.6 (Figure 6), which signifies that the tendency of ordering in the liquid alloy is higher at these compositions. Again the ratio of mutual and intrinsic diffusion coefficients computed from quasi-lattice theory is also steeper at the intermediary compositions indicating the higher probabilities of associations between Ni and Al atoms at these compositions as suggested by regular associated solution model (Figure 6).

We have computed concentration dependence of viscosity of Ni–Al alloys in liquid state at 1873 K using Moelwyn–Hughes approach, Kozlov approach and simple statistical approach. For the computation of viscosity using these approaches, we need different input parameters. The necessary input parameters have been taken from Ref. [30], which are given in Table 1.

The viscosity of Ni–Al melt at 1873 K computed from different approaches is plotted in Figure 7. The viscosity obtained from all approaches deviates maximally from ideal values; i.e. the concentration dependence of viscosity of Ni–Al melt shows non-ideal behaviour. The viscosity obtained from Kozlov approach is greater than these obtained from Moelwyn–Hughes and simple statistical approaches up to the concentration $x_{Ni} = C_{Ni} = 0.5$. Above this concentration, the value obtained from simple statistical approach exceeds the values obtained from Moelwyn–Hughes and Kozlov approaches.

4. Conclusions

The theoretical analysis reveals that Ni–Al liquid alloy at 1873 K is ordering in nature. All the interaction energy parameters are temperature-dependent and the alloy is found to be strongly interacting system. The Ni–Al melt is non-ideal system regarding the viscous property.

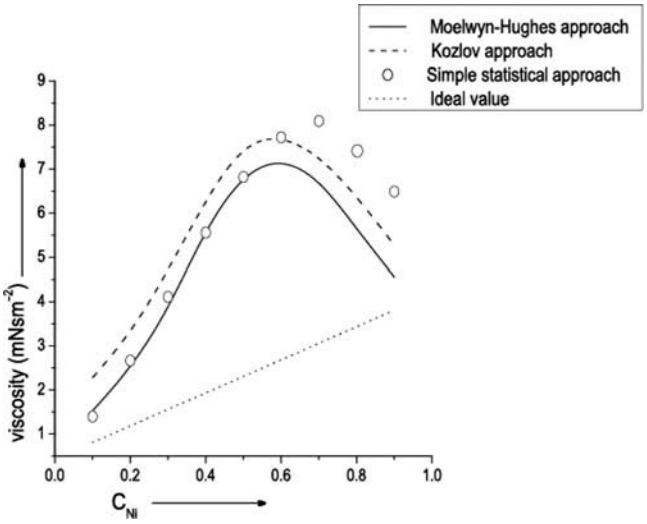

Figure 7. Viscosity (η) *vs.* concentrations of Ni (C_{Ni}) of Ni–Al liquid alloy at 1873 K.

Disclosure statement

No potential conflict of interest was reported by the authors.

References

[1] Tresa MP, Sammy T. Nickel-based super alloys for advanced turbine engines: chemistry, microstructure and properties. J Propul Power. 2006;22:361–374. DOI:10.2514/1.18239.
[2] Miracle DB, Darolia R. NiAl and its alloys. In: Westbrook JH, Fleischer RC, editor. Structural applications of intermetallic compounds. New York: John Wiley and Sons; 2000. p. 55–74.
[3] Adamiec J. Ni3Al alloy's properties related to high-temperature brittleness. Arch Mater Sci Eng. 2007;28:333.
[4] Li JJ-Z. Study of liquid metals by electrostatic levitation [Ph.D. Thesis]. Pasadena (CA): California Institute of Technology; 2009.
[5] Singh RN, Sommer F. Temperature dependence of the thermodynamic functions of strongly interacting liquid alloys. J Phys Condens Matter. 1992;4:5345–5358. DOI:10.1088/0953-8984/4/24/004.
[6] Hoshino K. Entropy of mixing of compound forming liquid binary alloys with two types of compounds. J Phys F: Met Phys. 1983;13:1981. DOI:10.1016/0022-3093(90)90580-F.
[7] Adhikari D. Disorder in liquid Cu-Pd alloys. Phase Transitions. 2011;84:308–314. DOI:10.1080/01411594.2010.536088.
[8] Ruppersberg H, Reiter H. Chemical short-range order in liquid LiPb alloys. J Phys F: Met Phys. 1982;12:1311–1325. DOI:10.1088/0305-4608/12/7/005.
[9] Adhikari D, Singh BP, Jha IS. Structural and energetic asymmetry in liquid Ag-Al alloys. Phys Chem Liq. 2010;48:787–796. DOI:10.1080/00319101003699008.
[10] Flory PJ. Thermodynamics of high polymer solutions. J Chem Phys. 1942;10:51. DOI:10.1063/1.1723621.
[11] Young WH. Structural and thermodynamic properties of NFE liquid metals and binary alloys. Rep Prog Phys. 1992;55:1769–1853. DOI:10.1088/0034-4885/55/10/003.
[12] Godbole RP, Jha SA, Milanarun M, et al. Thermodynamics of liquid Cu–Mg alloys. J Alloys Compd. 2004;363:187–193. DOI:10.1016/S0925-8388(03)00326-8.
[13] Bhatia AB, Hargrove WH. Concentration fluctuations and partial structure factors of compound-forming binary molten alloys. Phys Rev. 1974;10:3186–3196. DOI:10.1103/PhysRevB.10.3186.
[14] Kozlov LY, Romanov LM, Petrov NN. Izv. vysch.uch.zav. Chernaya Metallurgiya. 1983;3:7.
[15] Budai I, Benkő MZ, Kaptay G. Analysis of literature models on viscosity of binary liquid metallic alloys on the example of the Cu-Ag system. Mater Sci Forum. 2005;473-474:309–314. DOI:10.4028/www.scientific.net/MSF.473-474.309.
[16] Moelevyn-Hughes EA. Physical chemistry. Oxford: Pergamon; 1964.

[17] Lele S, Ramachandrarao P. Estimation of complex concentration in a regular associated solution. Metall Trans. 1981;12:659–666. DOI:10.1007/BF02654134.
[18] Jordan AS. A theory of regular associated solutions applied to the liquidus curves of the Zn-Te and Cd-Te systems. Metall Trans. 1970;1:239.
[19] Adhilari D, Jha IS, Singh BP. Transport and surface properties of Al-Mn alloy. Adv Mat Lett. 2012;3(3):226–230. DOI:10.5185/amlett.2012.3324.
[20] Novakovic R. Thermodynamics, surface properties and microscopic functions of liquid Al–Nb and Nb–Ti alloys. J Non-Cryst Solids. 2010;356:1593–1598. DOI:10.1016/j.jnoncrysol.2010.05.055.
[21] Koirala RP, Jha IS, Singh BP, et al. Thermodynamic and structural behaviour of liquid Al-Ga alloys. Adv Mat Lett. 2013;4:283. DOI:10.5185/amlett.2012.8412.
[22] Bhatia AB, Singh RN. Short-range order and concentration fluctuations in regular and compound forming molten alloys. Phys Chem Liq. 1982;11:285–313. DOI:10.1080/00319108208080752.
[23] Desai PD. Thermodynamic properties of selected binary aluminum alloy systems. J Phys Chem Ref Data. 1987;16:109. DOI:10.1063/1.555788.
[24] Prigonine I, Defay R. Chemical thermodynamics. London: Longmans Green and Co.; 1974. p. 257.
[25] Singh RN. Short-range order and concentration fluctuations in binary molten alloys. Can J Phys. 1987;65:309–325. DOI:10.1139/p87-038.
[26] Singh NKP, Singh RN, Chaudhary RB. Thermodynamic investigation of atomic order in AlMg liquid alloys. J Phys: Condensed Matter. 1991;3:3665. DOI:10.1088/0953-8984/3/20/024.
[27] Singh R, Sommer F. Thermodynamic investigation of viscosity and diffusion in binary liquid alloys. Phys Chem Liq. 1998;36:17–28. DOI:10.1080/00319109808035917.
[28] Darken L, Gurry R. Physical chemistry of metals. New York: McGraw Hill; 1953.
[29] Smithells B. Metals reference book. 6th ed. Oxford: Butterworth-Heinemann; 1983.
[30] Yih TS, Thompson JC. Chemical potentials and related thermodynamic properties of molten Na-Cs and Na-Bi alloys. J Phys F Met Phys. 1982;12:1625–1636. DOI:10.1088/0305-4608/12/8/009.

BIBECHANA
A Multidisciplinary Journal of Science, Technology and Mathematics
ISSN 2091-0762 (online)
Journal homepage: http://nepjol.info/index.php/BIBECHANA

Hydrogen storage on platinum decorated graphene: A first-principles study

S. Lamichhane, N. Pantha, N. P. Adhikari
Central Department of Physics, Tribhuvan University
Kirtipur, Kathmandu, Nepal
E-mail : npadhikari@gmail.com, npadhikari@tucdp.edu.np

Accepted for publication: February 15, 2014

Abstract

Adsorption of gaseous/molecular hydrogen on platinum (Pt) decorated and pristine graphene have been studied systematically by using density functional theory (DFT) level of calculations implemented by Quantum ESPRESSO codes. The Perdew-Burke-Ernzerhof (PBE) type generalized gradient approximation (GGA) exchange-correlation functional and London dispersion forces have been incorporated in the DFT-D2 level of algorithm for short and long range electron-electron interactions, respectively. With reference to the binding energy of Pt on different symmetry sites of graphene supercells, the bridge (B) site has been predicted as the best adsorption site. In case of 3×3 supercell of graphene (used for detail calculations), the binding energy has been estimated as 2.02 eV. The band structure and density of states calculations of Pt adatom graphene predict changes in electronic/magnetic properties caused by the atom (Pt). The adatom (Pt) also enhances the binding energy per hydrogen molecule in Pt-graphene comparing to that in pristine graphene and records the values within the range of 1.84 eV to 0.13 eV for one to eight molecules, respectively.

Keywords: Hydrogen adsorption; DFT; Geometrical stability; Hydrogen storage; Charge transfer.

1. Introduction

Graphene, one atom thick sheet of sp^2 bonded carbon atoms arranged laterally in a honeycomb crystal lattice, has been developed from theoretical model systems [1] to experimental reality [2]. Because of the two-dimensional crystal structure, it shows many interesting properties like observable quantum Hall effect even at the room temperature [3], an ambipolar electric field effect along with ballistic conduction of charge carriers [4], tunable band gap [5] and high elasticity [6]. After the experimental production of graphene in 2004 [7], considerable research interest has been shifted to explore its unique properties and various potential applications such as in energy storage [8,9], spintronics [10] and microelectronics [11]. Various theoretical and experimental works have been performed focusing on the electronic and magnetic behaviours of different adatoms [12-15] adsorbed on graphene system, and have been found to yield many interesting results. In addition to fascinating intrinsic electronic and mechanical properties exhibited by pure graphene, the structure and properties of graphene can also be controlled and modified by adsorption and/or doping of foreign atoms [16]. Very highly porous carbon materials offer a wide variety of chemical compositions that are suitable for the adsorption and storage of gaseous molecules like hydrogen, methane and carbon dioxide. Currently, gas storage in solids is an important technology with potential applications ranging from energy, environment and all the way biology to medicine [17].

The development of the fuel cell technologies, based on hydrogen, holds the promise for producing renewable energy. The safe storage of hydrogen is also crucial for the development of hydrogen energy [18]. Carbon nanomaterials are suitable for the hydrogen storage due to high surface to volume ratio. Dillion *et al.* [19] were the first to study the hydrogen by assemblies of single walled carbon nano tubes (SWCNT) and porous activated carbon [20]. Later, many works focused on carbon based materials such as nanotubes [21,22] and fullerene C_{60} [23] have been performed. Although the transition metal atoms such as Pt and Pd, can bind multiple H_2 molecule and metal adatom carbon material can adsorb more hydrogen molecules, exceeding the minimum requirement of 6wt% for practical applications, a reliable and quantitative analysis of binding character is still insufficient. After the synthesization of graphene, its capacity of binding hydrogen molecule should be the great matter of interest.

The remaining part of the paper is organized as follows. This section (Introduction) is followed by the computational method in section 2 where we describe the systems, algorithm, and approximations for the whole calculations. The section 3 presents and discusses the results of the present work. The last section 'Conclusions and concluding remarks' highlights the summary of the paper and also presents its possible extension in near future.

2. Computational Method

The DFT based first-principles calculations [26,27] are carried out to know the structural stability and electronic properties of adatom adsorption on graphene. Further, we have studied the adsorption of hydrogen molecule/s on Pt decorated graphene to investigate its hydrogen storage capacity. The long range dispersion forces are incorporated via London interaction [28] in DFT-D2 level of approximations, implemented with the quantum ESPRESSO code [29].

The interaction between electrons and ion cores is described by ultrasoft pseudo potentials, and generalized gradient approximation (GGA) formalism is adopted to treat the electronic exchange and correlation effects, as described by Perdew-Burke-Ernzerhof (PBE) [30]. The plane wave basis set with the kinetic energy cut-off of 35 Ry is used for the expansion of the ground state electronic wave functions. The plane waves are chosen to have a periodicity compatible with the periodic boundary conditions of the simulating cell. The supercell dimensions are kept fixed during the relaxation.

We have used calculated value of the lattice constant ($a = 2.46\,\text{Å}$), which overlaps with the experimental value [31], obtained from our convergence tests. The adatom graphene system is modeled using single adatom in 2×2, 3×3, and 4×4 supercells of graphene containing 8, 18 and 32 number of carbon atoms. In this work, the adsorption of single Pt atom on graphene is performed at three different high symmetry sites, top (T), hollow (H) and bridge (B). For each adsorption site of the adatom-graphene system, the adatom is relaxed along the z-direction and the C atoms on graphene in all x, y, and z directions. To estimate the binding energy of adatom (Pt), the calculations for the isolated Pt, graphene and adatom-graphene are performed within the identical supercell of graphene. The optimized geometry is obtained with fully relaxed BFGS (Broyden-Fletcher-Goldfarb-Shanno) scheme [32] until the total energy change between two consecutive scf steps becomes less than 10^{-4}Ry and force acting goes below 10^{-3} Ry. The brillioun zone of graphene is sampled in k-space using the Monkhorst-Pack scheme [33] with an appropriate number of k-points. Different sized supercells are considered to see the size effect of the interaction between the isolated adatom and graphene. In order to avoid the interaction between the adatoms at adjacent supercells, vaccum length of supercell was made large enough, i.e. 20Å along z- axis. The detail calculations to study the electronic properties, like density of states (DOS) and electronic band structure of pure graphene and Pt-adsorbed graphene are calculated in 3×3 supercell of graphene and 15×15×1 mesh in k-space.

The adsorption properties of molecular hydrogen are observed on the most stable geometry of platinum decorated 3×3 supercell of graphene. At first, we optimized H_2 molecule and found bond length of 0.75 Å

between two hydrogen atoms. The optimized molecule/s is then placed within the Pt-adatom graphene supercell of height 20Å, very large in comparison to the bond length of H_2, which prevents interaction between two hydrogen molecules at adjacent supercells. The calculations for a large number of molecular hydrogen (up to eight), with in the limit of computational power, has been covered in this study to observe the desirable binding energy and hydrogen storage capacity.

3. Results and Discussion

In the present work, we study the adsorption properties of single Pt on different symmetry sites of 2×2, 3×3, and 4×4 supercells of pure graphene and also present the binding strength/geometry of a number of hydrogen molecules on its preferred geometry.

A. Binding energy and geometry

The Binding energy (ΔE) of adatom on graphene is defined as,

$$\Delta E = E_A + E_G - E_{GA}$$

where, E_{GA}, E_G and E_A are the values of energy of adatom-graphene, pure graphene and an isolated adatom in 3×3 supercell of graphene. Out of the three adsorption sites (H, B and T) considered in present calculations, the configuration with the highest binding energy is defined as the most favored one.

The adatom height (h) is defined as the difference in z coordinates of adatom and the average of the z coordinates of the carbon atoms in the graphene layer. We have also calculated the distance d_{Ac} between the adatom and its nearest carbon atom. The adsorption of adatom on graphene produces a distortion (dz), which is quantified by computing the maximum deviation of C atoms along z-direction from their average positions in pristine graphene. The distortion of the graphene layer upon the adsorption of adatom is also calculated in terms of change in dihedral angles.

Table 1. The binding energy E_b, adatom height h and the nearest carbon distance d_{Ac} for adatom (Pt) in 2×2, 3×3 and 4×4 supercells of graphene are noted. Further, deformation produced in graphene layer due to adsorption of adatom is quantified in terms of distortion along z-direction (dz).

Size of graphene supercell	Adsorption site	Binding Energy (E_b,eV)	Height of Pt atom (h, Å)	Distance of nearest carbon (d_{Ac}, Å)	Distortion (dz, Å)
2×2	H	1.087	2.12	2.48	0.09
	B	1.175	2.09	2.12	0.11
	T	1.089	2.13	2.55	0.09
3×3	H	1.305	1.95	2.41	0.02
	B	2.022	2.15	2.10	0.17
	T	1.905	2.16	2.03	0.01
4×4	H	1.317	1.95	2.40	0.03
	B	2.048	2.20	2.10	0.22
	T	1.917	2.20	2.03	0.16

Table (1) shows that the adsorption of Platinum atom on different sites of pure graphene sheet is feasible. The table also reveals the most favored site for Pt as bridge site with the highest binding energy (E_b). The binding energy seems to increase on increasing the computed graphene size. However, the increment in E_b is nominal for 4×4 supercell with reference to 3×3, and this helps to conclude that size effect of graphene beyond 3×3 does not alter the quality of calculations. Taking care of size effect information and computational cost for bigger system, we consider 3×3 supercell for further calculations.

The distortion in the graphene plane due to the adsorption of adatom is observed maximum at the bridge site. This correlates the direct relationship of distortion with binding energy. The distortion can also be measured in terms of change in bond length, bond angle and dihedral angle. In case of 3×3 graphene sheet, maximum change in bond length, bond angle and dihedral angle are observed as 0.02Å, 0.9^o and 12.07^o from their initial values 1.42 Å, 120^o and 0^o, respectively.

B. Electronic structures

We have computed the electronic density of states (DOS) and band structures of pure graphene and adatom graphene. The Kohn-Sham DOS is computed for adatom at the most favorable (B) site of the 3×3 graphene supercell using 15×15×1 Gamma centered Brillouin zone-sampling. The energy eigen values are smeared by 'Marzari-Vanderbilt' smearing [35] of width 0.001 Ry.

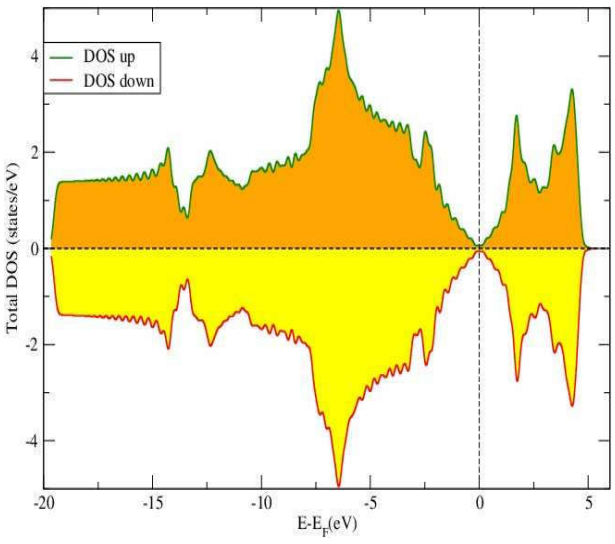

Fig.1 (a)

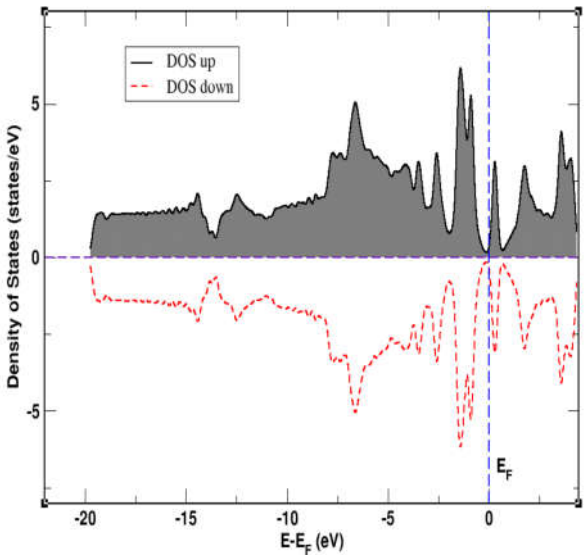

Fig.1 (b)

Figure 1: Plot of density of states for pure graphene (a) and Pt adsorbed graphene (b). The DOS is plotted assuming fermi level as the reference.

The spin up and spin down calculations of pure graphene are plotted by assuming Fermi energy as reference level (Fig. 1a). The Dirac point, where DOS is nearly equal to zero, lies at the Fermi level, and approves that the valence and conduction band meet at that point with zero band gap. The identical density of states for spin up and spin down in the figure approves the non magnetic nature of pure graphene.

From Fig. (1b) it is seen that Fermi level of adatom graphene again appears to remain at the Dirac point. On the other hands, DOS of adatom graphene system has been modified near the Fermi level. The contribution of different Pt orbitals in the DOS of Pt adatom system is shown in Fig. 2.

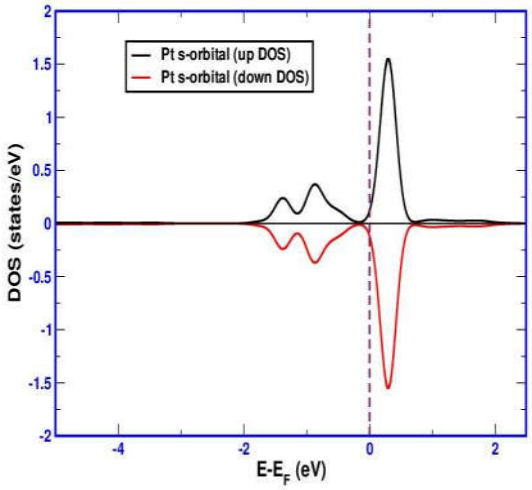

Fig. 2 (a)

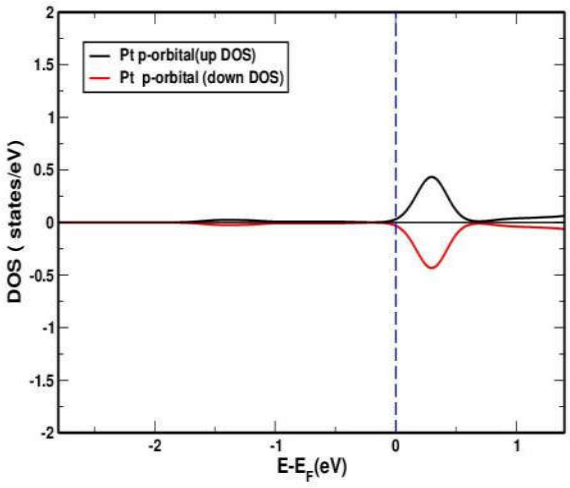

Fig. 2 (b)

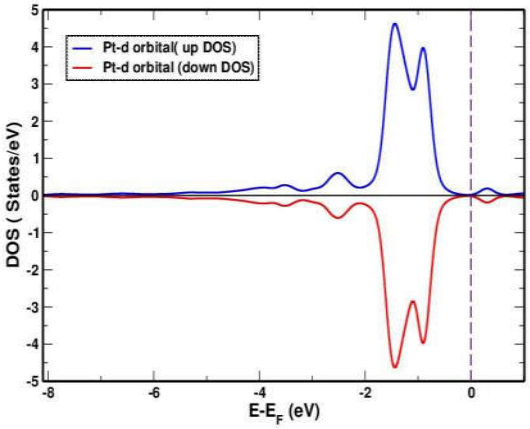

Fig. 2(c)

Figure 2: The projected densityof states (PDOS) for spin up and spin down of s (a), p (b), and d (c) orbitals of Pt, an adatom on graphene.

They show the different orbital's contribution on the DOS of pristine graphene.

The band structure of pure graphene exhibits its unique feature showing zero band gap at Fermi level. The bands meet at a point in Fermi level (observed at -2.351 eV) and form a conical structure, which are known as Dirac point and Dirac cone respectively (Fig. 3a).

The interaction of the adatom with Π and Π* states of the carbon atoms in graphene, however, breaks the symmetry of graphene and band gap occurs at the Fermi level. New bands originating from Pt modify the band structure of pure graphene and disclose a band gap of 1.10 eV in adatom graphene. This change in band gap from zero in pure graphene to 1.10 eV in Pt-added graphene shows the potential use of the material for practical applications.

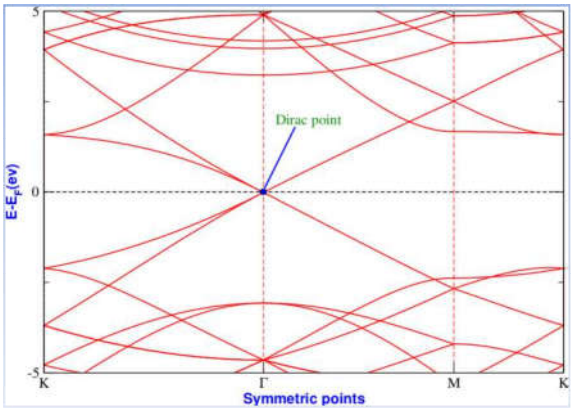

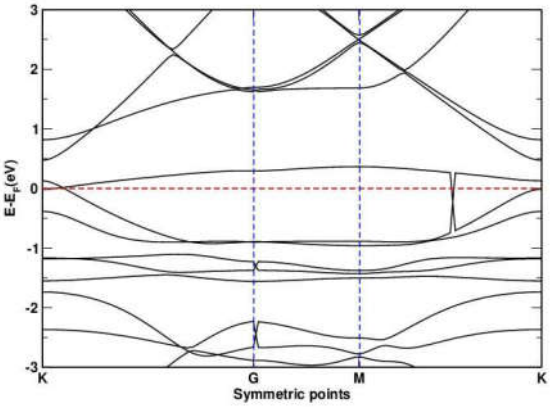

Fig. 3(a) Fig. 3(b)

Figure 3: Band structure of 3×3×3 supercell of pure graphene (a) and Pt-adsorbed graphene (b) along K-Γ- M-K path of irreducible Brillouin zone.

C. Charge transfer

Charge transfer, an ambiguous quantity [16, 17], is an important feature of adatom-graphene interaction in which transfer of electronic charge takes place between the adatom and graphene. In this section, we discuss and quantify the charge transfer due to the adsorption of adatom on bridge site of 3×3 graphene supercell, which we believe an essential part to study the nature of bonding between the interactive materials. By keeping in mind that the magnitude of charge transfer is highly method dependent and difficult to quantify as an absolute value, we have used one of the algorithms followed by previous studies [15], where we integrate differences in electronic charge density in planer basis.

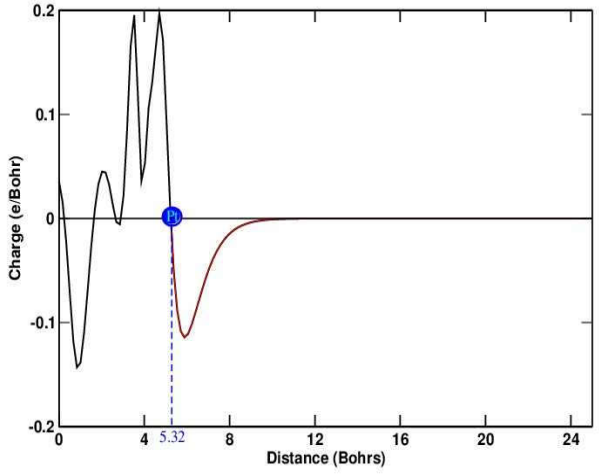

With the help of optimized structures, the charge densities for pure graphene layer, isolated adatom, and adatom graphene are calculated. The difference in charge-density is then defined as

$$\Delta\rho(r) = \rho_{AG}(r) - \rho_A(r) - \rho_G(r)$$

where $\rho_{AG}(r)$, $\rho_A(r)$ and $\rho_G(r)$ are the charge densities of the adatom-graphene, an isolated adatom, and graphene respectively, calculated in the same positions of the supercell as done for adatom-graphene calculations.

Figure 4: Planner averaged electron charge difference for Pt on graphene at B site as a function of position along z-direction. The vertical line at z=0 represents the position of graphene sheet and the line at z = 5.32 Bohr indicates Rcut. The integration between the region z=0 and z=5.32 Bohr quantifies the charge transfer.

Figure (4) shows the planar averaged linear charge density difference as a function of z, along the height of supercell, for Pt on B-site of graphene. The figure implies the position of planar graphene sheet and adatom (Pt) at z = 0 and 5.32 Bohr, respectively. Positive difference in electron density towards the region of graphene sheet and negative towards the adatom illustrates the transfer of electronic charge from adatom to graphene.

To calculate the charge transfer using the linear charge density difference, the region of the space belonging to graphene and/or adatom must be specified. As similar to the concept used by Chan et al., [15], an adsorbate-substrate cutoff distance R_{cut} is defined as the distance from the graphene plane to the point between the plane and the adatom at which charge accumulation changes to charge depletion. In the Fig. (4) the region with $z < R_{cut}$ is assigned to the substrate and the region with $z > R_{cut}$ is assigned to the adatom. The charge transfer is obtained by the integral of linear charge density difference in the substrate region, and the quantity in case of Pt adatom graphene has been found as 0.18e. Higher the value of charge transfer may cause more impacts on the electronic structure and therefore on the catalytic activities of the system.

D. Adsorption of hydrogen molecule/s on Pt adsorbed graphene

We have also performed the first-principles calculations to study the adsorption of hydrogen molecule/s in Pt decorated graphene. The system is modeled by allowing the adsorption of hydrogen molecule/s from one up to maximum eight in number on a single Pt decorated 3×3 graphene supercell. The binding energy (ΔE) of H2 molecule is then calculated using the formula,

$$\Delta E = E_{AG} + E_{H2} - E_{AGH}$$

where E_{AGH} is the energy of the system containing graphene, adatom and H2 molecules, E_{AG} is the energy of the Pt-graphene system and E_{H2} is the energy of the H2 molecule. Furthermore, binding energy/H2 molecule is calculated as,

$$B.E/H2 = \Delta E/N, \quad \text{with N as the number of the hydrogen molecules.}$$

Figure (5) represents the optimized structures for the adsorption of hydrogen molecule/s on Pt decorated graphene system. The figures show that two hydrogen molecules dissociate into atomic hydrogen and a complex, due to interaction with the adatom. Most of the H2 molecules in the larger systems seem to be attracted by long-range dispersion forces.

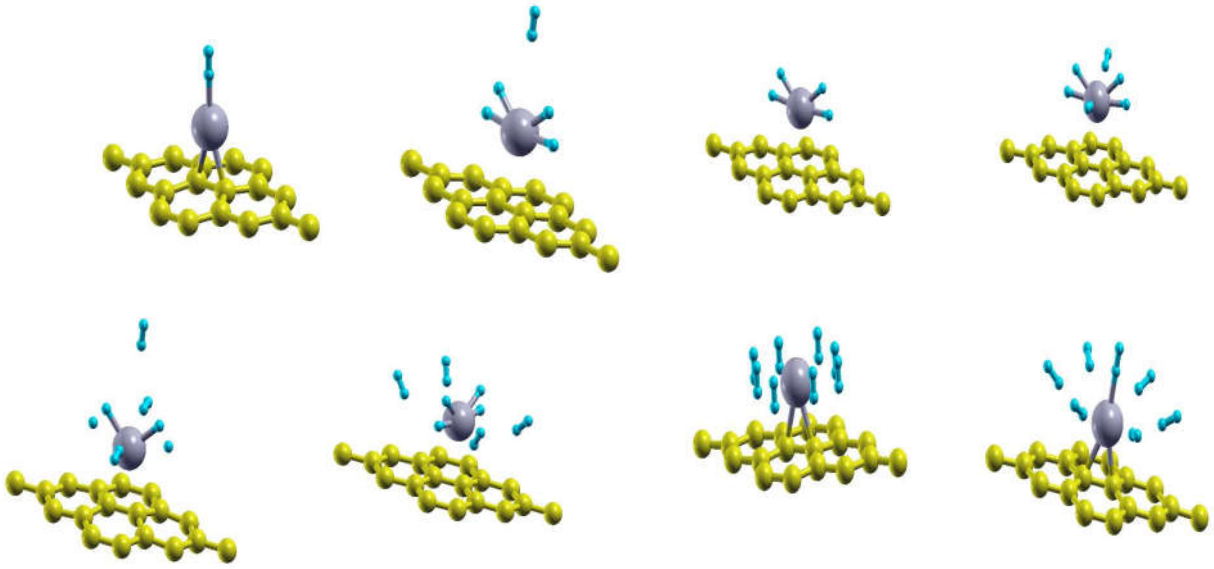

Figure 5: Optimized geometries for the adsorption of H2 in Pt-decorated graphene system.

The variation of the binding energy per H_2 molecule with the number of H_2 molecules adsorbed on Pt-decorated graphene is shown in figure (6). Table (2) presents the observed values of energy of total system, binding energy of H_2 molecules and binding energy per H_2 molecule. It can be seen that the observed binding energy per H_2 molecule decreases with increasing the number of adsorbed hydrogen molecules. When a single hydrogen molecule is adsorbed in Pt-graphene system, the binding energy for H_2 molecule is found 1.84eV. The decreasing pattern of the binding energy per hydrogen molecule, as seen in Fig. 6, for the adsorption of one to eight adsorbed H_2 molecules goes through the range of 1.84 eV to 0.13 eV. The binding energy values per hydrogen molecule from this work meet the U.S. DoE (Department of Energy) target (0.2eV-0.7eV) [36].

Table 2: The binding energy of hydrogen molecules (Eb) and binding energy per H2 molecule (Eb/H2), for the adsorption of H2 molecules in Pt decorated graphene are presented.

Number of H_2 molecule	Binding Energy (eV)	Binding Energy/H2 (eV)
1	0.415	1.847
2	0.914	0.957
3	1.957	0.652
4	1.937	0.484
5	1.985	0.397
6	2.076	0.346
7	1.137	0.162
8	0.904	0.134

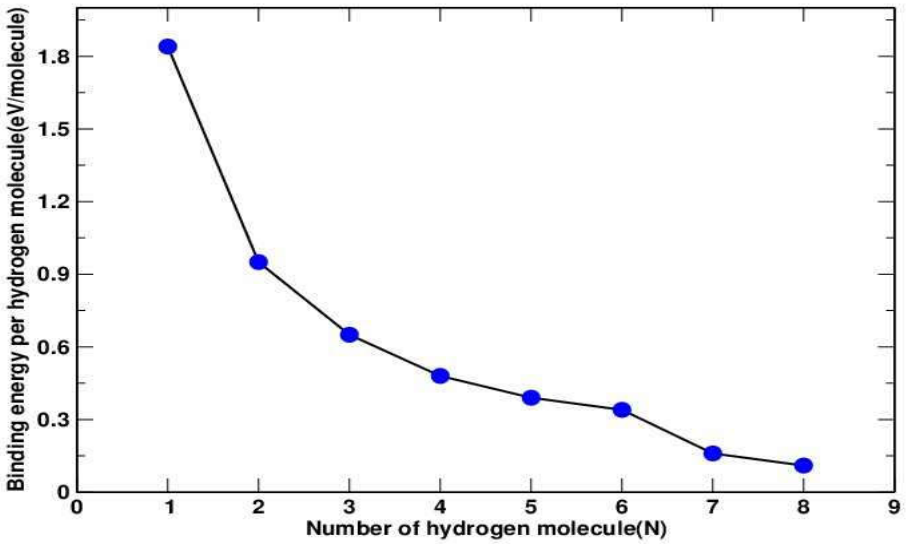

Figure 6: Variation of binding energy per H2 molecule with the number of hydrogen molecule adsorbed in platinum adatom graphene.

One of the major purposes of this study (adsorption of hydrogen molecules on graphene) is to explore the possibility of the gaseous storage at operating conditions. If we compare the strength by which H2 are bound in pure and adatom graphene system, the maximum possible binding energy per H2 molecule is enhanced remarkably in adatom (Pt) graphene (1.84eV) over the pure graphene (~ 0.07 eV). The hydrogen storage capacity of single Pt decorated graphene for the adsorption of 8 H2 molecules is 3.74 wt % per substrate, comparing to the DoE target (around 6 wt %) [9], for the practical applications. The estimated results display the potential application of Pt decorated graphene in hydrogen gas storage material.

4. Conclusion and Concluding remarks

We studied the structural and electronic properties of pure graphene and platinum adsorped graphene systems. Using the estimated values of binding energies of Platinum at three high symmetry sites (H, B and T) of 3×3×3 graphene supercell, it is found that the bridge site is energetically favourable with its magnitude 2.022 eV. The adsorption of adatoms on the bridge site of the graphene changes some of the graphene sp^2 like orbital character to a more covalently reactive sp^3 like character, which is accounted by calculating the deformation on graphene sheet. A small band gap of 1.10eV has been noticed in band structure calculations of Pt-added graphene over the zero band gap pure graphene, which causes the breaking of symmetry of the graphene.

We have also studied the adsorption of the hydrogen molecules on Pt-decorated graphene in order to investigate its hydrogen storage capacity. The binding energy per H2 molecule due to adsorption of one to eight number of hydrogen molecules on Pt adatom graphene ranges within 1.847 eV to 0.134 eV, where its value decreases on increasing the number of adsorbed hydrogens. Within the limit of our calculations, the maximum hydrogen storage capacity of single Pt decorated graphene for 8 H2 molecules is found 3.72 wt %. The results we discussed in this paper, in general, are progressive and interesting to move towards the US DoE criteria (around 6 wt %) for the practical applications.

We intend to extend this work to see the redistribution of charge density while adsorbing adatom and gaseous molecules on graphene. Adsorption of multiple Pt atoms or/and Pt-dimers and also more hydrogen molecules may enhance wt % of hydrogen and overall quality of the material.

Acknowledgments

We acknowledge the partial support from *The Abdus Salam* International Centre for Theoretical Physics (ICTP) through Office of External Activities within NET-56 project. We also extend our gratitude to S. Narasimhan and K. Ulman for their valuable suggestions and inspiration to work in this area.

References

[1] J. W. McClure, Phys. Rev., 104 (1956) 666.

[2] A. K. Geim, K. S. Novoselov, Nat. Mater., 6 (2007) 183.

[3] Y. Zhang, Y. W. Tan, H. L. Stormer, P. Kim, Nature, 438 (2005) 201.

[4] F. Schedin, A. K. Geim, S. V. Morozov, E. W. Hill, P. Blake, M. I. Katsnelson, K. S. Novoselov, Nat. Mater., 6 (2007) 652.

[5] M. Y. Han, B. Oezyilmaz, Y. Zhang, and P. Kim, Phys. Rev. Lett., 98 (2007) 206805.

[6] C. Lee, X. Wei, J. W. Kysar, J. Hone, Science, 321 (2008) 385.

[7] K. S. Novoselov, A. K. Geim, S. V. Morozov, D. Jiang, M. I. Katsnelson, I. V. Grigorieva, S. V. Dubonos, A. A. Firsov, Science, 306 (2004) 666.

[8] Y. Miura, H. Kasai, W. Dino, H. Nakanishi, T. Sugimour, J. Appl. Phys., 93 (2003) 3395.
[9] E. Durgun, S. Ciraci, Y. Yildirim, Phys. Rev. B, 77 (2008) 085405.
[10] J. J. Palacios, J. F. Rossier, L. Brey, Phys. Rev. B, 77 (2008) 195428.
[11] K. Nakada, M. Fujita, G. Dresselhaus, M. S. Dresselhaus, Phys. Rev. B, 54 (1996) 17954.
[12] V. C. P. Medeiros and F. de B. Mota, J. S. A. Mascarenhas, M. C. C. Castilh, Nanotechnology, 21 (2010) 115701.
[13] H. Johll, H. C. Kang, Phys. Rev. B, 79 (2009) 245416.
[14] R. Thapa, D. Sen, M. K. Mitra, K. K. Chattopadhyay, Physica B, 406 (2011) 368.
[15] K. T. Chan, J. B. Neaton, M. L. Cohen, Phys. Rev. B, 77 (2008) 235430.
[16] X. Lui, C. Z. Wang, Y. X. Yao, W. C. Lu, M. Hupalo, M. C. Tringides, K.M. Ho, Phys. Rev. B, 83 (2011) 235411.
[17] R. E. Morris, P. S Wheatley, Angew. Chem. Int. Ed., 47 (2008) 4966.
[18] R. Coontz, B. Hanson, Science, 305 (2004) 957.
[19] A. C. Dillon, K. M. Jones, T. A. Bekkedahl, C. H. Kiang, D. S. Bethune, M. J. Heben, Nature, 386 (1997) 377.
[20] J. S. Arellano, L. M. Molina, A. Rubio, J. A. Alonso, J. Chem. Phys., 112 (2000) 8114.
[21] K. Tada S. Furuya, K. Watanabe, Phys. Rev. B, 63 (2001) 155405.
[22] S. P. Chan, G. Chen, X. G. Gong, Z. F. Liu, Phys. Rev. Lett., 87 (2001) 205502.
[23] Y. Zhao, Y. H. Kim, A. C. Dillion, M.J. Heben, S. B. Zhang, Phys. Rev. Lett., 94 (2005) 155504.
[24] S. Dag, Y. Ozturk, S. Ciraci, T. Yildirim, Phys. Rev. B, 72 (2005) 155404.
[25] T. Yildirim, S. ciraci, Phys. Rev. Lett., 94 (2005) 175501.
[26] P. Hohenberg, W. Kohn, Phys. Rev. B, 136 (1964) 864.
[27] W. Kohn, L. J. Sahm, Phys. Rev., 140 (1965) 1133.
[28] J. Klimes, A. Michaelides, J. Chem. Phys., 137 (2012) 120901.
[29] P. Giannozzi et al., J. Phys.: Condens. Matter, 21 (2009) 395502.
[30] J. P. Perdew, K. Burke, M. Ernzerhof, Phy. Rev., 77 (1996) 3865 .
[31] A. H. Castro Neto, Physics World, 19 (2006) 33.
[32] R. Fletcher, Practical Methods of Optimization, Wiley, New York, 1987.
[33] J. H. Monkhorst, D. J. Pack, Phys. Rev. B, 16 (1977) 1748.
[34] Y. Kyun Kwon, Journal of Korean Physical Society, 57 (2010) 778.
[35] N. Marzari, D. Vanderbilt, A. de Vita, M. C. Payne, Phys. Rev. Lett., 82 (1999) 3296.
[36] J. G. Zhou, Q. L. Willians, J. Nano Research, 15 (2011) 29.

BIBECHANA
A Multidisciplinary Journal of Science, Technology and Mathematics
ISSN 2091-0762 (Print), 2382-5340 (0nline)
Journal homepage: http://nepjol.info/index.php/BIBECHANA
Publisher: Research Council of Science and Technology, Biratnagar, Nepal

Structural and electronic properties of perovskite hydrides $ACaH_3$ (A=Cs and Rb)

S. Lamichhane[1], B. Aryal[1], G. C. Kaphle[1,2,3], N. P. Adhikari[1*]
[1]Central Department of Physics, Tribhuvan University, Kathmandu, Nepal
[2]Tri-Chandra Multiple Campus, Ghantaghar, Kathmandu, Nepal
[3]Condensed Matter Physics Research Center, Butwal, Rupandehi, Nepal
[*]E-mail: npadhikari@tucdp.edu.np
Article history: Received 31 July, 2015; Accepted 20 September, 2015
DOI: http://dx.doi.org/10.3126/bibechana.v13i0.13437

Abstract

We have performed structural properties, electronic properties, charge density and potential distribution of $CsCaH_3$ and $RbCaH_3$ using TB-LMTO-ASA approach under local density approximation. Our findings show that both $CsCaH_3$ and $RbCaH_3$ are non-magnetic and then insulators with estimated direct band gaps (*M-M)* of 3.15 eV and 3.17 eV respectively. Our estimated values of band gap suggest to both materials as better candidate for the high frequency ultra-violet devices. Furthermore, role of corner atoms in perovskite hydrides are also presented in this study. Present calculations agree well with the previous work.

Keywords: Projected density of states; perovskite; charge density and TB-LMTO-ASA**.**

1. Introduction

Binary alloys of transition and post-transition elements, and also graphene related work have been studied with high effort by many researchers [1-6] but have no band gap. However, various potential applications in optics need significant band gap. The perovskite structure of ternary chlorides is applicable in optics due to their wide band gap [7, 8]. Perovskite compounds and its derivatives are the most popular field owing to their diverse physical properties while going to binary alloy to ternary alloy to perovskite material. Besides this, anomalous dielectric properties of perovskite and phase transition with increasing temperature have made fundamental interest in physics [9-11].

Perovskite hydride compounds belong to Perovskite family, symbolized as ABH_3 (A and B represent lighter metals) are well characterized with their optical properties. Perovskite hydrides have become a source of attraction to experimentalists due to presence of lightweight elements, low production cost and

wide range of applications in the industrial area. Alkali and alkaline earth-based complex hydrides are expected to have application for the hydrogen gas storage at certain temperature and pressure [12, 13]. The complexity in structural arrangement of perovskite hydrides and difficulties in establishing proper hydrogen position by x-ray diffraction method in previous attempt [14] motivated us to enter in this burning area of research. As increase in Ca-H distance, narrower the density of states (DOS) on moving from $LiCaH_3$ to $CsCaH_3$, predicted in previous work [15] is insufficient to address the factors for DOS variation and also the compound $NaCaH_3$ has shown absurd behaviour than others in regards to M-H and Ca-H distance. Hence, in the present work efforts have been taken to study the structural, electronic and charge distribution to explore the origin of band gap, contribution of orbitals and role of potentials to bands separation.

Moreover, the crystal structure, shape, size, and surface composition of materials plays vital role to control the hydrogen sorption properties for energy storage applications. For the efficient energy carrier, hydrogen should be absorbed and desorbed in materials easily in sufficient quantities in cheaper price. The complex compound based on Alkali- and alkalineearth hydrides are expected to have potential candidates for storing hydrogen at moderate temperatures and pressures [16-17]. This is another motivation of present work to study the electronic behavior of such materials.

The paper is organized as follows: in section II, the computational details of the present study are included. Results and discussion are presented in section III whereas section IV provides the conclusions of the present study and finally references are listed at the end of the paper.

2. Computational details

The unit cell of the perovskites hydrides $CsCaH_3$ and $RbCaH_3$ crystallize in to the cubic structure with space group Pm-3m. The atomic positions in the elementary cell are at Cs(0.0,0.0,0.0), Rb(0.0,0.0,0.0), Ca (0.5,0.5,0.5) and three hydrogen atoms are at three different positions as H_1(0.5,0.5,0.0) , H_2(0.5,0.0,0.5) and H_3(0.0,0.5,0.5) [8]. With reference to experimental lattice parameter of 4.609 Å for $CsCaH_3$ [18] and 4.547 Å for $RbCaH_3$ [19] unit cell structures thus obtained with the help of xcrysden visualization are shown in figures 1(a) and (b).

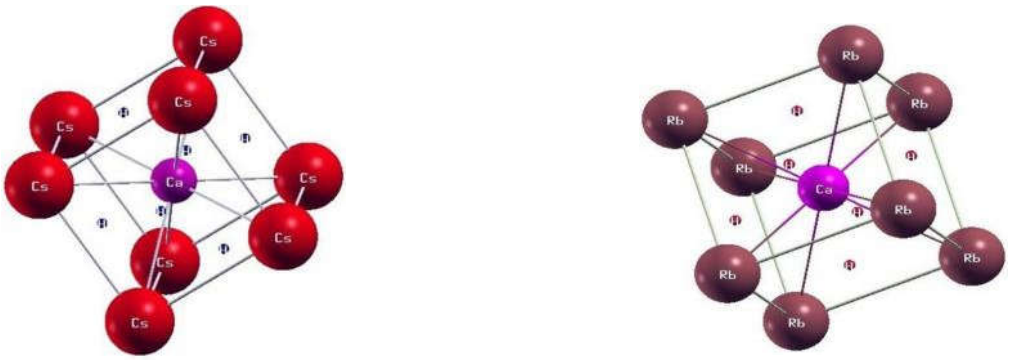

Fig. 1: (a) Unit cell of $CsCaH_3$ and (b) Unit cell of $RbCaH_3$.

All the calculations are done based on the density functional theory implemented with TB-LMTO-ASA code to carry out comprehensive analysis of structures along with electronic and magnetic properties. The standard local density approximation (LDA) is used to address exchange correlation potential. The concept of Wigner-Seitz spheres for each atom in the unit cell is taken into account to determine the potential of the crystal [20]. We have only included the energetically higher-lying valence states in the self-consistent calculations of the effective crystal potential [21] according to the norms of the TB-LMTO-ASA approach. The core states are treated fully relativistically while the semi-core and valence states as treated semi-relativistically. All the calculations were iterated to self-consistency along with accuracy of 10^{-6} Rydberg.

3. Results and discussion

The new findings from the calculations of band structures, DOS, charge density and potential distributions are described as follows.

A. Band Structures

The calculated energy bands of perovskites $CsCaH_3$ and $RbCaH_3$ along the high symmetry lines in the Brillouin zone are shown in Fig (2).

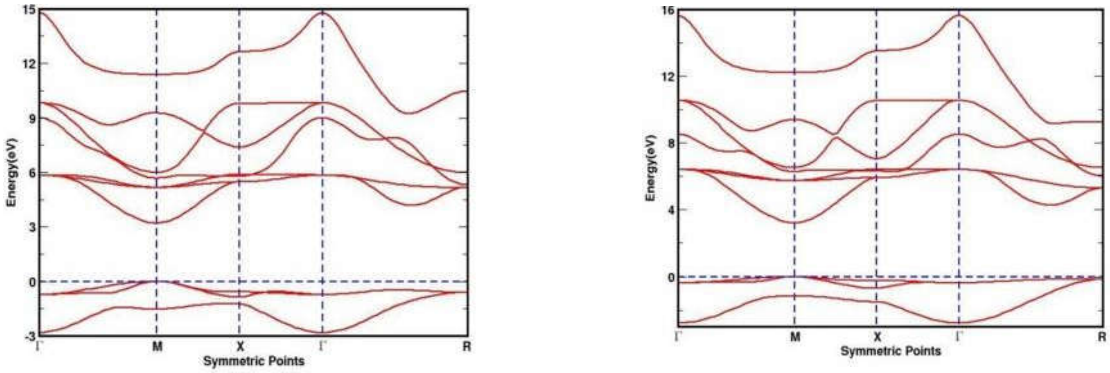

Fig. 2: Band structures of $CsCaH_3$ (left) and $RbCaH_3$ (right).

The horizontal dotted line in the above figures represents the Fermi level. We have found 10 different energy bands in both $CsCaH_3$ and $RbCaH_3$. Zero energy is chosen to coincide with the CBM and VBM both occur at same M point results the direct band gap in both of these perovskite hydrides which indicates that both $CsCaH_3$ and $RbCaH_3$ bear the non-metallic behaviour. Our estimated band gaps of $CsCaH_3$ and $RbCaH_3$ are 3.15 eV and 3.17 eV which indicates that $CsCaH_3$ and $RbCaH_3$ are insulators. Our results of band gap well agree with previous generalized-gradient approximation based theoretical calculations [8]. Resulting band gap of these perovskites meet the requirement for the applications in high frequency ultra-violet device [22].

B. Density of States

To observe the density of states, we have taken same value of the lattice parameter as in band structures calculations. The total DOS and PDOS of $CsCaH_3$ and $RbCaH_3$ are shown below. The total density of states are categorized into four different parts and the contributions of different states can easily be seen from the PDOS analysis.

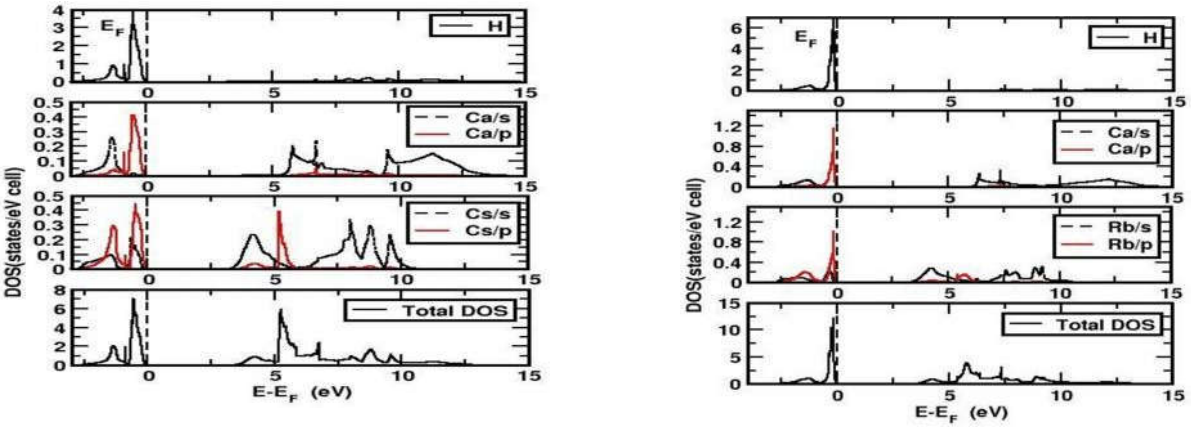

Fig. 3: Total DOS and PDOS of $CsCaH_3$(left) and $RbCaH_3$(right).

The Fermi energy line is in the valence band which supports the non-metallic behaviour. In both $CsCaH_3$ and $RbCaH_3$ Ca-*p* and H-*s* states are located in the vicinity of the Fermi level at the valence band. In $CsCaH_3$ Ca-*s* and $-p$ states are well-separated where as in $RbCaH_3$ Ca-*s* and $-p$ states are not well-separated. The symmetric nature of spin up and spin down DOS indicate the non-magnetic behavior of $CsCaH_3$ and $RbCaH_3$. The contribution to the valance band is maximum by s states of hydrogen and less contributions is seen from Ca and Cs. The contribution of Ca and H atoms to the DOS is major in the valence bands while Cs/s, Cs/p are responsible for that in the conduction band.

Further, one valance electron of Cs (or Rb) in $CsCaH_3$ (or $RbCaH_3$) fill the partially occupied s-orbital of one hydrogen and remaining two partially filled orbitals of hydrogen is filled by two valence electrons of calcium. Since the valence electrons are completely filled, $CsCaH_3$ and $RbCaH_3$ both acts as an insulating materials.

C. Charge density and potential distribution

The charge density distribution and chemical bonding behaviour of $MCaH_3$ is important to check the stability of these materials for hydrogen storage. The charge density plot of $CsCaH_3$ and $RbCaH_3$ obtained by using the same lattice parameters as in DOS and band structures calculations are shown in figure (4).

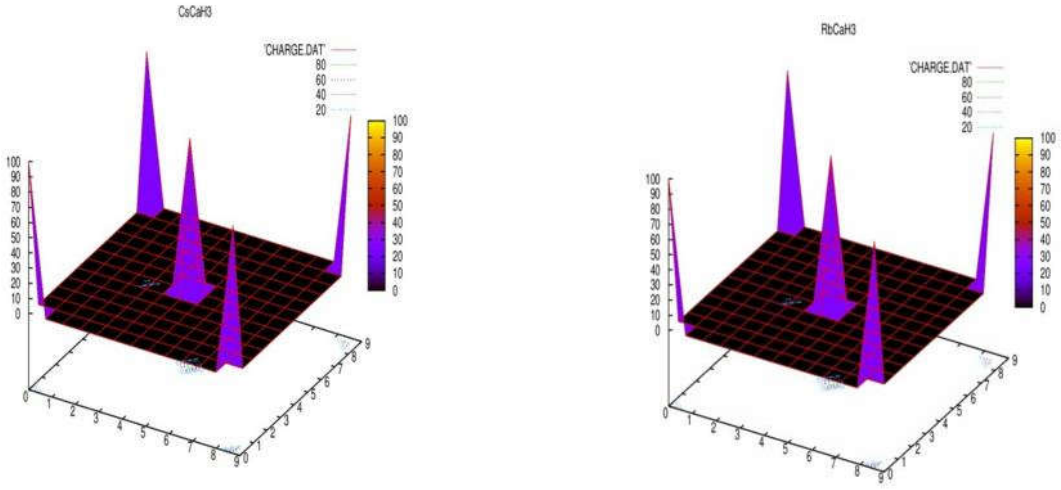

Fig. 4: The charge density distribution of $CsCaH_3$ and $RbCaH_3$.

From figure 4, we have found that there are five peaks along the corners and faces which shows the maximum distribution of the charges at the corners and faces. About 10-40 % of total charge occur along the corners and faces which has been shown by a high peaks lines while the distribution of the charges is negligible at other interstitial sites. This is the site at which adsorption and desorption of hydrogen takes place, indicating that such materials can be used for hydrogen storage purposes. The potential distribution plot of $CsCaH_3$ and $RbCaH_3$ are shown in figure (5) .

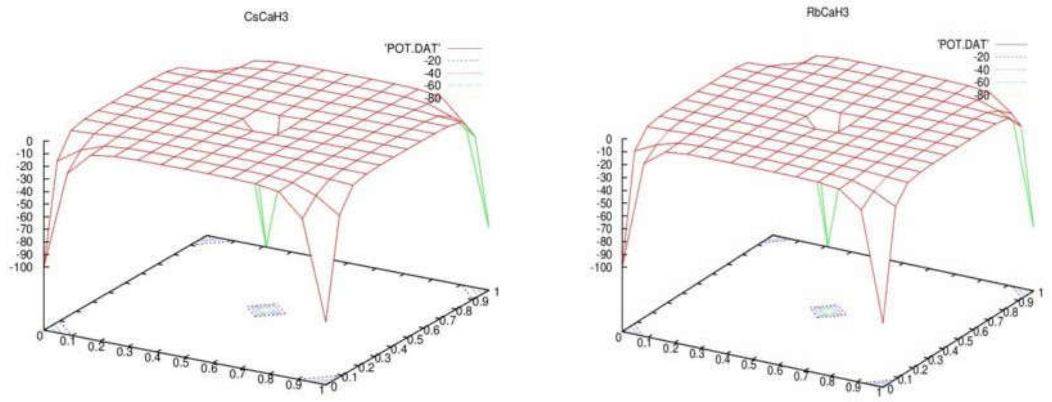

Fig. 5: Potential distribution in $CsCaH_3$ (left) and $RbCaH_3$ (right).

From figure 5, we can find that the potential is maximum in the vicinity of core whereas at the interstitial region the potential is found to be constant (flat). Our results agree well with the muffin-tin potential in which the potential is maximum near the core electrons and almost flat in the interstitial space. This kind

of potential distribution fully supports the maximum distribution of charge near the corner of crystal structure.

4. Conclusions

In this present work, we studied the band structures, density of states, charge density and potential distribution of perovskite hydrides $CsCaH_3$ and $RbCaH_3$ by using TB-LMTO-ASA. Taking the experimental lattice parameters, we calculated the electronic and magnetic properties of $CsCaH_3$ and $RbCaH_3$. The calculated DOS shows that $CsCaH_3$ and $RbCaH_3$ are non-magnetic. The direct band gap of 3.15 eV found in $CsCaH_3$ and 3.17 eV in $RbCaH_3$ meet the requirement for the application in high frequency ultra-violet device. The charge density plot of $CsCaH_3$ and $RbCaH_3$ indicate that the corner atom contributes mainly to increase charge density which also support from the potential distribution curve. From potential distribution of $CsCaH_3$ and $RbCaH_3$, we found that potential is maximum at core whereas flat at interstitial region. This may be the vital site to store the hydrogen and hence system acts as hydrogen storage materials. Finally we can conclude that TB-LMTO-ASA method can be used as a convenient method for studying the band structures and density of states of different solids. Our results may be useful to study the other various types of elemental solids and perovskites in future.

Acknowledgments

We are grateful to ICTP/OEA NET-56 program of Trieste, Italy for the partial support.

References

[1] B. I. Min, T. Oguchi, H. J. F. Jawsen, A. J. Freeman, Phy. Rev. B, 12 (2003) 1091.
[2] M. Fatmi, Rom. Journ. Phys. 56, (2011) 937.
[3] S. Lamichhane, N. Pantha, N. P. Adhikari, BIBECHANA, 11 (2014) 113.
[4] K. T. Chan, J. B. Neaton, M. L. Cohen, Phys. Rev. B, 77 (2008) 235430.
[5] S. Pandey, G. C. Kaphle, N. P. Adhikari , BIBECHANA, 11 (2014) 60.
[6] G. C. Kaphle, S. Ganguly, R. Banerjee, R. Khanal, C. M. Adhikari, N. P. Adhikari, A. Mookerjee Condens. Matter, 29 (2012) 295501.
[7] R. Hua, B. Lei, D. Xie, C. Shi, J solid State Chem., 175 (2003) 284.
[8] P. Vajeeston, P. Ravindran, H. Fjellvag, The J. Chem. Phys., 132 (2010) 114504.
[9] R. E. Cohen, Nature (London), 358 (1992) 136.
[10] C. Ang, A. S. Bhalla, L. E. Cross, Phys. Rev. B, 64 (2001) 184104.
[11] M. Dawber, K. M. Rabe, J. F. Scott, Rev. Mod Phys., 77 (2005) 1083.
[12] C. M. Jensen, K. J. Gross, Appl. Phys. A, 72 (2001) 213.
[13] B. Bogdanovic , M. Schwickardi, J. Alloys Compd., 253 (1997) 1.
[14] K. Shimamura, H. Sato, A. Bensalah, V. Sudesh, H. Machida, N. Sarukura, T. Fukuda, Cryst. Res. Technol, 36 (2001) 801.
[15] A. H. Reshak, M. Y. Shalaginov, Y. Saeed, I. V. Kityk, S. Auluck, J. Phys. Chem. B., 23 (2010) 1264.
[16] H. W. Brinks, B. C. Hauback, P. Norby, H. Fjellvåg, J. Alloys . Compd., 351 (2003) 222 .
[17] H. Morioka, K. Kakizaki, S. C. Chung, , A. Yamada, J. Alloys. Compd., 353 (2003) 310
[18] F. Gingl, T. vogt, E. Akiba, K. Yvon, J. Alloys. Compd., 282 (21999) 125.
[19] P. Vajeeston , H. Fjellvag, J. Chem. Phys., 132 (2010) 114504.
[20] H. L. Skriver, The LMTO Method: Muffin-Tin Orbitals and Electronic Structure, Springer-Verlag, 41, 1st Ed. 1984.
[21] U. Mizutani, The Electron Theory of Metals, Cambridge University Press, New York, 1st Ed. 2001.
[22] M. Maqbool, B. Amin, I. Ahmad, J. Opt. Soc. Am., B, 26 (2009) 2181.